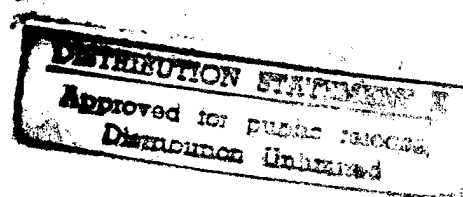SLL 84-U-117

SLL 84-U-117

PROCEEDINGS

OF THE SOCIETY OF PHOTO-OPTICAL INSTRUMENTATION ENGINEERS

Volume 171

Optical Components:
Manufacture & Evaluation

January 2

19980309 324

U4156

Accession Number: 4156

Publication Date: Jan 22, 1979

Title: Proceedings of the Society of Photo-Optical Instrumentation Engineers, Optical Components: Manufacture and Evaluation, Volume 171

Personal Author: Nicholson, D.

Corporate Author Or Publisher: Society of Photo-Optical Instrumentation Engineers, Bellingham, WA
Report Number Assigned by Contract Monitor: SLL 84-U-117

Comments on Document: Archive, RRI, DEW

Descriptors, Keywords: Optical Component Manufacture Evaluation Electrooptics Laser Fusion Data Reduction Interferogram Mirror Thermal Distortion Waxicon Accuracy Surface Aspheric

Pages: 00166

Cataloged Date: Dec 11, 1992

Document Type: HC

Number of Copies In Library: 000001

Record ID: 25792

Source of Document: DEW

Optical Components: Manufacture & Evaluation

Donald Nicholson
Editor

OPTICAL COMPONENTS: MANUFACTURE & EVALUATION

Volume 171

Contents

Seminar Committee

OPTICAL COMPONENTS: MANUFACTURE & EVALUATION

Volume 171

Chairman
Donald Nicholson
The Aerospace Corporation

Co-Chairmen
Lt. Col. Ron Prater
Defense Advance Research Projects Agency
Charles Hogge
AFWL/ALO, Kirtland AFB
Robert E. Parks
Optical Sciences Center
The University of Arizona
Verne Muffoletto
Muffoletto Optical Co.

Chairman Session 1—Evaluation of Systems
Charles Hogge
AFWL/ALO, Kirtland AFB

Chairman Session 2—Evaluation of Components
Robert E. Parks
Optical Sciences Center
The University of Arizona

Chairman Session 3—Components Descriptions and Fabrication Methods
Verne Muffoletto
Muffoletto Optical Co.

OPTICAL COMPONENTS: MANUFACTURE & EVALUATION

Volume 171

INTRODUCTION

This seminar addressed the production and evaluation of optical components. The first and second sessions were devoted exclusively to techniques used for the manufacture and evaluation of components for high energy laser systems. Topics covered included substrate preparation, surface generation and polishing, as well as the application of suitable coatings. A number of papers covered methods of assuring that components produced for high energy system applications comply with specifications. Techniques for nondestructive testing which correlate with those designed to determine limits of performance were examined. The third session dealt with components manufactured for other applications and included such topics as plastic components, replicated optics and electro-formed components. Techniques involving the use of computers and microprocessors to control the action of grinding and polishing tools were discussed, as were new, unusual, novel and unconventional techniques for the determination of product compliance with specifications. Other topics involved production methods appropriate to both volume and limited production runs.

OPTICAL COMPONENTS: MANUFACTURE & EVALUATION

Volume 171

SESSION 1

EVALUATION OF SYSTEMS

Session Chairman
Charles Hogge
AFWL/ALO
Kirtland AFB

THE NAVY ELECTRO-OPTICS (E-O) MANUFACTURING TECHNOLOGY PLAN

Andrew S. Glista
Naval Air Systems Command
Washington, D. C. 20601

Manuel R. Pablo
NAVMAT E-O Technology Program Office
Washington, D. C. 20375

Abstract

Until now, the development of an Electro-Optics Manufacturing Technology Plan has been primarily passive. That is, specific projects were selected from submitted Manufacturing Technology Proposal Briefs, (NAVMAT Form 4800/2) on the merits of each individual project. While some valuable projects came about as a result of this procedure, such an approach does not necessarily identify and address the most critical Navy needs in the area of Electro-Optics manufacturing. This paper has been prepared to:

Disseminate to the Navy E-O community, information on all E-O MT projects, either funded or submitted for funding.

Solicit comments on and prioritization for these existing E-O MT projects.

Solicit additional E-O MT projects or other valuable information (via a simple form).

Introduction

In order to provide a forum for the interchange of ideas useful for the development of a concerted Navy-wide Electro-Optics Manufacturing Technology (E-O MT) Program, an E-O MT Working Group was established in May 1978 with Andrew S. Glista as chairman. In October 1978 the Working Group, composed of representatives from all interested Navy Labs, formulated Table III, a list of anticipated Navy E-O MT projects, and the projected year of eligibility.

Definition and Interpretation of Manufacturing Technology

For the sake of completeness, the definition of Manufacturing Technology as contained in the governing Naval Material Command Instruction 4800.36C dated 26 April 1976 is presented below. In this instruction, Manufacturing Technology is defined as:

"The development of new, or the improvement of existing manufacturing processes, methods, techniques or equipment which when applied to production will reduce the cost of defense material and/or weapon systems. These new developments or improvements are normally based on R&D established feasibility or extrapolation of known technology and are production oriented. Manufacturing technology is not directed at design changes in the weapon system hardware as in value engineering, but instead to the fabrication/production of that hardware. It does include new methods of producing or processing the basic materials required for the fabrication of the hardware."

The instruction lists the manufacturing technology program objectives as follows:

a. To reduce the cost of Naval weapon systems.

b. To promote and establish improved manufacturing processes, methods, techniques and equipment for the most efficient and economical production of defense material, and to enhance the industrial manufacturing base.

c. To provide the manufacturing technology required to transition R&D advances to production status.

d. To stimulate industry to invest in and adopt new manufacturing techniques.

e. To assure that all manufacturing technology projects and actions are coordinated within the Department of the Navy and with the other Military Departments and government agencies to prevent duplication of effort.

f. To provide maximum dissemination of the results of manufacturing technology projects.

g.   To ensure the timely implementation of the results of manufacturing technology projects in weapon system production.

It should be understood that manufacturing technology is an identifiable line item in the budget. As such, it is subject to intense scrutiny in order to ensure proper expenditure of the assigned funds. Therefore, the Navy carefully reviews all proposals for compliance with the program requirements.

Criteria for a Manufacturing Technology Project

While the object of the Manufacturing Technology Program is cost reduction of procurred items, not all activities that result in reduced cost can properly be labeled Manufacturing Technology. The following programs are <u>not</u> considered as manufacturing technology:

    Plan Modernization
    Value Engineering
    Product Improvement
    Standardization
    Commercial Commodity Acquisition
    Integrated Material Management

Each of these programs is ultimately concerned with cost reduction but through a different medium than Manufacturing Technology. Thus, there are certain criteria that should be considered in the preparation of an MT proposal, namely:

a.   Cost reduction and improved productivity must result.

b.   Funds cannot be used for the express purpose of acquiring capital equipment or establishing a manufacturing facility.

c.   Feasibility must be proven.

d.   Funds cannot be used for basic product R&D. Recently, however, some funds from program element 63728 have been planned for FY 79 to be used for advanced development related to MT.

e.   Funds cannot be used for design changes which would alter form, fit, function or performance.

f.   Proposed MT is limited to the Navy mission requirements.

g.   MT funds will not be provided for a unique single use item. <u>Generic technology</u> will be supported. Single use item funding remains within the purview of the specific interested Navy program office.

h.   MT will provide seed funds only, beyond normal risk of industry.

i.   MT will not pay for technology in which private industry is expected to invest.

j.   Duplication of projects is to be avoided.

k.   Technology developed on MT funding will not be proprietary. Technology transfer between contractors will be expected.

Should a valid cost reduction scheme be identified that does not fit the definition and criteria for manufacturing technology, then an appropriate alternative program should be identified whose objectives are compatible with the means for cost reduction.

Scope of Navy Electro-Optics

An effort was made at the May meeting to display the scope of Navy Electro Optics and also bring about greater appreciation for the value of generic manufacturing technology projects. A set of electro-optical components was chosen, categorized by both their functional nature and some relevant manufacturing processes. The component categorization scheme is shown in Table I. Five generic types of components are listed: Sources, Sensors, Passive Components, Active Components, and Displays. Since no brief listing can be all exhaustive, the additional category of Non-Optical Devices was included to cover those that might not apply to any of the other categories.

Examples of devices for each of the component categories are shown to indicate the types of devices that form parts of Navy electro-optical systems. As such, each of them might conceivably be a candidate for a Manufacturing Technology program. If a component

were to be the basis of such a program, then the manufacturing process by which the component is made might be the subject of such a program.

The manufacturing processes that are applicable to some of the various components of Table I are shown in Table II. Again these are intended to serve as examples of the variety of processes that might be encountered.

Table III shows a list of Manufacturing Technology projects that have either been funded or are candidate programs for possible funding. It also lists the expected year of MT eligibility. The entries of Table I represent the elements from which operational systems might be composed.

Diversification of MT Project Sources

The more generic a Manufacturing Technology program is in terms of its ability to affect the cost of the basic components entering into a system, the greater the implication for overall reduced procurement costs and probably, the more difficult the documentation of these cost savings. Items such as assembly, test, inspection, packaging, mounting, etc., to which we have paid little attention, may represent a significant fraction of the cost of an electro-optical subsystem, and as such could be the subject of an MT project.

The objective of the Manufacturing Technology Program is to reduce cost. Return on Investment (ROI) and risk are the driving factors. Thus a low technology, low risk, manufacturing improvement with general applicability might be more effective as a cost saver than a high risk device improvement of less generic applicability even if the per-device savings is greater.

ROI is an important factor used in ranking projects. It is computed by adding the cost savings to be realized, and dividing by the cost of the MT project. That is,

$$ROI = \frac{(OLD\ COST - NEW\ COST) * N}{MT\ COST}$$

where: OLD COST = Original Cost
NEW COST = Reduced cost after application of MT process
N = Number of items to be purchased over 5 years
MT COST = Cost of MT proposal

ROI's of 5 or better are considered attractive.

TABLE I

COMPONENT CATEGORIZATION

SOURCES	SENSORS	PASSIVE COMPONENTS
DYE LASERS	SOLID STATE	MIRRORS
INJECTION LASERS	PMT	WINDOWS
GAS LASERS	IMAGING	GUIDES
SOLID STATE LASERS	CCD	LENSES
ARC–LAMPS	PIN	FACE PLATES
LED (ARRAY)	AVALANCHE	FILTERS
		POLARIZERS
		RECORDING MEDIA
		FIBER OPTICS
		INCOHERENT
		COHERENT BUNDLES
		COUPLERS

ACTIVE COMPONENTS	DISPLAYS	NON–OPTICAL
SCANNERS	LCD	COOLERS MECH THERM–ELECTRIC
SWITCHES	LED	SCANNERS
MODULATORS	CRI	ELECTRONICS RELATED DIRECTLY TO E–O DEVICES
NON–LINEAR DEVICES	PLASMA	TEST EQUIPMENT
	EL/TFT	
	ELECTRO–CHROMIC	
	TRITIUM	

TABLE II

MANUFACTURING PROCESSES

SOURCES	SENSORS	PASSIVE COMPONENTS
CRYSTAL GROWTH	MATERIAL GROWTH	COATINGS/DEPOSITION PROCESSES
MIRROR COATINGS	SEMICONDUCTOR TECH.	FORMING & SHAPING
SEALING & JOINING TECH.	VACUUM TUBE PROCESSING	REPLICATION
SEMICONDUCTOR PROCESSES	TESTING PACKAGING HERMETIC SEALS	POLISHING
FORMING & MACHINING		PHOTO PROCESSING
POLISHING		
PACKAGING, TESTING		
METROLOGY ETC.		

ACTIVE COMPONENTS	DISPLAYS	NON-OPTICAL
CRYSTAL GROWTH	SEMICONDUCTOR PRO-CESSES	CONTAMINATION CONTROL (COOLERS)
	VACUUM PROCESSES	
	MATERIAL GROWTH & DEPOSITION	

TABLE III - (continued)

PASSIVE COMPONENTS	80	81	82	83	84	85
Nd:YAG Laser Optics		X				
Precision Machining	X					
Protective Coatings		X				
Multispectral Coatings		X				
Optical Finisheing Techniques		X				
Low Reflectance Black Reticle (AIM-9M)		X				
Passive Optical Sensors			X			
UV Multilayer Filters		X				
Fiber Optics	X					

ACTIVE COMPONENTS	80	81	82	83	84	85
Second Harmonic Generation (COMPASS HAMMER)				X		
Acousto-Optic Modulator					X	
Integrated-Optics Spectrum Analyzer						X
LiNbO$_3$ Q-Switch		X				
Scanners (Sea Search)			X			

DISPLAYS	80	81	82	83	84	85
Flat Panel Holographic Displays						
NON-OPTICAL	80	81	82	83	84	85
Dark Field Schlieren		X				
Airy Apparatus		X				
Digital Interferometer		X				

TABLE III — Proposed E-O MT Projects

SOURCES	80	81	82	83	84	85
GaAlAs Injection Lasers	X					
Hi Power Pulse GaAs	X	X				
InGaAsP				X		
InP Substrates		X				
Arrays (diode)	X					
Dye Lasers					X	
MINI-TEA CO_2 Laser				X		
CO_2 Hybrid Laser						X
Nd:YAG Rods		X				
Arc Lamps					X	
InGaAsP LED				X		
Dual Wavelength Rods (COMPASS HAMMER)				X		
Excimer Lasers					X	

SENSORS	80	81	82	83	84	85
Visible CCD		X				
IR FPA			X			
IR Quad APD 1.06 μm			X			
IR Quad APD 10.6 μm						X
IR Single Crystal Alloy (SCA)	X					
SIT Tubes	X					
UV PMs		X				
Pyroelectric Vidicon (SEAFIRE)				X		

AN OPTICAL EVALUATION LABORATORY
FOR LASER FUSION*

J. L. Munroe and G. Woodfin
Los Alamos Scientific Laboratory
University of California
Los Alamos, NM 87545

Abstract

The Antares CO_2 laser system is being constructed at the Los Alamos Scientific Laboratory (LASL) to investigate inertial confinement fusion. Antares will be a very large laser system, with 72 beams and a total beam area of some 6 square meters. There will be thousands of optical components, predominantly copper-plated mirrors and sodium chloride windows. To coordinate the specification, procurement, evaluation, and disposition of these components, a centralized Optical Evaluation Laboratory (OEL) is being set up. The OEL is principally a quality-control facility for routinely evaluating the optical performance of components and assemblies with apertures of up to 18-inch diameter. However, the OEL has a much broader involvement and responsibility for the Antares optics. Virtually every piece of optics in Antares will be specified and ordered through the OEL. After acceptance, the OEL will be responsible for tracking the history of each optical component via a computerized data base. This paper describes the Optical Evaluation Laboratory facility and its operation.

Introduction

The Laser Fusion Program at the Los Alamos Scientific Laboratory (LASL) is developing high-energy carbon-dioxide (CO_2) lasers for the demonstration of scientific feasibility of laser fusion in the mid-1980's. This effort, supported by the Department of Energy, Office of Laser Fusion, has the goal of providing fusion energy for commercial power to help satisfy the nation's future energy requirements.

The short-pulse, high-energy CO_2 laser is a very promising candidate for a fusion reactor system. It has a demonstrated efficiency in excess of 2% with a potential efficiency as high as 10% and, because it uses a gaseous laser medium, it can be designed to operate at the high repetition rates required for commercial power generation. The 10.6-μm wavelength has been demonstrated to be effective in producing thermonuclear yield at modest power levels.

There are presently two operational CO_2 laser-fusion systems at LASL, the 1-kJ Gemini system, and the 10-kJ Helios system. Under construction and scheduled for completion late in 1983 is the 100-kJ Antares system. Antares has the goal of demonstrating scientific breakeven, in which the energy delivered by the laser is matched or exceeded by the energy produced by the fusion reaction. Scientific breakeven will be a major milestone toward commercial power generation from laser fusion.

Materials Consideration

The choice of materials for operation at a wavelength of 10.6 μm is limited. Laser fusion requires very short pulses, in the order of one nanosecond. Materials used must have sufficiently high damage thresholds to routinely withstand the resulting high instantaneous power densities. Early in the laser train, before full amplification, one has a relatively wide choice of materials and, consequently, zinc selenide and germanium are used extensively. After amplification, however, the energy densities and power densities become sufficiently high that the choice of materials becomes severely limited. The optics in the CO_2 lasers at LASL consist predominantly of polycrystalline sodium-chloride (NaCl) windows and copper-plated mirrors. The mirror substrates are aluminum or aluminum-bronze, a copper alloy.

The choice of these materials stems from many considerations including cost, stability, strength, and damage resistance. Polycrystalline NaCl offers a substantially higher yield strength over single-crystal NaCl, a major consideration because some of the windows separate 3 atmospheres of CO_2 mixture from vacuum. In the hands of an experienced optician, polycrystalline NaCl can be given a good optical figure. The choice of plating copper onto a substrate combines the virtues of very pure copper with the dimensional stability characteristics of an alloy. For our smaller mirrors, which are typically conventionally manufactured, the substrate choice is aluminum bronze, a copper alloy. The excellent

---

thermal match between aluminum bronze and the plated copper eliminates any significant bimetal effect. Bimetal effect is the result of different thermal expansion coefficients for the plated material and the substrate material, and causes the mirror to bow with temperature change. Aluminum bronze, being approximately 90% copper, has a thermal expansion coefficient very close to that of the plated pure copper. For our larger mirrors, which are typically single-point diamond turned (SPDT), the substrate choice is aluminum alloy type 2124. The copper plating is an almost inconsequential part of the total mass of the larger mirrors, which greatly reduces any tendency toward a bimetal effect. For the larger mirrors, the sheer weight of a much heavier bronze substrate would introduce more serious complications than any small, residual bimetal effect. The Antares environment will be controlled to $\pm1^\circ C$, which further reduces the impact of any bimetal effect.

Variety of Optical Components

Although most of the components used for laser fusion at 10.6 μm tend to be plated copper mirrors and NaCl windows, there is a very large variety of sizes, shapes, and materials. Component sizes range from less than 1 inch in diameter to 18 inches in diameter. Component shapes include round, annular, rectangular, and trapezoidal. Materials used include polycrystalline and single-crystal NaCl, zinc selenide, barium fluoride, calcium fluoride, cadmium sulphide, germanium, and copper. In addition, many of the copper mirrors are produced by SPDT, which gives them very different figure characteristics from conventionally manufactured parts.

The components are predominantly windows and plano mirrors. However, there are a substantial number of slow spheres, typically ranging from F/10 to F/40, and the final focusing element for Antares is a trapezoidal-shaped F/6.3 off-axis parabola. Antares will require some 2500 optical components.

Antares begins with a single oscillator that can produce up to six lines. The preamplifier annular output is divided into six smaller beams, each of which becomes input for one of the six driver amplifiers. The annular output from each driver amplifier is further divided into 12 smaller beams in each of the 6 power amplifiers. The fully amplified Antares laser output comes from the 6 power amplifiers each divided into 12 smaller beams. The power amplifier output travels through evacuated beam tubes into the target chamber where all 72 beams are focused onto the target. The Antares power amplifier and target system is a 72-beam system, requiring 72 of each component plus spares. Antares has both a large variety of optical component types and large numbers of identical components.

It is sometimes assumed that optics for use at 10.6 μm need not be of very good optical quality by visible standards. Antares has a very long and complex optical train consisting of many optical components. To achieve the required near-diffraction-limited performance, most of these components must be of an optical quality measured in fractional visible fringes. The error budget for Antares is dominated by the large SPDT mirrors, typically between 1 and 2 visible fringes in quality, and the 18-inch-diameter polycrystalline NaCl window, typically good to 1 or 2 visible fringes in transmission. The error budget has allocated nearly all of the allowable error to these state-of-the-art components by holding the smaller, conventional elements to a sufficiently high quality that they do not measurably impact the total error in the final wavefront. Thus, these smaller elements must be of moderately good quality, quarter to half fringe in the visible.

The Optical Evaluation Laboratory (OEL)

At LASL it has long been recognized that optics play a very major role in laser fusion systems. With Antares entering the construction stage, 10 times larger than any previous laser fusion system at LASL, the need for a centralized optical facility becomes clear. This facility, the Optical Evaluation Laboratory (OEL), is nearing completion adjacent to the Antares complex. The OEL will incorporate the capabilities of an existing, smaller facility, and will expand upon these capabilities. The OEL will also play a more centralized role at the optical component and subassembly level. The responsibilities of the OEL include the following:

1. Specifications and Drawings. The OEL will translate the end-user's requirements into a consistent and standardized set of drawings and specifications. Centralizing this effort eliminates needless duplication of effort and gives better assurance that the end user obtains what he requires. It also helps avoid putting unnecessarily tight tolerances on a part and increasing the cost.

2. Procurement and Source Development. The Laser Fusion Program has no plans to develop any internal optical manufacturing capability and thus plans to rely on the optical industry for manufacture and refinishing. We plan to inventory sufficient spares so that damaged components can be immediately replaced and sent out for refinishing. The OEL will

coordinate and centralize the technical aspects of all the procurement and refinishing activities for Antares. The OEL will also endeavor to identify and work with a sufficient number of sources that competitive procurements can be used wherever possible.

3. **Incoming Inspection and Quality Control.** The OEL will be the receiving point for all Antares optics. As described below, the OEL will be well equipped to perform all required tests to assure that the received parts conform to LASL requirements. The OEL will see that the specifications are reasonable and that we receive what is specified. Present plans call for 100% inspection.

4. **Cleaning, Handling, and Assembly Procedures.** The OEL will maintain a current set of procedures on the cleaning, handling, and assembly of the Antares optics. These procedures will incorporate the experiences of LASL and of our vendors. Since we are dealing with some unusual materials, these written procedures will be useful to all concerned.

5. **Inventory Control.** Using a computerized data base and the part number and serial number assigned to each component, the OEL will track the history of each optical component. Initially, the emphasis will be on knowing where a given part is. Later, we will undoubtedly discover differences in the behavior of certain components where knowing the manufacturer, and its original quality becomes important.

Major Capabilities of the OEL

The OEL will be a well-equipped facility, prepared to fully inspect and evaluate any component that we order. The capabilities will allow measurements on pieces ranging in size from as small as 0.25 in. in diameter to as large as 18 in. in diameter. Although most of our parts tend to be windows and flat mirrors (thus the emphasis on Fizeau type devices) the OEL will also be capable of evaluating concave and convex elements. The OEL is being equipped to maximize speed and reliability when evaluating many identical components, yet have the flexibility to respond to most foreseeable requirements.

The major capabilities of the OEL include:

1. **Zygo Fizeau-Type Interferometers.** Currently, we have a 4-inch-aperture Zygo Model GH with an 18-inch-aperture arm. This device can operate with either a 4-inch beam or an 18-inch beam. The Model GH will soon be replaced by a Zygo Mark II, which incorporates a 6:1 zoom, allowing easier and more accurate evaluation of intermediate diameter pieces. After the upgrading, the Model GH will be available for simultaneous small-aperture work.

The Zygo interferometer system, a Fizeau-type device, is used for the windows and flat mirrors, which are the bulk of our work. With attachments, the Zygo system is occasionally used to evaluate weak concave and convex elements.

2. **Tinsley Unequal Path Laser Interferometer (UPLI).** We have two Tinsley UPLI interferometers, both of a Twyman-Green configuration. These are used for evaluating concave spheres and related tests such as Ritchey tests. The chief virtues of the UPLI are its portability and versatility. For example, they will be used to test the off-axis parabolas.

3. **16" Diameter, 106" FL Davidson Collimator.** The Davidson collimator is an all-reflective system incorporating an on-axis parabola and a flat with a small central obscuration. The applications for this versatile device are limited mostly by lack of imagination. It can operate conveniently at almost any wavelength as a collimator, a beam expander, or even one arm of a very unequal path laser interferometer. We are finding this collimator particularly useful for measurements and experiments at 10.6 m.

4. **33-Foot-Long Optical Rail.** This rail was once a lathe bed in a ship yard. It is isolated from the floor by air mounts and provides a versatile, stable platform for many experiments and measurements. Most measurements involving the UPLIs are done on the optical rail.

5. **Data Reduction Capability.** The OEL operates and maintains the current version of FRINGE, the interferogram reduction computer program written by John S. Loomis of the University of Arizona. Our version of FRINGE, Version 3, has the capability to analyze noncircular apertures. This is particularly important to Antares, where most of the large mirrors are trapezoidal in shape.
Presently, the interferogram data is transferred to the computer via a platen digitizer. The operator moves a cursor along the fringe contours on a photograph and the digitizer unit relays the cursor location to the computer. Because of the large volume of optics involved and the tedious nature of manually digitizing large numbers of interferograms, the OEL is in the process of obtaining a Zygo ZAPP system. ZAPP, which stands for Zygo Automatic Pattern Processor, will automatically digitize a real-time fringe pattern

or a hard-copy interferogram. Initially, it will directly give peak-to-valley and rms wavefront variations, but the long-range plan is to feed the output directly into FRINGE. ZAPP will be used mostly for evaluation of conventionally manufactured, round optics.

6. Miscellaneous Equipment. The OEL has a number of optical quality flats and spheres ranging from 12 inches in diameter to 20 inches in diameter. There is also a large variety of smaller precision optics useful for experimental and quality-control type applications.

Unique Aspects of Optical Evaluation for Laser Fusion

The OEL at LASL deals with some rather unusual components. Probably the most unique and the most exciting is our involvement in the evolving technology of mirror manufacture by SPDT. This technology, whereby mirrors are literally cut on a lathe, is being developed with LASL support at the Y-12 Plant at Oak Ridge, Tennessee, operated for the Department of Energy by the Union Carbide Corporation. The quality of these mirrors is already very impressive, typically between one and two visible fringes peak to valley. SPDT allows the rapid manufacture of large quantities of nonsymmetric mirrors where the clear aperture extends nearly to the edge. SPDT is a technology which is almost a prerequisite for Antares to be successful.

The SPDT mirrors produce fringes with more intermediate and high spatial frequency content than one would obtain from conventionally manufactured mirrors. Although it does tend to make interferogram reduction a bit more complicated, the effect of the higher frequency terms is not as serious as one might first expect. It can be shown, by subjecting the fringe pattern to a Fourier decomposition, that the higher frequency terms tend to diffract light into very low intensity rings far from the image. These rings are of such low intensity that the energy is effectively lost and the influence of these high frequency terms can be equated to a simple reflection loss. However, these high frequency terms do tend to mask the more important low frequency terms and an experienced eye is required to detect their presence.

Polycrystalline NaCl windows produce similar interferograms. The overall figure can be quite good, one to two visible fringes for a 16-inch-diameter piece, but the figure error tends to be somewhat masked by high spatial frequency terms from discontinuities at the grain boundaries. Again, these high spatial frequency terms are more a cosmetic error. Their main impact is to make fringe interpretation difficult.

Another complication arises from the non-circular shape of many of our components. The larger, diamond-turned mirrors are quasi-trapezoidal in shape. The formalism of optics, Seidel coefficients or Zernike coefficients, is based on a circular aperture. The meaning of such terms as astigmatism and coma for a quasi-trapezoidal aperture may be clear qualitatively but are more difficult to quantify. More work needs to be done on how to properly interpret aberration coefficients when they are derived for a circular aperture but applied to a more general aperture shape.

Conclusion

Laser fusion is a very exciting program and optics is at its very heart. With Antares, the number and required quality of optical components has increased dramatically. The Optical Evaluation Laboratory will play a crucial and central role in helping make Antares the successful forerunner of the energy source of the future.
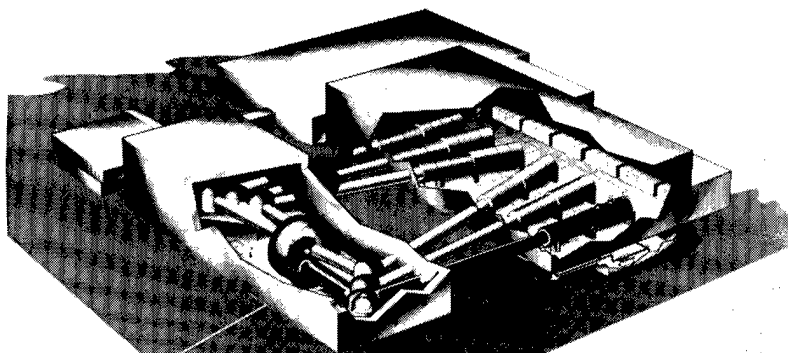
Fig. 1. Artist's conception of the High Energy Gas Laser Facility
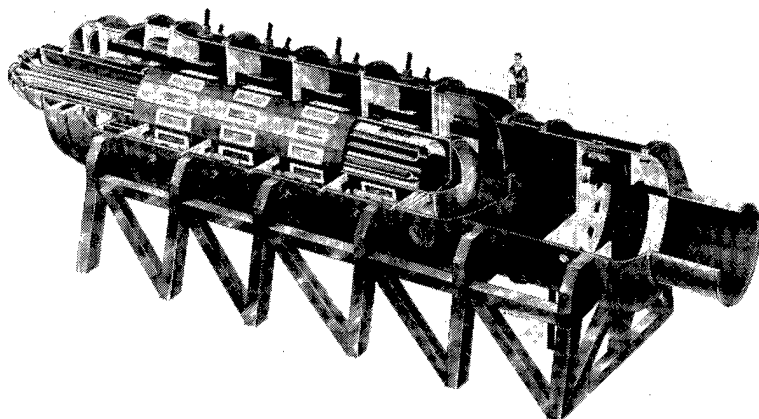incorporating Antares, the 100-kJ CO_2 laser system.

Fig. 2. Artist's conception of a single Antares power amplifier.
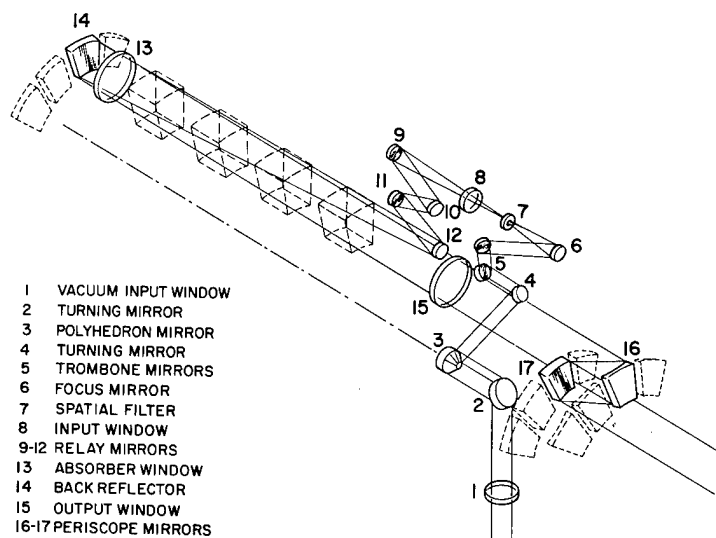Antares consists of six such power amplifiers.

1	VACUUM INPUT WINDOW
2	TURNING MIRROR
3	POLYHEDRON MIRROR
4	TURNING MIRROR
5	TROMBONE MIRRORS
6	FOCUS MIRROR
7	SPATIAL FILTER
8	INPUT WINDOW
9-12	RELAY MIRRORS
13	ABSORBER WINDOW
14	BACK REFLECTOR
15	OUTPUT WINDOW
16-17	PERISCOPE MIRRORS

Fig. 3. Optical Schematic of a typical Antares power amplifier
illustrating the splitting of the annular input beam into
12 quasi-trapezoidal beams.

OPTICAL CHARACTERIZATION OF HIGH ENERGY LASER COMPONENTS*

Gary A. Willinski
University of Dayton Research Institute
Dayton, Ohio 45469

Abstract

Techniques for assessing the performance of optical components for infrared high energy laser systems are described. The techniques include photometry and interferometry of large aperture components, diffraction grating efficiency measurements, absorption calorimetry, and reflectometry. A brief summary of the methodology of each type of measurement is presented.

Introduction

The Optical Component Evaluation Laboratory (OCEL) is operated by the University of Dayton Research Institute (UDRI) to support Air Force Weapons Laboratory (AFWL) high energy laser programs by assessing the performance of optical components. The facilities used include lasers and equipment to measure reflectivity, absorption, optical path difference, and diffraction grating efficiency at several wavelengths and under different optical and mechanical loadings. The OCEL contains five basic areas that can be used to make these measurements. These areas are: the Laser Window Test Apparatus (LWTA), High-Power Test Area (HPTA), Environmental Test Area (ENTA), calorimetry, and reflectometry areas.

The LWTA is a temperature and humidity-controlled area in which photometry and interferometry of transmissive samples can be measured. The samples can vary in size from 1 cm to 1 m and up to about 150 kg mass.

The HPTA consists of a Sylvania 971 1 kW CO_2 laser directed onto an optics table having beam diagnostic and precise shuttering capabilities. This laser is used as a torch type laser in most applications for studying component survivability, or for its heating effects, as in flash calorimetry.

The ENTA is a computer-controlled chamber capable of simulating environmental conditions of pressure, altitude, humidity, heat, or cold. An optics table is available to support the measurements of stress, strain, deformation, or possible destruction of the optical element being tested under one or more simulated conditions. The external windows for the Airborne Laser Laboratory were proof tested on this chamber prior to flight to insure their airworthiness.

The mirror calorimetry laboratory uses a laser to irradiate sample mirrors mounted in a vacuum chamber. The temperature rise of the sample is proportional to the absorption coefficient.

The reflectometry area uses a laser and two detectors to measure the ratio of the light reflected from a surface to the total incident light. Diffraction efficiency is characterized as a ratio of the light intensity incident upon the surface to the intensity observed as a function of diffraction order and polarization.

Although these five test areas are separate and distinct, their capabilities can and, in the past, have overlapped. This overlap insures better characterization of the optics.

Laser Window Test Apparatus (LWTA)

The LWTA has the capability of characterizing large component infrared optics by photometry, interferometry, and window calorimetry. These measurements are made on a point-by-point basis to map the entire optical component. The LWTA consists of a rastering device with a specimen mount, optical table with instrumentation, minicomputer, signal processing equipment, and an environmental enclosure.

The rastering device provides specimen movement horizontally or vertically to any position accurate to within ± 0.01 mm. A 120 cm x 60 cm flat-surfaced carrier is used for carrying specimen mounts and adapters. Carrier motion is controlled by a two-axis numerical controller which provides manual or completely automatic control through the Varian minicomputer.

The LWTA photometer uses a CO_2 laser radiation source to measure front-surface reflectance and single-pass transmittance of a window as a function of position on the window. The window is moved stepwise in a raster pattern to achieve the desired set of window locations at which photometric measurements are made. The laser beam is split into three components: (1) a reference beam from a beamsplitter to monitor the laser amplitude, (2) a reflected beam from the front surface of the window, and (3) a transmitted beam which has passed once through the window. Each of these beams, plus background, is independently presented to a detector in a predetermined sequence. The analog detector signal is immediately digitized, and appropriate data reduction algorithms are applied to generate reflectance and transmittance. From this data the single-pass attenuation is deduced. Reflectance, transmittance, and attenuation are the ratios of front-surface reflected power, single-pass transmitted power, and single-pass attenuated power respectively to the incident power. Attenuation includes both absorption and scattering. The minicomputer controls every aspect of the raster-machine operation, the photometer data acquisition and reduction, and the periodic calibration-sequences. Figure 1 is an optical schematic of the photometer and Figure 2 shows a general photometer flow chart. A more detailed explanation of the photometer operation is presented in References 1, 2, and 3.

Test specimens have been characterized with reflectances as low as .01 percent and as high as 99.7 percent. The photometer output is a map of the entire sample tested.

The LWTA interferometer uses a CO_2 laser radiation source to measure the relative double-pass optical-thickness variations of a candidate window as a function of position on the window. The window is moved continuously in a raster pattern to achieve the desired set of window locations at which interferometric measurements are gathered while the window is in motion. Figure 3 is an optical schematic and Figure 4 shows a general flow chart of the interferometer. The interferometer is essentially a double Michelson interferometer in that after the laser beam is split into two components, a reference beam and a window beam, each of these beams is further split. The reference beam is split into one beam which is directed to a fixed reference mirror and the other beam directed to a constant-velocity Doppler mirror. Likewise the window beam is split into two beams, one is directed to the window and the other to the same Doppler mirror. The reference Doppler-shifted beam and the reference beam are recombined and directed to the reference detector. The window Doppler-shifted beam and the window beam are also recombined and directed to the window detector. Each detector sees a sinusoidally varying output at the Doppler frequency caused by the motion of the Doppler mirror. The two detector signals are then compared using an electronic phase meter. The difference between the phase meter signals (phase angle) at two locations on the specimen provide a direct measurement of the double-pass optical phase difference between the two locations. The advantages of the Doppler technique are that the interferometer is essentially insensitive to intensity variations, is highly precise, and is non-ambiguous. The precision of the interferometer was calculated from the point-by-point difference between the data from several pairs of runs. The random component of the difference was consistently 0.01 λ so the precision can be assumed to be 0.01 λ. A more detailed explanation of the interferometer operation is presented in References 1 and 2.

Although the photometer and interferometer are the heart of the LWTA, many other measurements can be made because of the versatility of the LWTA area. In the past other measurements such as grating efficiency mapping, reflectometry (as a backup to the reflectometer, especially for large, heavy optics), and flash calorimetery have been made.

Flash calorimetry is the technique of measuring the local absorption of a transparent specimen by measuring change in Optical Path Difference (OPD) while it is being irradiated and then relating OPD to temperature rise and hence, absorbed energy. Figure 5 shows an optical schematic of the flash calorimetry setup. The parameters measured are torch beam power and window OPD versus time. The window thickness, the torch beam power distribution, and bulk absorption of the window material are known. Computer calculations are used to predict OPD versus time for different values of surface absorption, and then compared with the experimental data to determine localized surface absorption of the window.

Calorimetry Area

The precision calorimeter area uses a system that compares the change in temperature of a mirror sample, caused by the absorption of the incident radiation, to the temperature change in the same mirror sample when electrical calibration techniques are used. An optical schematic is presented in Figure 6, and a general calorimeter flow chart is presented in Figure 7. The components of the calorimeter: collection mirrors, calorimeter cones, and mirror mounts, are thermally isolated and mounted in a vacuum enclosure to insure a long thermal time constant. The system is based upon the ratio technique of Saito, et al presented in Reference 5.

During a measurement the calorimeter cone, collection mirror and specimen are electrically loaded to calibrate the apparatus. The specimen is then irradiated with a 10 watt

CO_2 laser for 40 seconds. The ratio of the electrically induced temperature rise and the optically induced rise determines the fraction of energy absorbed under operational loading. This method does not require knowledge of the heat capacity or temperature sensitivity of the sensors; however, it requires that all energy not absorbed by the sample be taken into account. The temperature sensors mounted on a duplicate set of components (collection mirror, calorimeter cone, and specimen) allow compensation for temperature changes from background radiation.

The present apparatus has been in operation since October 1977, and over 400 mirror samples have been measured. Absorption coefficients as low as 1×10^{-4} with a repeatability of 1 percent, and an accuracy of 10 percent of the absorbed value, have been observed. During the measurement accuracy analysis, it was observed that the accuracy was unaffected for chamber pressure between 1 and 100 millitorr. The accuracy decreased at 500 millitorr.

Tests that require rapid completion and can tolerate less accuracy are implemented using a separate production calorimeter. The production calorimeter has an accuracy of approximately 10 percent of the measured value, for absorption coefficients of 1×10^{-3}.

Reflectometers

Two methods are used for determining the reflectivity of mirrors. The WV type reflectometer is an absolute measurement because the reflectance of a reference mirror is involved in each measurement, hence its reflectance need not be known. The single bounce method requires a calibration standard to normalize the measurements.

The output beam of a CO_2 laser is directed to a set of turning mirrors to select a specific polarization; the beam is then chopped and split. One beam is used as a power level reference, and the other beam goes to the test specimen. Figure 8 shows an optical schematic and Figure 9 a general reflectometer flow chart. The WV technique utilizes a flat mirror on a rotating stage. After the first measurement is taken on the reference mirror M_1, the stage is rotated 180 degrees, and the front surface of the test specimen M_2 is placed over the center of rotation. The square root of the second intensity measurement divided by the first gives the reflectivity of the second mirror.

A separate single bounce method is used for testing gratings and large component optics that cannot be accommodated on the rotation stage.

Grating Efficiency Measurements

Gratings are set up on the indexed rotary stage of the correct angle of incidence and polarization. The intensity of each order is measured and the zero order is compared to a reference mirror of known reflectivity in order to normalize the data.

Summary

In conclusion the equipment and methods described are adequate to optically characterize most high energy laser components. The OCEL's major limitation is the size and weight of large components requiring characterization.

Acknowledgments

The author wishes to thank Dr. George T. Johnston for his unique inspiration and encouragement, and Dr. Marion L. Scott for constructive comments.

References

1. Dueweke, P. W., I. B. Fiscus, R. L. Fusek, D. D. Preonas, and H. F. Swift, "The AFWL Laser Window Test Apparatus," Third Conference on Infrared Laser Window Materials, Hyannis, Mass., 1973.
2. Dueweke, P. W., D. D. Preonas, D. G. Peterson, Jr., "The Air Force Weapons Laboratory Laser Window Test Apparatus" AFWL-TR-73-181, June 1974.
3. Preonas, D. D., "Ultra-Precision Photometry of AR Coatings," Fifth Annual Conference on Infrared Laser Window Materials, Las Vegas, Nevada, 1975.
4. Dueweke, P. W., J. M. Kester, R. J. McBroom, and D. D. Preonas, "Optical Characterization of Windows for the Airborne Laser Laboratory," Fourth Annual Conference on Infrared Laser Window Materials, Tucson, Arizona, 1974.
5. Saito, T. T., A. B. Callender, and L. B. Simmon, "Calorimeter to Measure the 10.6 μm Absorption of Metal Substrate Mirrors," AFWL-TR-76-63.
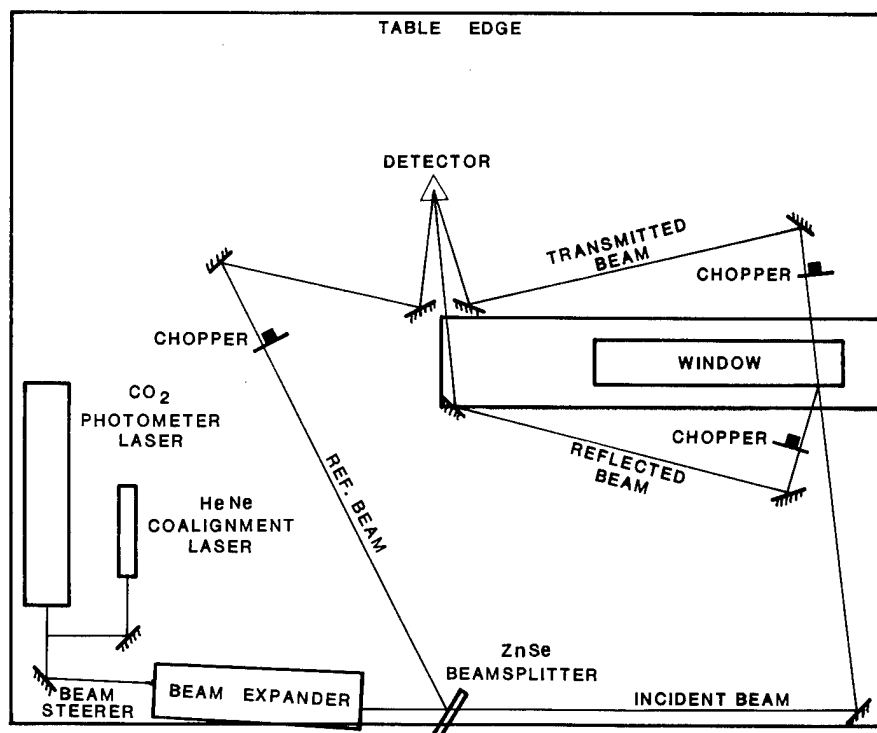
Fig. 1. Photometer Optical Schematic.

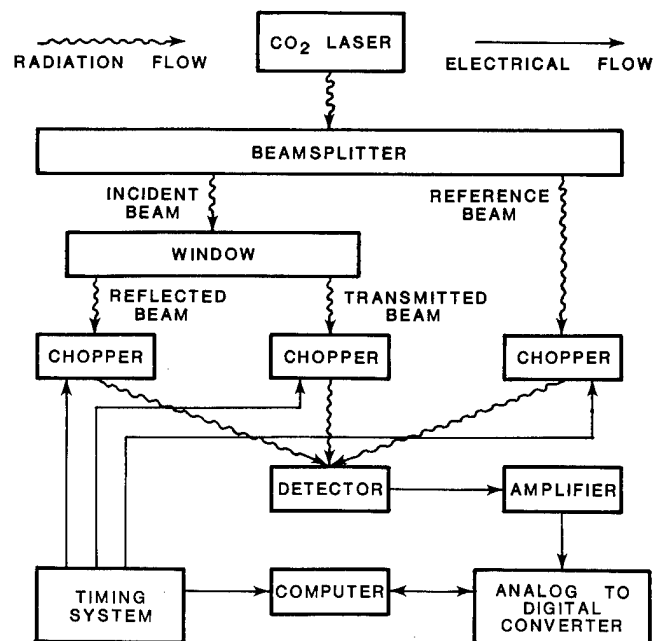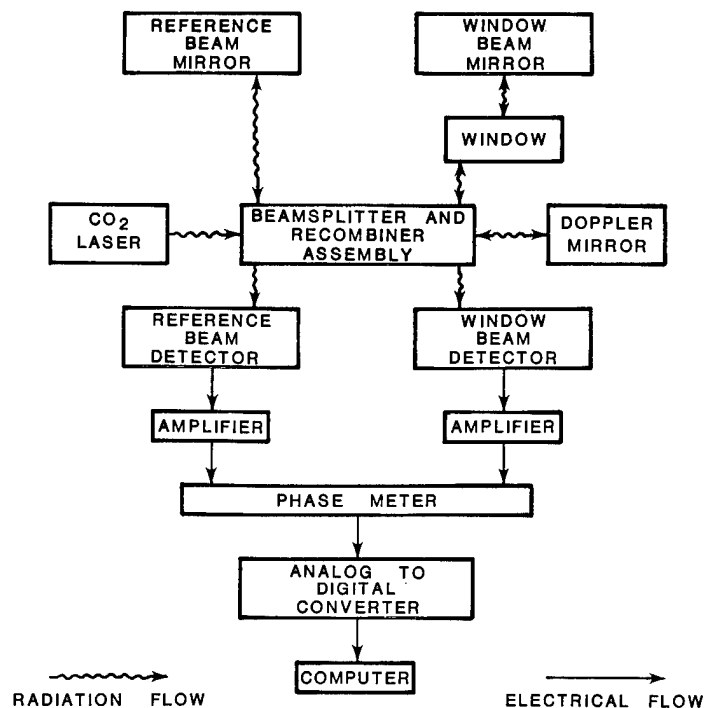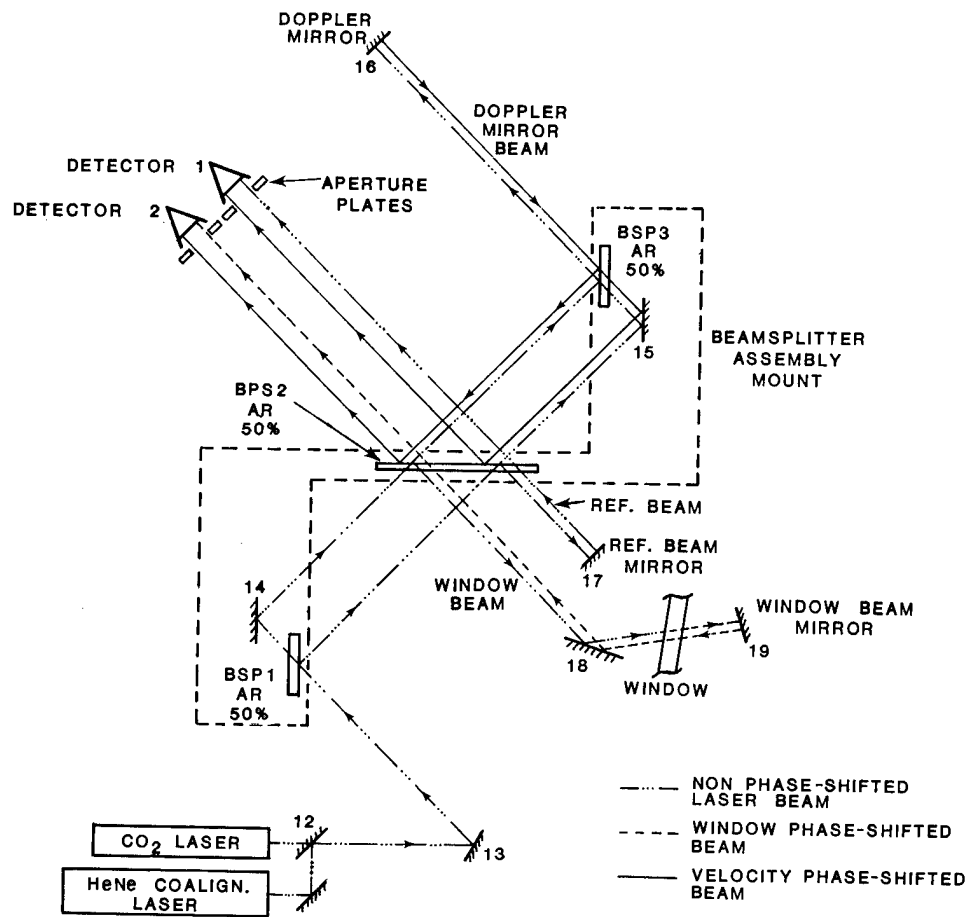Fig. 2. LWTA Photometer Flow Chart.

Fig. 3. LWTA Interferometer Schematic.
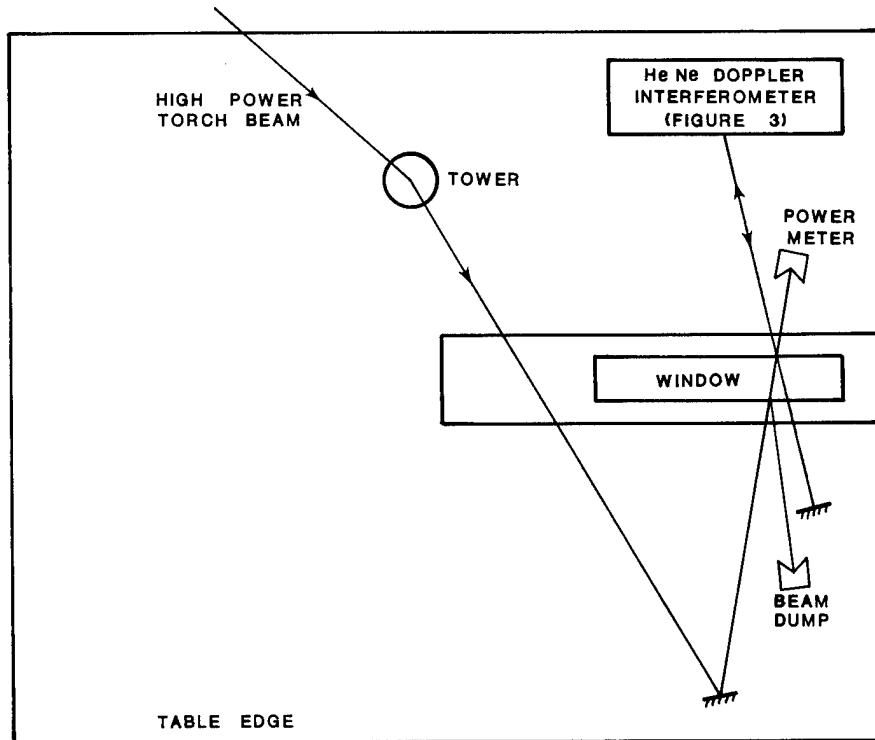

Fig. 4. LWTA Interferometer Flow Chart.

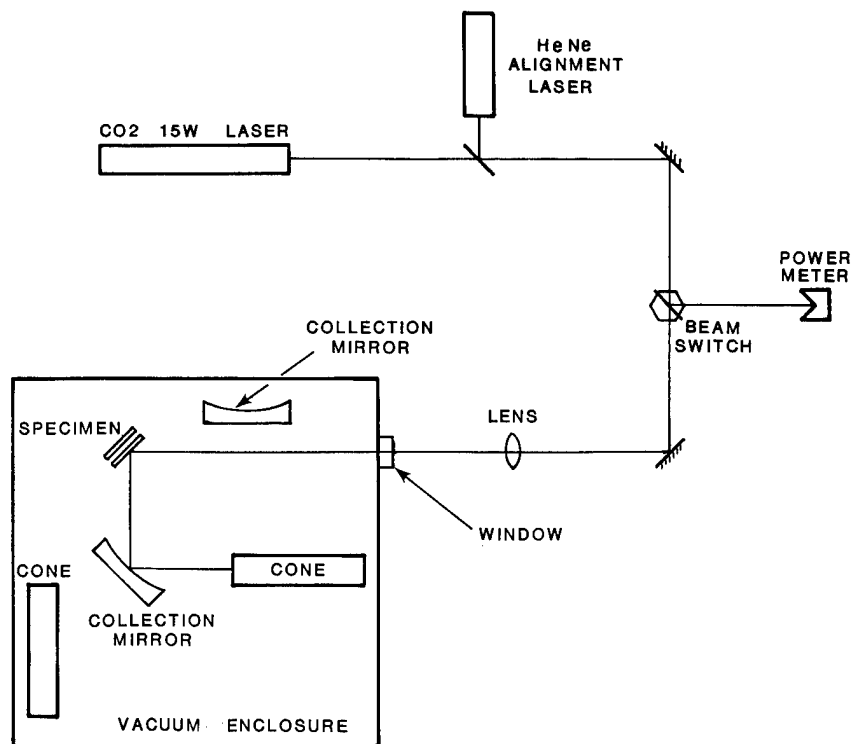Fig. 5. Flash Calorimetry.

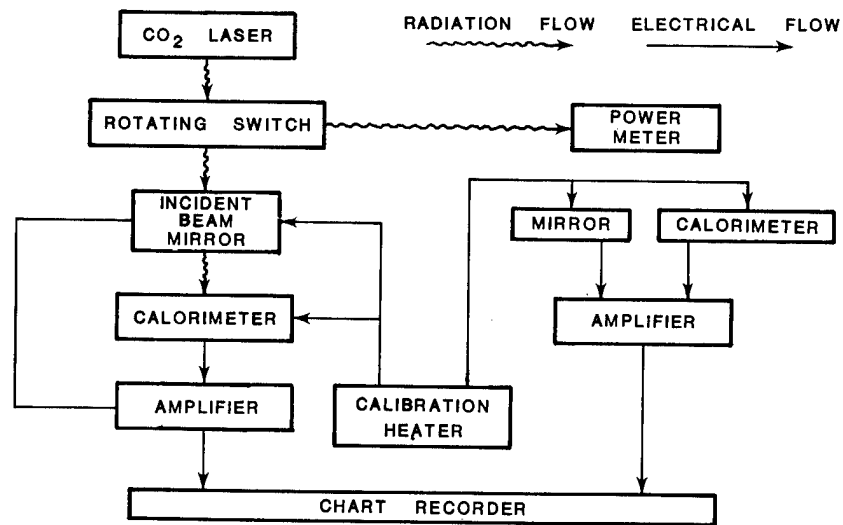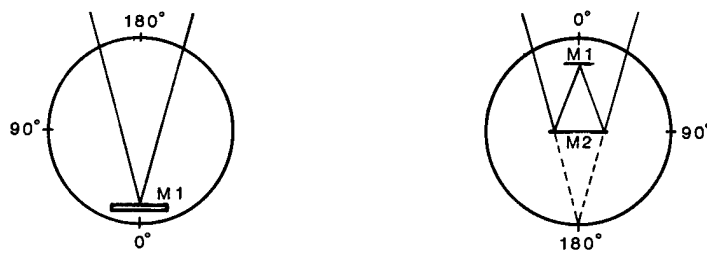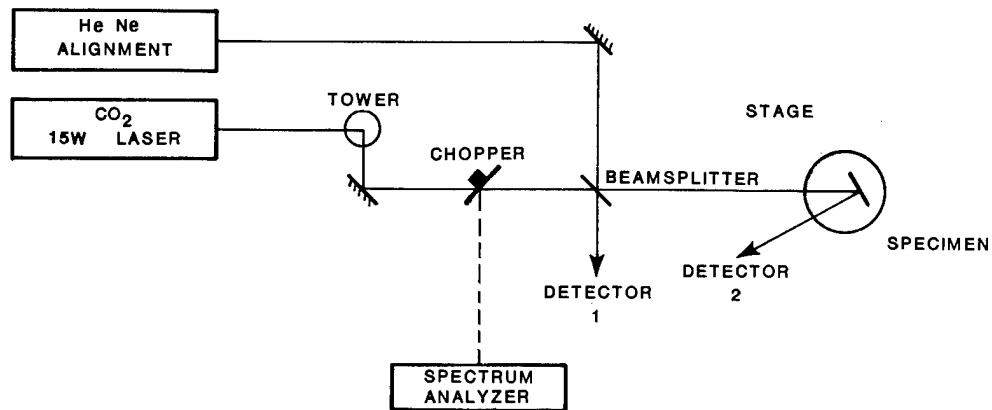Fig. 6. Precision Calorimeter.

Fig. 7. Calorimeter Flowchart.

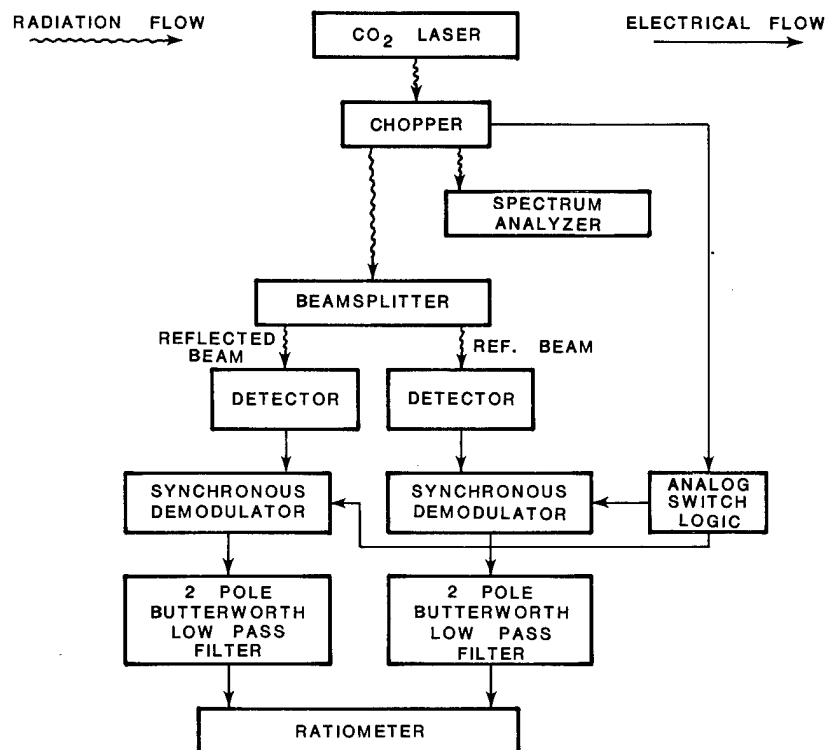Fig. 8. Reflectometer Optical Schematic.

Fig. 9.   Reflectometer Flowchart.

AUTOMATIC DATA REDUCTION OF BOTH SIMPLE AND COMPLEX INTERFERENCE PATTERNS

Walter H. Augustyn
Zygo Corporation
Laurel Brook Road, Middlefield, Connecticut 06455

Abstract

This paper describes an automatic pattern processor which can be utilized for re-
ducing both simple and complex interference patterns derived from high quality optical
surfaces. The complex patterns may be produced either by optical interference phenomena
or by contour patterns obtained from either holographic or Moiré techniques.

The rapid, accurate measurement and analysis of even simple interference patterns
has heretofore been tedious and time consuming due to the unavailability of objective,
affordable instrumentation. In practice, many interference patterns can have poor con-
trast, such as in some Moiré or holographic tests; large fringe deviations, such as in
aspheric testing; and high spatial frequency deviations, as with diamond turned surfaces.
For these cases, the measurement problems become significantly more formidable.

Introduction

Many interference patterns consist of an orderly array of nearly parallel fringes
with at most a few waves of curvature. Fortunately these patterns characterize a major
portion of the finished optical components or systems. Figure 1 is a typical pattern.
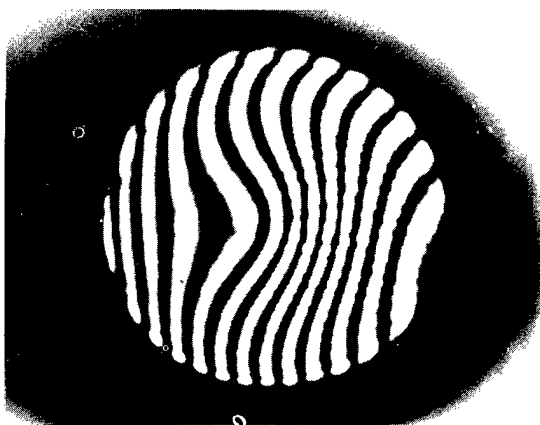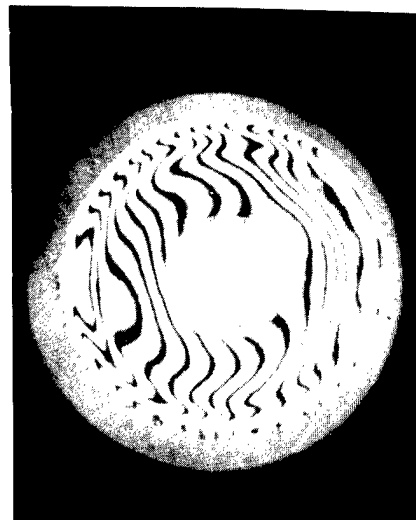

Fig. 1. Typical Interferogram

Fig. 2. Complex Interferogram

Often one wishes to know the quality of a component or system at a point prior to
the end of the manufacturing process when the interference patterns do not deviate in an
orderly fashion such as in Fig. 2. Furthermore, these patterns may be additionally com-
plicated by the nature of a manufacturing process, e.g. diamond turning.

The purpose of this paper is to describe the methods and limitations by which an
automatic interference pattern processor and an interferometer can be used to aid greatly
in the reduction of complex interference patterns. To this end, these techniques support
the in-process manufacturing activity.

Equipment Description

The instrumentation used to obtain the results described herein consists of the
Zygo Automatic Pattern Processor (ZAPP) and the Zygo Mark II Interferometer. It is
assumed that the use of an interferometer is sufficiently understood so that further
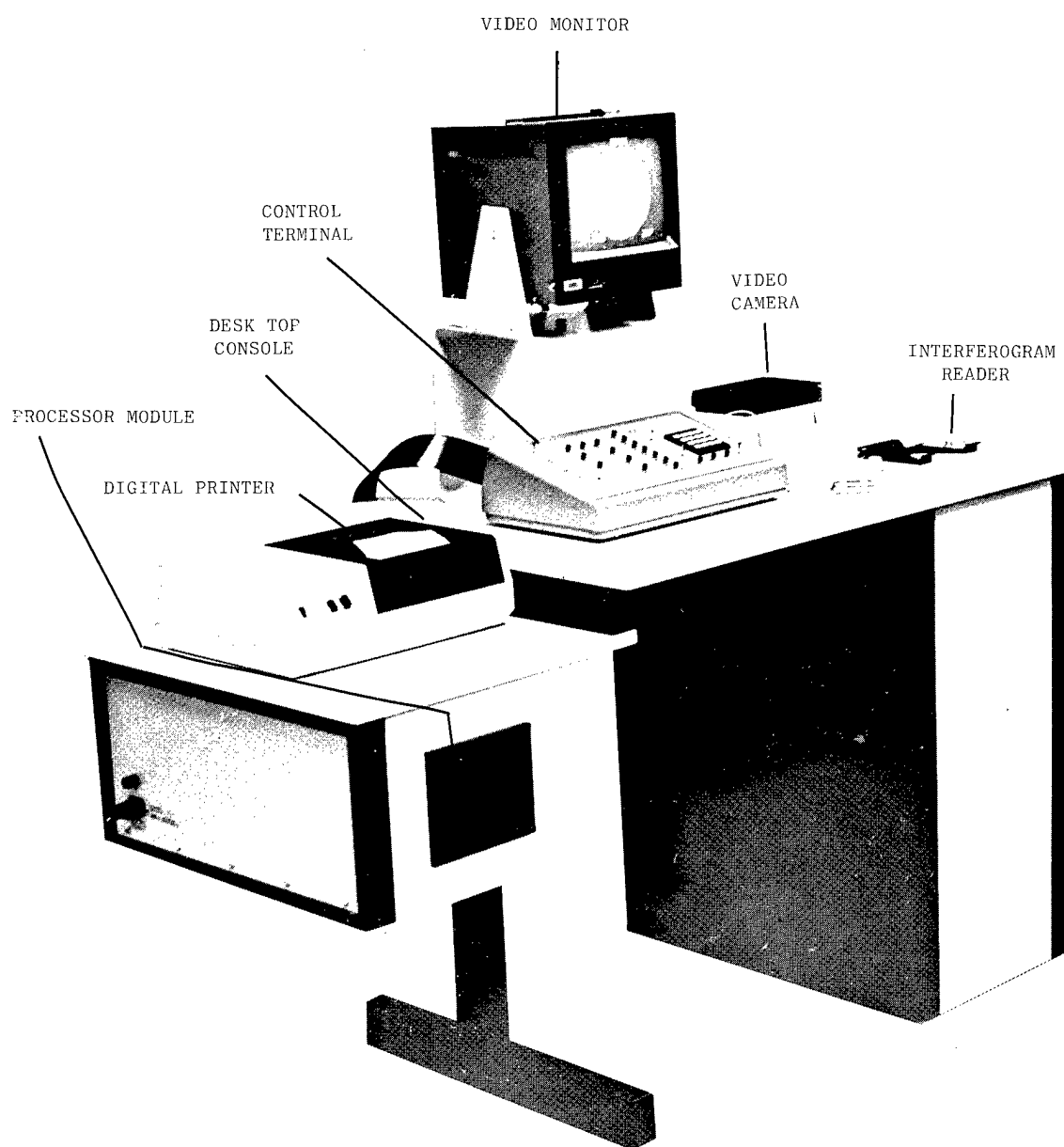
Fig. 3. Zygo Automatic Pattern Processor (ZAPP)

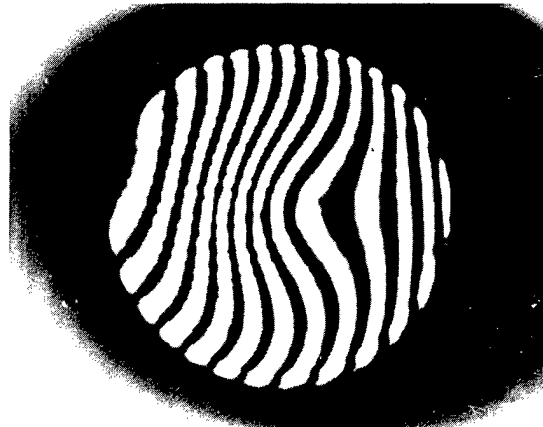Fig. 4. Interferogram
to be Reduced

Fig. 5. Set Aperture
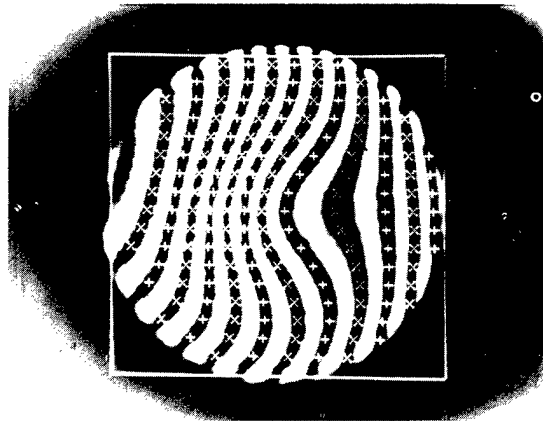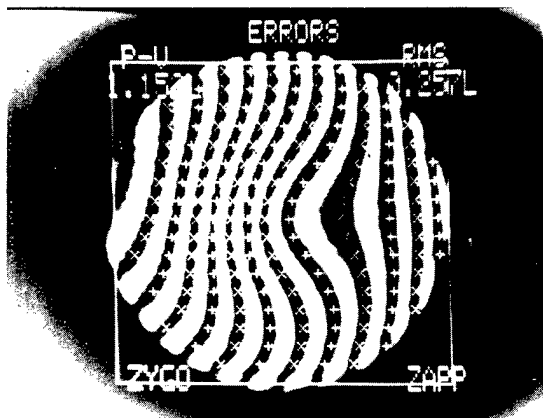Cursors and
Acquire Fringe
Centers

Fig. 6. Compute
Peak-to-Valley
and rms Analysis

discussion will not be provided here.   The ZAPP system shown in Fig. 3 has been described elsewhere,* but a brief review of its operation is presented here.

Several modes of operation may be selected including automatic, manual, and fiducial. Generally, the automatic mode is used for the rapid acquisition of the co-ordinates of the interference fringe centers. The manual mode is used either to edit the automatically acquired data, if needed, or to completely digitize the fringe pat-tern. The fiducial mode allows digitization of the coordinates of any fiducials in the aperture. Figure 4 depicts an interference pattern viewed on a CCTV monitor. The operator adjusts the cursors which define the clear aperture via the control console. In the automatic mode depressing the MEASURE pushbutton causes the system to measure the coordinates of the fringe centers falling inside the clear aperture in 1/60 second for up to approximately 500 fringe centers. The automatically acquired fringe centers are then displayed on the monitor viewscreen so that the operator can verify that the automatically acquired coordinates are correct (see Fig. 5). If any of the coordinates are incorrect they can be erased and new ones inserted. Depressing the COMPUTE push-button causes the processor module to perform the least squares analysis yielding the peak-to-valley and the root-mean-square deviations as shown in Fig. 6. In the automatic mode, the complexity of the fringe pattern which can be scanned is dependent upon the proximity of adjacent fringes and their maximum slope. In the manual mode, the com-plexity of the fringe pattern which can be digitized is limited by the system software to those fringe patterns which are not closed or horizontal and which do not have more than 25 fringes.

Complex Patterns

Interference patterns are characterized as complex because they contain much more information than is normally required by the user. In order to extract only the information pertinent to the user's requirements it is necessary to remove this extraneous information. The process used will depend upon the nature of the excess information and the information desired by the user. In general, reducing the com-plexity of interferograms is accomplished in two ways. The first involves the type of test setup that is used to create the interferogram and the second involves the nature of the fringe acquisition and data reduction. Only a limited number of examples will be given here, but these examples will be significant ones in the sense that they will use the key capabilities of the pattern processor.

Interferograms of aspheric surfaces can be complex because they are usually ob-tained using spherical reference wavefronts. Since these surfaces can depart by many wavelengths from the best fitting spherical wavefront, one obtains interferograms similar to that in Fig. 7. The departure at the edge of the aperture beyond the fluffed-out fringe is so great that the fringes can-not be resolved. Short of making a few diametral measurements to ascertain sym-metry, very little can be said about the quality of the surface. In order to avoid the superfluous information (which in this case is the large fringe departure from a sphere) one should look for a more suitable test configuration. Fortunately, many aspheric curves represent slightly higher order departures from pure conics. There-fore these curves may be tested to yield fringe patterns which possess only slight departures from purely spherical wave-fronts. The decision for each case is to select a test setup so that the closest fitting conic curve is nulled out. As an example, when the element in Fig. 7 was retested as an hyperboloid (which is the nearest fitting conic) using an inter-ferometer and a spherical mirror, the fringe pattern shown in Fig.2 was produced. This interferogram shows the residual zonal

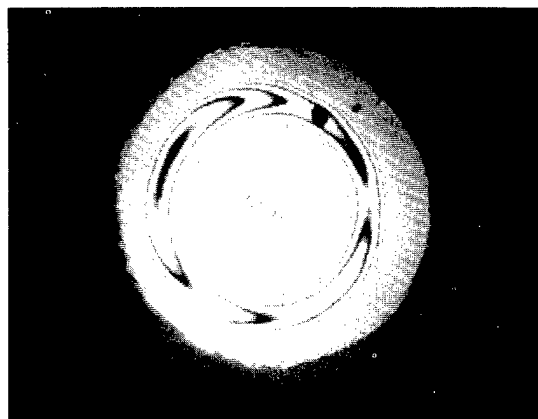
Fig. 7.   Aspheric Departure from
Best Fitting Sphere

*W. H. Augustyn, A. H. Rosenfeld, and C. A. Zanoni, "An Automatic Interference Pattern Processor with Interactive Capability," Proceedings of the Society of Photo-Optical Instrumentation Engineers (SPIE), Vol. 153 (to be published).
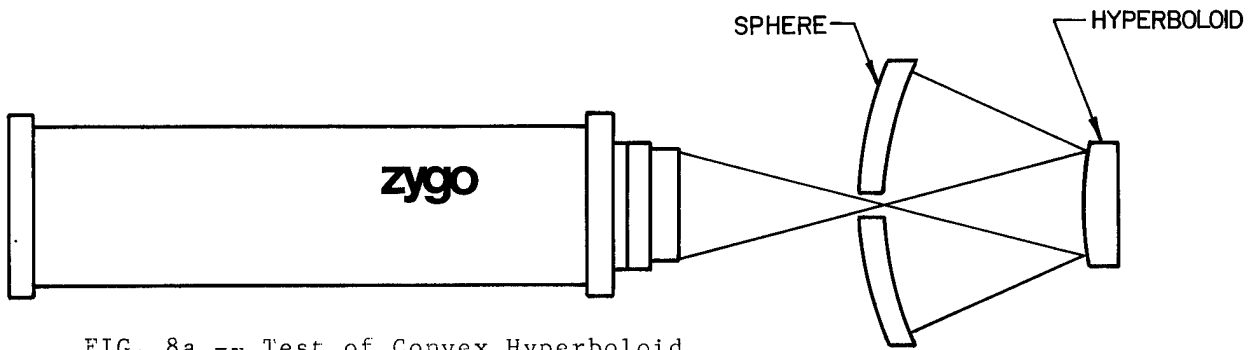
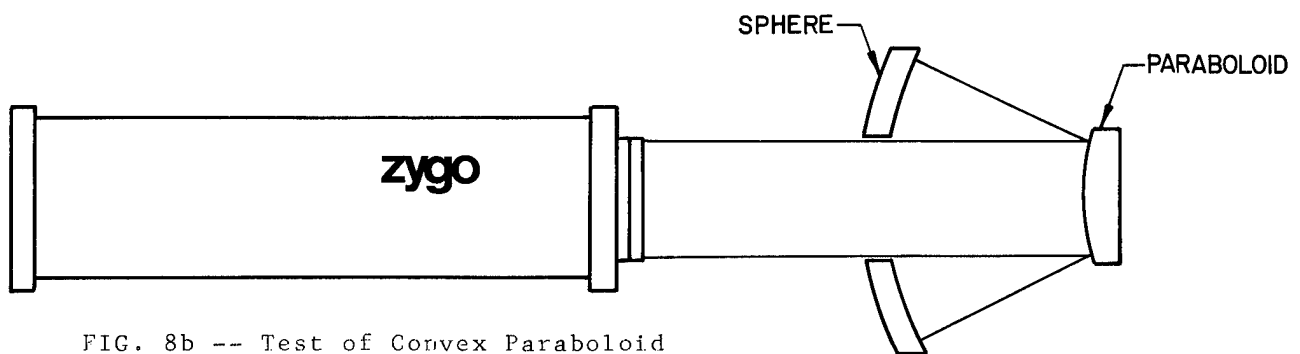FIG. 8a -- Test of Convex Hyperboloid

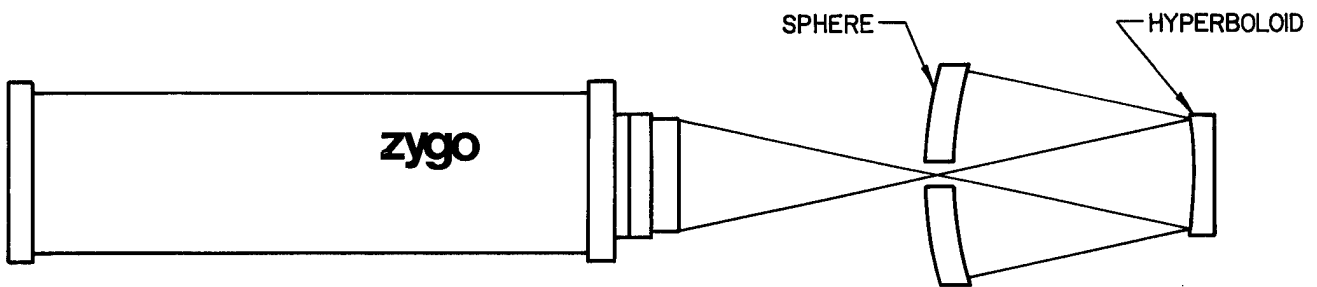
FIG. 8b -- Test of Convex Paraboloid
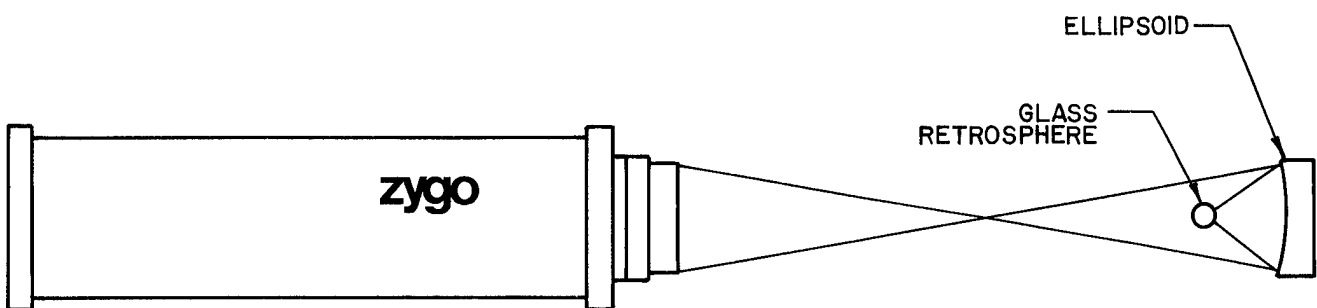

FIG. 8c -- Test of Concave Hyperboloid

FIG. 8d -- Test of Concave Ellipsoid

errors and asymmetry remaining in the surface. Furthermore, the fringes are clearly visible to the edge of the aperture. Figure 8a demonstrates the test configuration. Light emerges from a transmission sphere and is focused at the focal point of the imaginary sheet of the convex hyperboloid. This light is retroreflected by a spherical surface with its center of curvature coincident with the conjugate focal point of the hyperboloid. The interference cavity is formed between the reference surface of the transmission sphere and the spherical mirror. In this setup a one quarter wavelength surface error causes a one fringe departure in the wavefront; however, it will be shown that this does not affect the data reduction process. Test configurations utilizing conjugate imaging for other aspherics are shown in Figs. 8b, 8c, and 8d.

These tests do not remove the effects of the higher order aspheric terms which is seldom necessary since for most cases the resultant fringe pattern can conveniently be reduced. Additional null lenses can be incorporated with these tests when the resulting pattern has a large departure. These additional configurations would be necessary only for departures from conic sections of the order of a few fringes.

Fundamentally it can be stated that one should seek a method to eliminate by null test or desensitization the unwanted information present in the interference pattern. One obvious form* of desensitization is the use of a longer wavelength interferometer.

Data Reduction

One finds that even with null testing or desensitization residual wavefront departures from pure spheres remain. In these cases one is left with the problem of measuring all of the error and then somehow subtracting the effects of the residual aspheric departure from the measured optical path difference (OPD). The ZAPP system can perform this type of analysis in the subtract mode. The first step required is to construct an accurate artificial interferogram representative of the residual error for a given test setup. This pattern is then digitized and the OPDs stored in the ZAPP system memory. In a second step, the interferogram of the actual part is digitized. When the SUBTRACT button is depressed, the OPDs of the stored pattern are automatically subtracted from the OPDs of the actual interferogram. In this way the user has the pertinent information, namely, the difference between the two patterns. The interferogram of the hyperboloid shown in Fig. 2 was digitized and the errors calculated with and without power removed (see Figs. 9a and 9b). In this case only power is removed since the part is a perfect hyperboloid. The resultant OPDs can then be printed out or a
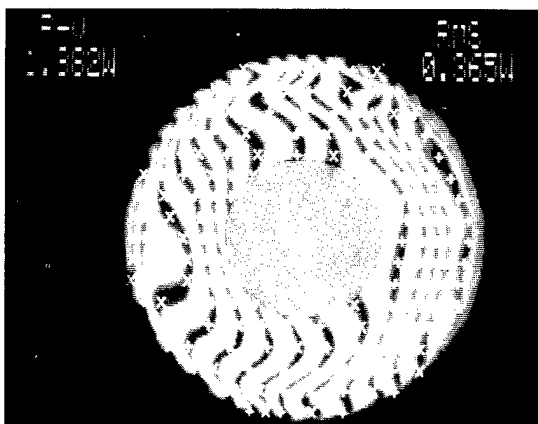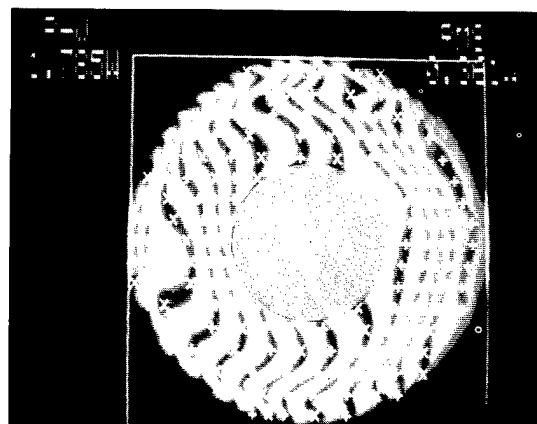

Fig. 9a.   Hyperboloid Data Reduction

Fig. 9b.   Hyperboloid Data Reduction with Power Removed

3-dimensional plot can be displayed on the monitor from which a hard copy can be

*Other forms include computer generated holograms and Moiré techniques.

obtained. This interferogram was digitized by using a combination of automatic and manual methods. The interactive mode allows erasure and insertion of points at the discretion of the operator.

As it was stated earlier, other forms of complex patterns arise due to the manufacturing process. Typical of such a pattern is the one shown in Fig. 10. In this case the nearest fitting conic section was an ellipsoid. The erratic pattern results from the diamond turning process used to manufacture the surface.

The interference pattern in Fig. 10 at first may appear to defy a sensible reduction in spite of the fact that it has no large deviations. The fringes are discontinuous and very densely packed. Recalling that one fringe equals one quarter wave surface error means that if every fourth fringe is measured then a direct one-to-one correspondence with the surface error is obtained. By placing a transparent overlay on Fig. 10 and tracing every fourth fringe allows construction of a surrogate interferogram providing the surface error. (See Fig. 11a.) (The tracing may be facilitated by first enhancing the fringes of interest on the interferogram.) The fringe spacing used on the overlay was approximately 12mm. Fringes can be drawn easily and quickly to within 1mm meaning the resultant error

Fig. 10. Diamond Turned Ellipsoid

would be 1/12 wave on the surface. The overlay shown (Fig. 11b) was then automatically reduced on the pattern processor with the result shown in Fig. 11c. In this way complex patterns can be reduced in minutes.
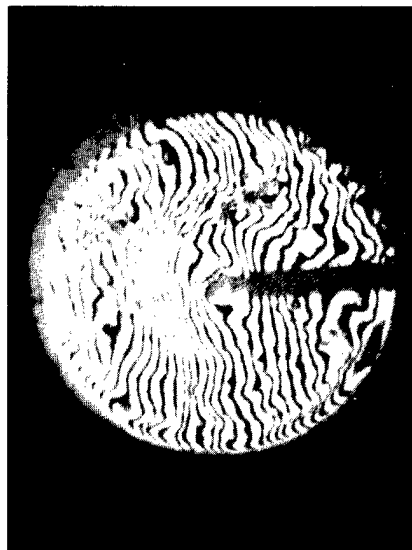
Perhaps the most difficult interference patterns are those containing very low contrast fringes with superimposed background fringes and artifacts. Typical of this type of pattern is the one shown in Fig. 12a. Because of the poor contrast, it would appear that the entire pattern needs to be manually digitized; however, this was not the case. The automatic mode of operation acquired approximately 70% of the fringe centers. The manual mode was then used to edit incorrect points with the final result shown in Fig. 12b. It would be virtually impossible to reduce this type of pattern with any other technique.

Finally, with regard to closed fringes or circular fringes, methods have been published* for reducing these types of patterns by scanning diameters and digitizing them accordingly. The automatic acquisition and analysis of data of this nature utilizing modest equipment awaits future software developments.

Conclusion

It has been shown that an automatic pattern processor combined with a judicious choice of test setup provides a powerful tool for reducing interference patterns that normally could not be completely evaluated. The combination of the automatic and manual modes of operation provides the necessary flexibility to the user enabling the types of reduction described. The further capability of reducing real time or hard copy interference patterns yields additional versatility particularly when complex patterns require analysis. The system's performance is not compromised when interference patterns contain greater than one wave phase shifts as is the case with other measurement systems. For those situations involving extremely complex patterns which cannot be reduced in real time, all that is necessary is a photograph that can then be processed utilizing one of the methods outlined.

*M. Francon, Optical Interferometry, Academic Press, New York (1966), p. 276.

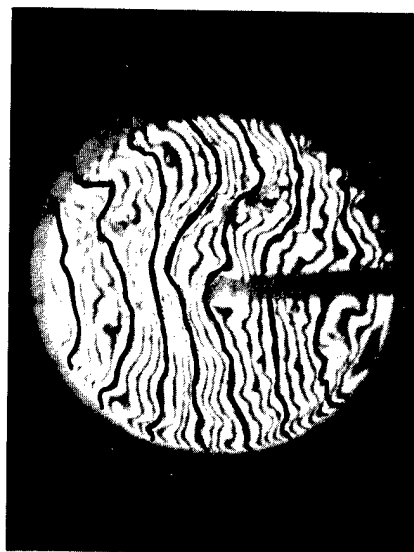Fig. 11a. Original Photograph with 4 fringes = 1λ (enhanced)
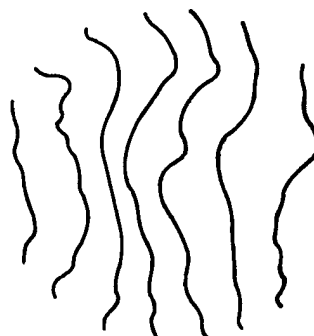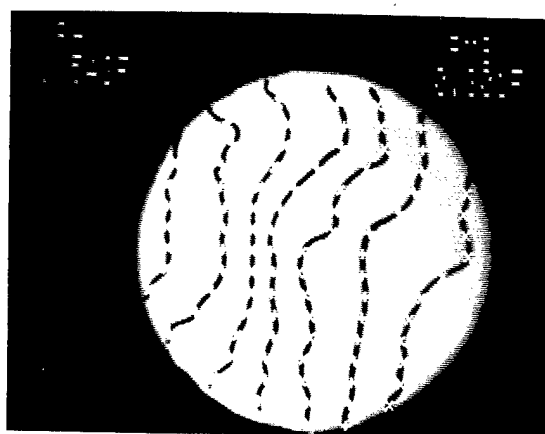
Fig. 11b. Redrawn Pattern

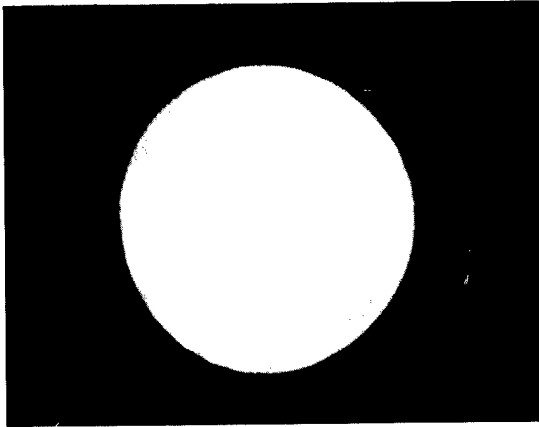Fig. 11c. Automatic Acquisition of Redrawn Pattern
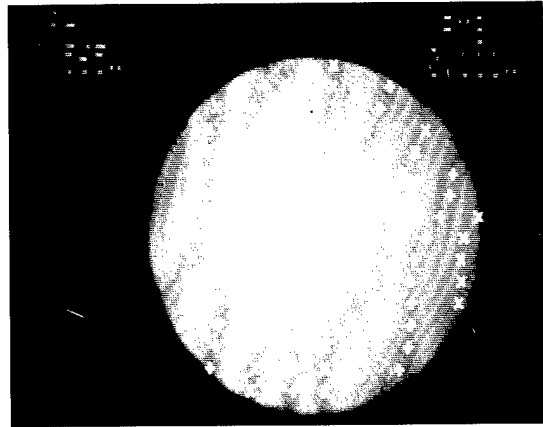
Fig. 12a.   Poor Contrast Interferogram

Fig. 12b.   Data Reduction on Poor
Contrast Pattern

The following questions were submitted at the conclusion of the paper--

QUESTION: Does your system provide for piecewise acquisition of interferograms if the tilt variation exceeds your system capability?

> --Francois M. Mottier
> United Technologies Research Center

ANSWER: By dividing the interferogram into subsets and limiting each subset using the clear aperture cursors will allow piecewise acquisition of interferograms. In addition, the subsets may be identified for later recombination using the fiducial mode of operation. After all of the fringe centers have been measured, they must be transferred to an auxiliary computer for recombination of the subsets and final analysis.

QUESTION: Does the Zygo ZAPP system have the ability to interface with FRINGE to supply full reduction of interferograms including Zernike description. Is Zygo working on such an interface and will it be generally available to purchasers of the Zygo equipment?

> --Lt. Col. Don Prater
> DARPA

ANSWER: The Zygo ZAPP system can provide the fringe center coordinates and the fringe order numbers through a standard RS-232C interface to an auxiliary computer capable of running the FRINGE analysis program. The auxiliary computer is not provided by Zygo but is assumed to be accessible by the user. FRINGE is capable of fitting Zernike polynomials to the measured data. The RS-232C interface is currently available with ZAPP.

MULTI-ACTUATOR DEFORMABLE MIRROR EVALUATIONS

John R. Kenemuth

Air Force Weapons Laboratory, Kirtland AFB
Albuquerque, New Mexico 87117

Abstract

Two high-speed, multi-actuator deformable mirrors have been characterized in terms of their abilities to provide low order Zernike mode shapes. Both mirrors are piezoelectrically activated with one having 61 actuators in a concentric circular array and the other having 52 actuators in a corner-truncated square array. Tilt, focus and astigmatism modes have been imposed with good linearity and fidelity. Superposition of multiple modes has also been successfully demonstrated. Problems encountered are listed.

Introduction

An evaluation program has been conducted on two high-speed, many-actuator deformable mirrors to determine how well they could be made to conform to low order Zernike mode shapes. Both single mode and superposition of modes implementations have been investigated. Detailed measurements of the imposed modes have been made only under static conditions. Satisfactory operation under dynamic conditions has been inferred from frequency response measurements at each of the actuator locations and from the satisfactory operation of the mirror in a system configuration. This modal approach was chosen because of the reduction in control system complexity which can be realized through implementation of this technique.

The voltages to be applied to the individual actuators were determined using the displacement required at each actuator location for the desired mode shape, average values for the influence coefficients between the various actuator locations, and the electromechanical gain calibration for the actuators. Although the conformity of the mirror surface to the desired mode shape can typically be improved by iterating the imposed voltages, the results presented here have not been refined in this manner and are the results achieved using the initial calculations of the required voltages.

The ability of the mirrors to assume the desired Zernike mode shapes was measured by placing the deformable mirror in a Twyman-Green interferometer which had been modified to include an expanding telescope in the sample arm in order to fully illuminate the polished area of the deformable mirror. Interferograms were obtained using 0.6328 micrometer illumination. These interferograms were digitized and then analyzed by fitting the data to a Zernike expansion using a least squares technique. The quantitative figure-of-merit for the surface fidelity was taken to be the RMS deviation of the mirror surface from the desired mode shape.

Mirror Characteristics

Significant characteristics of the two deformable mirrors are shown in Table 1. Although roughly comparable in size, they are considerably different in design and in displacement capability. In particular, the actuator array geometry is a series of concentric circles for mirror #1 and a square array with the corners truncated for mirror #2. Note also that, since the mirrors were designed for use at different wavelengths, mirror #2 has an absolute displacement capability approximately 3.5 times greater than mirror #1. These differing

Table 1. Deformable Mirror Characteristics

Characteristic	Mirror #1	Mirror #2
Mirror material	Molybdenum	Molybdenum
Active aperture diameter	16.5 cm	21 cm
Number of actuators	61	52
Actuator array geometry	Concentric circles (1,6,12,18,24)	Square (8x8 - 3x4)
Actuator spacing	~2 cm	3 cm
Piezoelectric material	Gulton HDT 31	Physics Int. PZWT 100
Hysteresis	2.4%	23% (2.8%)
Design wavelength (λ_0)	3.8 μm	10.6 μm
Displacement capability	±1.2 λ_0	±1.5 λ_0
Bias voltage for flat	0 V	500 V
Voltage range	±1500 V	0-1000 V
Frequency response (-3dB)	160 Hz	300 Hz

displacement requirements led to the different choices for the piezoelectric actuator material. Mirror #2 was not originally designed to be used in a modal fashion and the 23% hysteresis was acceptable for its original application. This large value of hysteresis was excessive for a predictive modal implementation, however, and an amplifier modification was made to reduce the effective hysteresis to the 2.8% value.

Evaluation of Mirror #1

Single Modes

A collection of interferograms representative of the tilt, focus, and astigmatism modes achieved with mirror #1 are shown in Figure 1. The actuator locations are denoted by the solid dots. The nominally flat initial condition of the mirror is shown at the upper left. Only the surface within the active area of the mirror is of significant interest for these evaluations. The conformity of the surface to the desired modes for this mirror is limited by the local bending moments occurring at many of the actuator locations.

The results of the quantitative analysis of the interferograms for this mirror are shown in Figure 2 for piston, tilt, focus, and astigmatism modes. The solid lines are fitted to the data for the amplitudes of the desired modes and the dashed lines are fitted to the RMS deviations of the actual surface from the desired mode shape. These results show good linearity between the mode amplitudes and input signals. The RMS deviation from the desired surface is between $\lambda/4$ and $\lambda/3$ at 0.6328 μm. Since this corresponds to $\lambda/18$ or better at the design wavelength, this mirror should exhibit very good performance when operated with any of these modes at the design wavelength.

Superposition of Modes

A collection of interferograms showing superpositions of focus and astigmatism modes is shown in Figure 3. The upper left interferogram shows the initial focus mode applied to the mirror. The lower left and upper right interferograms each resulted from an equal amplitude superposition of an astigmatism mode with the focus mode. The lower right interferogram resulted from the superposition of astigmatism and focus modes with an amplitude ratio of 2:1. This should result in a cylindrical surface. This interferogram nominally exhibits that shape although some residual tilt is also evident.

The results of the quantitative analysis of the superposition of focus and astigmatism modes are summarized in Figure 4. The graph on the left shows the results for the equal amplitude superposition of these modes. The amplitudes of the focus and astigmatism modes determined from the interferogram analysis of the superposition implementation are observed to be equal throughout the range of mode strengths which could be applied. The center graph is for the case where astigmatism and focus are superimposed with a 2:1 amplitude ratio. The data analysis shows that this configuration was successfully implemented. The graph on the right was for the case where the amplitude of the focus mode was kept fixed while the amplitude of an astigmatism mode was varied. Here again analysis of the interferograms shows that the desired surfaces were achieved. The RMS deviations from the desired surfaces were again better than $\lambda/3$ at 0.6328 μm, which would correspond to very acceptable surfaces at the design wavelength. Superpositions of other combinations of two Zernike modes and of more than two modes have been satisfactorily imposed in system operation although they have not been subjected to the interferometric analysis as presented here.

Evaluation of Mirror #2

As indicated previously, mirror #2 was not originally designed to be used in a modal application. In order to reduce the hysteresis sufficiently to allow a modal implementation, modifications to the actuator drive amplifiers were made. As a result of these modifications, only limited experimental results are available at this time on the imposition of Zernike modes on this mirror.

Amplifier Modification

A block diagram of the amplifier modification* is shown in Figure 5. The most basic feature of the modification is that the amplifier feedback has been changed. The sensing capacitor introduced in series with the actuator essentially produces a circuit configuration commonly used to determine the hysteresis behavior of ferroelectric materials. When connected in the feedback loop as indicated the effective actuator hysteresis with respect to

*The design for this modification was provided by the Charles Stark Draper Laboratory under contract F29601-76-C-0059.
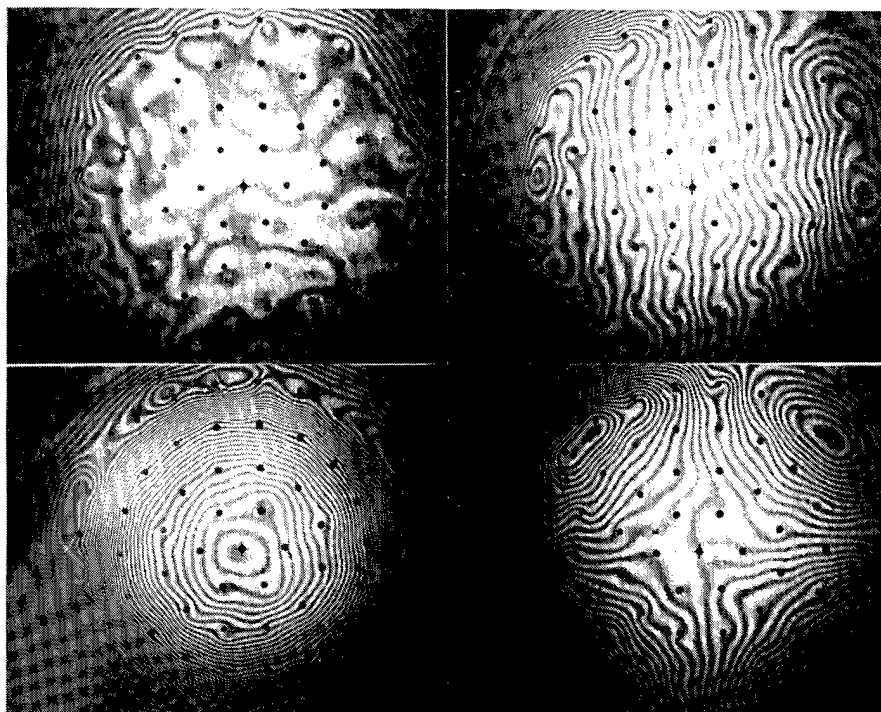
Fig. 1. Representative interferograms of the initial flat condition (upper left) and tilt (upper right), focus (lower left), and astigmatism (lower right) modes on mirror #1.
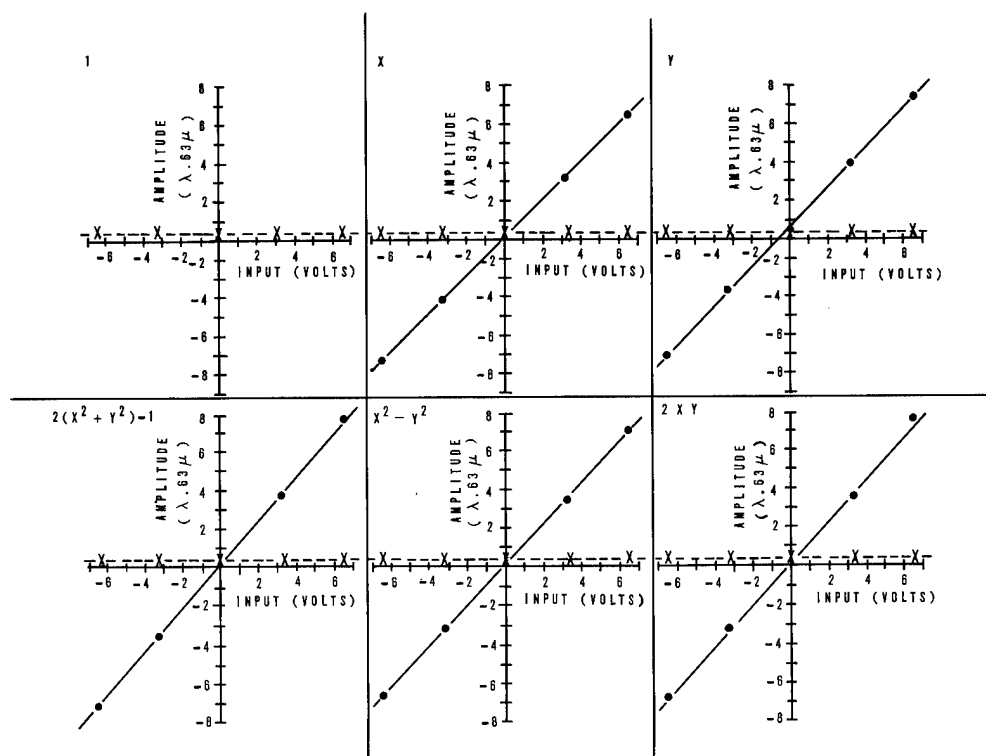

Fig. 2. Mode amplitudes (solid lines) and RMS deviations from the desired surfaces (dashed lines) obtained for piston (upper left), tilt (upper center and right), focus (lower left), and astigmatism (lower center and right) modes on mirror #1.
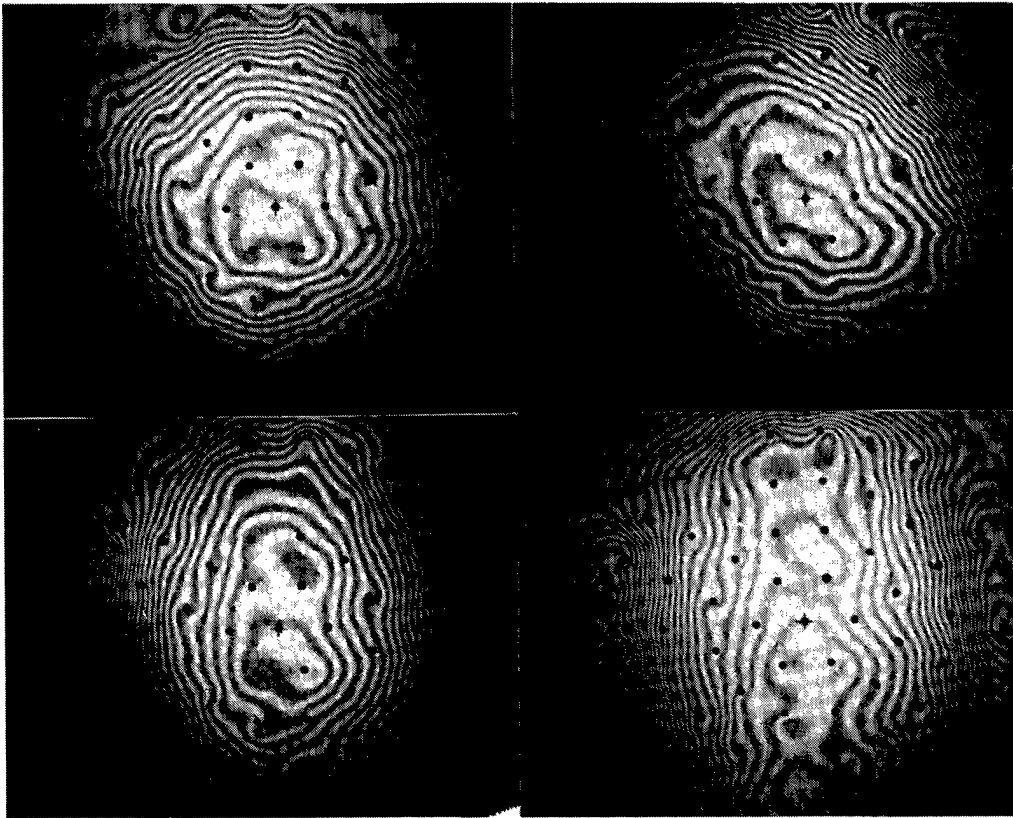
Fig. 3.   Representative interferograms of superpositions
of focus and astigmatism modes with astigmatism-to-focus
amplitude ratios of 0:1 (upper left), 1:1 (upper right
and lower left), and 2:1 (lower right) on mirror #1.
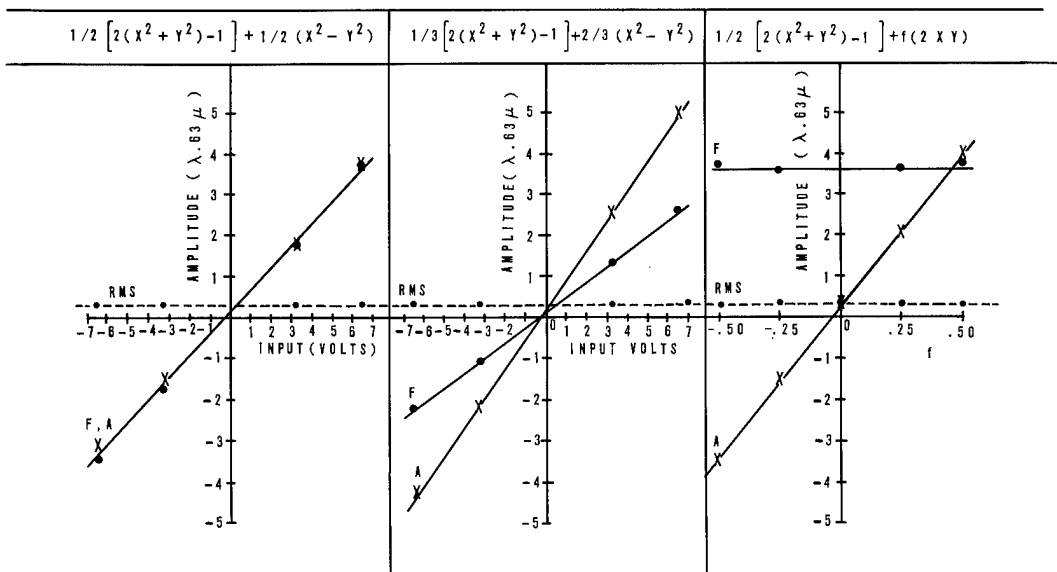
Fig. 4.   Mode amplitudes (solid lines) and RMS deviations
from the desired surfaces (dashed lines) for superpositions
of astigmatism and focus modes with astigmatism-to-focus
amplitude ratios of 1:1 (left), 2:1 (center), and 2f:1 (right)
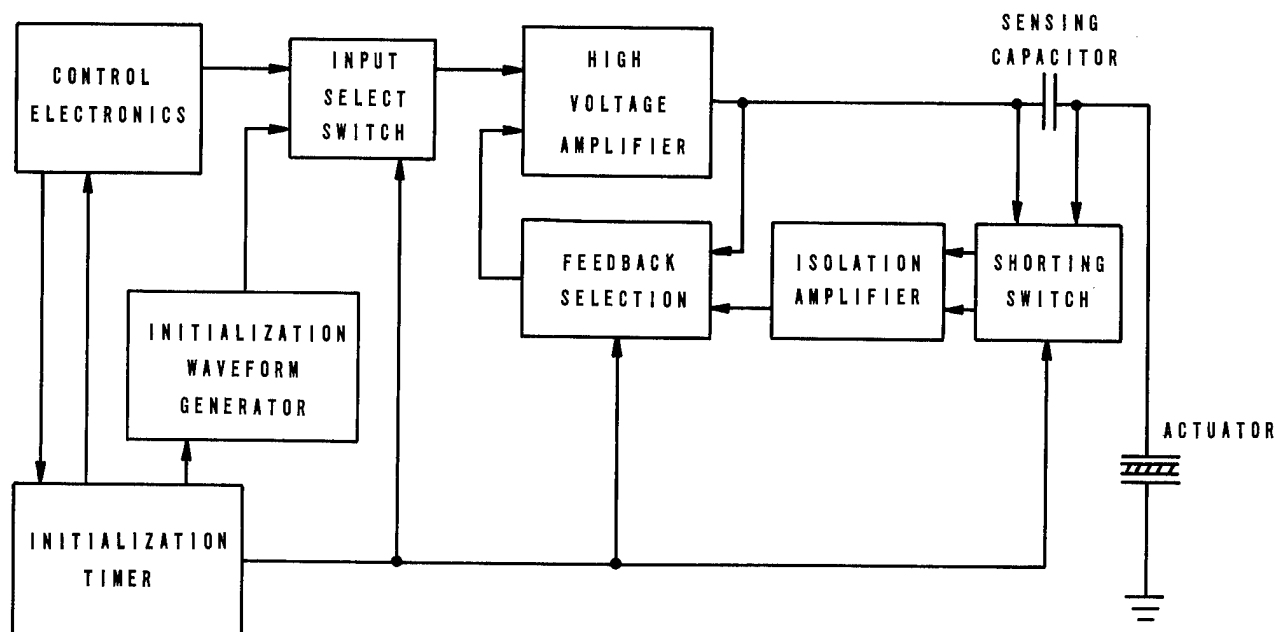
Fig. 5. Block diagram of modifications to the amplifiers of mirror #2.

the input signal is reduced to an acceptable level. Leakage in the circuit limits the time duration over which such feedback can be used. As a result, a timer periodically resets the amplifier system by returning it to its original voltage feedback configuration and reinitializes the actuators to the centers of their hysteresis loops. At present approximately 0.5 second during each 27 seconds is allocated to this reset function.

Focus Mode

At this time only a focus mode has been imposed on this mirror. A representative interferogram for such a case is shown in Figure 6. The greatly increased number of fringes is a result of the much greater actual displacement achieved with this mirror. Note that this design has considerably less local bending moment at the actuator locations than the other mirror has.

A summary of the quantitative analysis of the interferograms for the focus mode is shown in Figure 7. The observed amplitude of the focus mode is linear over the entire input voltage range. The initial nominally flat condition for the mirror was observed to have an amplitude for the focus mode of approximately 1λ at 0.6328 μm. Note that for this case the RMS deviation from the desired surface is larger than it was for the other mirror even though the high spatial frequency deviations due to local bending moments at the actuator locations are less than they were for that case. Also, the amplitude of the RMS deviation increases with the amplitude of the focus mode. The computer analysis of the interferograms shows a significant spherical aberration contribution which increases as the amplitude of the focus mode increases. This is believed to be an indication that the resistor matrix used to determine the voltages applied to the different actuators to achieve the focus mode was calculated incorrectly. A new computation of resistor values has been made and new resistor values have been installed. Measurements of the surface achieved using these new values have not yet been made.

Problems

Some of the problems encountered during the course of this investigation were the following:

1. The actuators for mirror #1 exhibited a creep phenomenon which lasted over many weeks. Although this problem is not well understood, it is believed that the piezoelectric material itself is responsible and may be undergoing a plastic flow in response to the compressive preload.

2. Actuator replaceability was a problem in that either local bending moments tended to be introduced when the actuators were changed or else the design was complex enough to make
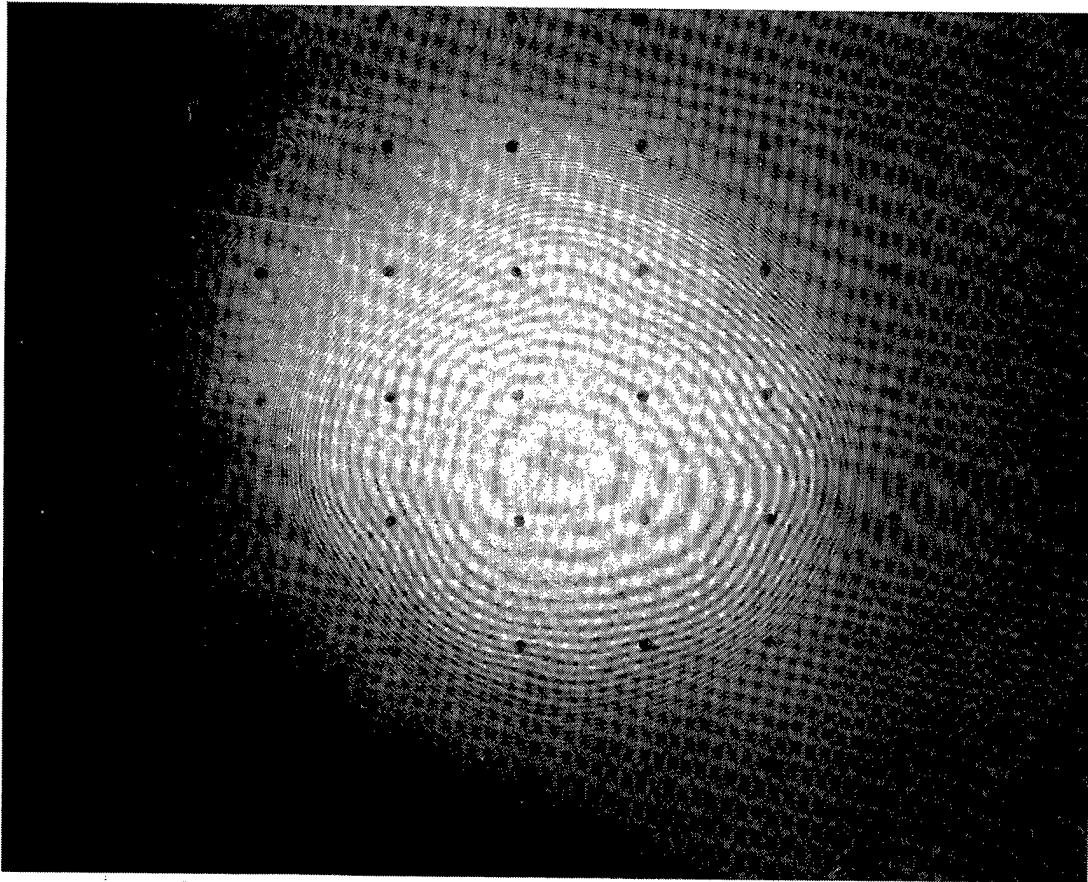
Fig. 6. Representative interferogram of the focus mode on mirror #2.
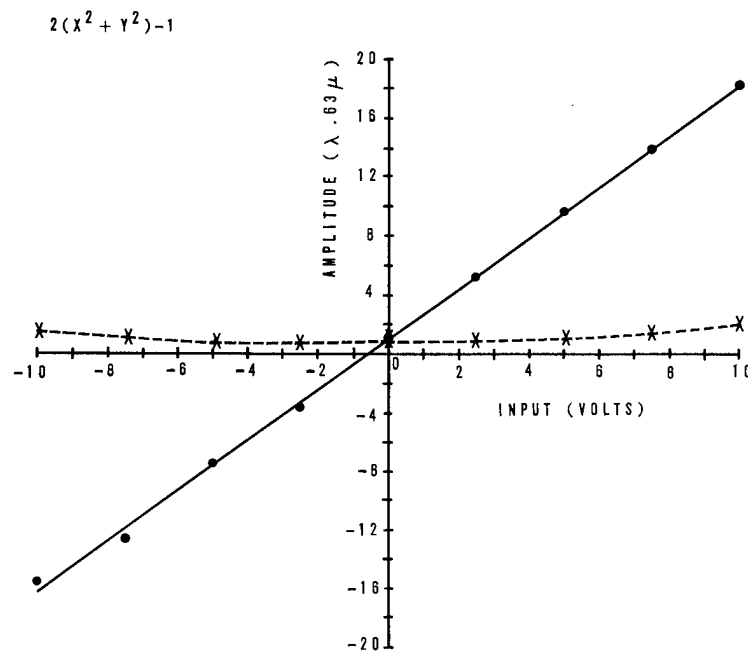

$$2(X^2 + Y^2) - 1$$

Fig. 7. Mode amplitude (solid line) and RMS
deviation from the desired surface (dashed
line) for the focus mode on mirror #2.

actuator replacement itself rather difficult.

3.   Thermal instability tended to be a problem for mirror #1 in that temperature changes on the order of 10°F would cause significant distortions of the mirror surface as a result of the differential thermal expansion between the piezoelectric material and the other mirror material.

4.   Although adequately low values of hysteresis were obtained, both mirrors exhibited nonlinearity in actuator response. This amounted to 10.5% for mirror #1 and 4.7% for mirror #2.

5.   Electromechanical gain variations with respect to the limiting low gain value were 145% for mirror #1 and 32% for mirror #2.

6.   The constrained edges of the mirrors tended to limit the acceptable active areas to regions well inside the outermost actuator locations.

7.   The increase of actuator capacitance and loss tangent with drive level can result in inadequately designed current drive and actuator cooling when designs are based on the low drive level values typically quoted by piezoelectric manufacturers.

8.   Although this modal approach does result in some reduction in system complexity, deformable mirrors with these numbers of actuators do remain relatively complex systems.

Summary

Low order Zernike modes have been imposed with good surface conformity using two multi-actuator deformable mirrors. In addition, a drive technique has been tested which permitted a piezoelectric material with large hysteresis to be driven so as to have low effective hysteresis. Significant improvements in design and material performance can yield improved modal performance of deformable mirrors.

Acknowledgments

INTERFEROGRAM EVALUATION PROGRAM FOR THE HP-9825A CALCULATOR

E. R. Freniere and O. E. Toler
Honeywell Electro-Optics Center
R. Race
Massachusetts Institute of Technology

Abstract

A method has been developed for evaluating interferograms using portable, inexpensive equipment. The method involves least square fitting the Zernike polynomials to interferogram data. An interferogram can be data reduced typically within 15 minutes, yielding information about the optical aberrations present.

Introduction

We present a technique for evaluating optical aberrations from interferometric data; a measured wavefront is approximated by the Zernike polynomials. While this idea is not a new one, and has been accomplished by previous workers[1,2], it has been implemented here on desk-top equipment, a Hewlett-Packard 9825A calculator and an Elographics E241 digitizer. Also, plots are made on a Hewlett-Packard 9862A plotter. This equipment has the advantage of being quite portable and economical when one considers the large machines that are usually used for this purpose.

A summary of the evaluation procedure follows:

1. A conventionally obtained interferogram is digitized, and the data read point by point into the calculator.

2. The calculator program performs a least square fit of the Zernike polynomials to the measured data. Since each datum is processed immediately after it is entered, it need not be stored. Thus, more calculator memory is available for programming, and an unlimited quantity of data may be accommodated.

3. After all the data is read and the Zernike polynomial coefficients obtained, the aberration coefficients are calculated and a summary of the results is printed on the calculator's internal printer. The coefficients can be stored on a tape cartridge for future use, including as input for the plotter program.

4. Optionally, the Zernike polynomial approximation of the wavefront can be plotted. The user may adjust any of the coefficients desired; for example, one may wish to set the tilt of the wavefront equal to zero, or isolate one or more of the aberrations.

5. Depending upon the complexity of the interferogram, Steps 1 through 3 require approximately 10 to 15 minutes. The plotting procedure takes about 30 to 50 minutes.

Polynomial Fitting

The least square condition is obtained by minimizing the quantity

$$\varepsilon = \sum_s \left[f(x_s, y_s) - z_s(x_s, y_s) \right]^2 \tag{1}$$

where $z_s(x_s, y_s)$ are the data, the sum is performed over the range of the data, and

$$f(x, y) = \sum_{i=0}^{N-1} a_i \, g_i(x, y). \tag{2}$$

The g_i are polynomials which are to be constructed so that they are orthogonal over the set of discrete data. One easily finds that ε is minimized when the coefficients a_i are

$$a_i = \sum_s z_s(x_s, y_s) \, g_i(x_s, y_s). \tag{3}$$

This constitutes the least square fit to the data. We now also demand that

$$f(x, y) = \sum_{j=0}^{N-1} b_j V_j(x, y),$$

(4)

where the V_j are the Zernike polynomials, and N is the number of polynomials used in the fit. To express the approximation as a sum of the Zernike polynomials, we must evaluate the coefficients b_j using the identity

$$\sum_{j=0}^{N-1} b_j V_j(x, y) = \sum_{i=0}^{N-1} a_i g_i(x, y).$$

(5)

Following the Gram-Schmidt orthogonalization procedure, we expand each polynomial V_j in a series,

$$V_j = \sum_{k=0}^{j} \alpha_{jk} g_k.$$

(6)

After some algebra, we find the recursive relations

$$\sum_s \left[V_j(x_s, y_s) \right]^2 = \alpha_{jj}^2 + \sum_{k=0}^{j-1} \alpha_{jk}^2,$$

(7)

$$\alpha_{jk} = \sum_s V_j(x_s, y_s) g_k(x_s, y_s),$$

(8)

and

$$g_j = \frac{V_j - \sum_{k=0}^{j-1} \alpha_{jk} g_k}{\alpha_{jj}}$$

(9)

which generate the orthonormal set of functions g_j, and their coefficients a_j are obtained from equation 3.

The coefficients b_j of the Zernike polynomials are linear combinations of the a_j coefficients. They (b_j) are obtained via equation 5.

A block diagram summary of the calculator program is shown in Figure 1.
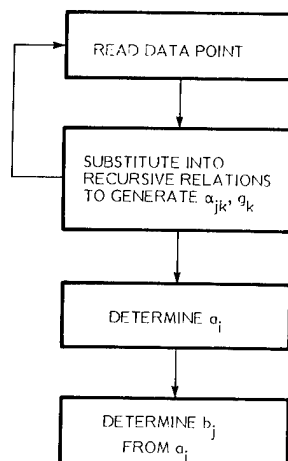
Fig. 1.   Block Diagram of Calculator Program

Examples

A synthetic interferogram was created with a known aberration (2.25 waves of defocus). This artificial interferogram was then processed by our interferogram data reduction station. The results are shown in Figure 2. The synthetic aberration is in the upper left, with the resulting Zernike polynomial and aberration coefficients in the lower left. The aberration function generated by the Zernike polynomial coefficients was plotted, and is also shown in Figure 2. Figure 3 shows the result of processing a real interferogram. Five minutes were required to digitize the interferogram and calculate the Zernike coefficients. Plotting the result required 45 minutes.

Figure 4 shows the result in Figure 3 plotted again, but with certain Zernike coefficients set equal to zero. In plot A, the constant and tilt coefficients (b_1, b_2, and b_3) were set equal to zero, and in plot B the spherical aberration term (b_{13}) was also set equal to zero, leaving a classical comatic plot whose rms value is 0.2074 wave.
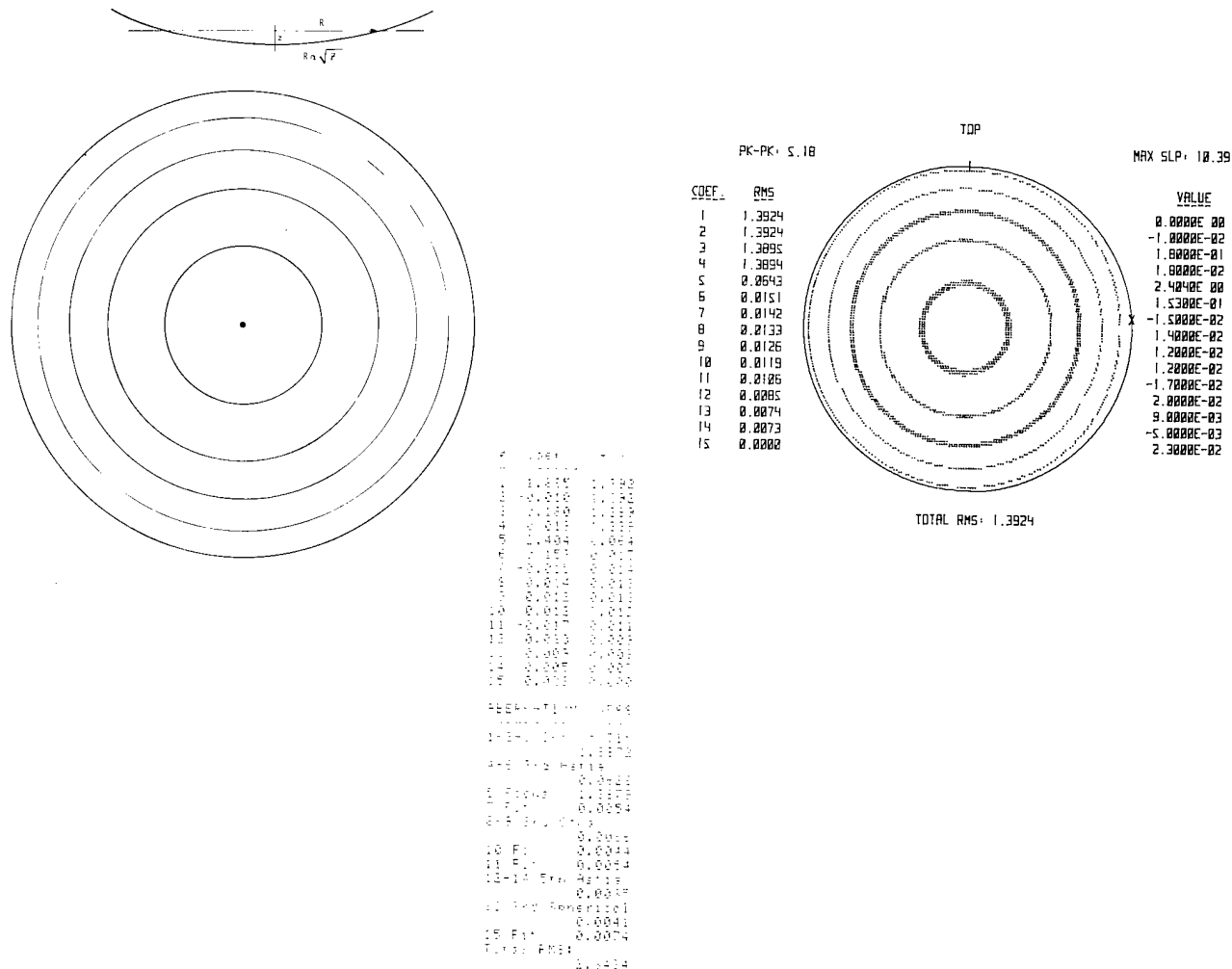
Fig. 2. Data Reduced Synthetic Interferogram and Plot.

References

1. John S. Loomis, FRINGE User's Manual, (Optical Sciences Center, U. Arizona, 1976).
2. Itek Corp. Technical Report SPG-72-022 (1972).

For further discussion of the Zernike polynomials, see:
   a. B.R.A. Nijboer, Ph.D. Dissertation, (U. Groningen, 1942)
   b. M. Born and E. Wolf, Principles of Optics, 5th ed. (Pergamon, Oxford, 1975), Chap. IX and App. VII.
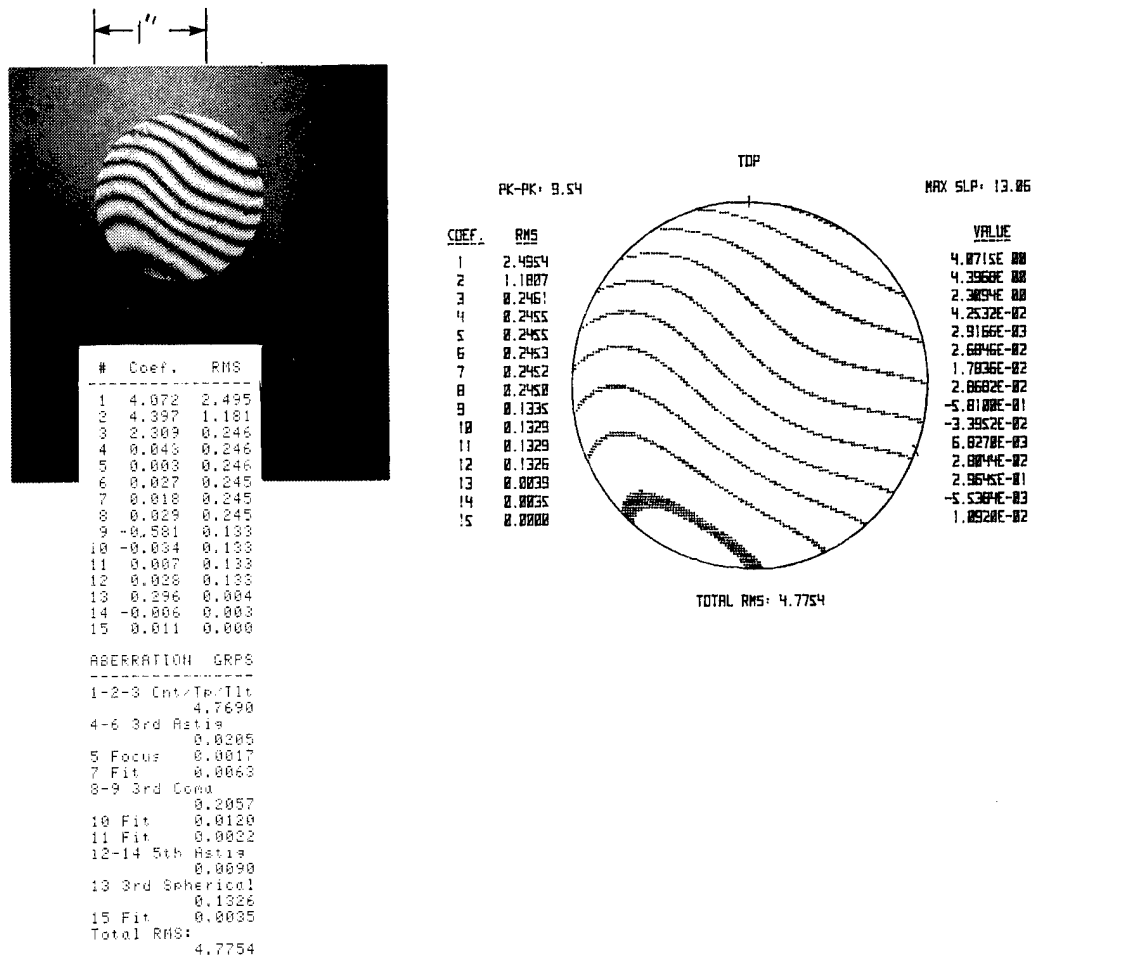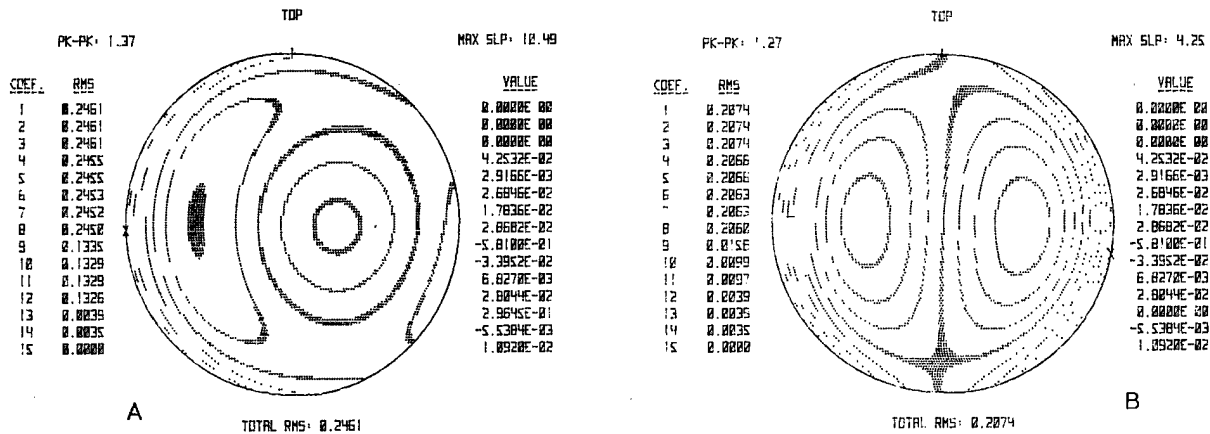
Fig. 3. Data Reduced Interferogram and Plot.

Fig. 4. Plots of a Real Interferogram with some Zernike Polynomial Coefficients set Equal to Zero. The contour interval in Plot A is 0.2 fringe, and in Plot B, 0.1 fringe.

OPTICAL COMPONENTS: MANUFACTURE & EVALUATION

Volume 171

SESSION 2

EVALUATION OF COMPONENTS

Session Chairman
Robert E. Parks
Optical Sciences Center
The University of Arizona

HIGH-ENERGY LASER MIRROR THERMAL DISTORTION TESTING TECHNIQUES*

Jeffrey Gierloff
University of Dayton Research Institute
AFWL/LRE, Kirtland AFB, NM 87117

Abstract

Mirrors are tested at the Thermal Distortion Test Facility (TDTF), Kirtland AFB, Albuquerque, NM, using a rastered electron beam (E-beam) to thermally load the mirrors. Typical test results and their implications are presented. The capabilities and accuracies of the facility are discussed. Verification tests performed with a CO_2 laser confirm the validity of using a rastered E-beam to simulate a HEL beam thermal loading.

Introduction

High-energy water-cooled mirrors are tested in the Thermal Distortion Test Facility (TDTF) with a rastered E-beam. The E-beam produces a thermal distortion that is measured by a real-time holographic interferometer. The resulting fringe images are used to generate input to a computer program that produces contour information of the mirror surface. Mirror coolant water flow rate and temperature rise are monitored to determine total energy absorbed.

Testing and data analysis techniques are discussed. The results were verified in the Optical Component Evaluation Laboratory (OCEL) with independent instrumentation and techniques.

Facility Description

High-energy water-cooled mirrors are tested in the TDTF with a focused, rastered E-beam. The beam is not intensity modulated, resulting in a thermal loading that is uniform over an arbitrarily shaped rectangle. Practically all of the beam energy is absorbed so that a low-power E-beam can simulate the thermal loading due to a high-energy laser beam, where only a small percentage of the laser energy is absorbed. The raster is usually varied from one to 50 cm^2 during a test. Transient effects can be observed by rapidly switching the beam on and off the mirror. Due to the danger of mirror damage by the E-beam, the beam will automatically be deactivated if the raster begins to collapse or problems are sensed in the water-cooling system. The TDTF is also capable of depositing up to 15 kW of power on the mirror.

Figure 1 is a schematic of the test apparatus. Note that the mirror needs to be mounted in a vacuum chamber to allow the operation of the electron gun (E-gun). Because of the chamber, the maximum diameter mirror surface that can be observed is about 12 inches. A water-cooled baffle is mounted in front of the mirror to insure that uncooled portions of the mirror surface or the mirror mount are not heated by the E-beam. The mirror tested should have leak-free construction and fittings to avoid contaminating the vacuum system.

Tests conducted to date have had roughly 20—30 data points. A typical test might take 1—2 weeks, with the data reduction taking a month. Future tests may require considerably more data points with a roughly proportional increase in test and data reduction time. Figure 2 shows the appearance of a mirror after testing. The brown stain of the mirror surface is caused by ions driven into it.

X-Ray Imagery

The location and magnitude of the incident thermal loading is determined by taking photographs of the X-rays emitted by the E-beam striking the metal surface of the mirror. The actual camera consists of a pinhole in the wall of the vacuum chamber and a Polaroid X-ray cassette. As the X-ray photographs in Figure 3 indicate, the E-beam rasters are generally well defined, with uniform loadings and sharp edges. This greatly simplifies data analysis.

Distortion Measurements

Thermal distortion is measured using a real-time holographic interferometer and an Argon laser (λ = .5145 μm). The resulting fringes are recorded on 35 mm film and a video tape recorder. Figure 1 gives a rough idea of the test configuration in the TDTF.

The hologram is taken when the mirror's surface is undistorted. When the reference beam is passed through the hologram, it reconstructs the wavefront produced by the undistorted mirror. During a test the wavefront of the distorted mirror is combined with the undistorted wavefront to produce fringes.

Figure 4 presents a typical fringe pattern resulting from thermal loading. The fringe patterns are converted into mirror surface elevations with a computer code called XFRINGE. The fringe location data is converted into elevation data on a regular X-Y grid by using linear interpolation. The data representing the undistorted reference surface is subtracted from the data for the thermally distorted surface so that the resulting surface depicted should be due only to thermal distortion. The distortion data can then be presented as a cross-sectional profile, contour map, or 3-D plot.

Figure 5A and B show cross-sectional profiles due to different sized rasters. For each raster size several different loading intensities are used (each identified by a six-digit clock number). Note that although the E-beam thermally loads the mirror with a sharply defined pattern, the resulting distortion is considerably smoothed. Figure 6 shows a contour plot of the thermally loaded surface. The contour patterns match the loaded areas well. In some mirrors the coolant water passing under the loaded region becomes heated enough to cause a "distortion tail" downstream from the raster (see Figure 6).

As Figure 7 illustrates, the mirror can deform in a complex manner. Distortion measurements are given as a single number-peak distortion referenced to undeformed surface. The deformation shown in Figure 7 is more complex than the usual case; selection of the "undeformed surface" becomes a value judgement. Note the appearance of "distortion tail" due to water heating.

Calorimetry

Mirror coolant water-flow rate and temperature rise are monitored to determine total energy absorbed. The cooling water is supplied from an external closed circuit water supply with an ambient inlet temperature. Flow can be varied from 0-600 psig and from 0-45 gpm. Flow measurement error is ± .05 percent of point.

The water temperature measurements are made by using two thermistors in an unbalanced bridge configuration (see Figure 8). As the downstream temperature is increased, the downstream thermistor's resistance decreases, creating a voltage differential given by:

$$\Delta V = V_0 \left[\frac{R_1}{R_1 + R_3} - \frac{R_2}{R_2 + R_4} \right] \tag{1}$$

For constant inlet temperature, R_3, R_4, and V_0:

$$\Delta V = f_n(R_2) = f_n(T_2) \tag{2}$$

We can have one calibration curve valid for all tests. V_0 does vary slightly from run to run and is measured before and after each test.

Two different bridges are used to provide redundant temperature measurements. Past performance has indicated the bridges agree to better than 0.01°C RMS.

Pressure and temperature are measured at the inlet and outlet of the mirror.

Typical Test Results

Figure 9 shows the basic presentation of the raw data. Distortion increases linearly with increasing intensity. It also increases with increasing area or decreasing flow rate at a constant intensity.

The data can be simplified by plotting the slope of the lines in Figure 10 versus the appropriate area. The slope, thermal growth/intensity, is called the distortion coefficient (see Figure 10). Interesting points to note are a distortion coefficient that goes to zero for small areas and a linearly increasing coefficient for large areas; thus, comparisons of mirror performance must take the distribution of the thermal loading into account. These results in general hold true for both transverse and radial flow mirrors. Figures 9

and 10 are for transverse flow mirrors. The results for radial flow mirrors are more difficult to interpret because the larger rasters would cover areas of the mirror surface with widely differing flow rates.

Technique Verification

A P&WA mirror was thermally tested in the Optical Components Evaluation Laboratory (OCEL) to verify the TDTF test results.[1] The mirror was thermally loaded with a 1 kW CO_2 laser. A coating was put on the mirror to absorb most of the 10.6 µm radiation while reflecting sufficient radiation at .5145 µm to allow interferometry. Completely separate instrumentation and computer codes were used.

Since the TDTF uses a rectangular uniform intensity distribution and the OCEL used a circular Gaussian intensity distribution, data comparison had to be done with a distortion coefficient curve to construct a Gaussian distribution from the TDTF data by linearly superimposing low-power rectangular loadings. The TDTF test data and OCEL test data agreed by ± 10 percent by this method.

Acknowledgments

The author wishes to thank Stephen C. Bayliss and Joe G. Campos for their long hours of support required to make the TDTF operate on a productive basis and the large quantities of data analysis they performed.

Reference

[1] R. J. Andrews, (C) Verification of TDTF Mirror Distortion Data (U), UDRI Test Report UDRI-A-106, Contract F29601-76-C-0140, June 1978.
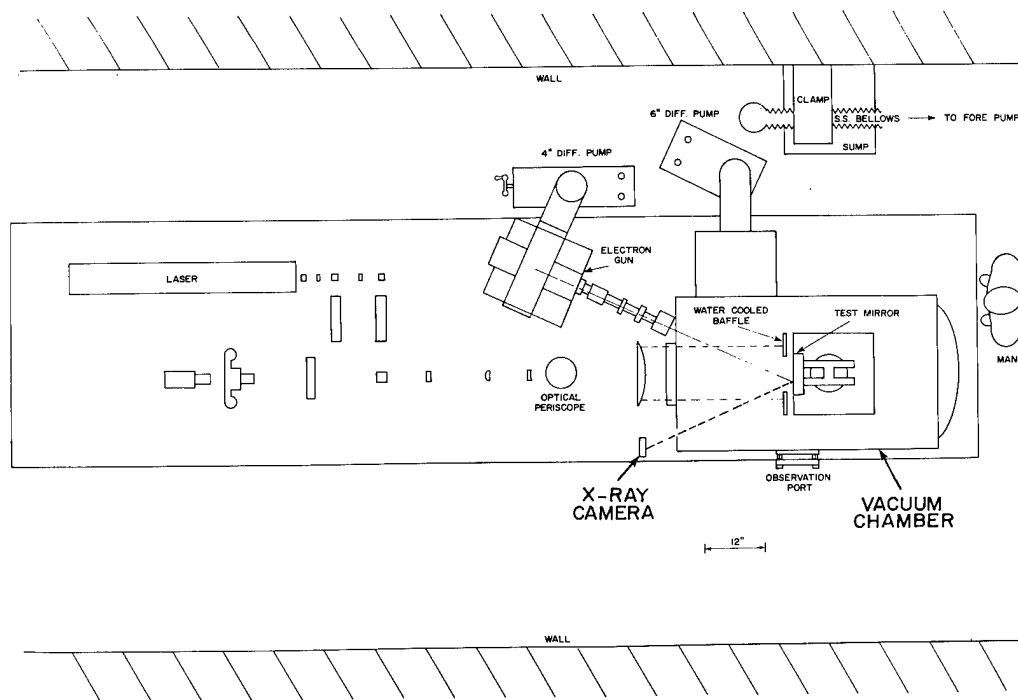
Fig. 1. Test Configuration.
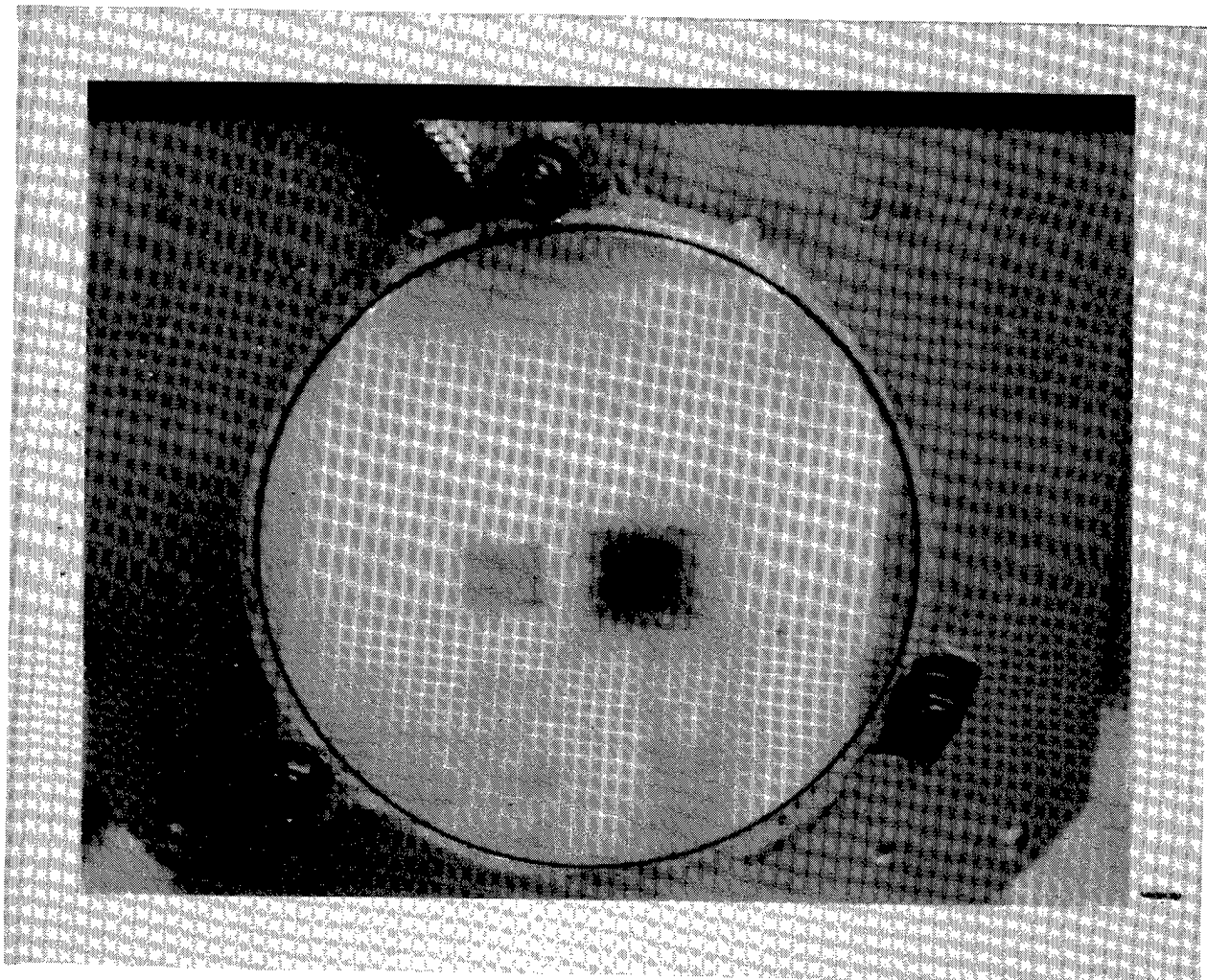
Fig. 2.   Mirror After Testing.

Fig. 3.   E-Beam Rasters.
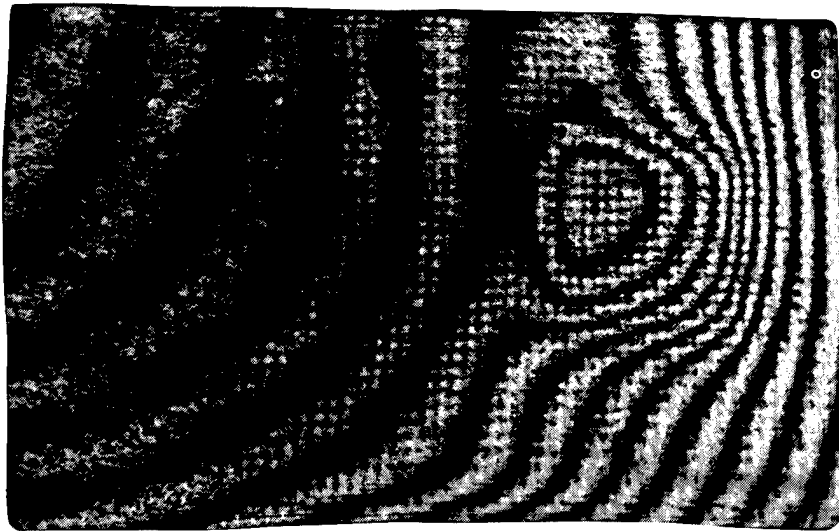
Fig. 4.   Interferogram Fringe Pattern.
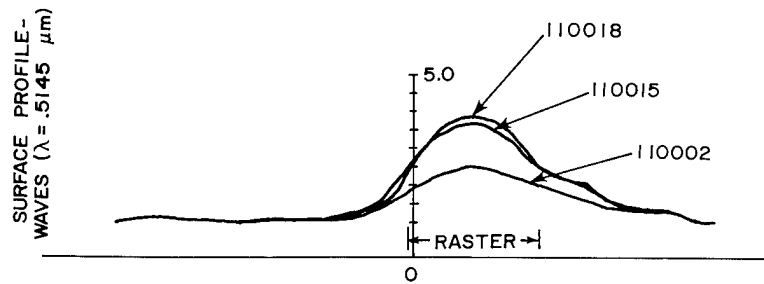
5a.   Cross-Sectional Profile Due to 6.1 cm^2 Raster.
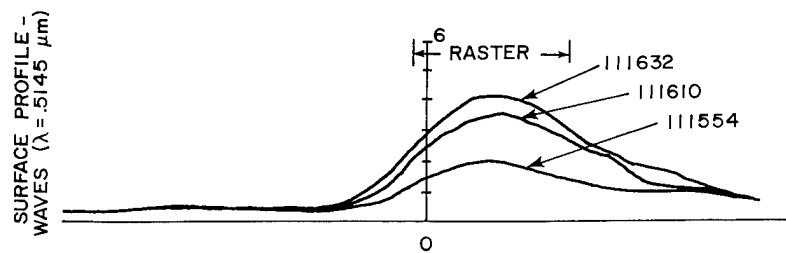
5b.   Cross-Sectional Profile Due to 9.9 cm^2 Raster.

Fig. 5.   Cross-Sectional Profiles Due to Thermal Loading.

ID= 111554.00 SEQUENCE NO.= 13.0000 TIME= 378.00
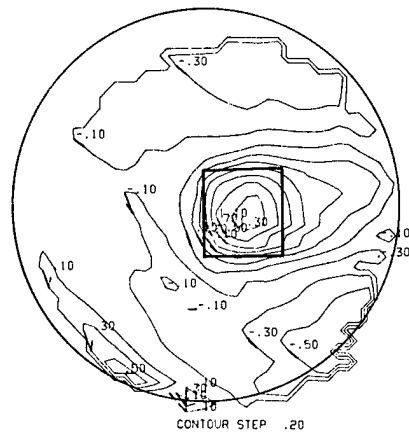SURFACE DEFORMATION IN WAVES

CONTOUR STEP .20
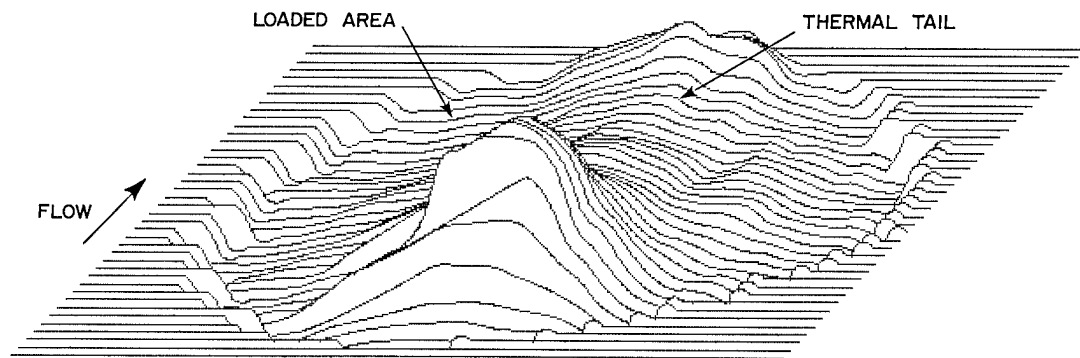
Fig. 6. Contour Plot of Thermally Loaded Mirror Surface.

LOADED AREA   THERMAL TAIL

FLOW

Fig. 7. 3-D Diagram of Thermal Distortion.

INLET TEMP.

R_1 R_2

V_0 ΔV OUTLET TEMP.

R_3 R_4
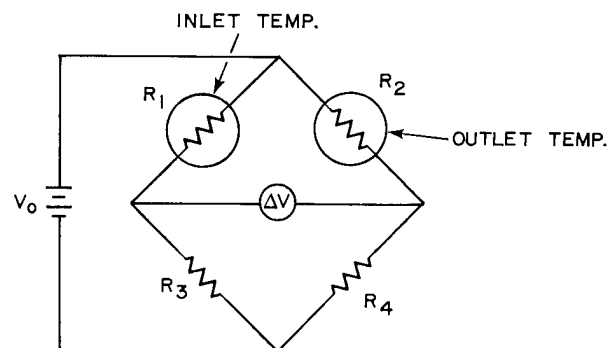
Fig. 8. Bridge Configuration.
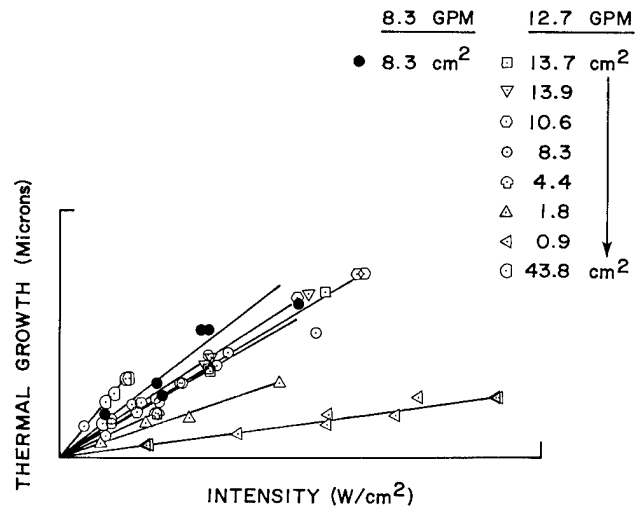
Fig. 9.   Thermal Growth vs. Intensity.
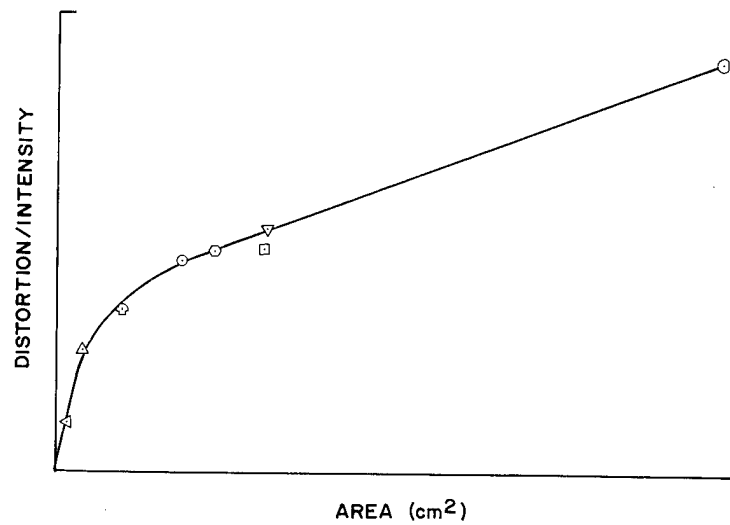
Fig. 10.   Distortion Coefficient vs. Area.

DIAGNOSTIC TECHNIQUES FOR AXICONS AND RELATED OPTICS

Malcolm MacFarlane and Graham Flint
International Laser Systems, Inc.
Box 9316 International Airport
Albuquerque, New Mexico 87119

Abstract

The use of axicons and related types of optical components is of increasing importance in high energy laser systems. To aid in the acceptance testing of these optics, a program for the development of diagnostic tools and techniques for axicon evaluation has been undertaken by the Developmental Optics Facility at the Air Force Weapons Laboratory. Analytical models describing both the wavefronts and far-field patterns of systems containing axicons have been developed. These models have been used to derive methods for testing axicons in the laboratory. They have also been used to develop suggestions for the initial parameter specifications of axicons. Finally, methods for the correction of certain types of axicon aberrations due to fabrication errors are discussed.

I. Introduction and Summary

Recognition of the merits of annular resonators for use in high energy laser applications has led to a need for ultraprecision axicons and related types of optical devices. An axicon is normally defined as an optical device which produced a line rather than a point image of a point object on its optical axis (McLeod, 1954).

The work presented here deals specifically with reflective, linear axicons having a nominal 90° included angle. The results can easily be generalized to axicons of arbitrary included angle, but the need for this extension has not yet arisen and certain simplifications used here disappear in the more general case.

Precision axicons of this type can now be fabricated using diamond-turning techniques. The quality assurance of such components, however, is a difficult problem. Interferograms of systems containing axicons are difficult to interpret although progress is being made in this area (Loomis, 1979). The thrust of this work in this laboratory has been to take a nominally plane wavefront from an axicon and to form a geometrical image (spot diagram). All such images formed by linear axicons shrink to a point radially so the spot diagram becomes a curved line as will be seen in Section III.

Simple analytical models for wavefront deformations have been applied and the resulting spot diagrams analyzed in Sections II and III. This analysis has lead to several suggestions for correction of wavefront aberrations due to fabrication errors in axicons. These suggestions are discussed in Section IV.

In the discussions which follow a right-handed coordinate system has been adopted with the Z-axis being the optical axis of the system and the axis of symmetry of the axicon. The (Y,Z) plane is the meridian plane. Polar coordinates at a surface are (ρ,θ) where $\rho^2 = x^2 + y^2$ and $\theta = \mathrm{Tan}^{-1}(x/y)$. The field angle is denoted by ϕ. Transverse ray aberrations in the x and y directions are given by $\delta\xi'$ and $\delta\eta'$ respectively.

II. Brief Analytical Development

The first and simplest error one would encounter in an axicon is an error in the cone angle. Assume an error δ in the <u>half</u> angle of an axicon. The half angle is used to make the results directly comparable with the ray tracing results of Section III. Simple geometry shows that a ray originally parallel to the optical axis (also assumed to be the axis of symmetry of the axicon) will suffer an angular deviation of 4δ from its nominal exit direction. This is shown in Figure 1 for a right-angle cone. The wavefront will clearly take a conical form whose half-angle is 4δ less than 90°. Since the wave aberration is clearly independent of the azimuthal angle, the wave aberration can be written as

$$W(\rho) = W_{1,0}\rho = 4\delta\rho. \qquad (2.1)$$

If this wavefront is subsequently imaged by a perfect optical system of focal length f, the geometrical image will be a ring of radius $4f\delta$.
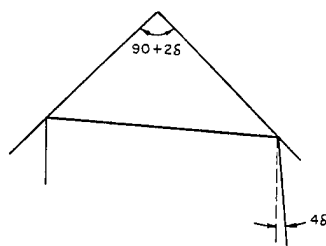

Figure 1. Cone Angle Error

It is of interest to know at what value of δ the geometrical ring becomes confused by diffraction effects. Let the coherent limiting spatial frequency be

$$\nu_0 = \frac{1}{2\lambda(F\#)} \tag{2.2}$$

where F# is the focal length of the imaging system divided by the diameter of the axicon. Typical values of F# = 30 and λ = .6328 μm give a limiting spatial frequency of

$$\nu_0 = 260 \text{ cm}^{-1}. \tag{2.3}$$

Equating the reciprocal of this to the radius of the ring discussed above, one has

$$8f\delta = 1/260,$$

or
(2.4)

$$\delta = 8 \times 10^{-7} \text{ radians.}$$

This, therefore, is roughly the magnitude of the smallest cone semi-angle error that can be measured in the presence of diffraction effects.

The next aberration to be considered is that due to a tilt of the wavefront normals (rays) with respect to the optical axis of the axicon. If θ is the azimuthal angle of a ray intersection on the axicon and ϕ is the angle of tilt of the incoming rays, then the wave aberration introduced by the axicon is given by

$$W(\rho,\theta) = W_{1,2}\rho\phi^2 \sin^2\theta \tag{2.5}$$

assuming that ϕ is small, which is true in all cases of interest here. If this wavefront is processed by a focusing system, the resulting image is somewhat reminiscent of a bow tie and will be discussed in detail in Section III. If one differentiates this wavefront according to Welford (1974, Chapter 6), the transverse ray aberrations are

$$\delta\xi' = W_{1,2} f\phi^2 \sin\theta \ (\sin^2\theta \ -2)$$

and
(2.6)

$$\delta\eta' = W_{1,2} f\phi^2 \cos\theta \sin^2\theta$$

The coefficient $W_{1,2}$ in equations (2.5) and (2.6) turns out to be identically equal to 2. Thus the size of the image formed by a tilted axicon is proportional to the square of the tilt angle. This immediately suggests a method for the precision alignment of an axicon. If the axicon be rocked back and forth about a nearly optimum position then the image will expand, without moving, on either side of this position. The angles at which the image expands to a precisely determined size can be measured quite accurately. The sum of these angles can be bisected to align the axicon with great precision without the need to minimuize the image at its smallest size.

Other errors which might be found in practice in an axicon are deformations due to gravity and deformations due to improper support. The former can be modeled by a surface (hence wavefront) deformation which is proportional to cos 2θ; the latter, in many cases, by a surface deformation proportional to cos 3θ.

These and other errors can be modeled analytically and differentiated to give far-field patterns but the process is tedious and gives no insight which cannot be gained from a study of the computer generated spot diagrams in the next section.

III. Interpretation of Spot Diagrams

The spot diagrams presented in this section are intended to simulate an actual test setup which is presently being constructed at the Air Force Weapons Laboratory, Kirtland AFB, New Mexico. The imaging optic is a 600 cm focal length parabolic mirror. The plane wave incident upon the axicon can be produced either by a plane-wave Zygo interferometer or by a Tinsley interferometer used in conjunction with a second parabolic mirror.

Since the spot diagrams of a linear axicon depend only on θ and not on ρ (cf. eq. 2.6), initial testing of such components will be done by simply placing in front of the axicon a mask which has an off-center hole. This mask will be rotated about the optical axis to give a scan in θ. The point by point position of the spot can then be recorded by a position-sensitive detector. The correlated outputs corresponding to mask and image positions can be recorded in various ways. Two methods of plotting the data will be used here: the

first being a true spot diagram in which the transverse ray errors $\delta\xi'$ and $\delta\eta'$ are plotted against each other: the second being a plot of the distance of the ray from the centroid against the azimuthal angle.

As stated in the previous section, a perfect axicon, when tilted with respect to an incoming wavefront, has a geometric far-field pattern which resembles a bow tie and whose size is proportional to the square of the tilt angle ϕ. This is shown in Figure 2 for values of ϕ ranging from 0 to 6 mrad in 1 mrad steps.
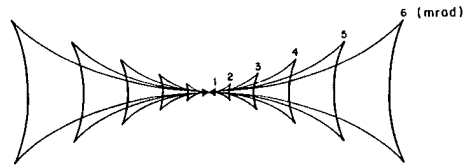
Figure 2. Effect of Tilt on the Spot Diagram of a Perfect Cone

Now, if an axicon which has a cone semi-angle error δ is tilted with respect to the wavefront, patterns such as those in Figures 3 and 4 will be found. In Figure 3, the value of δ is +3.2 μrad (i.e. the cone half-angle is greater than 45°) and in Figure 4 the value of δ is -3.25 μrad. In each of the figures the amount of tilt varies from 0 to 6 mrad in 1 mrad steps.
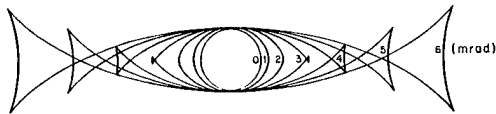
Figure 3. Effect of Tilt on the Spot Diagram of an Open Cone
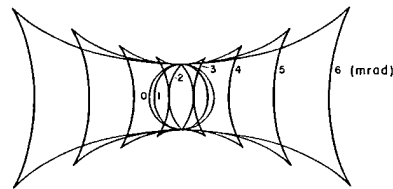
Figure 4. Effect of Tilt on the Spot Diagram of a Closed Cone

In addition to the plot format shown in Figures 3 and 4, it has proven instructive to plot the data in a slightly different form. If, as before, $(\delta\xi',\delta\eta')$ are the transverse ray aberrations in the image, we will define r' to be the distance from the centroid

$$r' = (\delta\xi'^2 + \delta\eta'^2)^{\frac{1}{2}} \tag{3.1}$$

We now plot r' against , the azimuthal angle of the ray in the pupil. Figures 5, 6 and 7 show these plots for an open ($\delta > 0$), perfect, and closed ($\delta < 0$) cone respectively. The tilt angles range from 0 to 4 mrad in 1 mrad steps.
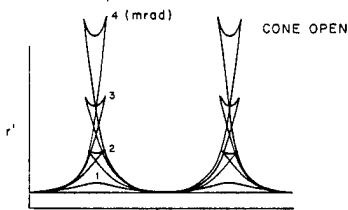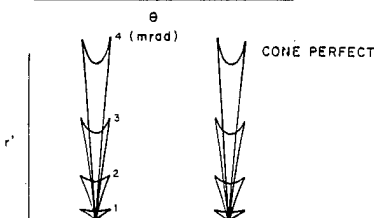

Figure 5. r' vs. θ Plot for an Open Cone

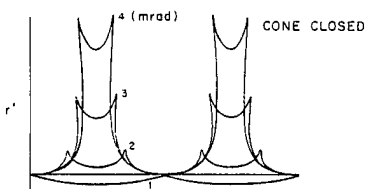Figure 6. r' vs. θ Plot for a Perfect Cone

Figure 7. r' vs. θ Plot for a Closed Cone

For an open cone (Figure 5) the value of r' can never be less than the value associated with a zero tilt angle. For a closed cone (Figure 7), however, it is clear that there are nonzero values of the tilt angle for which portions of the image shrink below the value due to cone-angle error alone. This immediately raises the question: can errors due to the cone angle of an axicon be eliminated or reduced by appropriate tilting? This question will be addressed in Section IV.

Consideration of errors other than cone-angle error and tilt are now addressed. The kinds of errors that have been investigated are of the form

$$W(\rho,\theta) = W_{1,m}\rho \quad \cos m\theta \qquad (3.2)$$

the method used to model this type of aberration is to define a perfect axicon in the usual fashion and then to add an appropriate deformation of the type defined by eq. 3.2 using bicubic spline functions (Vogl, Rigler and Canty, 1971). Although the algorithm uses rectilinear coordinates for defining the nodes of the splines, rather than curvilinear coordinates, the accuracy obtained seems to be more than adequate for this purpose.

A ray initially parallel to the optical axis will strike the axicon at some point (ρ,θ) and again at point $(\rho,\theta + \pi)$ before exiting the axicon. Thus if the multiplier m in eqs. 3.2 is odd, the aberrations introduced by opposite sides of the axicon will tend to cancel each other. If, on the other hand, m is even; the errors are additive. This has indeed proven to be the case. For m = 1, 3 and 5 the spot diagrams all shrink to points. For that reason, they are not presented here. For m = 2, 4 and 6 however, the spot diagrams are of the forms presented in Figures 8, 9 and 10. The spot diagrams are roughly star shaped having 2m cusps. The image spread is roughly proportional to m since the values of ρ and $W_{1,m}$ in eq. 3.2 were held constant for all cases.
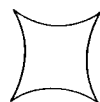

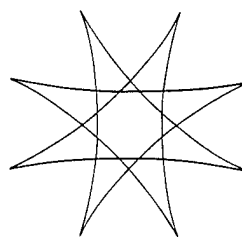Figure 8. Spot Diagram for an Axicon with a 2θ Azimuthal Error

Figure 9. Spot Diagram for an Axicon with a 4θ Azimuthal Error
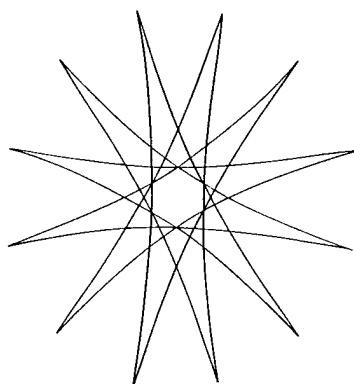

Figure 10. Spot Diagram for an Axicon with a 6θ Azimuthal Error

The implications to be drawn from the above are clear. Surface errors with m even must be avoided at all costs. The wavefront is much less sensitive to odd m errors; a fact which is important in the design of support systems and cooling channels.

IV. Error Compensation

Given an axicon with an error in the cone semi-angle $\delta<0$, it is possible to shrink the far-field pattern in one dimension, as was shown in the preceding section. Additionally if one has an annular resonator incorporating two axicons, it should be possible by using orthogonal tilts, to shrink the pattern in both dimen-

sions. This, in fact, proves to be the case, and is shown in schematic fashion in Figure 11.
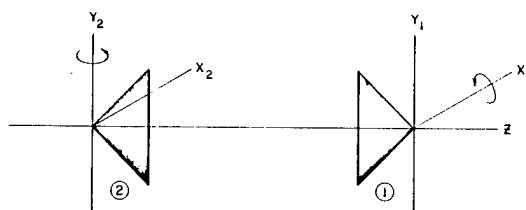

Figure 11. Cones Tilted for Cone Angle Error Compensation

If the two axicons are rotated about mutually orthogonal axes, each by an angle ϕ, as shown in Figure 11, the total aberration for a single pass through the system will be

$$W(\rho,\theta) = 4\delta\rho + 2\rho\phi^2 (\sin^2\theta + \cos^2\theta) \tag{4.1}$$

Remembering that $\delta<0$, the aberrations will be minimized if

$$\phi = \pm(-2\delta)^{\frac{1}{2}} \tag{4.2}$$

Figures 12 and 13 show the effect on the spot diagram of this process. It should be noted that the scale of Figure 13 is 25 times the scale of Figure 12. Perfect correction is not attainable sine, in general, the (ρ,θ) coordinates of a ray on the first axicon will differ slightly from those on the second so eq. 4.1 should properly be written

$$W(\rho,\theta) = 4\delta\rho + 2\phi^2 (\rho_1 \sin^2\theta_1 + \rho_2 \cos^2 \theta_2) \tag{4.3}$$
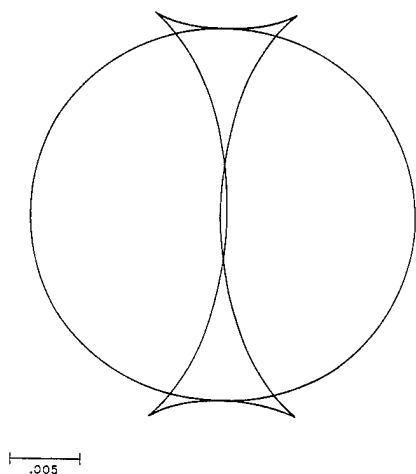
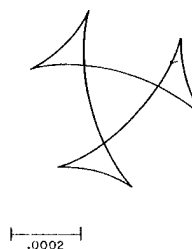Figure 12. Uncorrected (Ring) Cone Error and and Single Cone Tilted

Figure 13. Both Cones Tilted Showing Full Compensation

However, in spite of this, the wavefront aberration may be reduced by at least two orders of magnitude.

Note that each of the cones can have semi-angle errors δ_1, δ_2. The scheme just described will work as long as the condition

$$\delta = \delta_1 + \delta_2 <0 \tag{4.4}$$

is satisfied.

An immediate conclusion that can be drawn from the above argument relates to the initial specifications for axicons. If an axicon is specified to have a semi-angle of exactly 45° and the fabrication error is greater than zero, the resulting aberration cannot be corrected. If however, the cone semi-angle were specified to be

a few microradians less than 45°, a much larger tolerance could be placed on the angle with the knowledge that the associated wavefront aberration could be corrected almost perfectly by an appropriate tilt. Such a tilt might normally amount to several milliradians.

Returning to azimuthally periodic errors, even m errors can be drastically reduced if the same type of error is on both of the facing axicons. This time, one axicon must be rotated about the optical axis relative to the other by 180/m degrees. When this is done, and the fabrication errors on the axicons have the same magnitudes and azimuthal dependence, the correction is again almost perfect. There will be small residual aberrations since the ray coordinates on the two axicons will again be slightly different.

It can be expected that a given polishing technique will produce similar errors on similar axicons. Thus, the concept of mutual cancellation of aberrations would appear to have merit.

References

1. Loomis, J.S., "Analysis of Interferograms from Waxicons", These Proceedings.
2. McLeod, J.H., J.O.S.A., 44, 592, 1954.
3. Vogl, T.P., Rigler, A.K., and Canty, B.R., Appl. Opt., 10, 2513, 1971.
4. Welford, W., Aberrations of the Symmetrical Optical System, Academic Press, New York, 1974.

DIFFRACTION GRATING EVALUATION*

Marion L. Scott
University of Dayton Research Institute
Dayton, Ohio 45469

Abstract

Techniques for evaluating the diffraction efficiency of infrared gratings have been developed and utilized at the Air Force Weapons Laboratory as part of the high energy laser component development effort. The key to accurate infrared diffraction efficiency measurements is good angular alignment and linear detection. The AFWL OMEGA diffraction code has proven to be very useful in determining the expected efficiencies of various coated and uncoated grating designs. Successful use of this program requires a good method of determining the groove profile of the grating. One successful method that we have developed will be discussed.

Introduction

Diffraction gratings may be used primarily to implement two functions in high energy laser systems. The first of these is to sample a small fraction of the HEL beam for diagnostic and alignment purposes. Gratings are ideal for this use because the efficiency and angle of diffraction are controlled by the grating design. The second function for which gratings may be used is spectral separation in shared-aperture systems. One or both of these functions may be implemented in a particular grating, and the evaluation of the performance of such gratings may become exceedingly complicated.

Our aim in this paper is to discuss a general approach to the evaluation of a high energy laser grating. Supplemental measurements occasionally employed in our evaluation of gratings, such as calorimetry and the use of a spectrophotometer, will not be discussed here. The areas we will discuss include:

1. Grating profile determination
2. Computer code evaluation
3. Measurement of the specular or zero order efficiency
4. Measurement of the diffracted order efficiency

We try to determine from the grating user as much detail on the design and use of the grating as possible. In some instances, the exact profile of the grating groove cannot be obtained from the user, and we must measure the groove profile.

Grating Profile Determination

The method of groove profile determination discussed here may not be used on the actual HEL component because of the possibility of damage to the grating. In many instances, suitable witness samples are available, or "test" rulings may be used. The method we used is outlined in Figure 1. A replica of the grating surface is made with a celluloid acetate tape softened with a commercially available replicating fluid. The replica is allowed to dry in situ and the tape peels off as it dries. The dry replica is quick frozen in liquid nitrogen and then snapped into two parts along a direction orthogonal to the groove profile.

At this point the replica is edge mounted and metalized with gold so that the groove profile will be visible to the scanning electron microscope. The coated replica is inserted into the SEM, and a photograph of the edge is made with appropriate magnification. Examples of the results of this process are shown in Figures 2 and 3.

The groove profiles are obtained from the SEM photograph with the use of a graphics tablet and scaled with the known groove spacing. This numerical data is used to calculate the Fourier coefficients for the groove profile.

Computer Code Evaluation

The Fourier coefficients of the groove profiles obtained in the manner described above are used as inputs to the Air Force Weapons Laboratory diffraction grating code (OMEGA). This code is capable of calculating the diffraction efficiencies for the various orders of the grating, even if the grating has a coating. Loss is incorporated in the calculations

through the input of complex indexes of refraction for each layer. The incident wavelength and angle, the groove spacing, and profile are all inputs. Certain simple profiles such as blazed, sinusoidal, and lamellar can be input with a few parameters, and the code calculates the Fourier coefficients for these cases.

The OMEGA code has some limitations in its capabilities. One is that the ratio of incident wavelength to groove spacing must be greater than (or equal to) 0.2, i.e.,

$$\frac{\lambda}{d} \geqslant .2 \tag{1}$$

for this integral formulation. Another limitation was discovered when the evaluation of some overcoated gratings produced numerical difficulties in the computations. An example of this problem is given in Figure 4. In this case thin overcoatings yielded quite different efficiencies when the numerical constants used in the evaluation were varied. An example of the successful use of this code is given in Figure 5. The zero order or specular reflectance of this uncoated grating was measured at wavelengths in the 3—12 μm range on the AFWL Fourier Multiplex Spectrophotometer. In Figure 5 these results are compared to the theory.

Measurement of the Specular or Zero-Order Efficiency

Absolute W-V Reflectometer

We use an absolute W-V reflectometer to measure the specular or zero-order diffraction efficiency whenever possible in order to take advantage of the high precision of this instrument. We have demonstrated a precision of 0.06 percent with our reflectometer and intend to make further refinements in this instrument in the future.

The W-V technique is illustrated in schematic form in Figure 6a and 6b.[1] In the V configuration (Figure 6a) the beam is incident on a reference reflector of unknown reflectance, R, and the reflected beam is incident on a detector. This measurement yields the product of the incident intensity and the reflectance R,

$$M_V = RI_V \tag{2}$$

For the W configuration the sample to be measured is inserted in the beam, and the reference reflector is flipped over to a position symmetrically located on the opposite side of the specimen as indicated in Figure 6b. If the reflectance of the sample is r, then the detector now measures

$$M_W = r^2 RI_2 \tag{3}$$

In general, $I_W \neq I_V$ due to laser instability, and a portion of the incident beam must be split off and monitored for fluctuations. This monitor reading is used to normalize M_V and M_W so that effectively $I_W = I_V = I$, and the reflectance of the sample is obtained from the ratio:

$$\frac{M_W}{M_V} = \frac{r^2 RI}{RI} = r^2 \tag{4}$$

A schematic diagram of the W-V reflectometer in its present form is given in Figure 7, and a photograph of the equipment in Figure 8.

Single-Bounce Reflectance Measurement

In some cases, due to the size and weight of the grating or diffracted orders that might interfere with the W-V measurement, we measure the zero-order efficiency of the grating in a simple single-bounce arrangement. In order to have confidence in this technique, we must also measure a reference reflector (the reflectance of which is known) in the same configuration and normalize our zero-order efficiency to this reference.

Measurement of the Diffracted Order Efficiency

Since our HEL grating measurements must be performed in the infrared, we routinely use a visible HeNe coalignment laser to locate the invisible beam. However, when a beam is diffracted from a grating, the angle of diffraction is wavelength dependent and, in general, the infrared beam and the HeNe coalignment beam will be diffracted into different directions. The problem of locating the correct position for the detector in order to intercept the diffracted infrared beam has been solved with an alignment procedure using the zero order of the HeNe beam.

The diffraction angle for the nth order of the infrared beam is calculated from the grating equation

$$\sin\theta_n = \sin\theta_i + n\frac{\lambda}{d} \tag{5}$$

where θ_i is the angle of incidence, and the sign convention for the angles requires θ_n and θ_i be positive on opposite sides of normal. We can now calculate the angle through which the infrared beam will be deviated from the incident direction in the following equation:

$$\theta_D = \theta_n + \theta_i \tag{6}$$

In order to locate this angle with the zero order of the HeNe coalignment laser, we first retroreflect the HeNe to read the zero angular position on the rotating stage used as a mount for the grating. The stage is rotated through half the deviation angle

$$\theta_R = \frac{\theta_D}{2} = \frac{\theta_n + \theta_i}{2} \tag{7}$$

and the zero order of the HeNe is now in the correct position for detector placement. This position is illustrated in Figure 9. The rotating stage must be readjusted to the correct angle of incidence after positioning the detector. The angle of rotation from retroreflection for this position is just equal to the angle of incidence

$$\theta_R = \theta_i \tag{8}$$

This two-step procedure assures accurate detector alignment, which is essential for accurate diffraction measurements. An example of diffraction and scattering data measured with this technique is given in Figure 10 for a compound interlace grating.[2]

Summary

The general procedure outlined here for the evaluation of HEL gratings begins with a determination of the characteristics of the grating, such as, the groove profile. The AFWL diffraction code is then used to calculate the expected grating performance. If possible, the zero-order efficiency is measured on a reflectometer for accurate calibration of the subsequent measurement of the diffracted orders. The specular or zero-order HeNe coalignment beam is used to accurately position the detector for the measurement of diffracted orders.

References

[1] Baumeister, Phillip, "Reflectance and Transmission Measurements," Proceedings of the Society of Photo-Optical Instrumentation Engineers, Vol. 50, p. 37. 1974.
[2] Chi, Changhwi and E. J. Herman, "Compound Interlaced Grating Development," Journal of the Optical Society of America, Vol. 68, p. 1404. 1978.
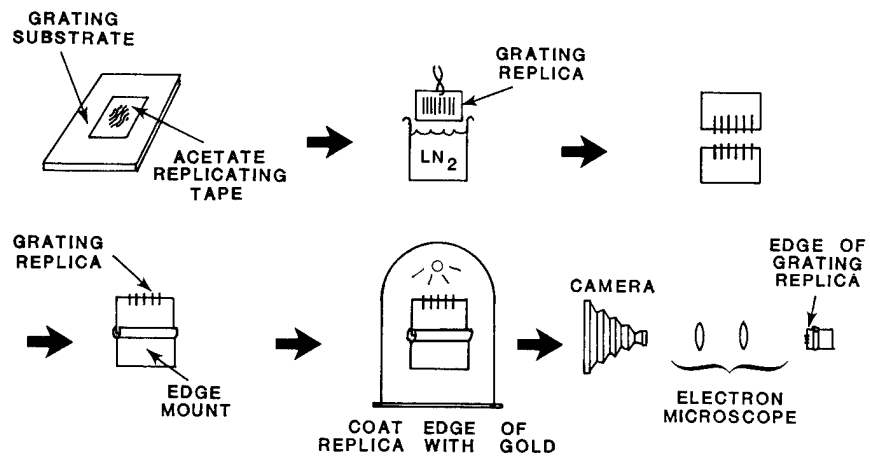
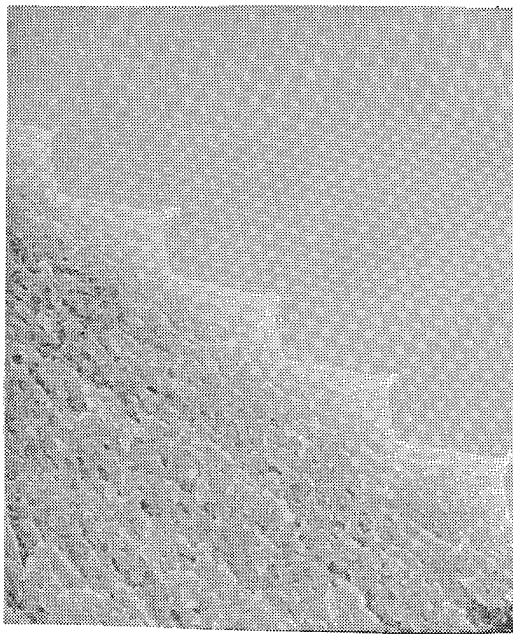Fig. 1.   Grating Profile Determination.

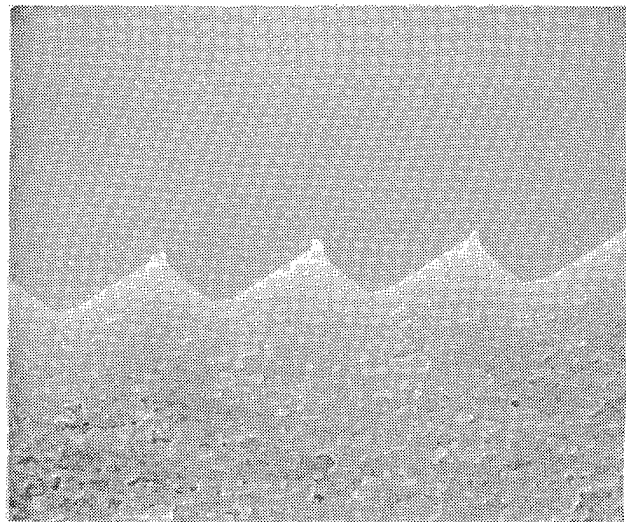Fig. 2.   SEM Photograph of a Grating Replica.

Fig. 3.   SEM Photograph of Grating Replica.

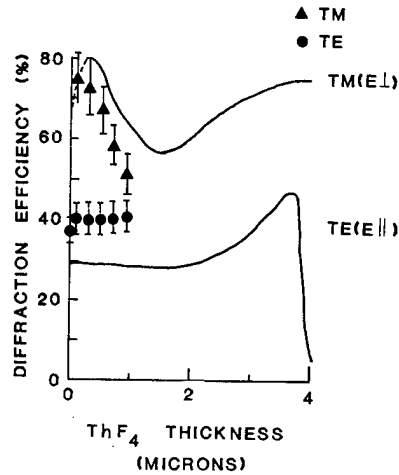Fig. 4.   Numerical Difficulties with the AFWL OMEGA Diffraction Code Occurred
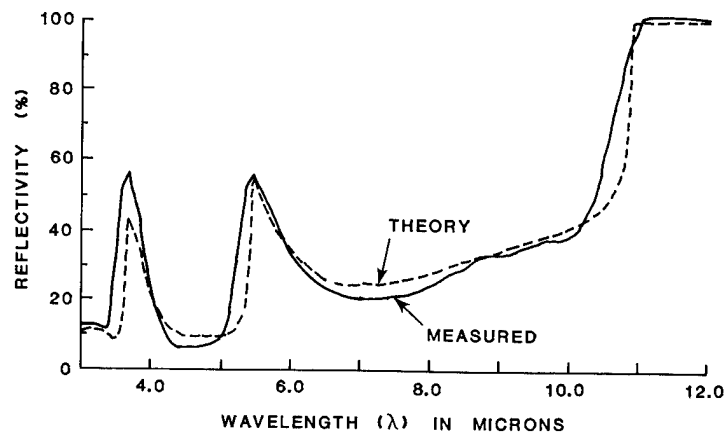   at Thin Overcoating Thicknesses for E⊥ Polarization.

Fig. 5.   Comparison of the Measured Zero Order Efficiency of a Grating with
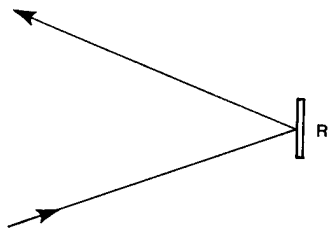   Theoretical Results Predicted by the AFWL OMEGA Diffraction Code.

Fig. 6a.   The "V" Configuration Involving   Fig. 6b.   The "W" Configuration with Sample
           a Reflector of Reflectivity R.   in Position and Reflector
                                                             "Flipped" to Second Position.
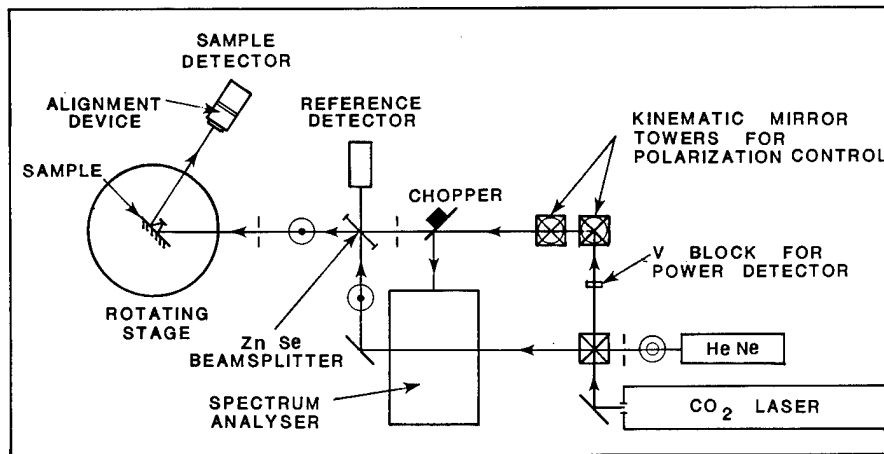
Fig. 7. Schematic Diagram of W-V Reflectometer.
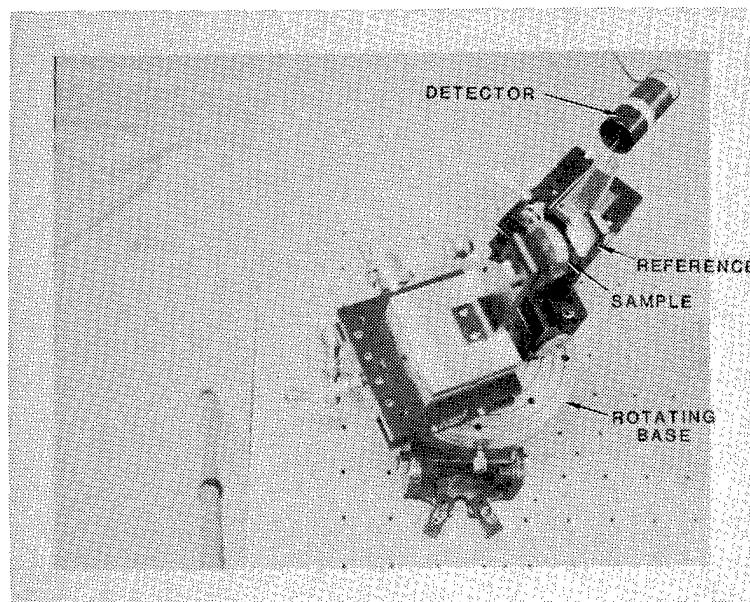
Fig. 8. Photograph of the W-V Reflectometer.
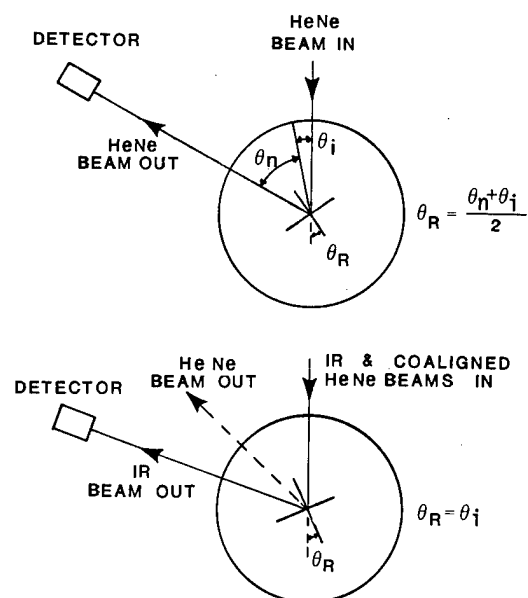
Fig. 9. Angular Alignment Using the Zero Order HeNe Coalignment Laser.
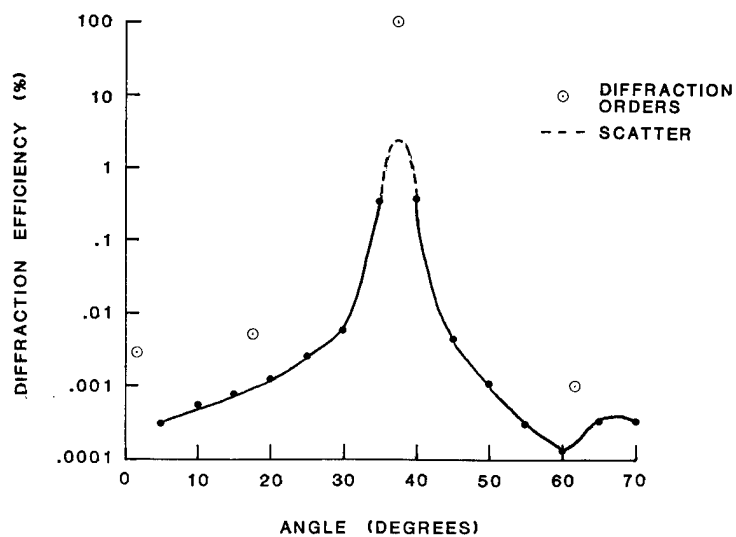
Fig. 10. Compound Interlace Grating Scattering and Diffraction Efficiency (El Polarization).

ANALYSIS OF INTERFEROGRAMS FROM WAXICONS

John S. Loomis

Optical Sciences Center, University of Arizona

Tucson, Arizona 85721

Abstract

Axicon elements are used in cylindrical optical systems such as high-power chemical lasers. Interferometric tests of such elements cannot be interpreted by standard methods. Axicon aberrations of cone error and decenter error are defined to help interpret such interferograms. A preprocessing option was added to FRINGE to treat axicon data. An example interferogram has been analyzed.

Introduction

The routine fabrication of unusual optical elements such as axicons was made practical by such techniques as single-point diamond machining of materials to optical tolerances. Current designs of cylindrical optical systems such as high-power chemical lasers call for combinations of axicon elements to transform a thin annulus of large inner radius into a smaller, more compact annular pupil. Nonlinear geometries may be imposed to improve the stability of a resonator design or to map the incoming distribution of intensity to a more desirable output distribution.

Axicons are axially symmetric conical elements, as shown at the left of Figure 1. They are generally used in pairs consisting of a small inner cone and a larger outer cone. The pair may be configured either as a waxicon (so-called because of its "W" cross section) as shown in the center of Figure 1, or as a reflaxicon, shown at the right of Figure 1. A waxicon returns incident light upon itself like a mirror. A reflaxicon transmits incident light in the same direction like a window.
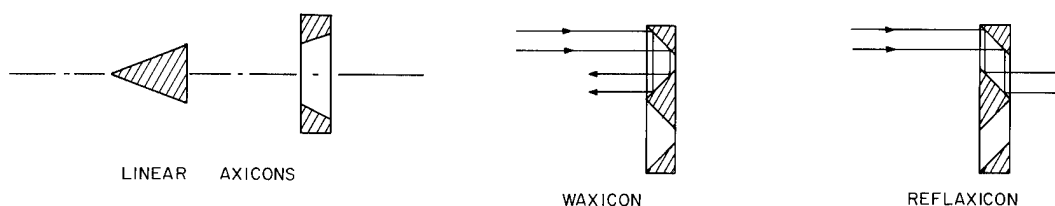

Fig. 1. Common axicon forms.

The geometry of nonlinear axicons is very similar to that of the linear axicons shown in Figure 1, except that the profile of the cross section is no longer a straight line. The use of such elements is described by Arnold et al.[1] and Mansell and Saito.[2]

The setup for testing a reflaxicon is shown in Figure 2. A very similar arrangement could be used to test a waxicon except that the flat retro-mirror must have a hole in the center to pass the incoming beam. The configurations could also be reversed, with a larger incident collimated beam and a small retro-mirror. However, this would require a much larger beam expander and would generate an annular pupil in the interferogram.

The test setup in Figure 2 shows a small aperture Twyman-Green interferometer. A high quality beam expander must be used to produce a collimated beam whose radius is no smaller than that of the inner cone. A reference flat may be used in place of the axicon elements to yield an interferometric measure of the quality of the beam expander. Generally the beam expander will have larger aberrations than those in a good flat mirror. The measured aberrations of the interferometer may be subtracted from the final data.

The reflaxicon in Figure 2 is tested double-pass. Each fringe in the interferogram represents 0.25 waves of surface error. The reflaxicon and the retro-reflector must be carefully aligned to insure that each ray samples

Fig. 2. Optical test layout for a reflaxicon.

the same points of the reflaxicon on the return pass as on the original pass.

An example of typical interferograms is shown in Figure 3. This example is taken from the paper by Arnold et al.[1] The axicon group is a waxicon configuration. The reference mirror in the Twyman-Green
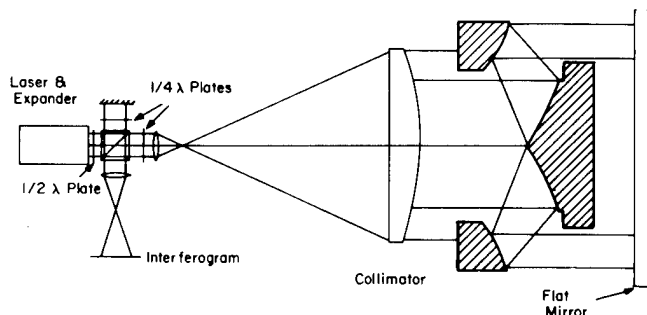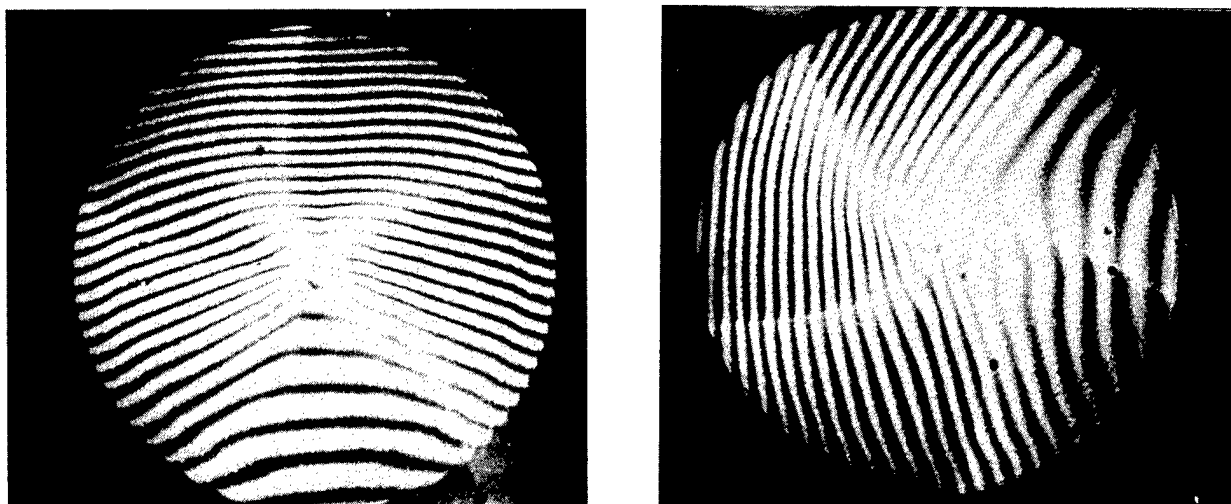
Fig. 3. Interferograms from test of Waxicon 5760 at Y-12 plant in Oak Ridge, Tennessee.

interferometer has been tilted in different directions to produce two pictures with orthogonal tilt fringes. No adjustment of the waxicon or of the retro-reflector was made between the two measurements.

The interferograms in Figure 3 reveal information about the residual manufacturing errors in the waxicon and about the alignment of the interferometer, axicons, and the retro-mirror. One problem in interpreting these interferograms is that of distinguishing between alignment errors and manufacturing errors. This paper identifies two principal errors. The origins of the errors are described. Their decomposition into Zernike polynomials provides further insight into the nature of the errors. Finally, the incorporation of an axicon analysis option in the computer program FRINGE[3] is discussed. FRINGE is a program for the analysis of interferometer patterns produced in optical testing situations.

Axicons vs Aspheres

Let us compare axicon aberrations to those found in aspheric optical systems. As a start, consider an overall sag error. The term sag error refers to an error in the coefficient that multiplies the sag equation. For example, in fabricating an aspheric surface, a certain conic constant or fourth-order aspheric coefficient may be required to produce an aspheric sag of

$$S = Ar^4$$

where S is the aspheric sag, A is the coefficient, and r is the radius at which the sag is measured. An error α in the aspheric coefficient will produce a variation in the fringe pattern given by

$$\Delta S = \alpha r^4$$

that has the same functional form as the sag equation. In a null test configuration only the sag errors will be observable in the interferogram. The spatial dependence will still be the same as for the original sag.

Since a linear axicon has a sag proportional to the radius, the corresponding sag error is also directly proportional to the radius. The sag error of an axicon system, tested in a null configuration, as in Figure 2, resembles a cone, and is often called cone error. It originates as an error in the tilt angle of the axicon cone. A projection plot of the cone error is shown in Figure 4. A contour plot would consist of equally spaced circular contours. Cone error is a continuous function, but has a discontinuous derivative at the origin.
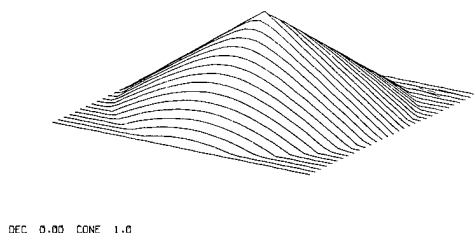

DEC 0.00 CONE 1.0

Fig. 4. Axicon cone aberration.

In a null configuration aspheric components are balanced so that aspheric terms cancel in the interferogram. If an aspheric surface is tilted or decentered with respect to the optical axis of the interferometer, an error is observed in the interferogram. For small decenters δ in the x direction, an aspheric decenter has the form

$$\Delta W = A[(x+\delta)^2 + y^2]^2 - A[x^2+y^2]^2$$

$$\Delta W \simeq 4A\delta(x^2+y^2)x.$$

This aberration has the familiar functional form of third-order coma.
The corresponding error for an axicon system is found from

$$\Delta\omega = A[(x+\delta)^2 + y^2]^{\frac{1}{2}} - A(x^2+y^2)^{\frac{1}{2}}$$

$$\Delta\omega \simeq A\delta(x/r).$$

For lack of a better name, this error is called axicon decenter error or simply decenter error. Figure 5 shows the functional form of the error. The contour plot consists of unequally spaced radial lines. The function is discontinuous at the origin. It is continuous along any path around the origin, as may be seen in the projection plot in Figure 5. The aberration is similar to tilt and coma in that it is linear in orientation angle. Rotating the decenter vector causes the aberration to rotate by the same amount.

DEC 1.00 CONE 0.0
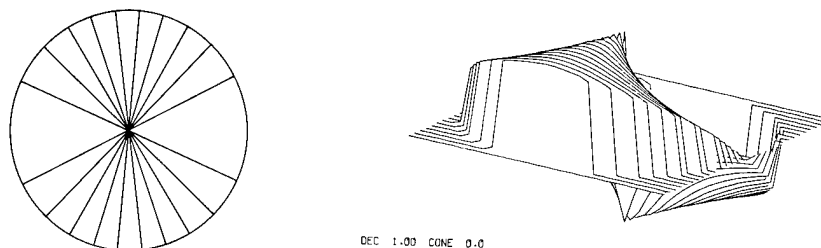
Fig. 5. Axicon decenter aberration.

A combination of axicon cone and decenter errors is shown in Figure 6. The cone aberration is twice the decenter aberration. The discontinuity at the origin still exists, but the magnitude is reduced to a smaller proportion of the total aberration because of the superimposed cone error.
A mixture of simple tilt and axicon decenter is shown in Figure 7. The amount of tilt was chosen to minimize the mean square error. The result is a symmetric pattern not unlike coma.

CONTOUR STEP .200
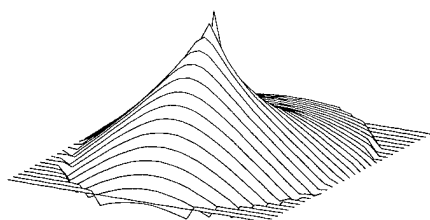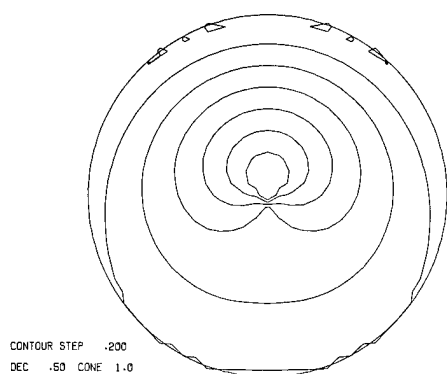DEC .50 CONE 1.0

CONTOUR STEP .200
DEC 1.00 CONE 0.0

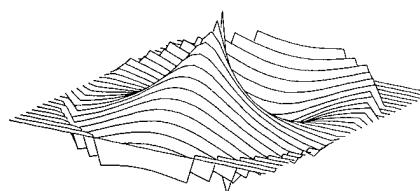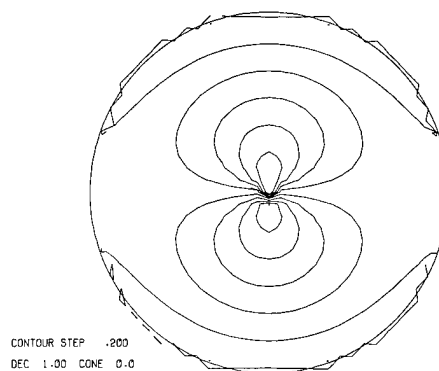Fig. 6. Superposition of coma and decenter aberrations.

Fig. 7. Superposition of tilt and axicon decenter.

Zernike Polynomial Expansion

Zernike polynomials can be used to represent optical aberrations defined within a circular pupil. The low-order polynomial terms correspond to the classical Seidel aberrations, but are referred to a "diffraction" focal point rather than the Gaussian focus. Zernike polynomials are orthogonal. The individual terms contribute independently to a total mean square wavefront error. Zernike polynomials are also complete. Any arbitrary function can be expressed as a sum of Zernike polynomials. Thus the axicon aberrations defined in the previous section may be expressed as a sum of Zernike polynomials. Of course, there is no requirement that this sum converge to a close approximation of the axicon aberration after only a few terms. One must not only define the expansion, but also investigate its convergence properties.

Let us express Zernike polynomials in cylindrical coordinates by the notation P_n where the nth Zernike polynomial is designated in some general ordering system. A full expansion of the arbitrary function $f(r,\theta)$ is given by

$$f(r,\theta) = a_1 P_1 + a_2 P_2 + a_3 P_3 + \dots$$

where a_i are numerical coefficients. For simplicity, a single integral sign will be used to represent the area (or double integration) over the interior of the circular pupil. The coefficients in the above expansion can be obtained by multiplying both sides by a single polynomial and integrating over the pupil:

$$\int fP_i = a_i \int P_i^2.$$

Because the polynomials are orthogonal, only one term on the right-hand side is non-zero. Then

$$a_i = \frac{\int fP_i}{\int P_i^2}.$$

For cone aberration the Zernike expansion given by this method is

$$r = \frac{2}{3} + \frac{2}{5}(2r^2-1) - \frac{2}{21}(6r^4-6r^2+1) + \dots.$$

Piston, focus, and spherical aberration have been included in the expansion. There is no angular dependence. For axicon decenter the Zernike expansion is

$$\frac{x}{r} = \cos\theta = \frac{4}{3}(r\cos\theta) - \frac{2}{3}(3r^2-2)(r\cos\theta) + \dots.$$

Tilt and coma terms have been included in the expansion. All terms carry an $r\cos\theta$ angular dependence.

The approximation of a truncated Zernike expansion to cone aberration is shown in Figure 8. Note that the function and its expansion are even functions. The expansion oscillates about the cone function. For focus there are two zero crossings where the function and its expansion match exactly. The fit is worst near the apex of the cone. Each new term adds one more zero crossing and decreases the apex error. After about 10 terms, the root-mean-square error is less than 1% of the total aberration and the maximum error is about 2% of the total aberration. The usual aspheric expansion, in contrast, is best near the center of the pupil (paraxial region) and worst at the edge.
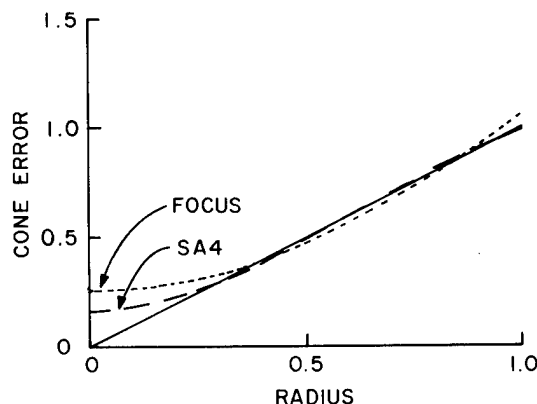

Fig. 8. Zernike polynomial approximation of cone aberration.

The approximation of a truncated Zernike expansion to axicon decenter aberration is shown in Figure 9. In this case the function and its expansion are odd functions. They must pass through zero at the origin. The cross section shown in Figure 9 is taken along the decenter direction. In other directions the fit improves. Along the direction perpendicular to the decenter the aberration is zero. As was the case in cone aberration, there is one zero crossing added for each new term in the expansion, and the fit is worst near the apex. For axicon decenter, however, the first few terms of the Zernike expansion do not approximate the axicon aberration very well at all. Many more terms are required to reduce the fitting error to acceptable limits.
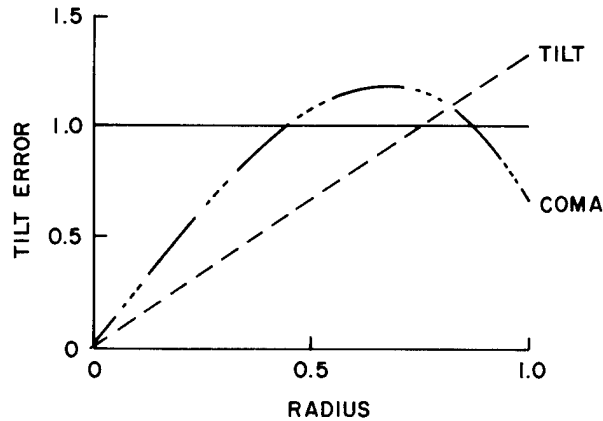
Fig. 9. Zernike polynomial approximation of decenter aberration.

FRINGE Program Modification

The FRINGE program uses either Zernike polynomials or a local interpolation scheme to generate wavefront errors over a uniform rectangular grid superimposed on the pupil. The Zernike polynomial expansion is also used to interpret the optical aberrations and to remove selected aberrations that represent alignment errors rather than fabrication errors. Presumably the alignment errors can be corrected without further work on optical surfaces.

An option to the FRINGE program was added to remove cone error and decenter error from interferometric data before processing by the usual methods. Cone error is fairly well represented by a polynomial expansion, but is calculated separately because its value has physical significance in the fabrication process. It represents an error in cone angle. The decenter aberration is calculated separately because it is not approximated by the truncated polynomial expansion used in FRINGE. It also has physical significance. The aberration is usually an alignment error rather than an optical figure error.

Figure 10 shows the results generated by the FRINGE program for the interferograms in Figure 3. The axicon option has not been used. The shape of the surface is not consistent with the interferogram and the fit to the data is poor, as a result of using a truncated Zernike series to represent decenter error. There is little agreement in the statistics evaluated at data points and the predictions for the polynomial evaluated on the uniformly spaced grid points. Figure 11 shows the results generated for the same data after the axicon option was used. In both cases tilt and focus were removed from the data. Figure 11 shows an optical surface with patches of high and low errors but no systematic or dominating aberration. The errors seem random. Analysis of both interferograms in Figure 3 produces about the same results.
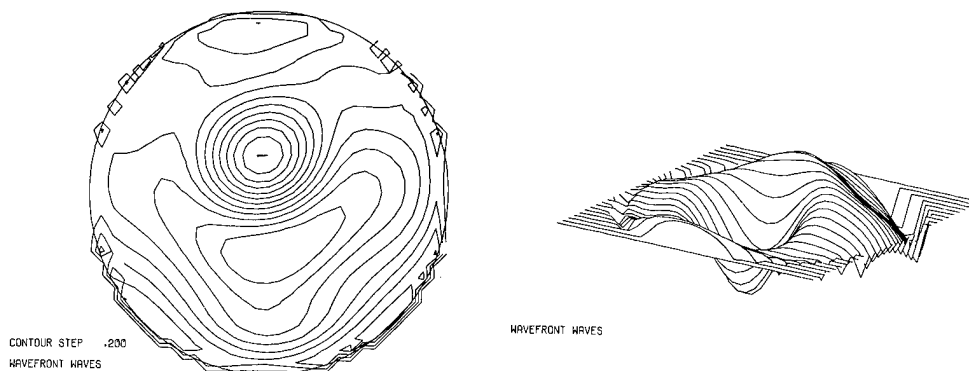

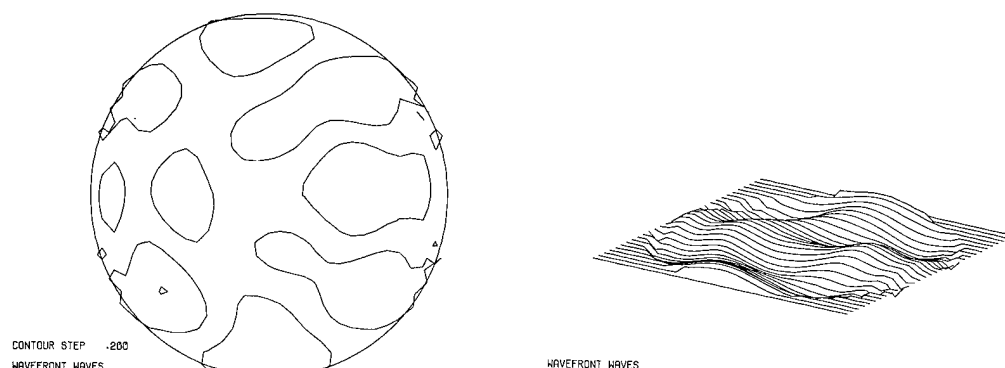Fig. 10. Interferogram reduction without removing axicon errors.

Fig. 11.   Interferogram reduction after removing axicon errors.

The numerical results are also of interest. The axicon fit gave 1.5 fringes of decenter aberration oriented at -80° to the x axis. This is consistent with the symmetry visible in the interferograms in Figure 3. The fit also found 4.1 fringes of cone error. A comparison of numerical resuls with and without removing axicon aberrations is shown in Table 1. Tilt and focus have been removed, and the residual data variations have been evaluated. The rms and peak-to-valley aberrations are greatly improved after removing the axicon terms. Most of the improvement can be attributed to the decenter error since the removal of focus acts to reduce the cone error. The large amount of coma before using the axicon fit was solely the result of the decenter error. Similarly, the fourth order spherical aberration was present only to match the cone error in the data. A significant focus error of almost one fringe remained even after explicitly removing cone error. There is more focus aberration, therefore, than can be accounted for by the cone error.

Table 1.   Comparison of FRINGE Reduction with and
without Axicon Option. Aberration Units
Are Fringes

	Without axicon fit	With axicon fit
rms	0.5	0.18
Peak/valley	3.2	1.2
Coma	2.7	0.06
Focus	4.4	0.86
Spherical aberration	-2.9	-0.005

Conclusions

Axicon, cone, and decenter aberrations have been defined as the primary figure and alignment errors found in axicon systems. The use of a polynomial expansion to represent the residual surface errors is likely to be suspect near the apex of the axicon cone. Higher order aberrations become more important near the cone tip so that alignment correction becomes more uncertain. Furthermore, the fringe spacing may not allow sufficient sampling near the tip to adequately survey the profile. Thus the exact shape of the tip, as determined by interferometric measurements, may remain uncertain.

An example was given in which axicon errors were identified. Removal of these aberrations left a residual surface profile that may represent manufacturing errors.

References

1.   Arnold, J. B., Sladky, R. E., Steger, P. J., Woodall, N. D., and Saito, T. T., "Machining Nonconventional-Shaped Optics," Opt. Eng. Vol. 16, pp. 347-354. 1977.

2.   Mansell, Dennis N., and Saito, Theodore, T., "Design and Fabrication of a Nonlinear Waxicon," Opt. Eng. Vol. 16, pp. 355-359. 1977.

3.   Loomis, John S., FRINGE User's Manual, Optical Sciences Center, University of Arizona, Tucson, Arizona, November 1976.

IN-PROCESS MEASUREMENT OF FAST ASPHERICS

John Bender and Graham Flint
International Laser Systems, Inc.
Box 9316, International Airport
Albuquerque, NM 87119

Abstract

In the fabrication of fast aspheric mirrors having diameters in the 20-30 inch range, it ceases to be practical to introduce the required correction by polishing alone. One is faced, therefore, with aspheric figure control of a surface which cannot be tested optically. To overcome this problem we have adopted the use of precision profile monitors which can provide a prepolishing surface having an accuracy of better than one micron. Upon reaching the polished stage we have found that a wire tester provides the most convenient means for figure control. However, for the final stages of polishing, where local hand correction may be required, it is desirable that the wire tester be replaced by a full aperture interferometric technique; usually a null lens. Described in this paper is a three stage monitoring procedure which uses a profile monitor, a wire tester and a null lens. Accuracy and convenience of each technique are discussed. Also, suggestions are made concerning the optimum point at which one instrument should be exchanged for another.

Introduction

In the fabrication of severe aspheric mirrors the surfaces of which depart from the starting spherical configuration by an amount which is not practical to introduce by a polishing process alone, one must utilize a monitoring device which does not require a reflecting surface for analysis. Additionally, it is desirable that the surface in process be brought sufficiently close to prescription so that subsequent interpretation of interferometric data is obvious and unambiguous. The requirements imposed upon the DOF[*] with the fabrication of a 27 inch diameter F 1.4 ellipsoidal mirror, the surface of which departed from the initial edge tangent spherical surface by approximately 400 microns, provides a good illustration of this requirement. In performing this task the DOF[*] has followed a three phase diagnostic program designed to monitor the progress and accuracy of the mirror throughout the fabrication process. This program utilized a Surface Profile Monitor while generating the basic aspheric contour with a free abrasive grinding process, a Wire Test Apparatus once polishing operations were commenced and ultimately a Null Lens/Interferometer for final quantitative analysis. While all of these instruments have been available, in one form or another, for many years their use both with modern metrology equipment and in conjunction one with another is worthy of note.

Surface Profile Monitor

The Surface Profile Monitor is a mechanical instrument capable of discerning small departures from a specific, pre-determined sphere. This device, as designed and built at the DOF, employs a ball pivot precisely positioned at the mean center of curvature; in this case a concave F 1.4 ellipsoidal mirror of 27 inch diameter. Suspended from the ball pivot is a pendulum to which an appropriate interrogating sensor is attached. The accuracy of the instrument is determined by:

1. The degree of precision achieved when locating the pivot point at the mean center of curvature of the mirror under test.

2. The effects of moments created when the interrogating pendulum is swung outward from the gravity vector to the 10° angle required to complete a full radial scan of the mirror's surface.

3. The resolution and reliability of the interrogating sensor itself.

4. The variables resulting from thermally induced distortions of the instrument structure while subjected to the lab environment.

Addressing the above considerations regarding precise location of the ball pivot led ultimately to the instrument configuration depicted in Figure I. In this design the ball pivot is rigidly held atop a thin-walled slotted aluminum cylinder; the base of which comprises an integral centering fixture and support pedestal. The centering fixture consists simply of a precisely machined lucite disc which fits into the central perforation of this specific mirror; thus providing repeatable radial registration of the instrument with respect to the mirror's optical axis. Positive registration along this axis is provided by the support pedestal which rests upon the fine ground surface of the mirror itself.

---

[*]Development Optics Facility of the Air Force Weapons Laboratory operated by International Laser Systems, Inc.
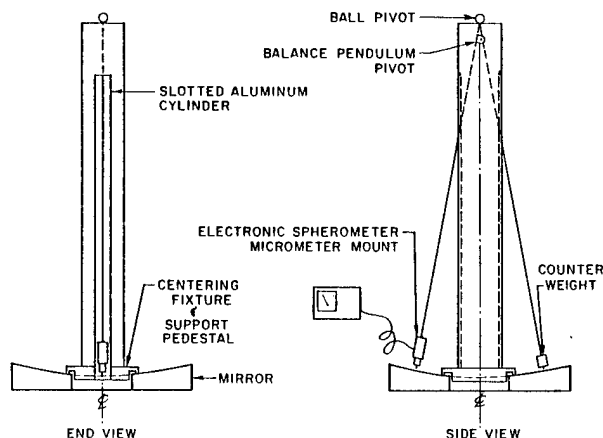
Figure 1   Surface Profile Monitor, Outline Diagram

The variables introduced by the effect of moments which would occur when the interrogating pendulum is swung outward from the gravity vector were counteracted by installing a balance pendulum and counter weight. In use the balance pendulum is moved to the same radial position as the interrogating pendulum, thus eliminating the tendency of the aluminum cylinder to deflect in the presence of a radial component of force.

Since the purpose of this instrument is to provide a fine ground surface, the accuracy of which is compatible with the corrective capabilities of the subsequent polishing process, no attempt was made to athermalize the instrument. In practice the thermal sensitivity manifested itself as a 45 minute stabilization period subsequent to placing the instrument on the surface of the mirror. A radial scan could then be performed with no apparent thermally induced anomalies. As an interrogating sensor, we chose to mount an electronic micrometer head to the end of the pendulum. This unit employs a large micrometer barrel, the finest divisions of which represent increments of 1×10^{-4} inches. Local radii of the mirror surface are then read to an additional significant figure with an electronic meter, the resolution of which can be set to increments as small as 1×10^{-5}". In actual use, when all the residual variables are compounded, a more realistic setting proved to be 2×10^{-5}" thus providing a reliable level of accuracy to less than one micron $(4 \times 10^{-5}$").

A typical measurement sequence while employing the Surface Profile Monitor would commence by placing the instrument on the mirror's surface, taking care to be certain that the lucite pilot disc is properly seated in the central perforation of the mirror. The instrument is then allowed to stabilize for about 45 minutes. During this time the exact positions to be measured along the radial scan are marked off with a pencil and a tape measure. During the early stage of correction, measurements taken at one inch intervals provide diagnostic data sufficient to identify the surface configuration. As the surface approaches the required aspheric prescription, measurements are taken at 1/2 inch intervals. Both the interrogating pendulum and the balance pendulum are swung outward to radial positions which are 180 degrees apart. A length of cord tied to the end of each and slipped into a snug cotter pin suffice to restrain both pendulums in the measurement position. A full measurement sequence results in a series of "readings" which are then punched into a pre-programed desk top computer which traces out an x,y coordinate chart illustrating the surface configuration relative to the specified aspheric prescription. An entire measurement sequence requires approximately 1-1/2 hours, with a large fraction of the time being taken by the required stabilization period. Figure 2 represents typical data derived with the Surface Profile Monitor. It also traces the progress made on the F 1.4 ellipsoidal mirror whilst in transition from sphere to the point where polishing operations could begin, and where non-contact optical test techniques such as Wire Testing could be employed. The vertical axis in this figure represents deviation from the desired surface where the prescribed ellipse constitutes any horizontal line.

Wire Testing

The wire test provides a convenient means for identifying an axisymetric aspheric contour by measuring the relative change of radius of specific annular regions of a mirror's surface. At the DOF, this technique is employed as an intermediate diagnostic tool; the purpose of which is to monitor the progress of severe aspheric surfaces as they advance through the polishing process to the point where interferometric test techniques can yield readily interpretable data. An optical schematic of the instrument employed can be found in Figure 3. The components illustrated are rigidly mounted on an x,y,z translation stage, the y axis of which is monitored by a linear encoder with an illuminated digital display. The instrument was designed and built by the University of Dayton's Research Institute as part of their optical testing and evaluation support for the Air Force Weapons Laboratory. The operating principles of this test technique are illustrated in Figure 4. In Illustration 4A it can be seen that a wire placed at the intersection of rays reflected from annular region A will block those rays while rays reflected from the remainder of the surface are
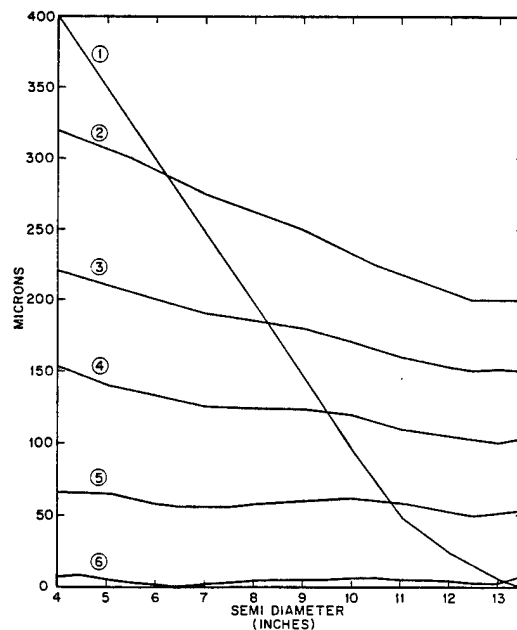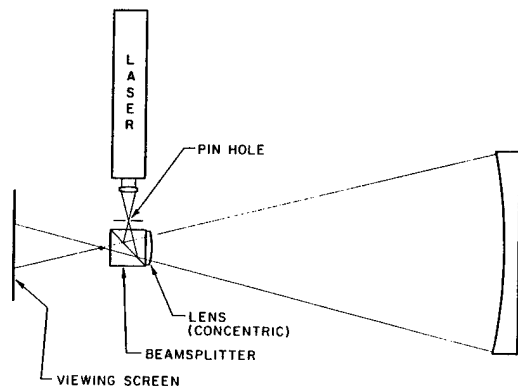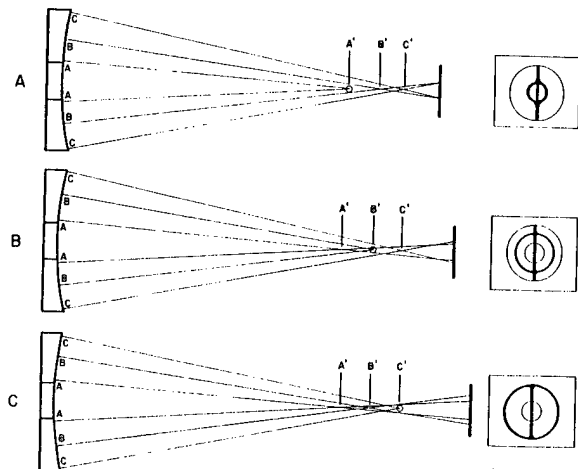
Figure 2

Figure 3

Figure 4

permitted to pass on to the viewing screen casting only the straight verticle shadow of the wire as it protrudes through the convergent cone of light. These effects are presented to the observer on the viewing screen as a projected image depicted on the right side of the illustration. Here, on the dark viewing screen, an illuminated image of the mirror can be seen with a dark annulus created by the absence of the rays reflected from the annular region A. The image is bisected by the straight vertical shadow of the wire itself. In Illustration 4B, the position of the wire has been moved along the optical axis to the point where the reflected rays from annular region B intersect, thus blocking their path to the viewing screen. In this case, the image presented to the observer will contain a dark annulus, larger in diameter and corresponding to the annular region of the mirror designated B. In Illustration 4C, the wire has again been moved along the optical axis to the point where the reflected rays from region C are blocked. The resultant image will contain a dark annulus corresponding to that region. The amount of spherical aberration, as indicated by the distance from A' to C', will be a direct function of the asphericity of the mirror's surface. The same

can be said of the center of curvature of any given zone falling between zones A and C. With this relation-ship in hand, a specific prescription can be formulated predicting the change in radius of curvature between any given zones of a concave aspheric surface. Measurement of the axial displacements of this series of zones can then identify the aspheric contour existing on the surface of the mirror. A convenient means of identifying specific zones of the mirror during the course of a measurement sequence is to place in front of the mirror a bar from which protrude vertical pins of 1 mm diameter and 1 cm. spacing. Care should be taken, when installing the bar, to assure that the distance from the outside edge of the mirror to the first visible pin is equal on each side of the mirror.
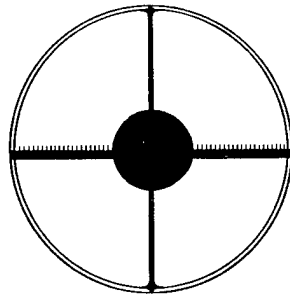
Figure 5

A typical measurement sequence entails placing the Wire Test apparatus, with the encoded axis of motion coincident with the optical axis of the mirror, at a position where the wire will obscure the reflected rays of a pre-selected zone from which all measurements will be made. The first visible pin from the edge of the mirror is a convenient starting position. The resultant image presented to the observer is depicted in Figure 5. The digital display is ""zeroed" and the y axis of motion is translated along the optical axis until the dark annulus is superimposed on the next pin. Some lateral translation may be required to maintain the wire on the optical axis. The "reading" appearing on the digital display is recorded and the apparatus is again advanced until the dark annulus is superimposed on the next pin. Again the displayed value is recorded. This sequence is repeated until a numerical value is assigned to each pin appearing within the semi-aperture of the mirror. This procedure yields a series of readings typified by Figure 6. These data can then be reduced to cognitive form by integrating the readings on an x,y graph upon which the prescribed radius displacements have been previously plotted as a function of the semi-diameter of the mirror. An example of such a graph is shown in Figure 7. The data presented therein represents the results of the first wire test performed on the F 1.4 ellipsoidal mirror; the aspheric surface of which was monitored previously through the fine grinding state by the Surface Profile Monitor previously described. It should be noted that this graph does not illustrate errors in terms of surface height but in terms of slope errors.

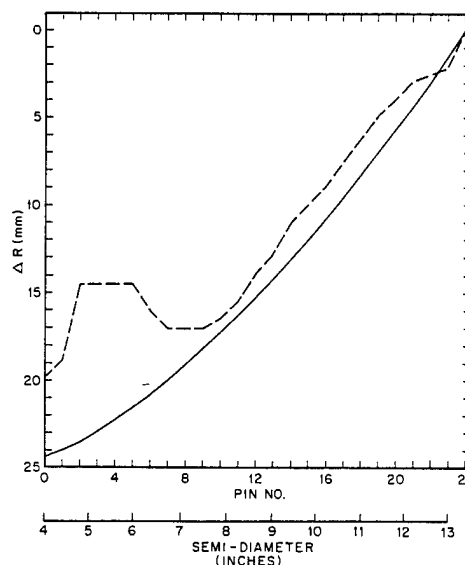| RADIAL ZONE (Pin No.)	READING MM
Edge	+ .80
24 Ref. Zone	000
23	1.58
22	2.27
21	3.03
20	3.84
19	4.96
18	6.33
17	7.61
16	9.27
15	10.34
14	11.63
13	12.88
12	14.30
11	15.93
10	17.49
9	18.39
8	17.49
7	15.92
6	14.30
5	14.30
4	14.30
3	14.30
2	15.92
1	19.17
0	24.76

Figure 6

Figure 7

In order to compare data resulting from the first wire test of the freshly polished surface with that of the final Profile Monitor measurement, the initial wire test data was further reduced to a comparable surface profile chart. A direct comparison of the results obtained from each technique can be found in Figure 8. It can be seen that the two techniques are in reasonably close agreement considering 10 hours of polishing had occurred between the measurements. The degree of accuracy·to which Wire Test measurements can describe an aspheric surface is, to a certain extent, influenced by subjective judgements made on the part of the operator. The eyesight of the operator, experience with the technique, and patience are all factors which affect the critical assessment made in judging when the dark annulus is at a precise location on the surface of the mirror. In order to ascertain the level of accuracy which one might ascribe to the wire test technique, the DOF re-examined the same F 1.4 ellipsoid after final figuring and interferometric testing had been completed. The wire test apparatus was reinstalled at its interrogating position and a careful series of measurements were made by three different operators. The results of these measurements can be found in Figure 9. Here it can be seen that measurements vary somewhat from one operator to another, indicating that additional refinements would be needed to elevate the technique to one limited only by the laws of physics. Such refinements would include more precise identification of the exact location of the zone being measured.
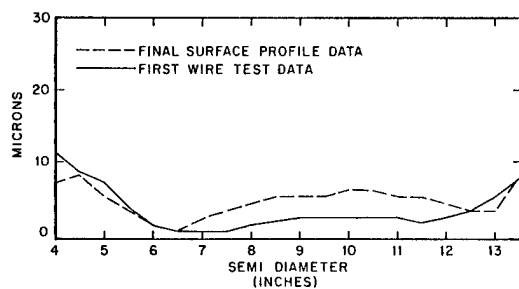
Figure 8
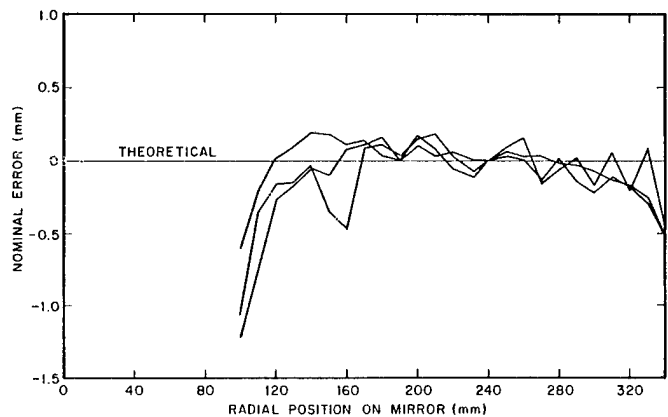
Figure 9

However, additional refinements do not appear necessary when utilizing the wire test as a preliminary mode of diagnosis, the intent of which is to prepare the mirror for interferometric testing. Figure 10 graphically illustrates this point. Here, the theoretical ellipsoidal prescription can be compared with the calibration data derived from the completed mirror, with the first wire test data taken from the freshly polished surface, and with that taken prior to transfering diagnostic responsibilities to the Null Lens/Interferometer. The residual errors indicated by the latter manifested themselves as a turned up edge of four fringes extending from pins 21 to 24, a low center of 13 fringes extending outward to pin 13, and a null area from 13 to 21. The 17 fringes of total error were quite discernible and unambiguous as the mirror advanced on to its third and final phase of correction employing a Null Lens Fizeau Interferometer as the final diagnostic tool.
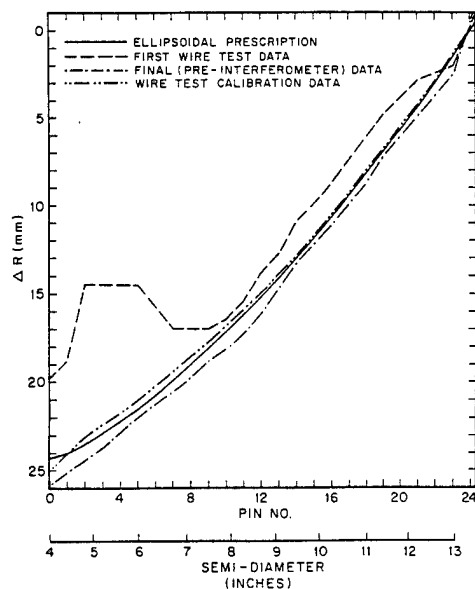

Figure 10

Null Lens Testing

The Null Lens/Interferometer is an optical diagnostic tool, the use of which, as an in-process test device, has only become practical with the availability of low cost, high intensity, mono-chromatic light sources. These instruments are typically employed at the radius of curvature of the component under test and provided the DOF with an attractive alternative to testing the F 1.4 ellipsoidal mirror at its prescribed foci , the longer of which was approximately 67 feet from the mirror. The Null Lens/Interferometer served as the final diagnostic tool to be employed in the three phase diagnostic program chosen to monitor the mirror figure as it progressed from a spherical surface to the final ellipse. The instrument used at the DOF was designed and built by B.C. Platt of the University of Dayton's Research Institute and M.C. Ruda of the Optical Sciences Center, University of Arizona. It employs a two element lens system which compensates for spherical aberration of the ellipsoidal mirror when tested at its center of curvature. In Figure 11, it can be seen that the spherical wavefront thus provided is interferometrically compared to a reference wavefront generated by an internal reflection from the concentric convex surface of a plano convex lens; the latter being optically cemented to the front of a beamsplitter cube. Since the interferometer is integrated into the Null Lens housing, alignment steps are held to a minimum. The ellipsoidal mirror, mounted on a tilt table polishing machine, could be swung to bring its optical axis horizontal, thus making the center of curvature accessible for interrogation. The pointing registration of the table was such that any necessary readjustment of the Null Lens/Interferometer could easily be accomplished with the x, y, z translator stage upon which the instrument was mounted. A typical test sequence requires approximately 20 minutes to complete and yields recorded data in the form of an interferogram to which the optician can refer during the ensuing polishing cycle.

Final interferograms (Figure 12) taken after all apparent symmetrical errors were polished from the surface and asymmetric errors were reduced to tolerable levels were numerically digitized and reduced by the University of Dayton's Research Institute. The resultant data revealed a surface accuracy of .7 waves peak to valley where λ is equal to .6328μ. Residual asymmetric errors were inherent to the structure of the mirror and are not representative of the quality of the Null Lens/Interferometric system. A test iteration performed at the ellipsoidal foci of the mirror confirmed the surface errors as indicated by the Null Lens/Interferometer. However, the relative difficulty encountered during the conjugate focus test illustrated profoundly the inherent convenience of the Null Lens.
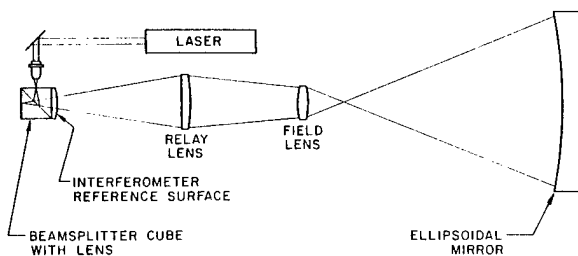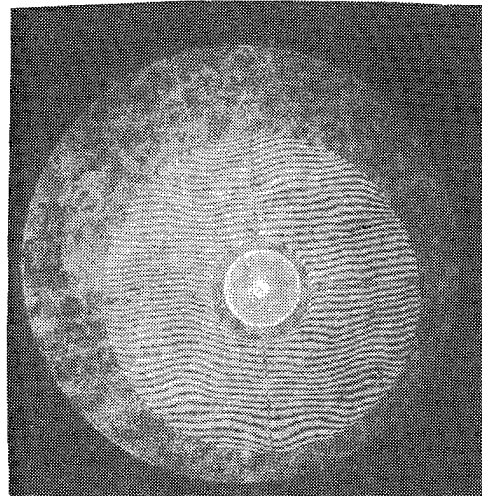

Figure 11

Figure 12

Conclusion

Although the procedures and instrumentation described proved themselves convenient and functional, there is no reason to consider them refined beyond improvement. The point at which diagnostic responsibilities were transferred from the Profile Monitor to the Wire Test was arbitrarily chosen. Based more on the fact that considerable polishing would be required to bring the fine ground surface to a full polish, the potential accuracy of the device was not fully exploited. Once polishing operations have commenced, it would not seem prudent to utilize a device which employs mechanical contact at both the points of interrogation and registration. However, the fine grinding sequence might possibly be lengthened to provide a surface which would be of sufficient accuracy to transfer diagnostic responsibilities directly to the Null Lens/Interferometer. The weight of the Profile Monitor would probably introduce some distortion to the mirror when striving for accuracies which would yield interferometeric data with few enough fringes to be resolvable by the human eye.

Having been asked to duplicate the ellipsoidal configuration described on a second mirror, the DOF has elected to design a second Profile Monitor. This instrument will be of lightweight construction, a tripod shaped device employing pyrex tubing which should reduce the thermal stabilization period required with the aluminum device. As an interrogating sensor, an electronic linear encoder will be installed at the end of the pendulum. This device, manufactured by Boeckelir Instruments, Inc., has a certified accuracy of ±1 micron and will interface with an L.E.D. Digital Display.

In the event that the need for a Wire Tester as an intermediate diagnostic tool is circumvented, the wire tester will remain a useful and valuable device. As a diagnostic tool for use when generating a moderate aspheric surface by polishing alone, it is superior to the classic Foucult Knife Edge. It also lends itself more readily to description and explanation when introducing the technique to someone new to the craft. The incorporation of the linear encoder/digital display provides a welcome improvement over trying to read a micrometer thimble in a darkened test tunnel.

The use of the Null Lens/Interferometer reduced the test space requirements from 80 feet to 10 feet and also effected a significant reduction in the number of man/hours dedicated to in-process testing during the final figuring phase. Such a device would be invaluable for testing either general aspherics or concave hyperboloids which, by their nature, do not lend themselves to convenient test configurations.

IN SITU BIDIRECTIONAL REFLECTANCE DISTRIBUTION FUNCTION (BRDF) MEASUREMENT FACILITY

Dr. B. M. Kale
Aerojet ElectroSystems Company
P. O. Box 296
Azusa, CA 91702

Barry Broome
Aerojet ElectroSystems Company
P. O. Box 296
Azusa, CA 91702

Abstract

The angular distribution of light scattered from optical surfaces is best described by a Bidirectional Reflectance Distribution Function (BRDF). Scattered light in spaceborne optical systems may be induced by surface contaminants that are present only under the combined conditions of extreme cold, high vacuum, and strong ultraviolet radiation. An instrument is described that generates surface contaminants and measures BRDF in situ. Measurements are performed at 10^{-8} Torr pressure and at 77K for angular scatter ranging from one degree away from the specular reflected beam to sixty degrees away from the specular reflected beam. Measured BRDF intensity ranges from 10^{-0} watt per incident watt per steradian to 10^{-6} watt per incident watt per steradian.

Introduction

The effective design of many classes of optical systems requires knowledge of the component scattering properties. Scatter phenomena are especially important in optical systems which detect low radiance targets when high radiance objects are also in the field of view.

Scatter by optical components can be induced by surface micro-irregularities associated with manufacturing processes by inclusions within refractive media, or by surface contaminants. Surface contaminants may be associated with assembly and storage exposure to particulate matter or associated with outgassing effluents which form condensates on optical surfaces. Particulate scatter theory and measurements have been extensively described by Scheele[1], R. P. Young[2], H. E. Bennett[3], P. J. Young[4], and other investigators. Arnold[5] has also investigated surface cryocontaminants. The in-situ BRDF facility uniquely addresses the measurement of contamination induced scattering associated with outgassing effluent condensates on cryogenically-cooled optical surfaces.

The Bidirectional Reflectance Distribution Function

Figure 1 illustrates the geometry associated with generalized BRDF measurements. BRDF as defined by Nicodemus[6] is a function of four variables:

$$f_r(\theta_o, \phi_o; \theta_s, \phi_s) = \frac{dL_s(\theta_s, \phi_s)}{L_o(\theta_o, \phi_o)\cos\theta_o \, d\Omega_o} \ (Sr^{-1}). \tag{1}$$

When the surface is irradiated by a collimated source, Scheele[7] has shown that the BRDF can be expressed as

$$f_r(\theta_o; \theta_s, \phi_s) = \frac{d\phi_s(\theta_s, \phi_s)}{\phi_o \, d\Omega_s \cos\theta_s} \ \frac{watt}{incident \ watt - Sr}. \tag{2}$$

The Aerojet ElectroSystems facility limits measurements to the case $\phi_s = \phi_o = 0^o$, and θ_o has been set to 2.5^o. For this arrangement the measured BRDF is given by

$$f_r(2.5; \theta_s, 0) \simeq \frac{d\phi_s(\theta_s, 0)}{\phi_o \, d\Omega_s \cos\theta_s} \ \frac{watt}{incident \ watt - Sr}. \tag{3}$$

The scattered radiation may be polarization dependent. The BRDF facility provides incident radiation that can be $\phi_{o,\perp}$, $\phi_{o,\parallel}$, or $\phi_{o,CIR}$. Measurements are presently performed at both 0.6328 μm and at 10.6 μm.

A 10.6 μm test beam originates from a Sylvania Model 948 CO_2 laser (8 watts TEMoo), passes through a PTR 1200 lines/mm wire grid polarizer, becomes circularly polarized by a II-VI Inc. quarter wave retarding plate, and is attenuated over a six decade range in a manner equivalent to the 0.6328 μm beam. The attenuated beam is chopped at 100 Hz with a selectable duty cycle and injected through a germanium window.

After reflection from the sample, both the 0.6328 μm and the 10.6 μm specularly reflected beams exit the chamber via windows adjacent to the entry windows. Baffles are located adjacent to the exit windows to prevent reflected energy from re-entering the chamber. Rejection of stray light by six decades at the radiometer apertures is mandatory for successful operation.

During the measurement sequence a clean mirror sample mounted on the rotating sample support is turned to face the contaminant source and a measured contaminant load is deposited (as determined by a quartz crystal monitor located on the sample support). The support subsequently rotates the mirror into the He-Ne sample beam and the radiometer arm is driven across the 60° viewing angle to record BRDF at 0.6328 μm. The support is rotated a third time to locate the mirror in the CO_2 sample beam and the radiometer arm is driven back across the 60° viewing angle to record BRDF at 10.6 μm. The mechanisms used to move the sample support and to drive the radiometer arm must operate reliably at 90K and at 10^{-8} Torr.

The sample support consists of a copper plate located on the shaft of a Huntington Laboratories, Inc. VF180-3 manipulator. This manipulator is unique in construction and provides positive mechanical displacement (3 inch linear) and rotation (360°), so that two mirror samples can be alternately placed in the sample beams, or rotated to the contamination station. The sample support normally sits on a cryoplate that is LN_2 cooled to 77K.

The radiometer arm is driven by a geneva mechanism through a link chain operated by a rotary motion feed-through. The geneva mechanism consists of a cogged wheel (2 pins) engaging in a slotted track that is divided into 60 one degree increments. Figure 4 illustrates this mechanism. This arrangement ensures positive displacement of the arm in precise one degree increments when operated at 90K.

Optical Design Considerations

Effective instrument design demands careful attention to several optical design features.

Measurement of BRDF at angles close to the specular beam requires that the laser beam divergence and the scatter introduced by the circular polarizer and beam attenuator components be substantially lower than the scatter associated with the test surface. A scheme proposed by R. Young[2] which utilized spherical test mirrors to minimize these effects was found to be inconsistent with the thermal vacuum chamber geometry and the contamination geometry; instead, the test beam profile is measured with a scanning pinhole and these effects are subtracted from the BRDF measurements. Useful measurements can be made to within one degree of the specular beam. An aperture stop located in each radiometer restricts the observed range of scatter angle to 0.50°.

The design of the radiometers restricts the area observed by the detectors to a portion of the test sample surface that is substantially larger than the $1/e^2$ sample beam diameter, but less than the test sample diameter. This is accomplished by a lens in each radiometer that images the detector area on the test sample surface at a diameter that is 80% of the test sample diameter. This arrangement ensures that the radiometers do not observe the light scattered inside the chamber, but always observe all of the irradiated sample surface. The 0.6328 μm radiometer uses an E.G.&G. HUV 1000B photodetector/amplifier mounted on a heated plate held at $+20^{\circ}$C. The 10.6 μm radiometer uses a PbSnTe photovoltaic detector mounted on a cooled cryoplate held at 85K. The detectors were chosen for both D* and linearity properties.

Stray light scattered within the chamber can effect BRDF measurements, and can be attributed to two sources. Radiation scattered from the test sample will be multiply scattered within the chamber analogous to the behavior of an integrating sphere with low surface reflectance. This contribution to stray light can only be observed by the radiometer via specular reflection from the test sample. The chamber geometry minimizes this effect when higher scatter angles are measured; this effect is negligible.

Radiation reflected from the exit port back into the chamber would produce high stray light contributions. This effect is prevented by high efficiency coatings on the windows, and by baffles located adjacent to the windows which trap the reflected beams before re-entry into the chamber.
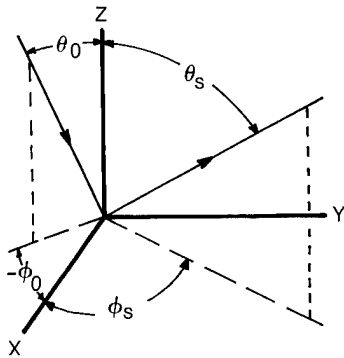
System Description

The measurement facility is incorporated into the thermal-vacuum chamber shown in Figure 2. A series of roughing pumps, adsorption pumps, and ion pumps maintain pressure at less than 10^{-8} Torr. Liquid nitrogen cooling of an internal shroud and of the BRDF apparatus maintains temperature below 90K.

A baseplate assembly located within the chamber consists of a contaminant source, a sample support, a radiometer arm, a 0.6328 μm radiometer, a 10.6 μm radiometer, and mechanisms for displacement of the radiometer arm subassembly mounted on a cooled baseplate. Figures 4 and 5 identify these components. Two sample beams are introduced to the test sample through two ports in the chamber.

A 0.6328 μm test beam originates from a Spectra Physics Model 123 He-Ne laser (7mW TEMoo), passes through a Nicol prism linear polarizer, becomes circularly polarized by a quarter-wave retarding plate, and is attenuated over a six decade range. Attenuation is provided by introducing pairs of reflective filters into the optical path at a 45° incidence angle; the transmitted beam can be attenuated by densities of 0,2,3,4, or 6. The attenuated beam is chopped at 100 Hz with a selectable duty cycle and is injected through a fused silica window. Figure 3 illustrates this arrangement.

Figure 1. Definition of the angles which appear as arguments of the Bidirectional Reflectance Distribution Function.
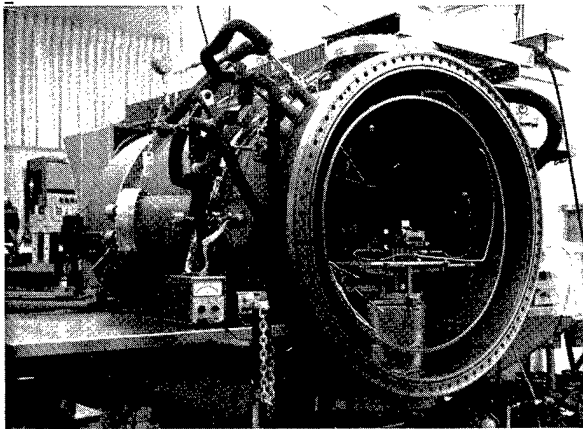
Figure 2. Photograph of the open vacuum chamber and HeNe laser and associated optics.
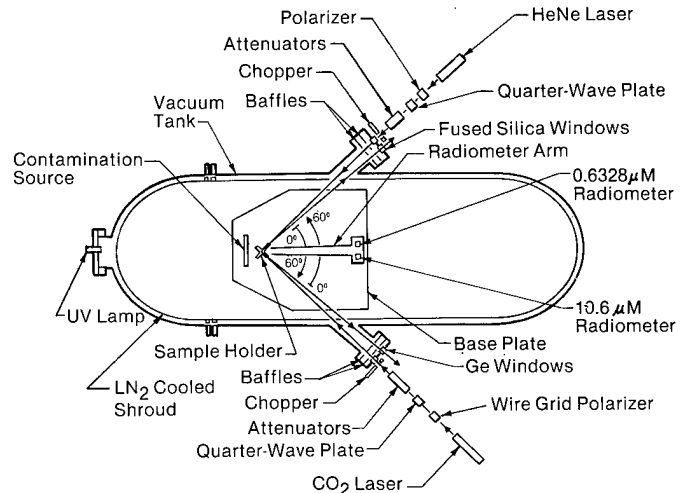
Figure 3. Schematic diagram of the BRDF test facility.
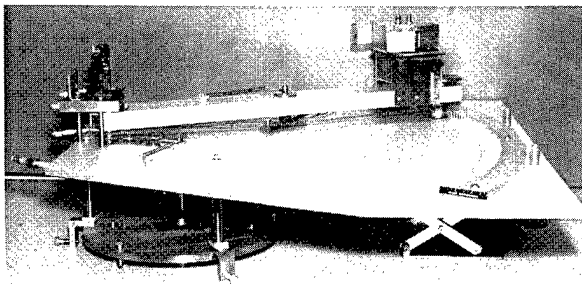
Figure 4. Photograph of the baseplate with sample holder and radiometers in position.
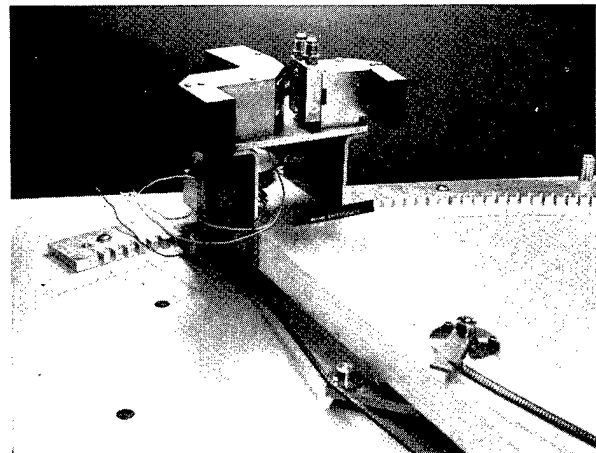
Figure 5. Photograph of the two radiometers.

Signal Processing

Figure 6 describes the signal processing electronics used for the BRDF facility. Detection of very low light levels against a high background environment (especially at $10.6\,\mu$m where the chamber wall radiance is high) requires a phase-locked system.
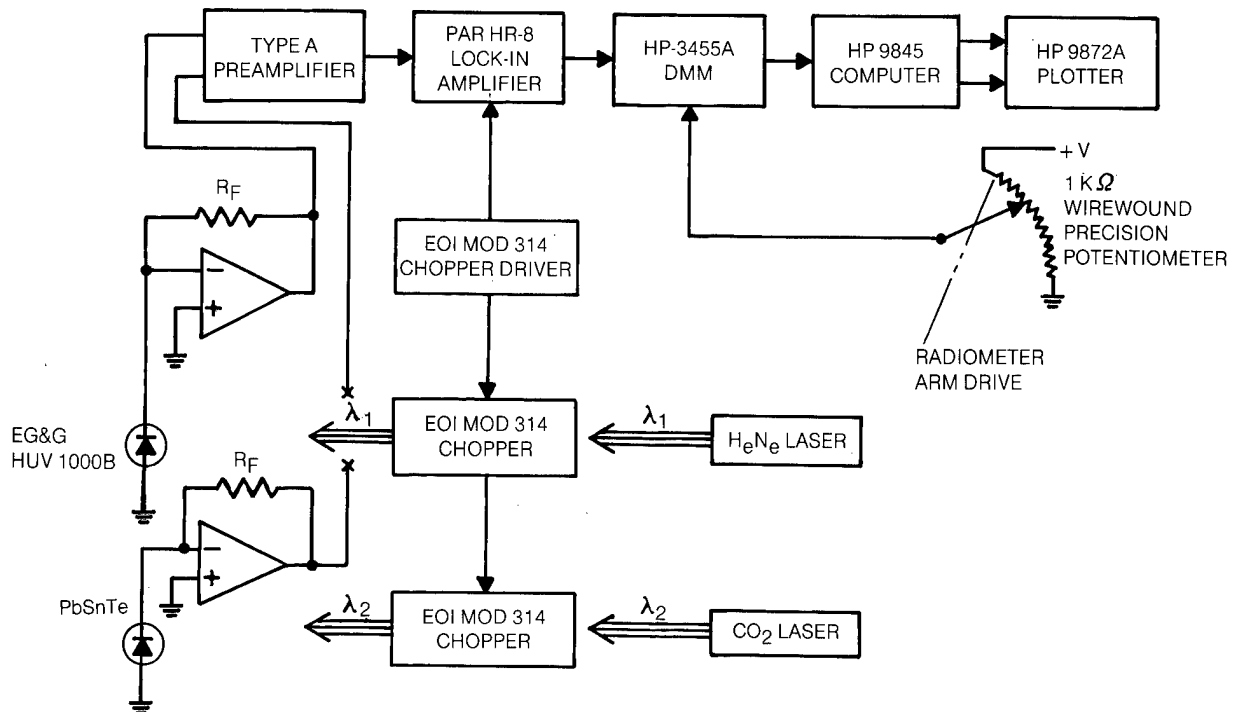
Figure 6. Schematic diagram of the signal processing and data acquisition system.

Two Model 314 Electro Optical Industries mechanical choppers are driven at 100 Hz by an E.O.I. Model 314 controller. The controller also provides a phase locking reference signal to a P.A.R. Model HR-8 lock-in amplifier. Voltages developed by either of the detectors are preamplified, conditioned by a P.A.R. Model A preamplifier, and measured by the HR-8. The analog output of the HR-8 is converted to a digital voltage signal by an HP 3455A DMM, and this digital signal recorded on a tape file by an HP 9845 calculator which also records the voltage associated with the radiometer angular position. This tape file is subsequently plotted by the HP 9845 calculator on an HP 9872A plotter as a BRDF curve on a log-log scale. The data file can be plotted in other formats to exhibit specific BRDF features of interest to the experimenter.

Results

Verification of correct system performance is assured by measuring the BRDF of a Lambertian (diffuse) scattering surface. The measured BRDF data and the expected curve have the form

$$f_r \ (2.5; \ \theta_s, \ 0) \ = \ \frac{R_T}{\pi} \ (R_T = \text{TOTAL SCATTERED RADIATION}). \tag{4}$$

Correlation between measured and predicted BRDF was found to be good at both wavelengths.

References

1. S. R. Scheele, Scattering Characteristics of Mirrors and the Inverse Scattering Problem, University Microfilms International, Number 74-11,569 (1974).

2. R. P. Young, Proceedings; AIAA Tenth Thermophysics Conference Paper 75-667, American Institute of Aeronautics and Astronautics (1975).

3. H. E. Bennett, S.P.I.E. Proceedings; Stray-Light Problems in Optical Systems, Volume 107, Society of Photo-Optical Instrumentation Engineers, pp 24-33 (1977).

4. P. J. Young, Effects of Out-of-Field Radiation on Earth-Observing Telescopes, Optical Engineering, Volume 14, Number 4, Society of Photo-Optical Instrumentation Engineers, pp 306-311 (1975).

5. F. Arnold, Degradation of Low Scatter Metal Mirrors By Cryocontaminant Contamination, AEDC Report TR-75-128.

6. F. E. Nicodemus, Directional Reflectance of an Opaque Surface, Applied Optics, Volume 4, Number 7, p 769 (1965).

A HIGH ACCURACY SURFACE CONTOUR MEASURING MACHINE

Daniel Bajuk
Tinsley Laboratories, Inc.
Berkeley, California 94710

Abstract

A surface contour measuring machine is described which can measure general aspheric or axi-symmetric aspheric surfaces repeatably to .000005 inches or better in most cases. The computer system which controls the measuring machine and which performs the data analysis is discussed. Aspheric production applications are shown in which the measuring machine plays a vital role.

Introduction

The use of aspheric surfaces in optical designs for military and scientific applications has increased greatly in the last five years. One of the challenges presently being attacked by the optical industry is the ability to produce high accuracy aspheric surfaces in production quantities. Significant progress towards the fulfillment of this goal has been made by recent advances in micro machining technology and also by the application of computers to the classical approach of grinding and polishing optical surfaces. The success of these and any method of aspheric surface manufacture is largely dependent upon the capability of testing the aspheric surface during production and of proving the accuracy of the finished surface. For many aspheric elements, relatively simple optical tests may be performed to prove final accuracy. These same tests can be used in the production phase to measure surface contour if the surface error is not greater than about .0002". However, many optical designs employ aspheric elements whose deviation from the nearest sphere exceeds from .001 to .020 inches, and often more. Furthermore, aspherics are often specified to be made from visually opaque materials. In most of these cases, no simple optical test exists which will fulfill final and/or production test requirements.

In an effort to solve the aspheric test problem, a high accuracy surface contour measuring machine has been constructed which is capable of repeatedly measuring surface contour to fractional wavelength tolerances. In addition, all functions of the measuring machine are directly controlled by a computer which gathers and stores the surface contour data for subsequent analysis.

Measuring Machine Design

The measuring machine consists of three basic components: (1) an XY positioning table, (2) an air bearing Z axis, and (3) a laser interferometer to measure the Z axis position.

The XY positioning capability (Figure 1) is provided by a #3 Moore Jig Borer with the boring head removed. The positioning of the table has been certified by Moore to be accurate to + .000025" over 18" of travel on the X axis and to + .000015" over 12" of travel on the Y axis. The table is positioned via stepper motors through a 5 to 1 gear reduction. Thus, a single step of a motor causes a .0001" table move. The machine is mounted on three pneumatic pads to reduce vibration. The Moore Jig Borer provides a structurally sound base for the mounting of additional components.

The Z axis (Figure 2) is a 24" long, hard anodized square cylindrical column. The column is captured in a double box air bearing assembly which has 16 jeweled orifices in each box. The column is straight to .000010" per inch. A counter weight system balances the 14 pound weight of the column so that the column-counterweight differential is approximately 5 grams. The Z axis assembly is mounted on the column slide of the jig borer. The slide is driven by a DC motor and provides a means of grossly positioning the entire Z axis. Positioning of the Z axis column is effected by a cable and pulley system driven by a small DC motor. Mounted at the bottom of the Z axis column is a probe assembly which houses a .250" diameter sapphire ball (Figure 3). When a surface is measured, this ball is placed in contact with the surface to establish the relative surface height.

The laser interferometer is manufactured by Hewlett Packard. The laser tube, mounted at the top of the jig borer column, feeds a remote interferometer cube which is housed in the Z axis slide assembly. The remote interferometer splits the laser beam in two parts, retaining one as a reference and transmitting the other to a cube corner mounted near the bottom of the Z axis column. The two beams are recombined to form a fringe pattern which

is scanned by electronics in the laser tube housing. Any movement between the fixed remote interferometer and the cube corner produces a shift of the fringe pattern which is measured by the laser interferometer. The interferometer calculates the change in distance between the remote interferometer and the cube corner relative to an arbitrary origin point. The change is displayed in digital form on an external console. The units of display are either millimeters, inches, or quarter waves ($\lambda = .6328$ μ).

Control of the measuring machine, either manual or computer, is via an electronics package (Figure 4) which includes X and Y axis indexing units, interferometer readout, Z axis indexing units, interferometer readout, Z axis slide and probe positioning controls and an interface between the measuring machine and the controlling computer.

Minimizing Measurement Error

Although the components of the measuring machine are individually accurate, care must be taken in combining the components to insure that allignment errors are minimized. First, the parallelism of the jig borer table to the X and Y axis was measured. Then the interferometer laser was set perpendicular to the table to an accuracy of 1 arc minute. The Z axis measurement error due to this amount of laser misallignment is less than .0000001 inches per inch of Z axis travel. Finally, the Z axis column was set perpendicular to the table to an accuracy of 2 arc seconds which results in an immeasurable Z axis error contribution.

A problem whose related error is more difficult to eliminate completely is thermal variations of the machine due to surrounding environment. Thermal variations have a dual effect upon the machine. First, temperature changes cause the machine structure to expand or contract, thus changing the distance between the remote interferometer and the cube corner. Second, temperature variations, and related pressure variations, change the wavelength of light in air, affecting the interferometer readout accuracy. The measured effect of temperature change has been minimized by positioning the remote interferometer approximately 5" from the cube corner reflector. Temperature variations have been minimized by housing the machine in a small isolated room whose temperature is allowed to 'float' with the temperature outside the room. As far as is practicable, all heat sources have been removed from the room. The door to the room is opened only to place an optical element on the XY table. Under these conditions, the temperature of the room normally varies about 1 degree Fahrenheit during a two hour period. The resultant measurement variations seen during the time required to measure a surface is usually less than .000005". However, because the error increase is approximately linear during the measurement cycle, the thermal error can effectively be eliminated during data analysis.

Another problem area surfaced when we first attempted to measure a surface with slopes greater than .5. This problem was due to the quality of the sapphire ball used in the Z axis probe. Balls are readily available with sphericity tolerances of .000025". When tested interferometrically, they exhibit small zones of .5λ to .75λ magnitude ($\lambda = .6328$μ) covering 5-10 degrees of surface. When measuring anything other than a flat, the local zones impress their image on the recorded data showing up as asymmetric zones. To solve this problem, we have optically polished the ball using a hard pitch lap and ¼μ diamond powder. Interferometer test indicates that local zones have been reduced to less than $\lambda/10$ over a selected 60° area of the sphere.

A final error arises as a function of the slope of the surface being measured. Small unknown mispositioning errors due to lead screw and stepping motor inaccuracy cause errors in Z axis positioning as a function of the slope of the surface. If the slope of the surface is 1., a positioning error of 10μ inches will produce the same error in the Z axis. By measuring surfaces with large slopes and comparing the results to interferometric measurement, we have found mispositioning errors to be approximately 5 to 10μ inches over an 8" length of the axis. The effect of mispositioning on a shallow surface is, of course, smaller in proportion to the surface slope.

After adding up all the errors, what level of measurement accuracy can be expected? On an absolute basis, about the 10 to 20μ inches per inch of surface height for 80% of the surfaces measured. From the standpoint of zonal deviation and their related slope errors, approximately 2 to 4μ per inch is a reasonable limit.

Aside from machine accuracy, care must be given to handling and cleaning of optical surfaces. A finger print or a dust particle may show up as a high zone on the optical surface. Similarly, if an element is not held securely in place or is mounted on an unstable base, errors will creep in due to part movement during measurement.

Computer System Design

The measuring machine as described is a powerful tool, which provides surface contour data not obtainable by other methods. However, the machine and the gathered data would be of limited usefulness if manual operation of the machine and hand analysis of the data were required. The obvious solution to this problem is the automation of the measurement and analysis process by linking the machine to a computer system. Figure 5 shows a schematic of the system, which we are using. As shown in the diagram, the System/7, a process control computer, is connected to the measuring machine via a multiplexer. The System/7 sends commands which direct the movement of the XY table, control the positioning Z axis probe, and reads the output of the laser interferometer which is stored on a memory disk for analysis.

The 1130 and the 7/16 are Fortran oriented computers which share a dual role in the measurement process. First, they are used to generate a sequence of instructions which direct the motion of the measuring machine. The sequence, called a 'Command File', is computed from information describing the size and shape of the surface to be measured. The file is assigned a unique code name and is transferred from the 1130 or the 7/16 to the System/7 where it is permanently stored on disk for reference whenever needed. Present provision allows up to 128 command files to be stored.

The second function of the 1130 and the 7/16 is the analysis of the measured data. At the completion of the surface measurement process, the measured data is stored on one of the 8 available data disk files in the System/7. The data file is then transferred to either the 1130 or the 7/16, depending upon availability. After transfer, the data is analyzed by a program which compares the measured data to a designed curve. The method used to compare the data is as follows:

1) the measured data is modified to compensate for error introduced by the spherical ball probe contacting a sloped surface. This is accomplished by computing the real contact point of the ball with the surface and subtracting from the measured data the sagitta of the ball below the contact point.

2) The sag of the designed curve is calculated for each computed contact point. Optional allowance is made to decenter and tilt the design curve in order to compensate for related errors in the measured data.

3) The sag error is computed by subtracting the sag of the designed curve from the corrected measured data.

4) Power may optionally be removed from the sag error by fitting the error to the equation $S = a + b R^2$

   where S= Sag Error
          a= Vertical Translation
          b= Power Coefficient
          $R= X^2 + Y^2$
          X= X axis contact point coordinate
          Y= Y axis contact point coordinate

   The values of a and b are determined by a least squares approach. The sag error is then recomputed as $SN = SO - (a + b R^2)$

   where SN= New Sag Error
          SO- Old Sag Error.

5) The sag error may be optionally smoothed by a maximum of 1μ inch. The method employed computes a weighted average of Z_{N-1}, Z_N, $Z_{N=1}$

   where Z_N = Data point being smoothed

   Z_N-1 and Z_{N+1} are the data points surrounded Z_N.

6) The sag error may be optionally tilted to allow for linear thermal changes which may have occurred during the measurement cycle.

After the sag error is computed, a graph of the error is plotted on a graphic display CRT. The analysis results can now be examined and the analysis rerun with different options if desired. When the analysis is finalized, a hard copy of the CRT display can be produced and the analysis results are stored on a history disk file and/or on punched

cards for future reference.

Method of Operation

The measurement of a surface contour involves the following steps:

1) the Z axis is roughly positioned through manual controls above the maximum height of the optical element to be measured. This sets an upper Z axis limit switch. The lower limit is the surface to be measured.

2) The optical element is placed on the XY table approximately at the center of travel of the X & Y axes. Holding blocks are placed around the element to prevent movement.

3) The Z axis probe is positioned above the center of the element.

4) The Z axis probe is placed in contact with the surface. The interferometer readout is set to 0.

5) The optical element is allowed to thermally stabilize. This is detected by monitoring the interferometer reading for a change which indicates contraction or expansion of the part. The period of time required for stabilization varies depending upon the material from which the element is made and the degree of measurement accuracy required. Typical stabilization times are 5 minutes for work in production to 45 minutes for final buy off.

6) The name of the command file to be used is typed in on the System/7 console and a data file is assigned for data storage.

7) The measuring machine is set to computer mode, and the computer program begins execution. Instructions are sequentially read from the command file, executed by the measuring machine, and the Z axis data is stored on the assigned data file.

The command file structure for an axisymmetric surface directs the machine to measure across a diameter of the part. The number of data points recorded varies from about 40 to 200 with an increment between data points of .020" to .200". The values used depend upon the diameter of the part and amount of surface detail desired. The command file structure for a general aspheric surface directs the machine to measure the entire surface in a rectangular grid pattern whose border may be rectangular or elliptical.

Measuring Machine Performance

To this point, we have described the measuring machine and its control system. To demonstrate the capability of the machine, we have chosen 2 test cases, which demonstrate the machine's accuracy.

The first test of a 12" diameter fused silica flat, will show the vertical accuracy of the XY table and the positioning repeatability of the Z axis. The interferogram (Figure 6) and its analysis (Figure 7) indicate the flat is accurate to 1.8μ inches over a 10" central section. The flat was measured across the same 10" section in increments of .100 inches. The data analysis (Figure 8) shows a deviation of 4.4μ inches. The dip near the middle of the graph is due to the probe falling into one of a large number of scratches on the flat. Moving the X axis .020 inches to the left eliminated the dip when the part was remeasured (Figure 9) and also demonstrates the repeatability of the measurements. The analysis of the 'flat' data brought out another interesting feature of the Moore Jig Borer. The XY table runs parallel to the X and Y axes to a measured value of .000002 inches per inch.

The second test of a 10" diameter concave Pyrex sphere with a radius of 20 inches, will indicate the positioning accuracy of the XY table and stepping motors and the measurement accuracy of the Z axis. The interferogram (Figure 10) and its analysis (Figure 11) show the sphere accurate to 1.8μ inches. Analysis of measuring machine date (Figure 12) indicates an accuracy of 5.3μ inches or a deviation of only 3.5μ inches from the true peak to valley error. It should be noted that a significant part of the difference between the sphere interferogram analysis and the sphere measurement can be attributed to XY table errors as indicated by our flat measurements.

The Measuring Machine in the Optical Shop

Although a measuring machine may be used in many applications, ours is employed primarily to support the manufacture of aspheric optical surfaces.

One type of aspheric element which has benefitted by our ability to measure its shape is a specialized lens known as a color television exposure lens or, more simply, a TV lens. This lens is used by the color television tube manufacturer to put the phosphor dots on the tube face in the position that the electron beam will fall where the tube is assembled. Typically, different lens designs are required for each of the three primary colors and different lens design are required for each tube type. The geometrical and electrical properties of a given tube design requires that a general aspheric lens be employed to accurately place the phosphor dots. The process used to manufacture such a surface employs a DNC contouring machine to diamond generate the surface (Figure 13 and 14) and grinders and polishers designed to conform to rapidly changing surface curvature. Normally, the performance of the finished lens is checked optically by a modified Hartman test. When lens accuracy problems occur which are related to manufacturing technique, the Measuring Machine has been used to monitor contour changes produced during various production phases and to isolate the major error causing factors. Figure 15 illustrates the surface contour of a typical TV lens.

By far, most of the Measuring Machine time is spent in support of the manufacture of axi-symmetric aspheric surfaces. For several years, we have been developing computer directed techniques for generating, grinding, and polishing axi-symmetric aspheres.

In the area of generating, the Measuring Machine is used to monitor part accuracies during initial machine setup and to verify part contours prior to grinding and polishing. Figure 16 shows a 2.2 inch diameter convex germanium lens being cut with a single point diamond. The series of graphs in Figure 17 demonstrate how the measurements of the generated surface can be employed to improve the surface contour by permitting better machine alignment and by compensating for basic machine errors. In the sequence of graphs shown, the final peak to valley error is less than .0001 inches when the central peak is not considered. The same techniques are used to aid the generating of glass aspherics.

When the departure of an aspheric surface from a best fitting sphere is small, the choice is often made to polish in the aspheric correction rather than generate, grind and/ or polish. The term 'small' departure is weighted by such factors as part diameter and material type but is typically less than .001 inches. To aid in the correction process, we have developed techniques to computer predict the shape of a polisher which will impart the desired aspheric curve to the lens surface. Figure 18 shows one such polisher. In this application, data from the Measuring Machine is used to make slight modifications to the polisher shape. By employing an iterative correction approach, we have been able to attain surface contour accuracies of .000004" on a part with .0001" departure. In production, errors levels of 10% to 20% of the initial aspheric departure are readily produced. Figure 19 shows the departure of approximately .0008" on an 8" germanium lens prior to aspheric polishing and the results after polishing. The error has been reduced to .0002" in one polisher cycle.

When making an aspheric surface by traditional hand methods, more time is spent removing the final 10% of surface error than in correcting 90% of the error. To help improve this relationship and also to improve aspheric production predictability, we have implemented a process called Computer Controlled Optical Surfacing (CCOS). This process employs computer controlled polishing machines and sub-diameter polishers to correct an optical surface. Applying deconvolution techniques, CCOS makes predictions about how much time and in what areas a given polisher operating under given conditions must spend to correct a surface error provided by the Measuring Machine. These predictions are converted to commands which direct the motion of the polishing machine. Figures 20 thru 22 exhibit several aspects of three machines which are built around used three axis mills. Figure 23 indicates the efficiency of CCOS in removing contour errors.

Conclusion

In conclusion, we have described a measuring machine which is capable of measuring surface contour to fractional wavelength tolerances. The machine is coupled to a computer system which enables automatic machine operation, data acquisition, and data analysis. The design of the machine allows great versatility in measuring parts of any size up to 18", any sag depth up to approximately 10", and any optical material.

The machine has been in operation for about 3 years. It is an integral part of our computer controlled aspheric generation system and has been used daily to measure as many as 15 surfaces in support of that project.
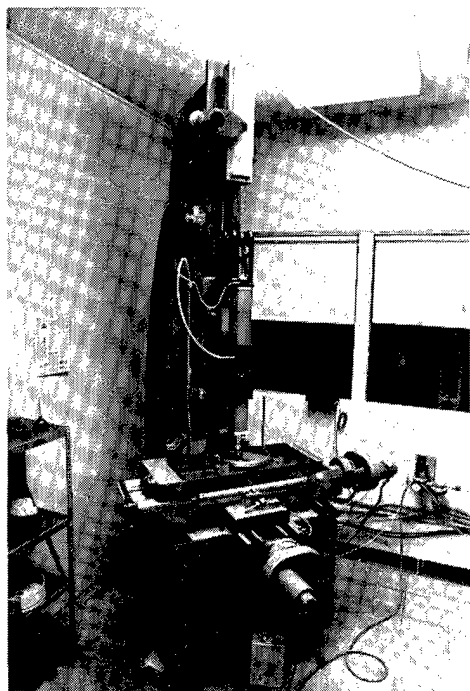
Fig. 1. The High Precision Measuring Machine. The basic machine is a #3 Moore Jig Borer.
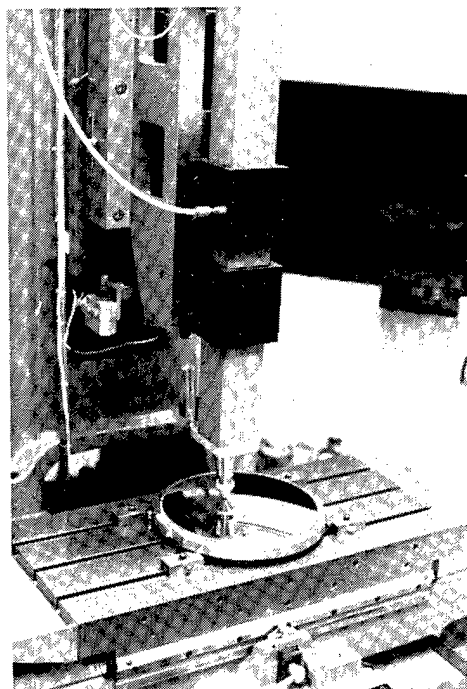
Fig. 2. Z axis slide assembly.
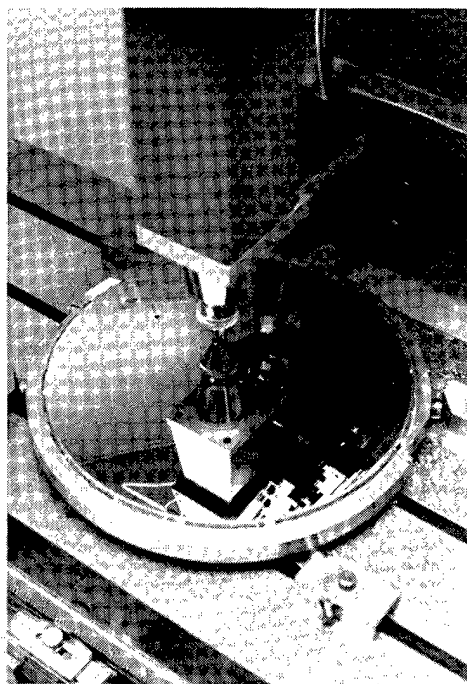
Fig. 3. Z axis probe reflected in germanium aspheric surface.
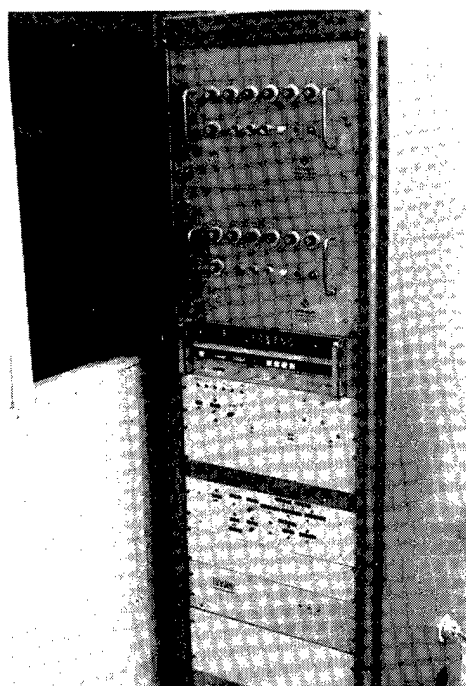
Fig. 4. Electronic Control Package.
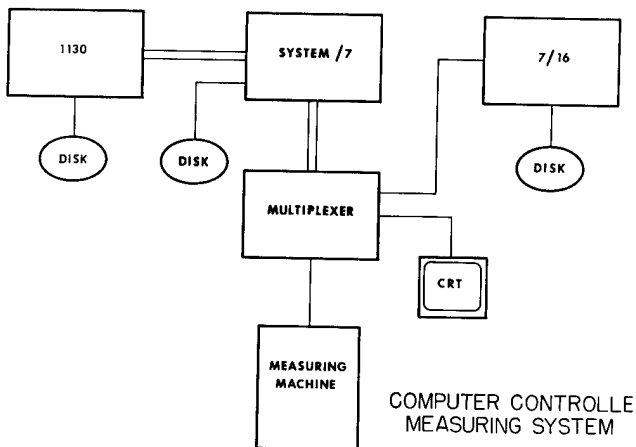
Fig. 5. Diagram of the computer controlled measuring system.
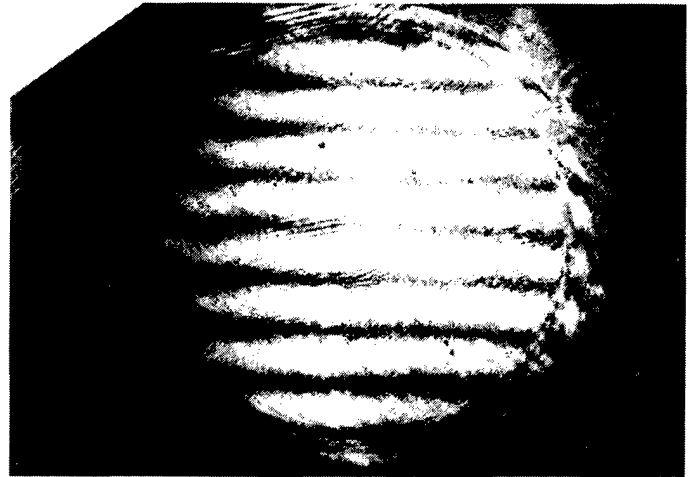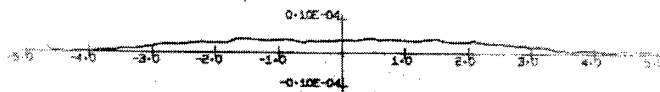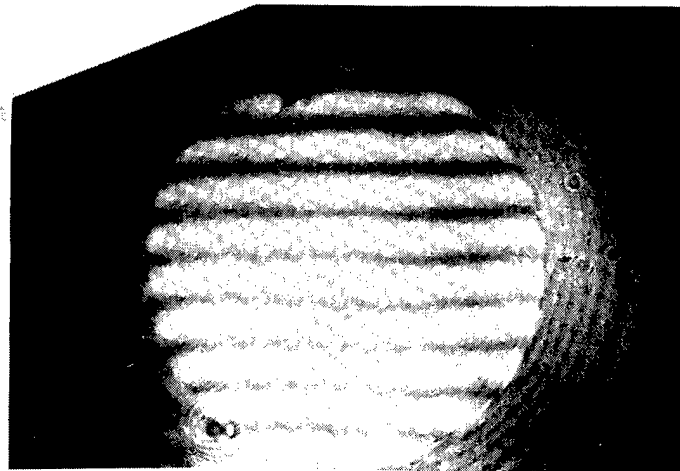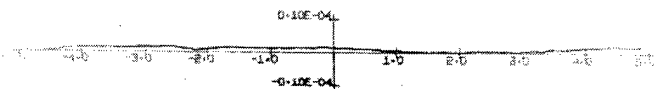

Fig. 6. Interferogram of flat test sample.
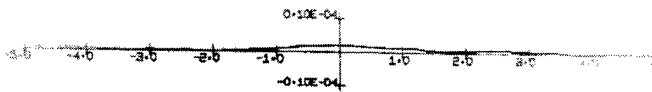
SAG ERROR PLOT OF FLAT SAMPLE INTERFEROGRAM ANALYSIS
MAXIMUM ERROR = 0.0000018   MINIMUM ERROR =-0.0000000
MAXIMUM GRADIENT ERROR = -0.0000027 AT X =   1.404
AREA WEIGHTED RMS SAG ERROR = 0.0000004
AREA WEIGHTED AVERAGE GRADIENT ERROR = 0.0000005
SAG ERROR PLOT IS ROTATED -0.000000 RADIANS
SPHERICAL POWER = 0.000000 UNITS PER X**2

Fig. 7. Interferometric analysis of flat test sample.
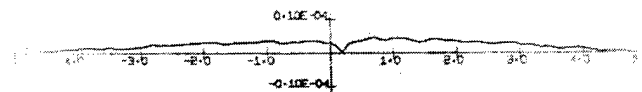
SAG ERROR PLOT OF FLAT TEST SAMPLE
MAXIMUM ERROR = 0.0000044   MINIMUM ERROR =-0.0000000
MAXIMUM GRADIENT ERROR = 0.0000155 AT X =   0.300
AREA WEIGHTED RMS SAG ERROR = 0.0000017
AREA WEIGHTED AVERAGE GRADIENT ERROR = 0.0000023
SAG ERROR PLOT IS ROTATED -0.000001 RADIANS
SPHERICAL POWER = 0.000000 UNITS PER X**2

Fig. 8. Analysis of measured flat test sample.

SAG ERROR PLOT OF FLAT TEST SAMPLE
MAXIMUM ERROR = 0.0000040   MINIMUM ERROR =-0.0000000
MAXIMUM GRADIENT ERROR = -0.0000089 AT X = -4.700
AREA WEIGHTED RMS SAG ERROR = 0.0000016
AREA WEIGHTED AVERAGE GRADIENT ERROR = 0.0000021
SAG ERROR PLOT IS ROTATED -0.000002 RADIANS
SPHERICAL POWER = 0.000000 UNITS PER X**2

Fig. 9. Analysis of remeasured flat
test sample.

Fig. 10. Interferogram of 10" diam.
F/2 sphere.

SAG ERROR PLOT OF SPHERE SAMPLE   INTERFEROGRAM ANALYSIS
MAXIMUM ERROR = 0.0000018   MINIMUM ERROR =-0.0000000
MAXIMUM GRADIENT ERROR = 0.0000033 AT X = -4.296
AREA WEIGHTED RMS SAG ERROR = 0.0000011
AREA WEIGHTED AVERAGE GRADIENT ERROR = 0.0000008
SAG ERROR PLOT IS ROTATED -0.000000 RADIANS
SPHERICAL POWER = 0.000000 UNITS PER X**2

Fig. 11. Interferometric analysis
of sphere.
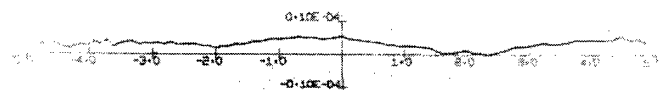
SAG ERROR PLOT OF SPHERICAL TEST SAMPLE
MAXIMUM ERROR = 0.0000053   MINIMUM ERROR =-0.0000000
MAXIMUM GRADIENT ERROR = -0.0000242 AT X = 4.832
AREA WEIGHTED RMS SAG ERROR = 0.0000033
AREA WEIGHTED AVERAGE GRADIENT ERROR = 0.0000037
SAG ERROR PLOT IS ROTATED -0.000323 RADIANS
SPHERICAL POWER = -0.000000 UNITS PER X**2

Fig. 12. Analysis of measured sphere.
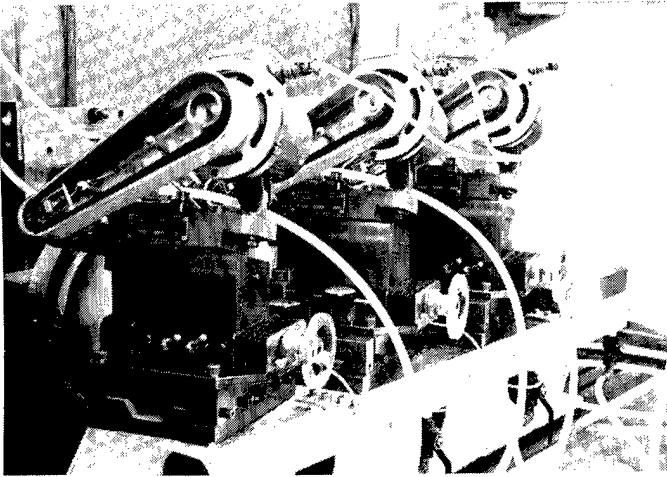
Fig. 13. Three diamond grinding
spindles of the DNC TV lens
generator.
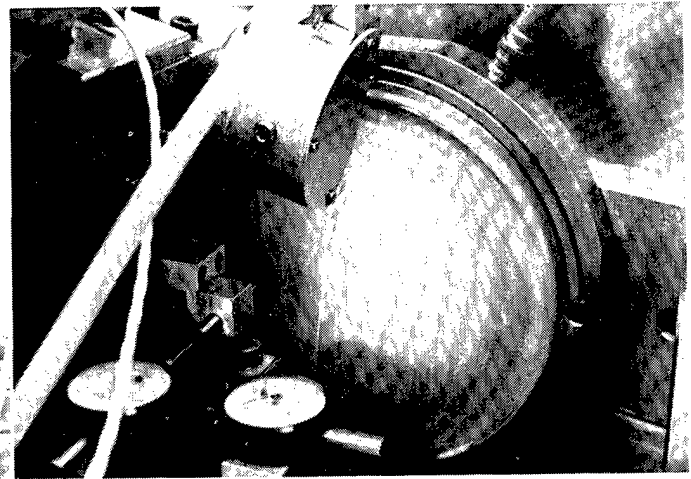
Fig. 14. TV Lens during generation.

R-3E-L LEFT STRIPE 031177
HORIZ SCALE= 1.000
VERT SCALE= 30.000
OFFSET ANGLE= 30 DEGREES
SURFACE TILT= 60 DEGREES
TINSLEY LABS DISK 0011
NOV 22, 77
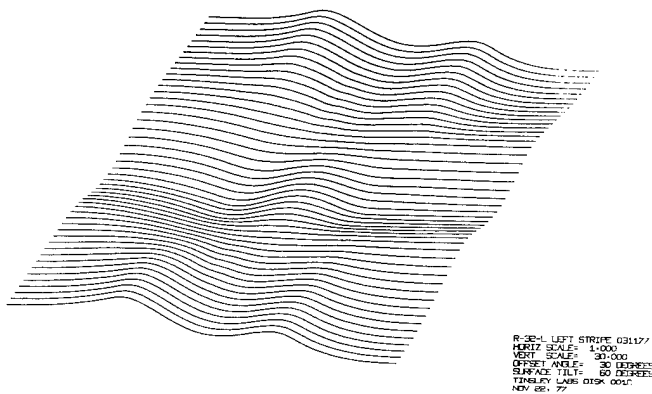
Fig. 15. Isometric plot of data
gathered from TV Lens measurement.
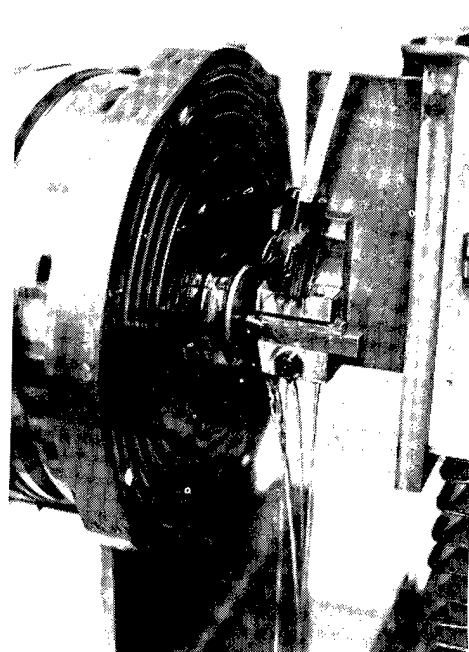
Fig. 16. 2.2" diameter axi-symmetric
germanium lens during single point
diamond generation.
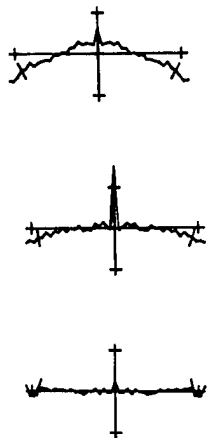
Fig. 17. Improving the contour of the 2.2" germanium lens by improving generator alignment. Final accuracy of .0001".
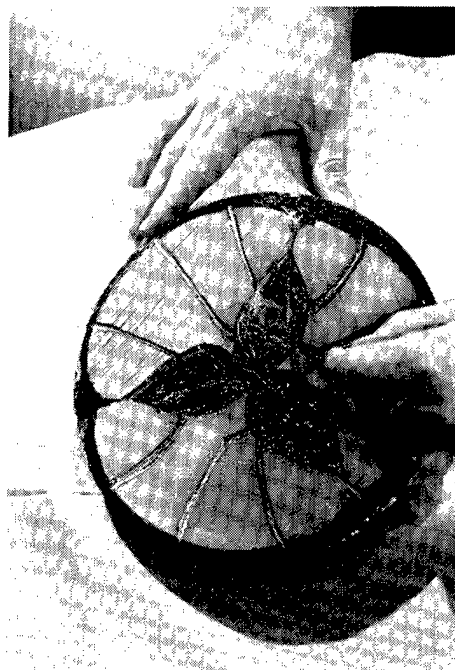
Fig. 18. Polisher designed to correct the difference between a sphere and an asphere.
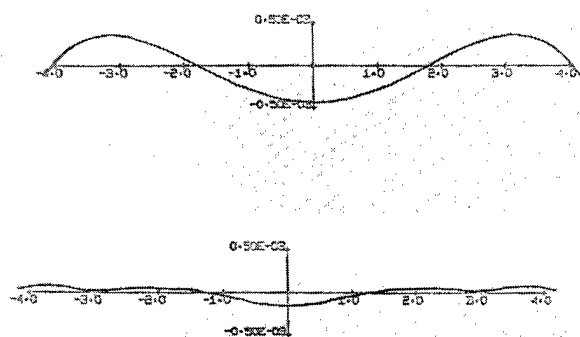
Fig. 19. Results of applying the computer design polisher. The initial error is .0008". The final error is .0002".

Fig. 20. CCOS personnel and machines in operation.

Fig. 21. Spindle and stroke mechanism of a CCOS machine.

Fig. 22. 1/4" x 3/4" polisher used to zonally correct an aspheric surface.
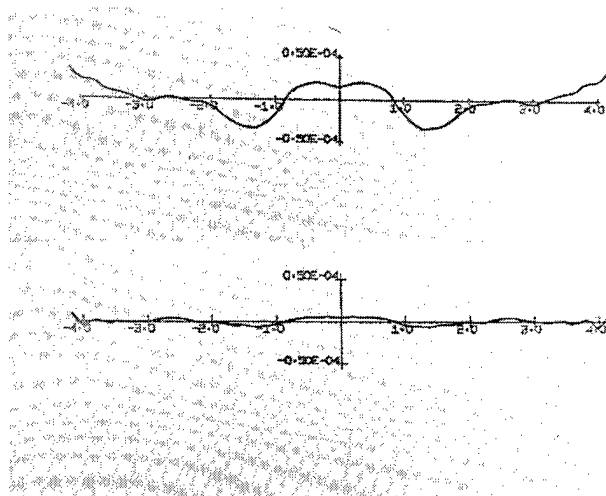
Fig. 23. Results of a CCOS correction run. Initial error was 70μ inches. Final error was 15μ inches.

A NEW INSTRUMENT FOR ROUTINE OPTICAL TESTING OF GENERAL ASPHERICS

Peter M. Emmel
Tropel Inc.
Fairport, New York 14450
and
Kang M. Leung
Honeywell Corporate Materials Sciences Center
Bloomington, Minnesota 55420

Abstract

A unique and versatile laser interferometer has been jointly developed by Honeywell, Tropel and the University of Arizona. The system is designed for routine non-contact testing of aspheric optical surfaces (using a Computer-Generated Hologram [CGH] to provide the aspheric component of the reference wavefront) while retaining the features and capabilities of the standard Tropel Vertical Interferometer. Thus it is capable of measuring radius and/or optical figure of spheres, flats, conics and general aspherics. The instrument provides convenient interchangeability among Fizeau, Twyman-Green, CGH and Lateral Shearing modes of operation in a single compact unit. It is also capable of direct interfacing with a computer for wavefront measurement or analysis. The operation of the system is described and data is presented from a CGH test of an f/2 paraboloid (using a spherical test wavefront) for which independent comparative data is also given.

Introduction

Precision lens molding and, more recently, ultraprecision machining techniques are narrowing the gap in production costs between spherical and non-spherical optical surfaces. Indeed, from the fabrication standpoint, in either of these technologies, there is little difference between making a sphere and making an asphere. However, when it comes to measuring the surface figure, aspherics have always posed serious problems. The rapid commercialization of aspheric manufacturing technology requires a corresponding development in measurement capability.

Interferometric equipment for non-contact testing of various optical surfaces has been in use for many years. However, with a few exceptions, commercially available instruments have been limited to the testing of flats and concave spheres. The exceptions are those offering a variety of focusing lenses, with reasonably large apertures, for testing a useful range of convex spheres. Using simple auxilliary optics, most available instruments can also test conic surfaces such as paraboloids, ellipsoids and hyperboloids. General asphers, however, with more than a few waves departure from the nearest conic, usually exceed the capability of these instruments to even view, let alone accurately measure.

The literature contains many laboratory setups for overcoming the difficulties in testing asphers.[1,2] The most promising are those using holographic techniques to generate a reference wavefront which matches the wavefront reflected by the aspheric test surface.[3] The resulting interference fringes are interpreted in the same way as those in conventional two-beam interferometers.

Another method for testing asphers is lateral wavefront shearing, where the test beam is divided into two identical beams with a slight lateral displacement. Interference between these displaced beams produces a fringe pattern which, for small displacements, is directly related to the slope of the wavefront, but only indirectly related to its total depth. Obtaining accurate depth information from such a fringe pattern requires numerical analysis best performed by a computer.[4]

This paper describes the implementation of both of these techniques - holography and shearing - in a commercially oriented laser interferometer, thus adding asphers to its other surface testing capabilities. The interferometer was developed jointly by Honeywell, Tropel and the University of Arizona. The intent was to provide a single instrument versatile enough to satisfy the needs of several groups for a convenient interferometric means of testing a variety of optical materials and surfaces including asphers. Since these groups were engaged in developing various production technologies, the system had to be practical in routine production-level use where ease of setup and adjustment are key factors. It was also intended to be adaptable to possible future needs, such as real-time holography and direct computer interfacing.

The Tropel Model 4000 was chosen as a starting point because of its convenient vertical test beam and its Fizeau testing capability for flats, spheres and conics. The internal layout of the Model 4000 along with its single-frequency HeNe laser and its relatively small internal beam diameter, all proved to be particularly advantageous.

The interferometer design was modified to allow use of computer-generated holograms (CGH) and lateral wavefront shearing for testing of known and unknown aspherics having up to several hundred waves departure from the nearest sphere. The design also permits the generation of real-time holograms in cases where a master aspheric surface is available. The range of radius and figure measurement was extended to 450mm and a motor drive was added to the vertical slide. All other features of the standard interferometer were retained.

Several additional features were necessary in order to implement the CGH mode of operation. The most important of these was that a real image of the test surface had to be projected onto the hologram plane. Failure to satisfy this condition causes systematic measurement errors which increase in proportion to the asphericity of the surface under test. Accuracy was maintained over the full range of radii by providing variable (stepwise) magnification and independent focusing between the test surface and the hologram plane.

System Description

The system is essentially a two-beam interferometer with its test and reference beams separated according to their polarization states. In order to minimize system wavefront deformation and maximize repeatability, the system was designed so that all the lenses are used on-axis. To achieve efficient use of light, polarizing beam splitters are used with quarter-wave retardation plates appropriately located to obtain the desired beam paths, as shown in figure 1.
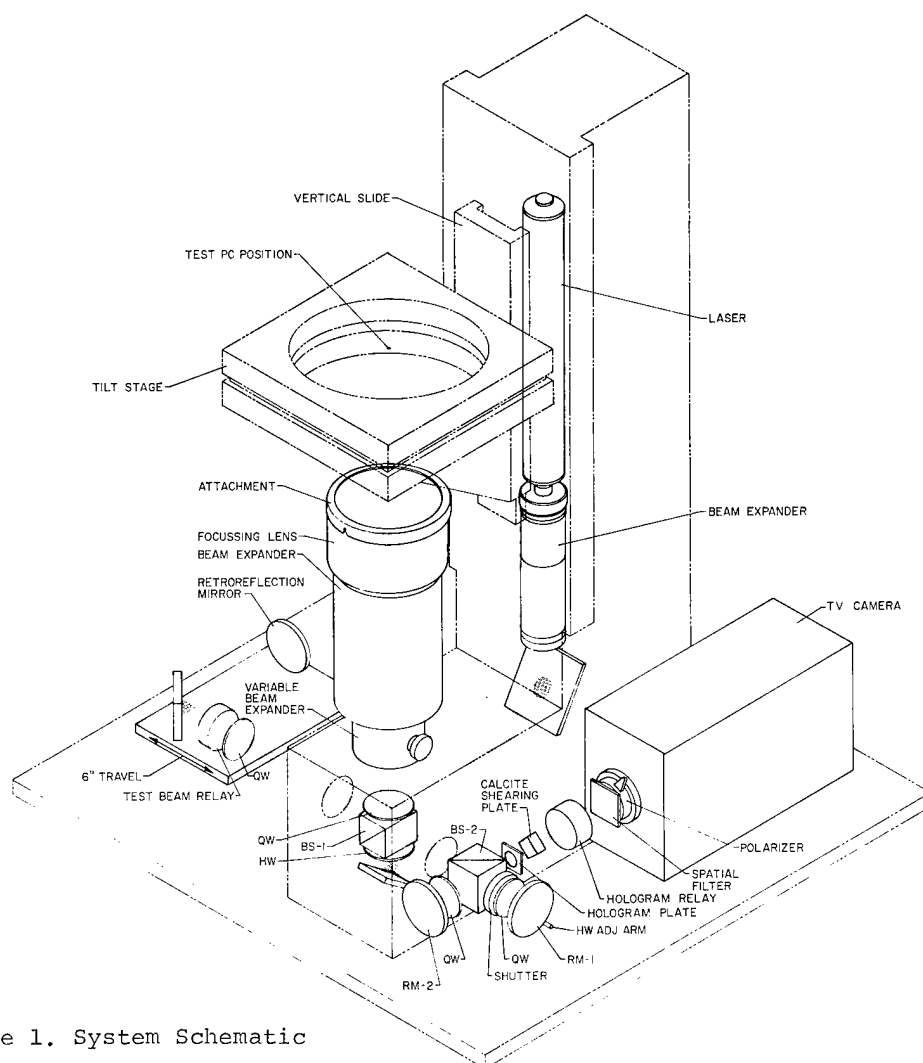
Figure 1. System Schematic

The layout is best described by identifying its five "arms": the source arm, the test arm, the relay arm, the reference arm, and the viewing arm. In the source arm the linearly polarized beam is expanded and collimated. Its plane of polarization is rotated according to the half-wave plate (HW) adjustment. The first polarizing beamsplitter (BS-1) reflects the S-polarized component, which becomes the reference beam, and transmits the P-polarized component, which becomes the test beam. Quarter-wave plates (QW), located in the test and relay arms, control the polarization of the test beam and thus determine whether it is transmitted or reflected on each succeeding encounter with BS-1.

The vertically oriented test arm consists of a series of interchangeable beam expanding and focusing lenses. A particular combination is chosen to provide an appropriate spherical (or plane) wavefront to nearly match the test surface. The test surface, positioned for the best "fit" to this wavefront, reflects the beam back through the test arm optics. Any mismatch between the test surface and the illuminating wavefront is captured as a deformation of the returning wavefront. Three beam sizes may be selected by adjusting the variable beam expander, which also varies the viewing magnification.

The returning test beam is reflected by BS-1 and enters the relay arm. The relay is a retroreflector consisting of a lens with a plane mirror located at its focus. It reflects a real image of the test surface back through the beamsplitter toward the hologram in the viewing arm. The relay is adjusted along its track to bring the test surface into sharp focus at the hologram plane, without affecting its magnification.

In the space between the two beamsplitters the test and reference beams are recombined, but they are still orthogonally polarized. They are separated by the second beamsplitter (BS-2), which transmits the reference beam and reflects the test beam along the axis of the viewing arm. The viewing arm contains the hologram, a second relay lens and a closed circuit television camera. Figure 2 gives a more detailed view of the reference and viewing arms of the interferometer. The path of the reference beam is determined by two sets of quarter-wave plates and adjustable plane mirrors (RM-1 and RM-2). Adjustment of the mirrors gives the necessary reference beam angle at the hologram.
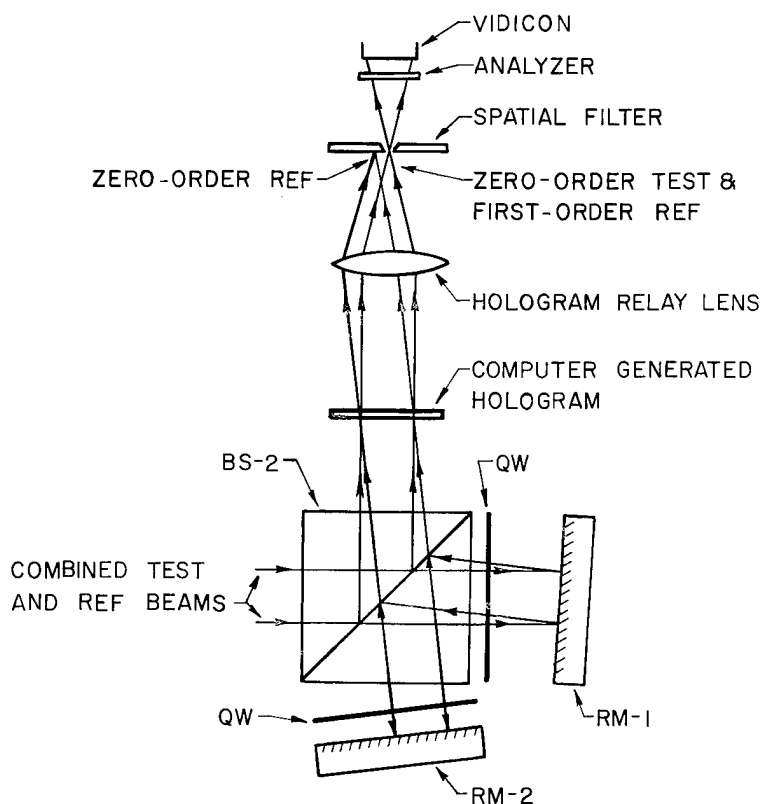
Figure 2. Viewing Arm Schematic

The hologram itself is a fringe pattern, up to 14mm diameter, plotted from a computer raytrace of the complete interferometer system and recorded on film. Some of the energy in the test and reference beams is diffracted by the hologram into plus and minus first-order beams. These are brought to focus, along with the zero-order beams, on a white pinhole plate (spatial filter) where they are easily viewed. When the reference beam is properly adjusted, the first-order reference and zero-order test beams are superimposed. The pinhole is adjusted to block all but these two beams.

The TV camera is located behind the pinhole, at the image of the hologram. A rotatable linear analyzer is mounted on the front of the camera with its axis oriented at 45°. This allows the two beams to form visible interference fringes which are displayed on the video monitor. These fringes are interpreted as ordinary Twyman-Green fringes, showing the contour of any mismatch between the test surface and the desired figure "encoded" in the hologram. The accuracy of this testing technique is limited mainly by the geometric accuracy of the hologram and is currently estimated to be within 1% of the total asphericity for any particular surface.

A surface whose asphericity exceeds the limit for CGH testing (currently about 300 waves per radius slope) may be measured by lateral wavefront shearing. To do this, the reference beam is blocked by closing the shutter, and a calcite block is installed in the viewing arm ahead of the hologram relay lens. Proper adjustment of the analyzer gives lateral shearing fringes which can be digitized for computer analysis. The shear distance is measured by inserting a reticle in the hologram holder and measuring the separation of its double images.

Flat or spherical surfaces require neither a hologram nor a shearing block, and are generally tested in the Fizeau mode. In this case the reference arm is again blocked and the appropriate Fizeau reference attachment is installed in the test arm. The top surface of such an attachment is a partial reflector polished to an extremely accurate flat or spherical figure. The fraction of the beam reflected by this surface becomes the reference beam. Since it follows essentially the same path as does the test beam, system wavefront deformations do not show up in the observed fringe pattern. The accuracy of this test is 1/10 wave or better, but its range is limited to surfaces within a few waves of being flat or spherical. If a suitable high quality auxilliary mirror is used, conic surfaces may also be tested in the Fizeau mode.

Aspheric Surface Test

This has been an extremely brief discussion of the interferometer. A case history will serve to better illustrate the use of the instrument to test a particular aspheric surface. A 4-inch diameter f/2 paraboloid was chosen because it is a conic and could be relatively easily fabricated and independently tested for comparison. The surface equation for the test surface (parabola) was entered into the raytrace program along with the optical design data for the interferometer system. For this particular surface the f/1.8 setting of the variable beam expander was used. The program found the best position for the surface in the test beam and calculated the fringe pattern that would be produced at the hologram plane if the test beam were interfered with a plane reference beam at a particular nonzero incidence angle. The incidence angle was chosen to be about three times the maximum slope angle of the test wavefront, so that the diffracted orders would be sufficiently separated at the pinhole. This fringe pattern was output in the form of plotter commands on magnetic tape. The tape was then transferred to a Dicomed Digital Image Recorder which plotted the pattern on a high resolution, low distortion CRT and recorded it on 35mm Plus-X film. This image was then rephotographed on Kodak SO173 at the correct magnification to give a 14mm pattern at full beam diameter using a fiducial mark. The resulting negative was bleached to enhance its diffraction efficiency.

After installing the appropriate test arm lenses (125mm diameter f/1 in this case) and checking the alignment of the interferometer, the test surface was installed and adjusted to the correct position as specified by the computer raytrace. The relay was adjusted for a sharp image of the test surface and the hologram was installed. The reference beam was adjusted to superimpose the proper orders at the pinhole and obtain a fringe pattern on the monitor. Fine adjustment of the hologram centration and the reference beam tilt resulted in the best "fit" leaving a fringe pattern, shown in figure 3c, representing the residual error in the parabola.

Figures 3a,b illustrate the asphericity of the test surface by showing Twyman-Green fringe patterns produced independently by the surface (in-position on the interferometer) and by the hologram alone. The "asphericity" measured in this example was actually the difference between the parabolic test surface and the spherical test wavefront illuminating it. Thus, the hologram removed about 40 waves of spherical aberration and defocus from the fringe pattern, allowing the residual figure error to be accurately measured. Digitization of the lower fringe pattern showed an rms surface deviation of 0.03 waves and a peak-to-

valley depth of 0.15 waves. An independent autocollimation test was made at the University of Arizona using a different interferometer and a precision optical flat. The interferogram from this test is shown in figure 4. Digitization of this interferogram shows 0.035 waves rms and 0.17 waves peak-to-valley agreeing with the CGH results within a few hundredths of a wave.
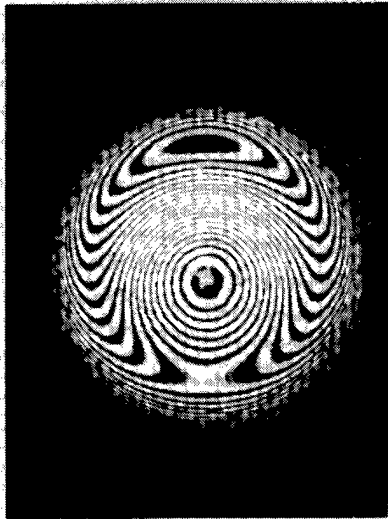

Figure 3a

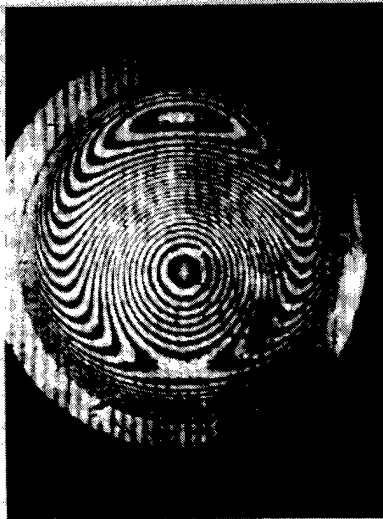4" Dia. F/2 Parabola
Twyman-Green Interferogram

Figure 3b

Wavefront Diffracted by
Computer-Generated Hologram
To Simulate perfect F/2
Parabola and Compensate
Instrumental Error
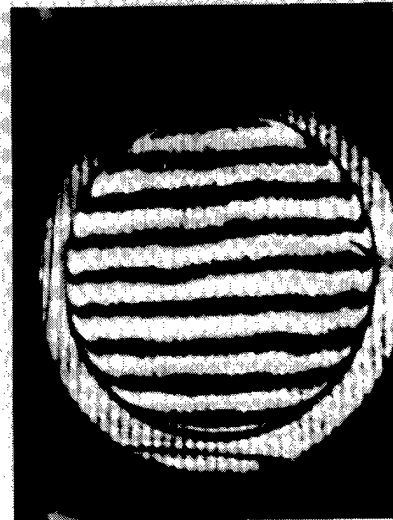
Figure 3c

CGH Test of the F/2
Parabola

Surface Deviation is:
  0.03 waves RMS (6328Å)
  0.15 waves P-V
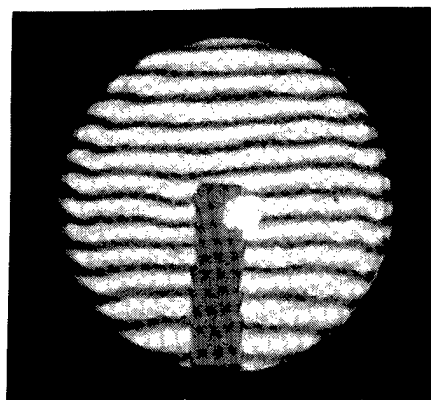
Figure 4

Autocollimation Test of F/2
Parabola

Surface Deviation is:
  0.035 waves RMS
  0.171 waves P-V

The paraboloid was also tested in the shearing mode. Interferograms were taken with the shear in orthogonal directions, as shown in figure 5. Aberration theory predicts 39.2 waves of spherical aberration for this setup. For comparison both the shearing and the Twyman-Green interferograms were measured, giving values of 39.2 and 39.0 waves respectively. It was the extremely fine fringe spacing that hampered the measurement of aspheric Twyman-Green fringe patterns and led us to seek better ways of testing aspherics in the first place. In the lateral shearing technique this problem is controlled because the fringe spacing is partially a function of the shear distance, which can be varied. The CGH technique completely eliminates the problem for aspherics up to a few hundred waves.
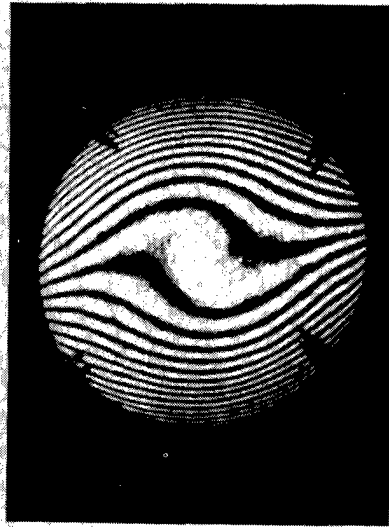
Figure 5a

Lateral Shearing Interferogram
Using Calcite Block to test
F/2 Parabola
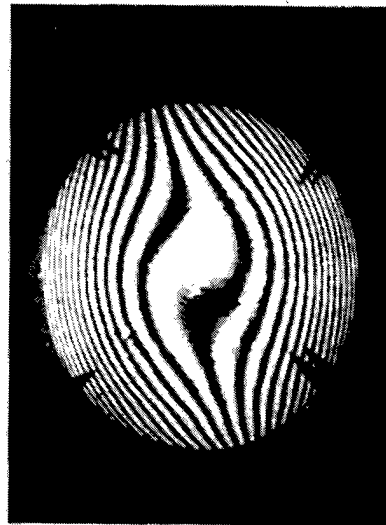
Figure 5b

Lateral Shearing Interferogram
(Calcite Block Rotated 90°)

These comparative results confirm the soundness of the techniques and the quality of the equipment. Another very important comparison is the time required to obtain results in each of these modes. In all cases the setup and adjustment of the interferometer was straightforward and convenient. In terms of turnaround time from scratch for testing a new surface, the CGH mode took by far the longest because of the time required for calculating and making the hologram (a matter of days with the present arrangements). However, once the hologram was ready, the fringe pattern was observed in a few minutes. If several of the parabolas had been available, they could all have been measured, using the same hologram, in a time period comparable with any other production-oriented interferometer. In order to obtain comparable results, both the Twyman-Green (when fringes are resolvable) and shearing modes require fringe digitization and data reduction for each surface tested. Clearly the CGH mode is preferable for situations where several nominally identical surfaces are to be measured, while shearing is most practical for occasional or one of a kind surfaces.

Further Considerations

There are a few ways in which the CGH turnaround time could be drastically reduced. At the moment the various operations are not all in-house. Under one roof, the turnaround time could be less than 24 hours. Even shorter times could be realized if the hologram were exposed directly from mag tape onto the final film (or thermoplastic). This is within the capability of a (hopefully) growing number of X-Y laser beam recorders.

If a quantitative analysis of the residual fringe pattern is required, there are two sophisticated techniques currently in use. One of them is fringe digitization, in which the intersections of the fringes in a particular interferogram with a set of parallel, equally spaced lines are supplied to the computer for curve fitting or other analysis. The least tedious way of getting this fringe data into the computer is to let the computer help by using an interactive video terminal with software that can find most of the fringes for itself. The other analysis technique is direct phase measurement, in which the interferometer is connected directly to the computer. Tropel's minicomputer-based System 70, for example, measures the equivalent of over 300 interferograms during its 6-second data

taking period and has the wavefront data (32 X 32 grid) available for analysis or redisplay in less than one minute. This gives it a very high signal to noise factor and tends to eliminate transient effects which are often "frozen" in a single interferogram.

It is not hard to visualize the interferometer, CGH recorder, and keyboard, all connected to the computer, with access to software for ray tracing, CGH calculation and wavefront analysis. When one considers the equipment that is now being developed for fabricating precision aspherics, a surface measurement system like this is clearly an essential, independent measurement tool compatible with the machine control systems in both accuracy and data format.

Acknowledgement

The authors wish to acknowledge the valuable personal assistance of Dr. James C. Wyant, at the University of Arizona's Optical Sciences Center. His work in the field of aspheric surface testing formed the basis for the design of the instrument we describe.

References

1. Polster, H. D., et al, "New Developments in Interferometry", Applied Optics, Vol. 8, pp. 521-556. 1969.
2. Wyant, J. C., "Testing Aspherics Using Two-Wavelength Holography", Applied Optics, Vol. 10, pp. 2113-2118. 1971.
3. MacGovern A. J., and J. C. Wyant, "Computer Generated Holograms for Testing Optical Elements", Applied Optics, Vol. 10, pp. 619-624. 1971.
4. Rimmer, M. P., and J. C. Wyant, "Evaluation of Large Aberration Using a Lateral-Shear Interferometer Having Variable Shear", Applied Optics, Vol. 14, pp. 142-150. 1975.

OPTICAL COMPONENTS: MANUFACTURE & EVALUATION

Volume 171

SESSION 3

COMPONENTS DESCRIPTIONS AND FABRICATION METHODS

Session Chairman
Verne Muffoletto
Muffoletto Optical Co.

GRINDING AND POLISHING WITH SMALL TOOLS UNDER COMPUTER CONTROL

Robert A. Jones
The Perkin-Elmer Corporation
Norwalk, Connecticut 06856

Abstract

Small grinding and polishing tools are useful for certain applications since they can closely follow the curve of an aspheric surface and are less affected by workpiece distortion than larger tools. Also, the use of a computer to control the action of grinding and polishing tools can increase the efficiency and accuracy of the process. The computer controlled polisher (CCP) takes advantage of both features, moving a tool assembly with small pads over the workpiece under computer control. By varying the amount of time the machine works any region, a controlled amount of material may be removed. Using computer modeling, the best tool configurations are developed to perform any figuring operation. Based upon experimentation, the proper operating parameters for the CCP have been obtained. The machine has been used to fabricate a number of difficult mirrors. As a result of this work, the CCP will be used on important fabrication efforts.

Description

Conventional polishing uses a tool approximately the same size as the workpiece. However, the use of smaller polishing pads has certain advantages. The smaller pad can fit the aspheric workpiece surface better, can correct localized surface error more rapidly, and is less affected by workpiece distortion than a large pad.

The CCP (computer controlled polisher) uses these small tool features in an automated machine to provide an efficient, repeatable, accurate polishing operation.[1] The instrument has a rotating tool assembly which travels over the workpiece surface with the tool path and velocity controlled by a minicomputer. The desired material removal can be achieved for each workpiece surface region since the removal is inversely proportional to the velocity of the polishing tool.

The tool assembly is shown in Figure 1. The polishing tool consists of small pads which individually tilt and rotate to conform to the workpiece surface. These pads are maintained at constant polishing pressure by use of an air pressure plenum which contains the ends of the rods on which the pads are mounted. The polishing pressure can be higher than conventional polishing since workpiece distortion produces negligible effects with use of the small pads. The entire polishing head, consisting of the air plenum tank, rods and pads, is rotated by a hydraulic servomotors. In addition, the head is mounted on a plate which is driven in rotation by a motor and drive system. This dual rotation produces an epicyclic tool motion which has good figuring characteristics. By varying the number, size and locations of the polishing pads, various tool configurations can be produced. Computer modeling is used to determine suitable tool configuration geometrics for specific polishing objectives.
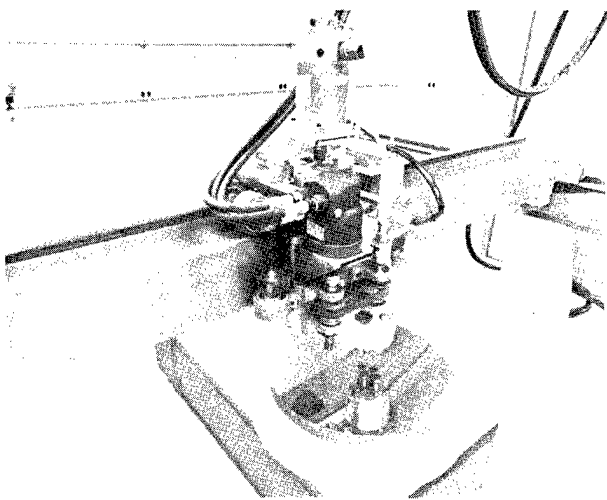
Fig. 1. Computer controlled polisher head.
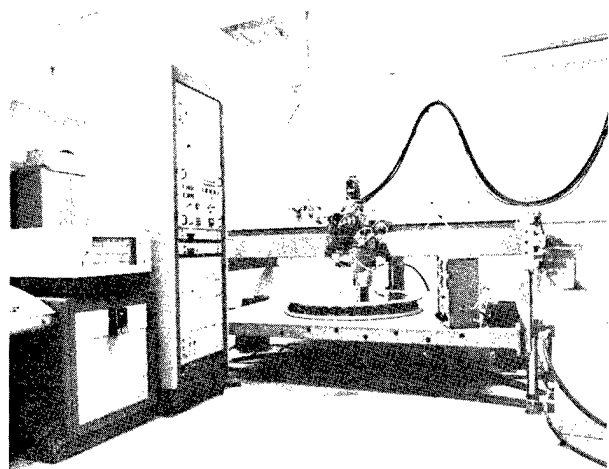
Fig. 2. Computer controlled polisher.

Figure 2 is a photograph of the CCP. The polishing tool assembly is moved over the workpiece surface under computer control. The computer bus is connected to a digital interface which drives two analog servosystems: the velocity of the polishing tool carriage along a central beam and the velocity of this beam along two support rails. Positional information for the carriage is obtained from incremental

position encoders and fed back to the computer. This data is used by the controlling computer to constant-
ly correct the carriage velocities, preventing any positional error buildup which could cause a drift from
the prescribed path.

The velocity of the polishing tool along its prescribed path is controlled by a minicomputer. The com-
puter operates from data contained on a control tape generated from an interferometric test. The data
analyses steps are shown in Figure 3. First, suitable interferograms are obtained for the workpiece sur-
face. One or more interferograms are scanned with a microdensitometer or a comparator. The scan data is
analyzed to produce surface height error values. The desired path is then generated and the surface errors
obtained via interpolation for each path segment. This data is used to generate a control tape for regula-
tion of the CCP. The machine varies the velocity of the polishing tool assembly along the polishing path,
causing the desired varying material removal. After the desired amount of polishing, the workpiece surface
is tested again. By use of iterative interferometric testing, the workpiece surface can converge to the
desired figure despite minor test errors.
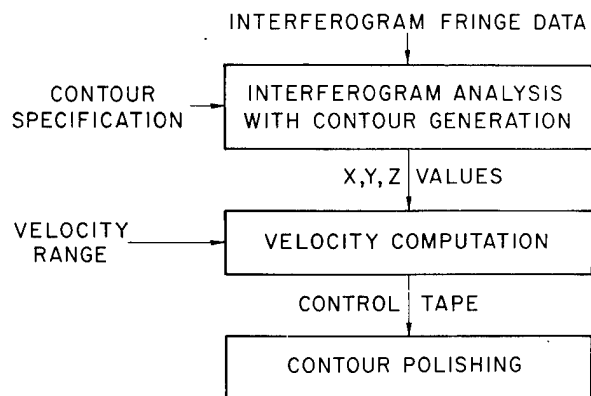
Fig. 3. Data analyses flow diagram.
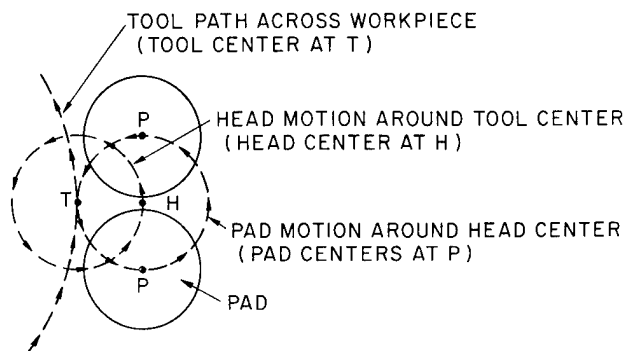
Fig. 4. Epicyclic tool configuration.

Computer Modeling

In order to optimize the operation, the removal process was modeled on a computer. The CCP uses a small
tool assembly which travels over the workpiece surface along a predetermined path. The polishing motion
consists of a dual rotation producing an epicyclic pad motion. The paths of the polishing pads for a typi-
cal tool configuration are shown in Figure 4. As the tool (T) travels over the workpiece, the head (H) re-
volves in a circle, while the pads (P) rotate around the center of the head. The computer program deter-
mines the removal along the tool path and parallel to the tool path, using the tool configuration geometry,
the rotational motions and the linear tool (path) velocity. The computer model sums this removal effect
for worksurface points as the tool travels along its path over the piece.

The computer model was used to determine how well various tool configurations could be expected to per-
form. Typical removal curves for a static tool (no velocity along path) are shown in Figure 5. For these
cases, E is the slower (epicyclic) rotation radius, R is the faster rotation radius, and the pad radius is
slightly less than R. Typical error correction curves obtained from the computer model are given in Figure
6. This graph shows the modeled surface figure error for the workpiece remaining after CCP removal cycles
for the same three cases as described for Figure 5. The cases with no epicyclic motion (E=0) amd with a
large epicyclic radius produced poor figuring results. The case with two equal rotation radii slightly
greater than the pad radius produces good figuring results.

Based upon modeling, the best tool configuration for normal figuring has a static tool removal profile
with a central peak and a fairly smooth decrease to zero. As shown by the E=R curves of Figures 5 and 6, a
good method for generating the desired tool removal profiles is with the use of epicyclic motion.
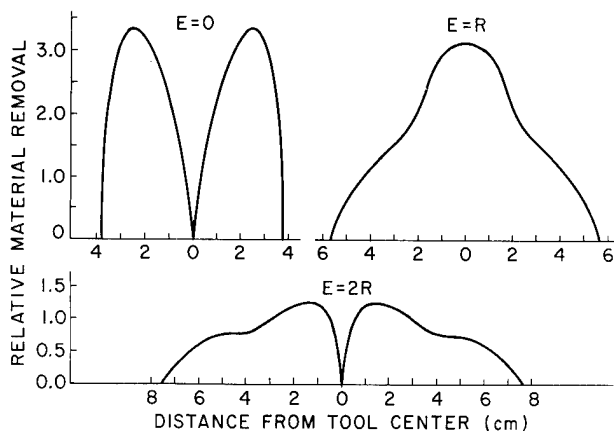
Fig. 5.   Tool removal profiles for several
           epicyclic motion tools.
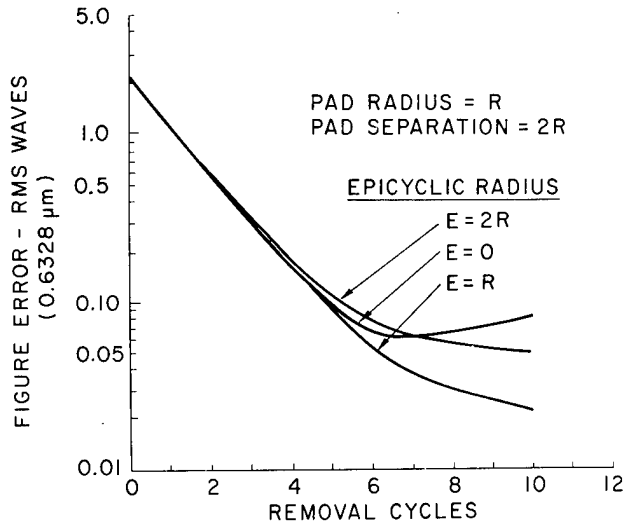
Fig. 6.   Modeled figure process for several
           epicyclic motion tools.

Experimentation

A series of experiments were conducted to obtain information on the effect of various polishing para-
meters on the removal process. A Cer-Vit testpiece was polished flat using a continuous polisher. The
CCP was programmed to move back and forth over a straight line. This operation was repeated for different
regions of the workpiece using different polishing parameters. Interferograms taken before and after this
process were analyzed to determine removal. This experimental procedure was repeated for every set of
polishing parameters of interest. In order to minimize the test and repolish time, a small tool configur-
ation was used, permitting eight separate runs on the surface of the testpiece.
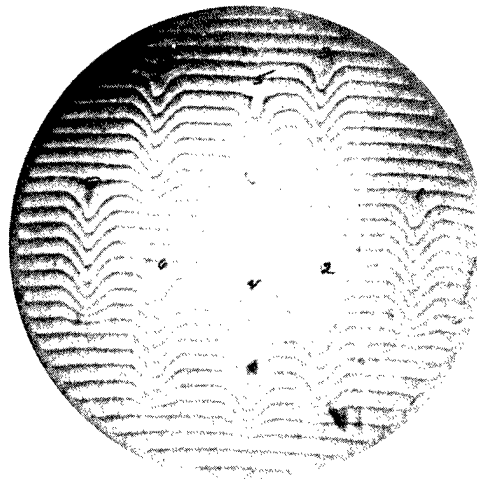
Fig. 7.   Interferogram for removal precision experiment.

The first experiment examined the repeatability (precision) of the test process. The eight test cases
were run with identical CCP parameters, and the resulting interferogram (Figure 7) was analyzed to produce
results shown in Figure 8. The standard deviation for the removal depth variation was found to be 0.012 μm.
or 2.3% of the mean depth. Figure 9 shows one experimental removal profile and the modeled removal profile.
The experimental profile reasonably matches the modeled case, having the desirable central peak with the
gradual off-center decrease.
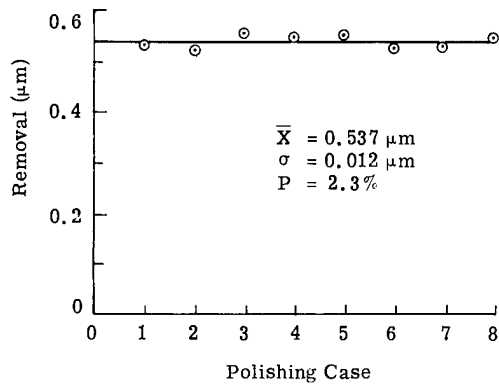
Fig. 8. CCP removal precision results.

$\overline{X}$ = 0.537 μm
σ = 0.012 μm
P = 2.3%
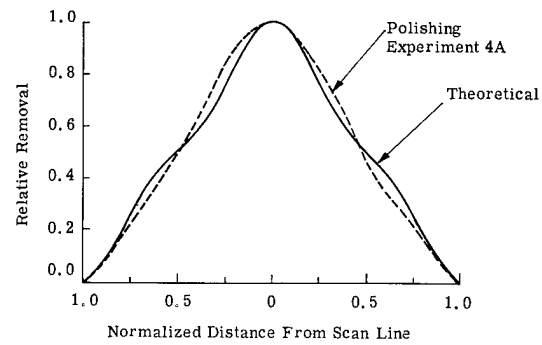
Fig. 9. Comparison of theoretical and experimental removal profiles.

An experiment was conducted to confirm the linear relationship between removal and polishing time. Two runs each were made with polishing times of 7½, 15, 22½ and 30 minutes. An interferogram was obtained and measurements made. The removal depth as a function of polishing time is shown in Figure 10. The removal was found to be linear with polishing time.
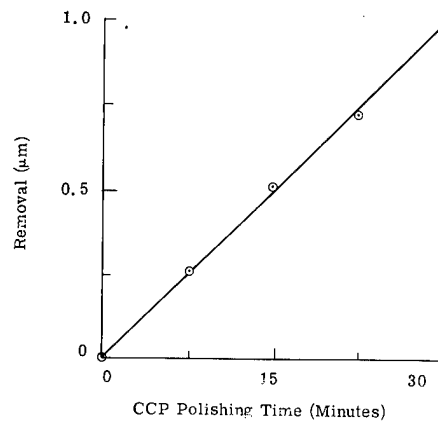
Fig. 10. CCP removal versus polishing time.

Experiments were conducted to determine the effect of various polishing parameters upon the removal process. In this manner the polishing operation could be optimized. Similar experiments were also conducted to optimize grinding by finding the effect of various grinding parameters upon the removal process.

Fabrication

A number of mirrors have been fabricated using the CCP. In order to determine how rapidly the process could figure an optical surface, a 38 cm. diameter Cer-Vit mirror was polished flat. With only four hours of polishing time, the workpiece was taken from an RMS surface deviation of 0.22 waves to an RMS surface deviation of 0.012 waves, where a wave is 0.63 μm. · Figure 11 shows interferograms of the mirror surface before and after polishing.
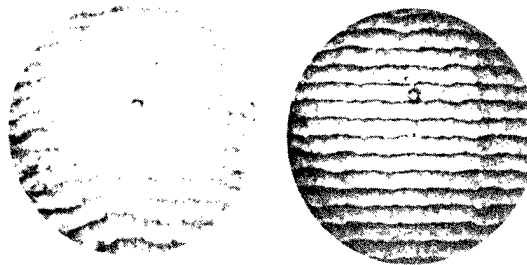
Fig. 11. CCP removal versus slurry dilution.

A 31 by 33 cm. Cer-Vit corrector mirror was selected as an appropriate piece to verify techniques. The corrector element, a segment of a circular, symetric, aspheric mirror, did not have a symetrical surface figure, and would have been an extremely difficult polishing assignment for conventional techniques. The mirror was conventionally ground and polished. The mirror was tested interferometrically. The departure from the desired surface was so large that the interferograms were too erratic to be scanned. Until better interferograms were obtained, data tapes for fabrication runs were generated using manual interferogram analyses. It was not necessary to polish the parent piece since the CCP can work noncircularly symmetric pieces. The path used was an arc raster: travelling along an arc over the mirror surface and stepping to the next arc on the piece border. After final CCP figuring, the mirror had an RMS surface error of 0.17 waves. Interferograms showing the mirror surface before and after figuring are given in Figure 12. The test setup uses double reflection from the mirror, so that fringe separation is a quarter-wave. As the mirror test did not produce null data for the proper surface figure, the fringe curvature approximately represents the desired surface.
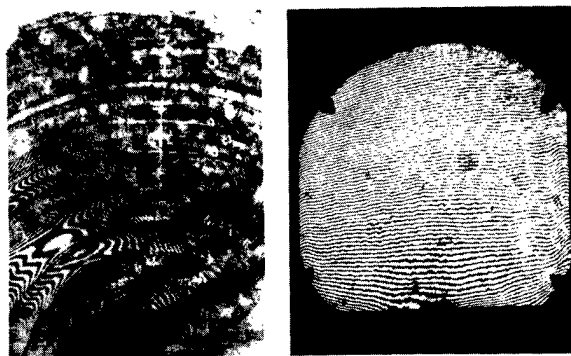
Fig. 12. Corrector plate interferograms showing surface before (left) and after CCP operation.

A demonstration was conducted to show the ability of the CCP to fabricate a flexible aspheric mirror. A 1.52 m. diameter, 9 cm. thick ULE mirror was figured to a hyperbolic surface using the CCP. Initially, the mirror had a 1.35 wave RMS departure from the desired surface. The mirror was polished on its metrology mount to avoid the risk associated with removing and reinserting the mirror in that mount. The polishing tool assembly was moved over the mirror in an annular circular spiral path. Testing was accomplished in a vacuum chamber using a precision reflective null corrector and a coaxial reference beam interferometer. The mirror was supported by a multiple-point metrology mount to simulate a zero gravity environment. After polishing, the mirror was tested and found to have a 0.074 wave RMS error over the 1.45 m. aperture region. Interferograms before and after figuring are shown in Figure 13.

In addition, the CCP has been used to fabricate a number of other difficult substrates including hard metal mirrors.[2,3]

Fig. 13. Mirror interferograms before CCP polishing (left) and after preliminary CCP figuring.

Conclusions

The CCP takes advantage of both the small tool and computer controlled features to grind or polish aspheric surfaces by controlling the amount of time the machine works any region. Using computer modeling, the best tool configurations are developed to perform any figuring operation. A general-purpose CCP tool could consist of multiple pads, each free to tilt, rotate and raise to insure proper surface match with dual rotation - epicyclic motion.

Based upon experimentation, a number of conclusions can be reached. The precision of removal with the CCP can be expected to be better than 2.3% - the precision of the removal experiments. The removal was found to be linear with polishing time - a necessary condition for efficient figuring. Also, the removal profiles have the desired shape matching the profiles obtained for computer modeling.

The CCP has been used to fabricate a number of difficult mirrors. As a result of these successful efforts, the process is being used presently to fabricate an aspheric beryllium mirror, the primary for the IRAS system, and will be used on other important fabrication efforts.

References

1. Jones, R. A., Appl. Opt., Vol. 16, pg. 218. 1977
2. Jones, R. A., Proc. SPIE, Vol. 65, pg. 48. 1975
3. Jones, R. A., Appl. Opt., Vol. 17, pg. 1889. 1978

A TECHNIQUE FOR THE RAPID FABRICATION OF NICKEL PLATED ASPHERIC METAL MIRRORS FOR INFRARED OPTICAL SYSTEMS

John J. Hizny
Honeywell Electro-Optics Center
2 Forbes Road
Lexington, Massachusetts 02173

Abstract

A simple method is described which permits the rapid fabrication of nickel plated aspheric metal mirrors for infrared optical systems. The method employs precision machining of the substrate and the plated mirror with a calculated series of tangent radii designed to closely approximate the desired aspheric curve. The process described has several advantages; it removes irregularities from the substrate and the plating, it provides an even plating layer, it produces a smooth machined surface close to the desired shape and ready for polishing and figuring, and it can be done on most precision machine lathes. Since most of the asphericity is machined into the surface at the start, a considerable reduction in fabrication time can be realized over conventional methods.

Introduction

The use of aspheric metal mirrors in infrared optical systems have many advantages for the designer, such as; simplification of overall design, reduction in the number of optical components, the use of novel design approaches, and resultant space, weight, time and cost savings. While there are many attractive aspects to the use of such aspheric surfaces, they tend to be difficult to fabricate owing to their characteristic surface slope changes. This is even more pronounced with fast mirrors when the f/number becomes small and in the case of so called general aspheric shapes (non-conic sections).

Standard optical shop fabrication practices for aspheric metal mirrors usually begin with initial machining and grinding to a "best fit sphere" followed by grinding and/or polishing to remove the residual material left in order to obtain the desired aspheric curve (aspherizing). This is illustrated in figure 1. Other techniques employ NC or template tracer machining of substrates followed by conventional grinding, polishing and figuring. While this is generally sutable for relatively large f/numbers, the departure from the best fit sphere increases drastically for smaller f/numbers. Figure 2 shows this relationship graphically.
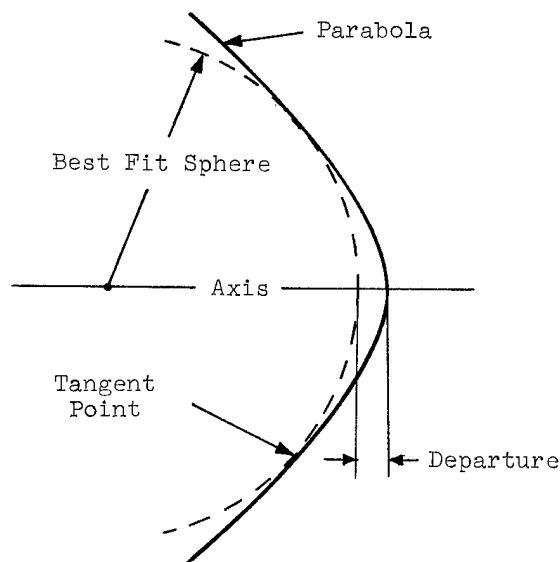
Fig. 1. The Best Fit Sphere Applied To A Parabola. The Tangent Point Is Adjusted For Minimum Departure At Center And Edge

$$\simeq \text{Departure} = \frac{y^4}{8r^3} \quad (1)$$
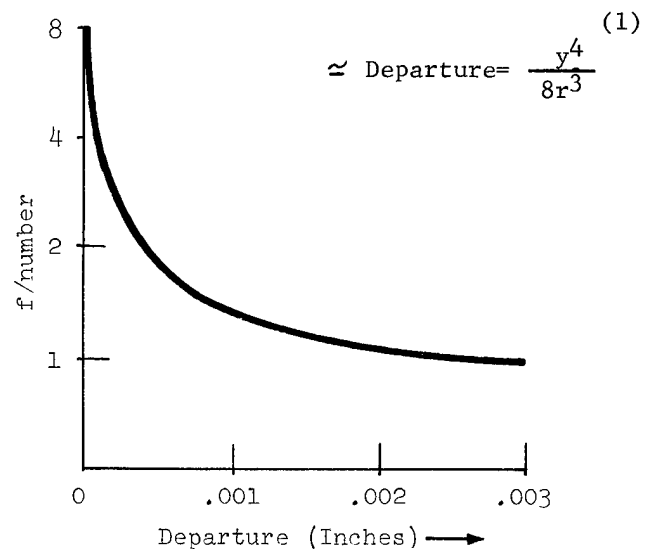
Fig. 2. Departure From The Best Fit Sphere For A 6-Inch Parabola Of Various f/numbers

Scope

The principal goal of this investigation was to prove experimentally that the novel optical finishing technique described can provide significant time and cost savings when compaired to conventional metal mirror manufacturing methods. The experiment consisted of fabricating identical aspheric mirrors, one by conventional methods and one employing the multiple tangent radii machining process outlined previously.

This paper describes the theory and application of multiple tangent radii machining of nickel plated aspheric metal mirrors.

Test Mirror Configuration

The test mirror involved in the fabrication experiment was an axial symmetric hyperboloid shown in figure 3. Substrate material was optical grade beryllium (I-70-A) plated with a low stress electroless nickel plating .0035-inches thick. Beryllium was chosen for its light weight and high strength. The mirror comprised the second element in a light weight all beryllium infrared telescope design which utilized liquid helium cryogenic cooling. (2)

Mounting Holes

.223"

Machining Radius

Pilot

Mounting Seat

.730"

1.950"

$$Z = \frac{Y^2/R}{1+\sqrt{1-(K+1)Y^2/R^2}}$$

$$R = +\ 4.242"$$
$$K = -\ 2.80412$$

.090"
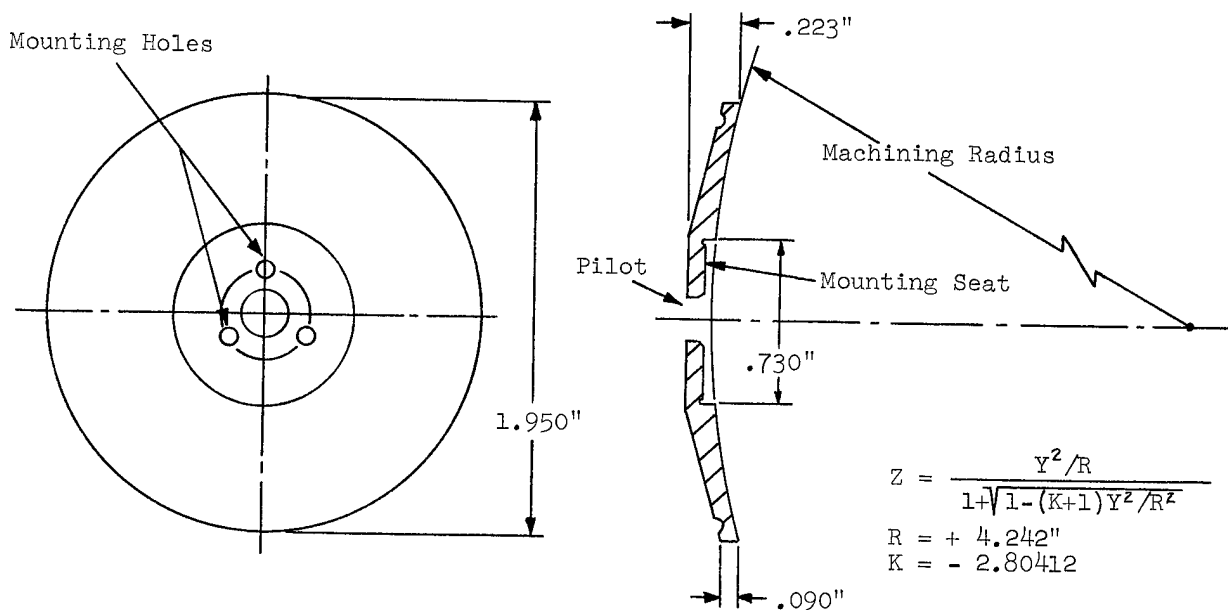
Fig. 3. Hyperboloid Test Mirror Configuration And Optical Perscription

The shape of the mirror was dictated by critical system design constraints, i.e. mirror mounting location, weight budget, thermal and mechanical properties.

The optical design required the mirror surface to follow the aspheric figure to within 1λ peak to peak with an allowable surface slope error not to exceed 2λ per inch at a wavelength of .6328µm. System off-axis-rejection specification necessitated a low scatter surface finish with a BRDF of 1×10^{-3} at 1° from the specular at a wavelength of 10.59µm.

Theory

The use of multiple tangent radii machining to accurately prepair aspheric metal mirrors for optical finishing is essentially an extension of the single best fit sphere approach most widly used today. Instead of one spherical curve several different radii and vertex distances are employed to provide a series of overlapping cuts tailored to the required aspheric shape. Using this method the departure of the machined mirror from the desired aspheric can be reduced to $1/10$ or less than that of a single best fit sphere. Figure 4 illustrates the advantage of using multiple tangent radii compared to the single best fit sphere.

$R_1 = -4.3226"$

$R_2 = -4.3847"$

$R_3 = -4.4748"$
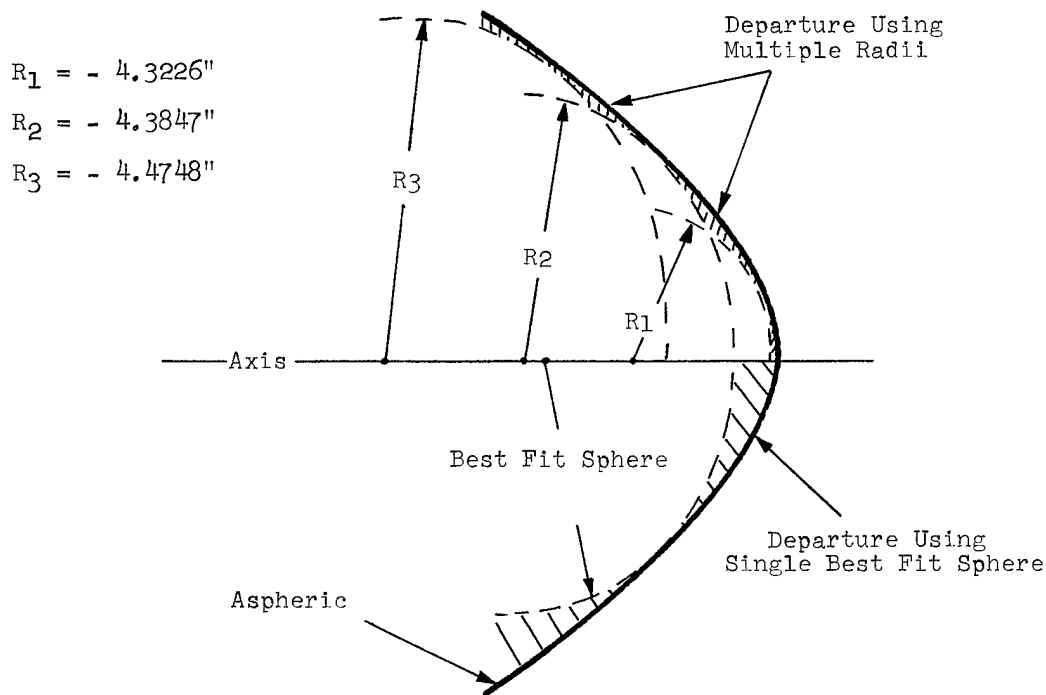
Fig. 4. Comparison Of Residual Departure Between Multiple Tangent
Radii Technique And Single Best Fit Sphere From Test Hyperbolas

Multiple Radii Formulation

The process required for the computation of multiple radii for approximating an aspheric
surface consists initially of establishing dimensional limits, mathematically describing
the desired surface, and setting surface fit tolerances. For the test hyperbolas involved
in the experiment, the parameters necessary for radii computation consist of the following

Table 1. Parameters Used For Test Mirror Machining

Parameter	Multiple Radii Test	Best Fit Sphere Test
Aspheric Perscription	Fig. 3	Fig. 3
Aperture Limits	O.D. - 1.950" I.D. - .730"	O.D. - 1.950" I.D. - .730"
Surface Fit	.0001"±.000025"	------------

Actual computation of the radii dimensions and vertex spacings was done with the aid of
a computer. While this was not necessary for the simple case of a single best fit sphere,
it proved invaluable in handling the more difficult multiple radii problem. The computer
provided calculations of radius, vertex spacing and departure of the hyperbola for the
single best fit sphere test. This is shown in table 2. For the multiple radii test the
computer figured the number of radii required to produce the required fit and the resultant
departures.

Table 2. The departure from the desired hyperbola for the best fit
sphere and the multiple radii test. Three radii were required for
an optimum curve fit using a minimum number of cuts. *

Ray Height	Best Fit Sphere	Multiple Radii			
		R_1	R_2	R_3	Least Departure
.365"	.00062"	.00006"			.00006"
.385	.00057				
.405	.00052	.00003			.00003
.425	.00046				
.445	.00041	.00001			.00001
.465	.00036				
.485	.00031	.00000			.00000
.505	.00026				
.525	.00022	.00000	.00012"		.00000
.545	.00018				
.565	.00012	.00002	.00007		.00002
.585	.00010				
.605	.00007	.00006	.00003		.00003
.625	.00005				
.645	.00002	.00011	.00000		.00000
.665	.00001				
.685	.00000		.00000	.00028"	.00000
.705	.00000				
.725	.00001		.00003	.00017	.00003
.745	.00002				
.765	.00005		.00008	.00009	.00008
.785	.00008				
.805	.00012		.00017	.00003	.00003
.825	.00017				
.845	.00024			.00000	.00000
.865	.00032				
.885	.00041			.00001	.00001
.905	.00051				
.925	.00063			.00006	.00006

The maximum departure for the best fit sphere is .00063" while the least departure
for the multiple radii is .00008" at the maximum. This shows a calculated difference of
.00055" between the two approaches.

Mirror Machining

The two test hyperbolas were initially machined in the same manner utilizing standard
progressive machining followed by heat treating, stress releaving, and stabelizing of
optical grade beryllium I-70-A. Final machining of the mirror surfaces were done on a
Hardinge lathe. After nickel plating the mirrors were remachined to remove irregularities.

Best Fit Sphere Machining

The final cut on the mirror surface was made with a special radius cutting fixture using
a sharp, small radius tool of tungsten carbide. The setup is illustrated in figure 5.

Multiple Radii Machining

The multiple radii test mirror employed the same apparatus as that used to machine the
best fit sphere. The different radii were machined successively after adjusting the tool
holder to the proper radius and vertex spacing.

* Computation of multiple radii was performed by Mark Hatch, Optical Design Dept.,
Honeywell Electro Optics Center.

Chuck   Mounting Plate   Tool   Tool Pivot Point

Lathe

Bed

Mirror   Cross Slide
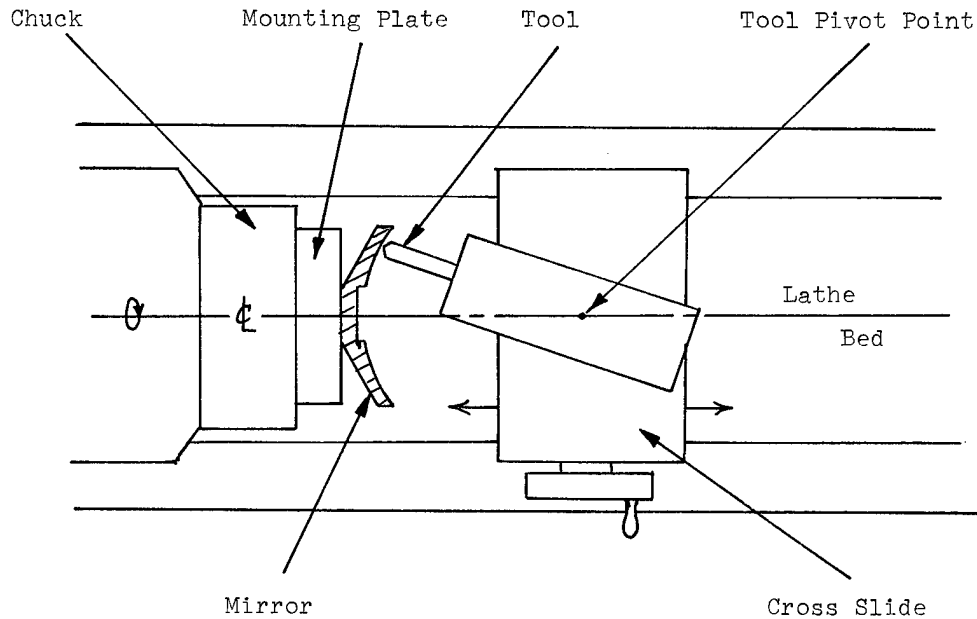
Fig. 5. Setup For Machining Single Best Fit Sphere And
Multiple Radii Test Mirrors On A Precision Machine Lathe **

Multiple Radii
Intersections

R_1

R_2

R_3
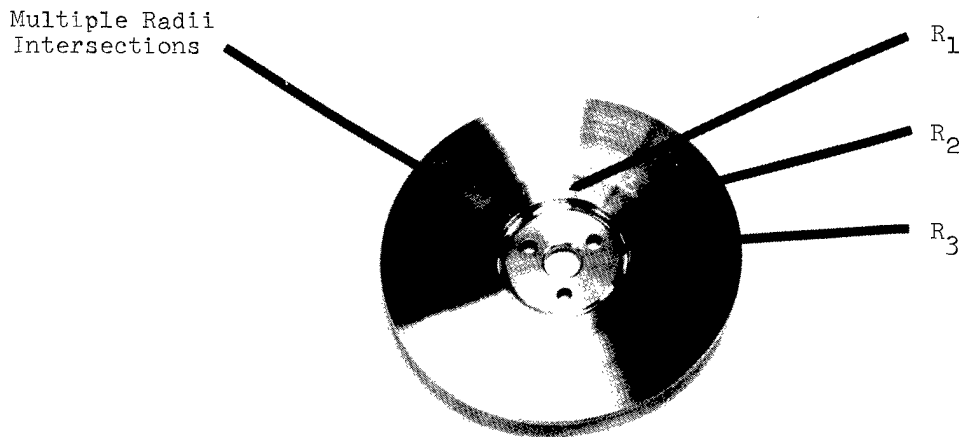
Fig. 6. Hyperbola After Machining Multiple Radii
On The Nickel Plated Surface. Differences In The
Machined Surface Finish Reveal The Use Of Several
Successive Cuts

After final machining of the nickel plated optical surface the test mirrors were given a thermal stabelization to remove residual stresses induced by plating and machining. This process consisted of temperature cycling between +200°F oven bake and -405°F liquid neon quenching. This process also provided a qualification test of the adhesion of the nickel plating, since the mirrors are designed for operation in a low temperature regime.

** Mirror machining was done at LDL Precision Corp., Plainview, Long Island, N.Y.

Optical Finishing

The single best fit sphere was fabricated first followed by the multiple radii test mirror. Established polishing and figuring methods, materials and equipment were utilized in manufacturing the test mirrors.

Apparatus

The optical finishing equipment employed in the polishing and figuring of the two test hyperbolas were identical with the exception of necessary differences in polishing lap configurations owing to variations in the machined surface shapes. Polishing and figuring was carried out on a Strasbaugh 6UR Polishmaster shown in figure 7. Mirror mounting and handling fixtures were designed to provide maximum stability and support during polishing.

Conventional polishing and figuring was done on premixed Swiss pitch using aluminum oxide (A) in a filtered water slury in the standard manner. Low scatter surface preparation was carried out with a special compliant felt lap with graded aluminum oxide in a mild detergent solution.
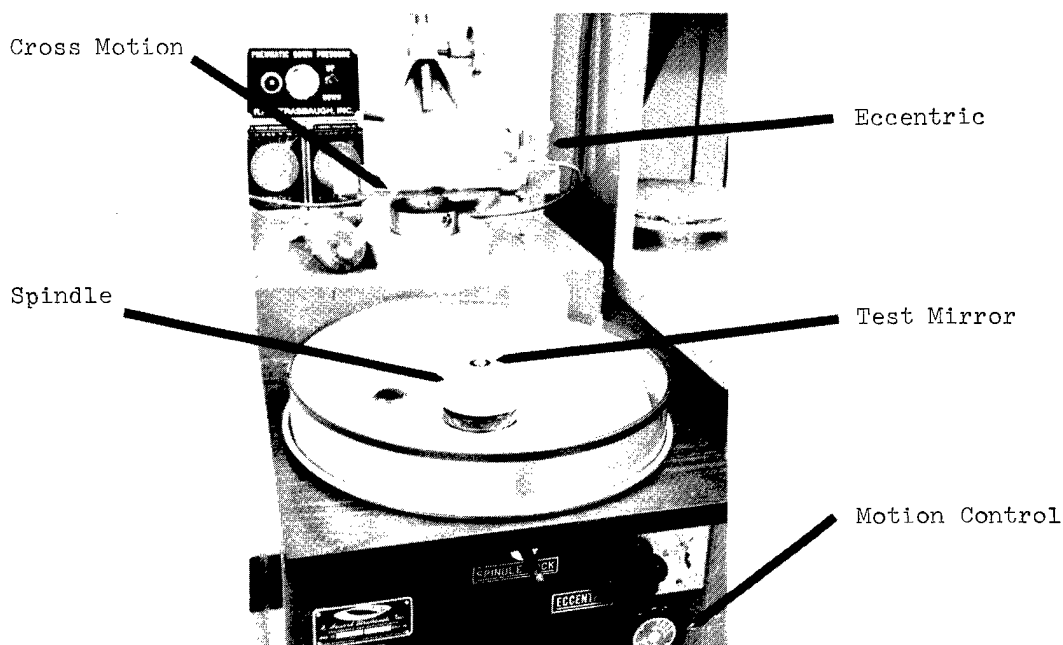
Fig. 7. Polishing Machine Showing Principal
Components With Test Mirror Under Fabrication†

The principal test instrument used for the fabrication experiment was a bread board laser unequal path interferometer.[3] It was employed for inprocess tests and final acceptance testing. A Hindle sphere null test arrangment was used to provide a simple and convenient test capability.[4] Figures 8 and 9 show the Hindle sphere test cell and the laser interferometer. The Hindle cell was designed with a piloted mounting seat at one end for the test mirrors, this feature allowed rapid test turn around since it was self aligning.

† The test mirrors were polished and tested by the author at Honeywell Electro Optics Center, Lexington, Mass.

Laser Unequal Path Interferometer
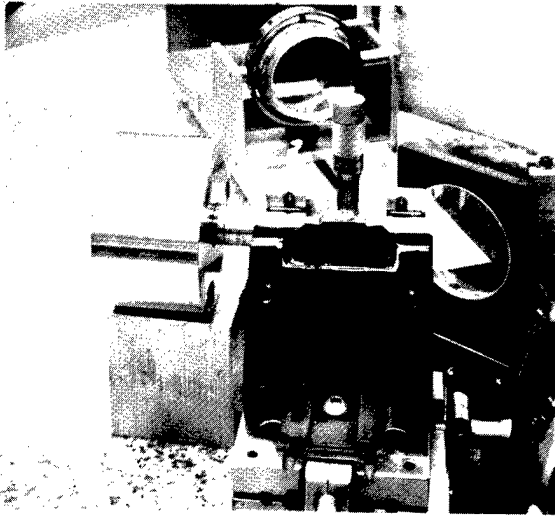
Fig. 8. Hindle Test Cell
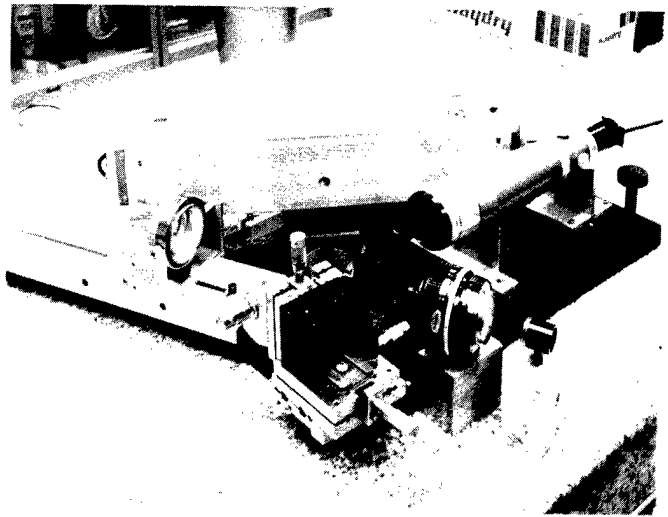
Fig. 9. Laser Test Interferometer
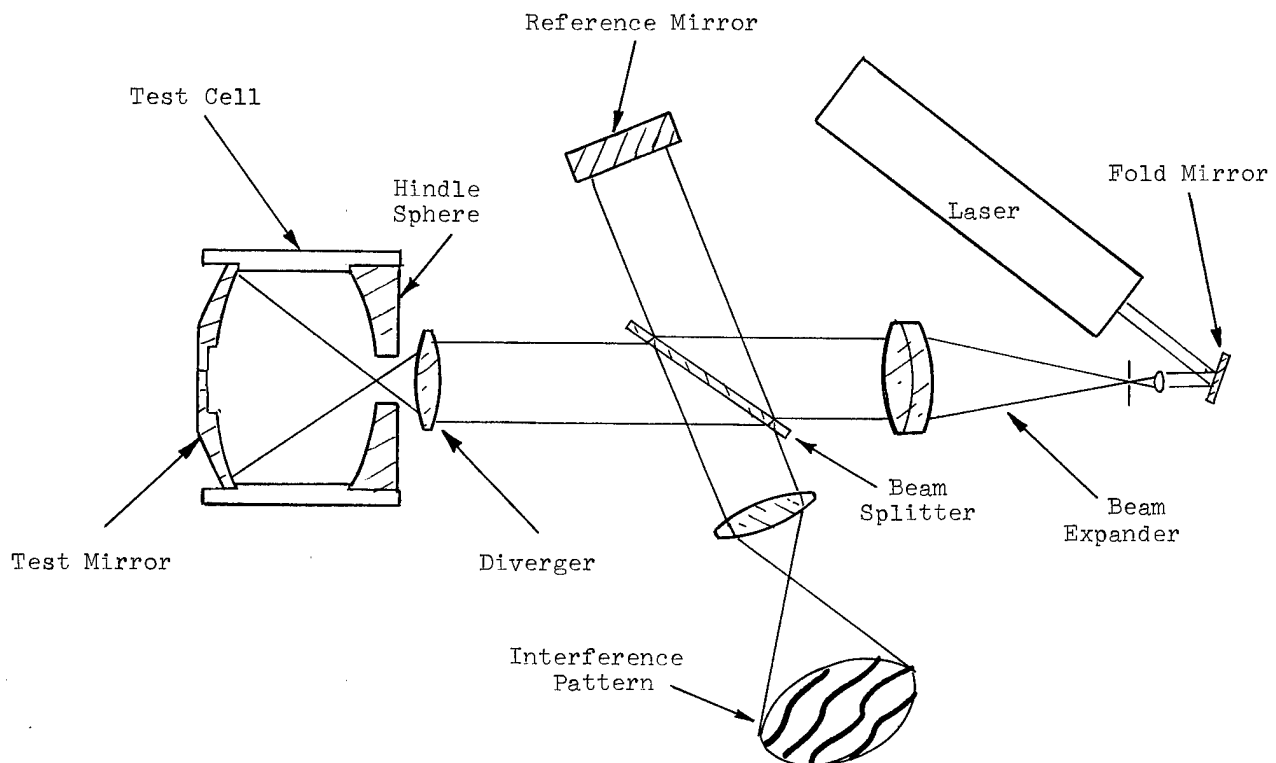
Fig. 9A. Diagram Of The Hyperbola Test Mirror Setup Shown In Fig.9.

Optical Fabrication Test Results

Best Fit Sphere Test Mirror   Multiple Radii Test Mirror
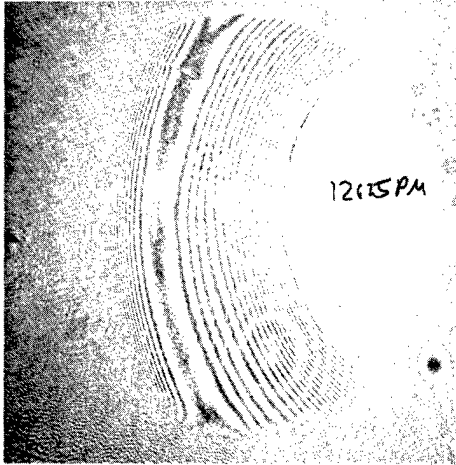
Fig. 10.

Surface Peak-To-Peak = 20-25 λ
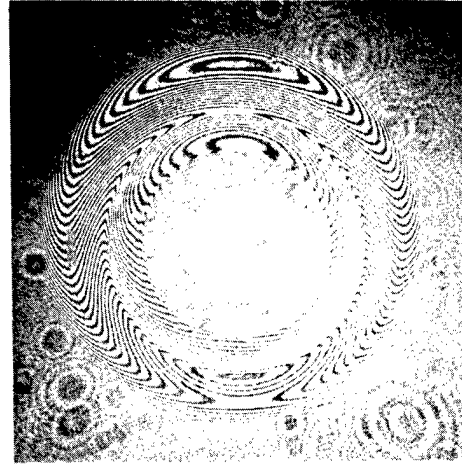
Fig. 11.

Surface Peak-To-Peak = 2-3 λ

Interferograms showing results of initial polishing of test mirrors
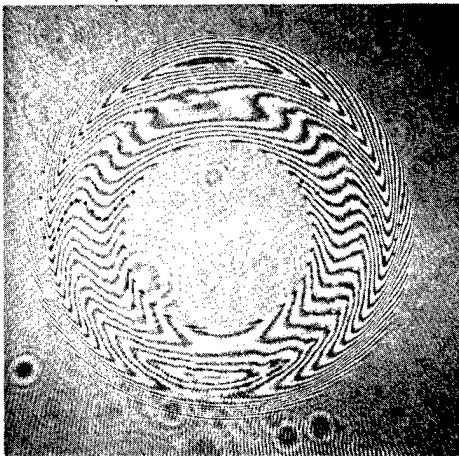
Fig. 12.

Surface Peak-To-Peak = 2 λ
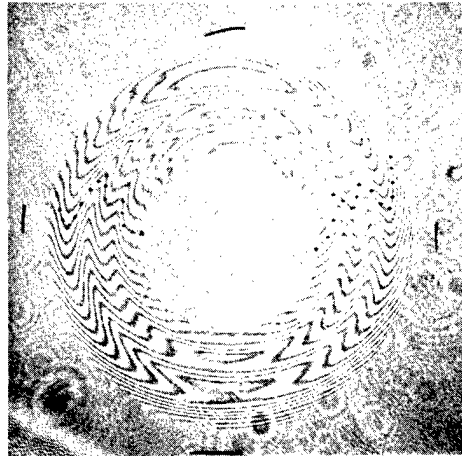
Fig. 13.

Surface Peak-To-Peak = 1.25 λ

Interferograms after final figuring of the test mirrors

	Best Fit Sphere	Multiple Radii
Total Fabrication Time	104-man hours	24-man hours
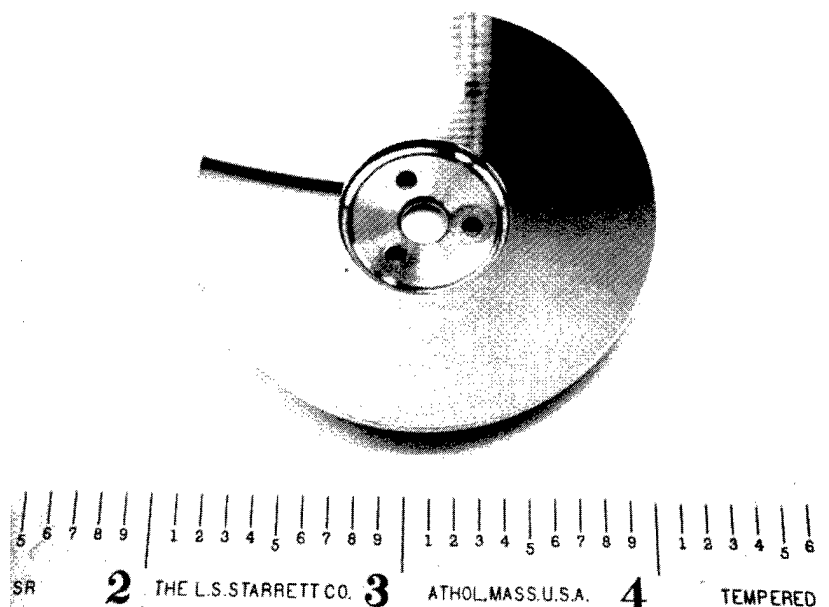
Fig. 14. Finished Hyperbola

Results

The experiment resulted in the successful fabrication of two identical nickel plated beryllium hyperbolic mirrors, one using the conventional best fit sphere approach and one employing a novel multiple radii machining preparation technique of the substrate and the plated surface. Polishing was done with identical materials and standard methods. The final optical figure achieved on the two test mirrors were comparable, however it required 104-man hours to finish the conventional mirror while it took only 24-man hours to complete the multiple radii test mirror. The drastic reduction in the polishing and figuring time was the direct result of residual material removal between the single best fit sphere to the hyperbolic surface. Residual departure of the best fit sphere was .00063" while the departure for the multiple radii was .00008" , thus after machining the multiple radii mirror was within $\sim 4\lambda$ from the desired figure and the best fit sphere was $\sim 32\lambda$ off.

Conclusions

It has been demonstrated that by using multiple radii machining operations on an aspheric metal mirror a significant reduction in optical finishing time can be realized compared to the conventional best fit sphere method.

Acknowledgments

The author wishes to thank Marcus Hatch, Optical Design Dept., Honeywell Electro Optics Center, Lexington, Mass.,for his thorough calculations of the multiple machining radii which were the heart of the experiment. In Addition, thanks and appreciation are extended to LDL Precision Corp. for their superb machining and plating of the mirrors

Refrences

1. Strong, John., Concepts of Classical Optics, p. 293, Freeman, 1958.
2. Pacquin, Roger A., Selection of Materials and Processes for Metal Optics, pp. 12-19, Proceedings SPIE, Vol. 65, Design Manufacture and Application of Metal Optics, Aug. 19-20, 1975, San Diego, Ca
3. Malacara, Daniel., Optical Shop Testing, p66, Fig. 2.17, John Wiley, 1978.
4. Hindle, J.H., A New Test for Cassegranian and Gregorian Secondary Mirrors, Royal Astronomical Society, 91.592, 1931.

LOW-ABSORPTION GRATING BEAM SAMPLERS

Jayanta K. Guha* and James A. Plascyk
The Perkin-Elmer Corporation
Norwalk, Connecticut 06856

Abstract

A development program involving the design, fabrication and testing of low-efficiency, low-absorption grating beam samplers is described. Two different basic designs were selected for development. The first design is a low-efficiency grating with a high reflectivity multi-layer dielectric coating. The second design is a "buried grating", which consists of a blazed grating under a ZnSe spacer layer, with a high reflectivity multilayer overcoat. The fabrication problems associated with each type of beam sampler are discussed. The comparison of experimentally measured absorptivity and efficiency with values obtained from computer calculations are presented. An additional effort currently underway to make very low absorptivity beam samplers by generating periodic refractive index variations in the dielectric stack is also discussed.

Introduction

For many high-energy laser applications, it is necessary to monitor continuously the intensity and phase profile of a laser beam using, for example, a laser wavefront analyzer.[1] In such devices, a small fraction of the intensity of the beam is sampled out by the so-called "beam sampler". For high-power applications, refractive elements are not suitable because of absorption problems. Gratings have been used successfully for such applications in a configuration such as that shown in Figure 1. The main laser beam is specularly reflected off grating GR-1. The first-order beam is again diffracted off complementary grating GR-2. Therefore, if the laser is not monochromatic, the dispersion at GR-2 recollimates the beam. The resulting arrangement is commonly known as a Grating Rhomb.**
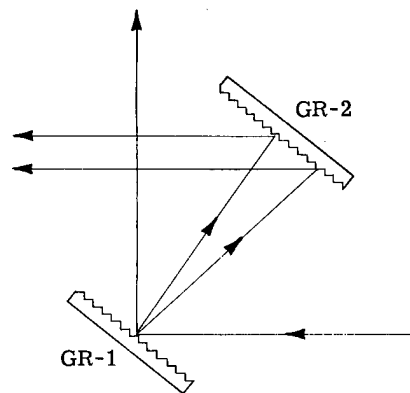
Fig. 1. Grating rhomb configuration.

Typically, a well-designed grating on gold at 3.9 μm has an absorption coefficient of the order of 2%. Although in most cases this absorption is not large enough to cause damage to the grating, it does cause distortion even in water-cooled gratings. This distortion has the effect of aberrating both the main laser beam and the sampled beam. This paper will describe the effort at Perkin-Elmer to devise techniques for reducing the absorption at the grating.

Three schemes to reduce absorption at the grating were studied. The first scheme is one in which a high-reflectivity multilayer dielectric coating is applied on a shallow grating (Figure 2). As is well known, such coatings on a plane metal mirror can produce very high reflectivity and low absorption (0.1% or less). Typical coatings consist of alternate layers

---

of ThF$_4$ and ZnSe (or ZnS) of quarter-wave optical thickness. However, since the surfaces of the dielectric layers follow the grating profile, the absorption is higher than that for an ideal system with a plane mirror and plane parallel coatings. As the depth of the grating is increased (to increase the sampling efficiency), the absorption also increases, so that a tradeoff between the two desired goals of efficiency and low absorption must be made.
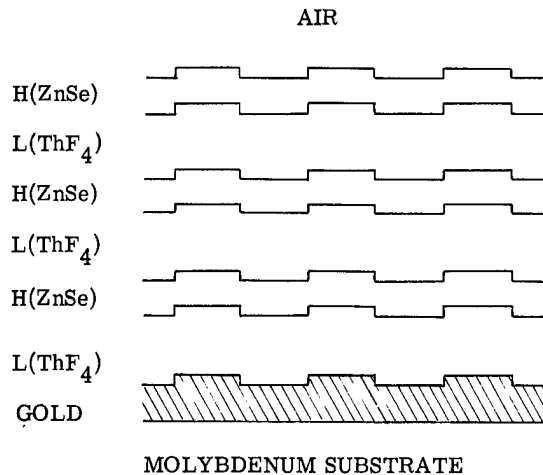
Fig. 2.   Low-efficiency grating with dielectric overcoat.
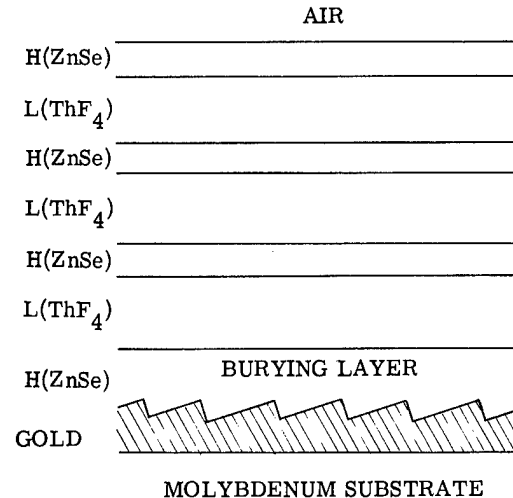
Fig. 3.   High-efficiency buried grating.

A buried grating is the basis of the second scheme. The grating is embedded in a 1/2 wave dielectric coating, and the top surface of the dielectric is polished flat. The dielectric is then coated with a high-reflectivity multilayer stack. However, if the grating is shallow with an efficiency of about 1% in the configuration shown in Figure 2, the efficiency is of the order of 10^{-5}, which is too low for most applications. Therefore, in general, a high-efficiency, echelette-type grating must be used (Figure 3).

The third scheme investigated is the very low-efficiency "phase grating". Periodic refractive index variations are induced in the dielectric thin films on a plane metal surface. The system should act as a weak phase grating and, since all the surfaces are plane parallel, the absorption should be close to that of an ideal enhanced reflector.

One technique by which such refractive index variations can be obtained is illustrated in Figure 4. Since the refractive indices of ZnSe (n = 2.434) and ZnS (n = 2.520) at 3.9 μm are different, the grooves form a weak phase grating because of the periodic refractive index variation. However, since the refractive indices are comparable, there is an approximate index matching, so that the absorption should be comparable to an ideal enhanced reflector. Such a groove profile can be produced by ion etching. The top ZnSe layer is a half wave thick and hence is practically "transparent" in regard to interference effects.
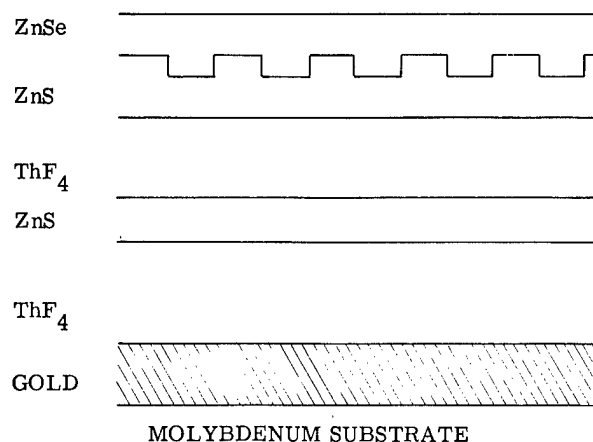
Fig. 4.   Conceptual design for the very low-efficiency "phase grating".

This type of grating would have a much lower diffraction efficiency than that of the other designs. Therefore, although gratings GR-1 and GR-2 can be identical for the two previous designs, for this concept, secondary grating GR-2 must have a high efficiency in order to achieve adequate overall sampling efficiency, or the angular separation of the various wavelengths of the sampled beam must be tolerated.

Enhanced Reflectors - General Theoretical Discussion

The theoretical treatment of an enhanced reflector consisting of a plane mirror overcoated with a series of dielectric layers is fairly standard[2]. The usual boundary conditions are applied to the electric and magnetic field components for air, metal, and the dielectric media. It can be shown that the fields are related by 2 x 2 matrices.

$$m^P = M_2^P (d_2) \; M_3^P (d_3 - d_2) \; \ldots \ldots \; M_{L+1}^P (d_{L+1} - d_L) \tag{1}$$

$$m^S = M_2^S (d_2) \; M_3^S (d_3 - d_2) \; \ldots \ldots \; M_{L+1}^S (d_{L+1} - d_L) \tag{2}$$

where the superscripts P and S identify parallel and perpendicular polarizations. The variable d identifies the location of each different boundary. The matrices M are given by:

$$M_n^P (d_n - d_{n-1}) = \begin{bmatrix} \cos p_n & - \dfrac{q_n^{(o)}}{(\omega/c)^2 \, \epsilon_n} \sin p_n \\ \\ \dfrac{(\omega/c)^2 \epsilon_n}{q_n^{(o)}} \sin p_n & \cos p_n \end{bmatrix} \tag{3}$$

$$M_n^S (d_n - d_{n-1}) = \begin{bmatrix} \cos p_n & (\sin p_n)/q_n^{(o)} \\ \\ -q_n^{(o)} \sin p_n & \cos p_n \end{bmatrix} \tag{4}$$

where

$$p_n = q_n^{(o)} (d_n - d_{n-1}) \tag{5}$$

$$q_n^{(o)} = \left[(\omega_o/c)^2 \epsilon_n - k_o^2 \right]^{1/2} \tag{6}$$

$$k_o = \frac{\omega_o}{c} \sin \theta_o \tag{7}$$

Here, ϵ_n is the complex dielectric constant for the nth layer.

The specular reflectivities and absorptions for gold with ThF_4 and ZnSe coatings calculated by the above technique are shown in Table 1. It can be seen that the absorption decreases as the number of dielectric pairs is increased. Similar results were obtained for ThF_4 and ZnS.

Theoretical Results of Sampling Techniques Investigated

Shallow Grating With Multilayer Dielectric Coating

The analysis of shallow gratings with dielectric coatings has been discussed by Elson.[3] This analysis was done on the basis of the perturbation approach, where the grating profile is considered to be a small departure from a plane surface. The surfaces of the individual dielectrics were assumed to have the same shape as the grating. The results shown in Table 2

Table 1.   Theoretical Specular Reflectivities at 3.9 μm for Plane Gold Mirror Coated with ThF$_4$/ZnSe Stack (i = 38°)

No. of Pairs	P-Pol (%)	S-Pol (%)	Average (%)	Absorption (%)
0	97.71	98.57	98.14	1.86
1	98.96	99.49	99.22	0.78
2	99.52	99.80	99.66	0.34
3	99.75	99.91	99.83	0.17
4	99.85	99.95	99.90	0.10
5	99.90	99.96	99.93	0.07

NOTE: The following refractive indices were assumed: Gold: (2.9, 25.0), ZnSe: (2.434, 5 x 10^{-5}) and ThF$_4$: (1.5, 2 x 10^{-4}).

Table 2.   Theoretical Diffraction Efficiency and Absorption Values at 3.9 μm for a Low-Efficiency Grating with Dielectric Coating (Angle of incidence 38°.   Three ThF$_4$/ZnSe pairs.)

Groove Depth (Å)	Efficiency (%)			Absorption (%)		
	P	S	Avg.	P	S	Avg.
500	0.467	0.196	0.332	0.247	0.091	0.169
1000	1.870	0.784	1.327	0.247	0.091	0.169
1500	4.207	1.764	2.985	0.247	0.091	0.169

were obtained with a computer program, MULTI, prepared by Elson.*   These results apply to a grating with rectangular profile and 40% duty cycle (valley width/total width).   To a first order, the absorption values are assumed to be the same as those in Table 1 for a flat gold surface.   As will be shown later, however, the absorption actually increases with groove depth.

Buried Gratings

The analysis of the buried gratings is somewhat more complicated for two reasons. First, the calculation of the diffraction off the grating is more complicated since the perturbation approach used by Elson is not applicable for deep-groove echelette-type gratings. Second, even if the grating is designed for only one order, within the burying layer of ZnSe there will be several other orders, as shown in Table 3, that will get trapped in the burying layer. In addition, there will be trapping due to fractions of the specular and the first order reflected back from the top of the burying layer.

A computer code has been developed at Perkin-Elmer to account for the above factors. Calculations for buried gratings with six ThF$_4$/ZnSe pairs indicate, as shown in Table 7, that the absorption at the 3.9- μm band (DF laser) should be of the order of 0.5%. Although adding more dielectric pairs would lower the absorption, it is not desirable to add any more layers because of the lowered laser damage threshold.

Table 3.   Diffracted Angles for a Grating Buried in ZnSe

λ = 3.9 μm, d = 4.63 μm
Angle of incidence in air = 38.0°
Angle of incidence in ZnSe = 14.65°

Order	Angle in ZnSe	Angle in Air
-3	-51.75	
-2	-26.05	
-1	- 5.35	-13.10
0	14.65	38.00
1	36.80	
2	70.92	

(Orders on the same side of the normal as the incident beam are assigned negative signs)

* MULTI computer program was supplied by Dr. J. M. Elson, U.S. Naval Weapons Center, Michelson Laboratories, China Lake, California.

Very Low-Efficiency "Phase Grating"

Elson's program MULTI was modified to calculate the efficiency of the very low-efficiency phase grating (Figure 4). This program also calculates the absorption but only under the approximation that all the layer interfaces are plane. (More work is required in order to calculate the absorption more exactly.)

The ideal absorption values for different numbers of the ThF_4/ZnS pairs are shown in Table 4. For a larger number of pairs, a point of diminishing return is reached where adding extra pairs does not significantly lower the absorption.

Table 4. Absorption and Efficiency for 500Å Groove Depth Phase Grating (Theoretical)

No. of ThF_4/ZnS Pairs (on gold)	Absorption (%) (Ideal)	Efficiency ($\times 10^{-4}$) (Unpolarized)
3	0.227	3.07
4	0.144	3.27
5	0.105	2.03
6	0.088	4.30
7	0.080	1.08
8	0.076	5.15
9	0.075	0.38

Refractive Indices: Gold: $(2.9, 25.0)$
ThF_4: $(1.5, 2 \times 10^{-4})$
ZnS: $(2.25, 5 \times 10^{-5})$
ZnSe: $(2.434, 5 \times 10^{-5})$

The efficiencies for a given number of pairs with the grooves in the outermost ZnS layer are given in Table 4. The physical reason for the large variation when a new pair is added is not well understood. These results are for a 500-Å groove depth. The efficiency for any other groove depth can be calculated from the simple assumption that for shallow gratings the efficiency varies as the square of the groove depth.

The efficiency for the device is lower if the phase grating, instead of being on the surface of the outermost ZnS layer, is on the surface of another ZnS layer deeper in the stack. The efficiency for grooves in different ZnS layers is given in Table 5. In the Efficiency column of Table 5, E_n represents the efficiency of a specific layer on which the groove profile is ruled. The layers are numbered counting from the substrate. Thus, for the three-pair sample, E_3 gives the efficiency for the case when the grooves are in the outermost ZnS layer, E_2 is the efficiency when the grooves are in the middle ZnS layer, and E_1 is the efficiency when the grooves are in the innermost ZnS layer.

Based on the above calculations, it seems possible to build an element of absorptivity less than 0.1% and an efficiency of more than 10^{-4}.

Table 5. Efficiency for Grooves in Different ZnS Layers (Phase Grating Theoretical)

No. of ThF_4/ZnS Pairs	Efficiency ($\times 10^{-4}$) (Unpolarized)
3	$E_3 = 3.070$
	$E_2 = 0.679$
	$E_1 = 0.154$
4	$E_4 = 3.270$
	$E_3 = 0.737$
	$E_2 = 0.166$
	$E_1 = 0.037$
5	$E_5 = 2.030$
	$E_4 = 0.458$
	$E_3 = 0.103$
	$E_2 = 0.023$
	$E_1 = 0.005$

Experimental Results

In the experimental part of the program, shallow gratings overcoated with dielectric coatings and buried gratings were fabricated, and their performance was tested and correlated with theory. So far, the work on the very low-efficiency phase gratings has been restricted to theoretical calculations, but plans have been made to fabricate and test these elements.

Low-Efficiency Gratings

The grating substrates were 1.54-inch diameter, 1/8-inch thick molybdenum, coated with gold. The gratings were ruled in the gold by Diffraction Products, Inc., at three different depths - 500 Å, 1000 Å, and 1500 Å. The gratings were coated with three pairs of the ThF_4/ZnS quarter-wave layers. (ZnS was selected instead of ZnSe because of its higher laser damage threshold.)

The results of the measurements on these gratings, and the comparison with theory, are shown in Table 6. The efficiency at $3.4\,\mu m$ was measured by using an HeNe laser operated at that wavelength. For the absorption measurement, a broadband (3.7 to 4.1 μm) DF laser was used. (A 3.4 μm laser was used for the efficiency measurement because a monochromatic single mode laser at 3.9 μm is unavailable.) For the absorption measurements, the rate of temperature rise in the substrate after laser turn-on was measured with a thermocouple, and the absorption coefficient was indirectly calculated from these data. These absorption measurements were performed at TRW in Redondo Beach, California.

Table 6. Comparison of Theoretical and Experimental Results for Low-Efficiency Gratings. (Angle of incidence 38°. Three ThF_4/ZnS Pairs.)

Description	Efficiency at 3.4 μm(%)		Absorption Coefficient at 3.7 μm – 4.1 μm Band (%)	
	Theory	Exp't	Theory	Exp't
Low-Efficiency 500Å deep	0.45	0.33	0.77	0.56
Low-Efficiency 1000Å deep	1.80	2.36	0.77	0.93
Low-Efficiency 1500Å deep	4.05	3.60	0.77	1.00

The results show fairly good correlation of experiment and theory. As can be seen by referring to Table 2, the absorption can be decreased by using ZnSe instead of ZnS. The same effect can be achieved by using more dielectric pairs. Since the theoretical absorption calculation neglects the effect of the grating, the values in the fourth column of Table 6 are all the same.

Buried Grating Design

In order to fabricate the buried grating, a high-efficiency echelette-type grating was ruled on a gold-coated molybdenum substrate. Since the performance of such a grating depends critically on the blaze angle, special care was taken to assure that the desired blaze angle was achieved. It was found that the angle at which the ruling diamond is set is not accurately reproduced in the angle of the blaze. There are complicating factors, such as the springback action of the gold surface, distortion, etc., which create errors. Therefore, grating trial rulings were made, the blaze angle was measured, and the tool setting was adjusted until the correct blaze angle was obtained.

The blaze angle, θ_B, was measured indirectly, by measuring the intensity of a particular order of a 0.6328-μm HeNe beam diffracted by the grating as a function of the angle of incidence. For a grating blazed for the m_{th} order, the blaze angle is such that θ_d^m is the blaze direction

$$\theta_d^m = \theta_i - 2\theta_B$$

$$\theta_i - \theta_d^m = 2\theta_B \tag{8}$$

If the intensity in the mth order is plotted as a function of $(\theta_i - \theta_d^m)$, the maximum will occur at a value of $2\theta_B$ so that the blaze angle can be determined.

The results for three test rulings are shown in Figure 5, and are plotted with the theoretical curve for a grating with a 10° blaze. Because of fluctuations in the laser intensity, the results are good to only about $\pm 0.5\%$.

#1 → 8.4 ± 0.5°
#2 → 9.6 ± 1.0°
#3 → 11.2 ± 1.7°
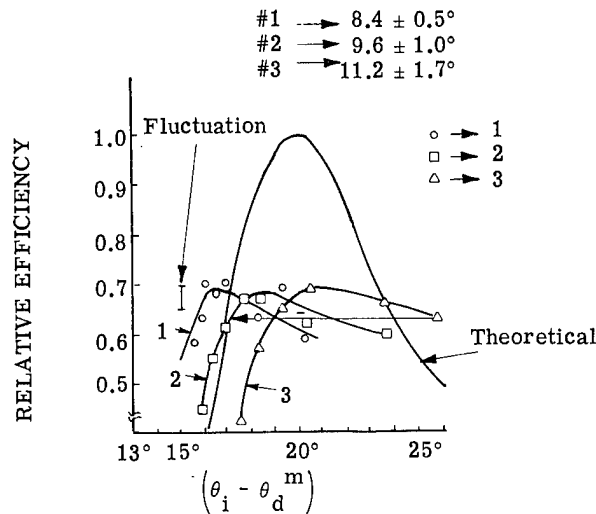
Fig. 5. Results of trial grating ruling

In order to "bury" the grating in ZnSe, it was coated with ZnSe and polished. Even though the absorptivity is minimum when the spacer thickness is 1/2 wave (in which case the spacer layer does not contribute to any interference effects), calculations indicated that small changes from this thickness can increase the efficiency significantly, without an appreciable increase in absorption. The calculations indicated an optimum thickness of 0.46 wave at 3.9 μm.

The comparison between the theoretical and experimental absorption measurements is shown in Table 7. There is a fairly good correlation between theory and experiment. However, the data for efficiency were extremely ambiguous. It was found that the efficiency varied as much as a factor of 10 from one element to another of the same design. Even for the same sample, the efficiency varied very strongly as a function of the angle of incidence.

Table 7. Comparison of Theoretical and Experimental Absorption Values for Buried Gratings

| Sample No. | Absorption (%) over the 3.7 - 4.1 μm Band | |
	Exp't (TRW)	Theory
B-01	0.60	0.50
B-03	0.67	0.50

Samples had 0.46 wave of ZnSe as spacer layer, and six ThF_4/ZnSe pairs. Theoretical results from Perkin-Elmer code.

Conclusions

The theoretical and experimental data indicate that the shallow grating with four or five dielectric pairs would yield efficiencies of the order of 1% with absorptions of the order of 0.2%. The absorption could be further reduced by making the grating shallower (and hence sacrificing the efficiency). But, for very shallow gratings, it is difficult to control the depth; therefore, such elements would lack reproducibility.

The buried grating seems to be beset with two problems. First, the absorption is as high as 0.5%, even for six or seven dielectric pairs. Second, the efficiency of an element is not reproducible.

If the object is to generate a very low-efficiency element, the phase grating seems to be promising. However, it will be necessary to have some experimental corroboration of the theoretical results.

References

1. J. Van Workum, J.A. Plascyk, and M.L. Skolnick, "Laser Wavefront Analyzer for Diagnosing High-Energy Lasers", in SPIE Proceedings, Vol. 141, Adaptive Optical Components, p. 58 (1978).

2. M. Born and E. Wolf, Principles of Optics, 4th edition, Pergamon Press, 1970, p.51-70.

3. J.M. Elson, "Infrared Light Scattering from Surfaces covered with Multiple Dielectric Overlayers", Appl. Opt., 16 (11), pp.2872-2881 (1977).

PLATED COPPER SUBSTRATES FOR THE LOS ALAMOS SCIENTIFIC LABORATORY (LASL) ANTARES CO₂ LASER SYSTEM*

David J. Blevins and James L. Munroe
Los Alamos Scientific Laboratory
University of California
Los Alamos, NM 87545

Abstract

Antares is a large carbon-dioxide laser system presently under construction at the Los Alamos Scientific Laboratory (LASL). Antares will be part of the LASL High Energy Gas Laser Facility (HEGLF). Its purpose will be to investigate inertial confinement fusion with light of 10.6-μm wavelength. Most of the optics comprising Antares will be reflectors and, for many reasons, copper is the material of choice. The mirrors range in size from 2.5 cm in diameter to 45 cm in diameter.

The copper must be very pure to help maximize damage threshold, making plated copper an attractive solution. The final mirror should be very stable, i.e., characterized by very low microcreep. This makes an alloy a more suitable substrate candidate than pure copper. For Antares, all of the smaller mirrors will be made of copper plated onto an aluminum-bronze substrate, and all of the larger mirrors will be made of copper plated onto aluminum alloy 2124. This paper discusses how this design was arrived at and the methods used to assure a satisfactory mirror.

Introduction

The Los Alamos Scientific Laboratory is engaged in experiments designed to determine the feasibility of laser-driven inertial confinement fusion. At LASL, the emphasis is on very short-pulse (<1 ns) CO₂ lasers operating at a wavelength of 10.6 μm. LASL currently has two operational laser fusion systems, the 1.0-kJ Gemini system, and the 10-kJ Helios system. The 100-kJ Antares system is under construction and scheduled for operation late in 1983. Antares has the goal of demonstrating scientific breakeven, a very significant milestone in the national laser fusion program. Scientific breakeven means that the energy released by the fusion reaction equals or exceeds the energy delivered by the laser.

Antares uses 432 mirrors of roughly trapezoidal shape that measure approximately 0.3 by 0.4 m. Of these, 72 are off-axis parabolas, 72 are spherical, and the remainder are flats of varying geometries. In addition to these large mirrors, Antares will use approximately 1000 small mirrors, typically 10 cm in diameter.

Large Mirror Design

Basic Design

The basic design of a representative large Antares mirror is shown in Fig. 1. It consists of an aluminum alloy substrate electroplated on one face with pure copper. After plating, the copper is trimmed, then single-point diamond turned (SPDT) for final finish and figure.

Mirror weight is a major factor in establishing the basic design. It is most desirable to keep weight moderate so that natural frequencies of the mirror systems will be well above expected input frequencies yet not require massive support structures.

Solid aluminum substrates meet the weight criteria and are of considerably lower cost with fewer unknown problems than any light-weight-mirror concept.

Copper surfaces are dictated because of the high damage threshold required. Copper plating is preferred over any other cladding approach (such as explosive bonding) because of the metallurgical cleanliness of the copper, its reliability, and its low cost. A finished copper plate thickness of 1.3 mm was established to allow several refinishings of the mirrors by SPDT.

A disadvantage of this basic design is the inherent bimetallic distortion with changes in temperature when mirrors are plated on only one side.
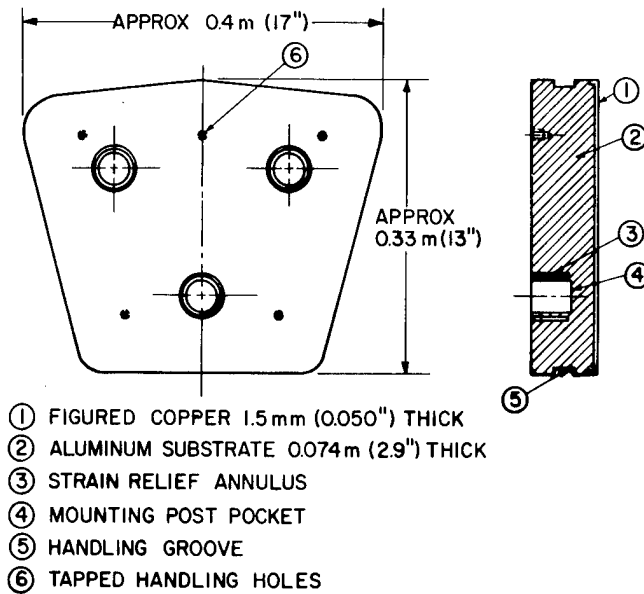
Fig. 1. Representative design of large Antares mirror.

Bimetallic Effect. Figure 2 illustrates the bimetallic effect inherent in copper-plated aluminum mirrors.* If the mirror is flat at an initial temperature of T_0 and is raised in temperature by T, the aluminum tries to expand more than the copper. The copper tries to restrain the aluminum, and the net result is that the mirror warps to a roughly spherical figure. The tabular data represents analytical results. The analysis has been confirmed qualitatively by preliminary experiments at LASL. Further experiments to confirm the results quantitatively are underway. The Antares mirror environments will be held within about 1°C of set point. The resultant drift in large-mirror figure is tolerable since focus error falls within the error budget.

Fig. 2. Bi-metallic effect in Cu/Al mirrors.
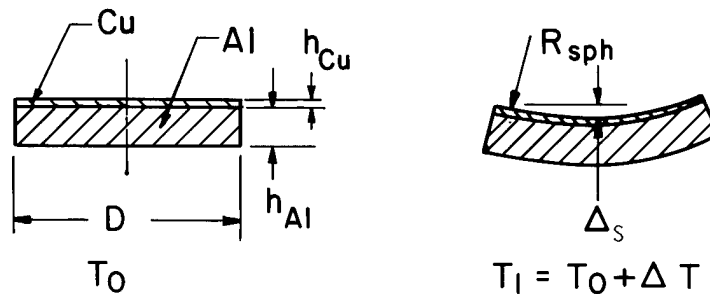
D		h_{Al}		h_{Cu}		Δ_s		$R(\Delta T=1^oC)$
(m)	(in.)	(mm)	(in.)	(mm)	(in.)	(nm/^oC)	(μ in./^oC)	(m)
0.10	4	16	0.63	2.3	0.089	430	17.1	2970.
0.10	4	16	0.63	0.94	0.037	250	9.9	5130.
0.10	4	16	0.63	0.64	0.025	180	7.2	7060.
0.10	4	16	0.63	0.33	0.013	86	3.4	14900.
0.30	12	74	2.9	1.3	0.050	200	7.9	57900.
0.30	12	74	2.9	0.51	0.020	86	3.4	134000.
0.30	12	74	2.9	0.25	0.010	46	1.8	254000.

Substrate Alloy. 2124 aluminum alloy was selected for the substrate material. Several aluminum alloys were considered. Cast alloys were rejected in favor of wrought material because the inherent porosity, microcracks, inclusions, and segregate in castings result in unpredictable adhesion of the copper plate. The best wrought alloys are 6061, 5456,

*The bimetallic effect analysis was done by Dr. Jerry Stoneking of the University of Tennessee for LASL.

and 2124. 6061 (T6) has been the traditional substrate material in the LASL laser program prior to Antares. It has several advantages but it is not as stable dimensionally as 5456 or 2124 and the metallurgical cleanliness of commercial 6061 plate varies widely. 5456 (H321) is attractive, especially if welded. Clean 5456 is difficult to obtain and it has a relatively low yield strength. 2124 is a very stable, isotropic, metallurgically clean, high-strength alloy. It is basically a low-iron, low-silicon, closely controlled version of 2024. It plates well and because it is clean, it has few foci for poor adhesion of the plating. The major problem with 2124 is availability. It is not normally stocked by metal suppliers. It must either be procured in mill runs of 7000 lbs or more, or found as excess material. We have, so far, filled our program needs from federal excess property stocks. In addition, we have found excess material at commercial supply houses. The 2124 is procured in T851 condition, certified to federal specification QQ-A-00250/29.

After rough machining, the substrate blanks are given an additional stabilizing heat treatment by soaking at 525-575°F for 5 hours, then still-air cooled.* This heat treatment over-ages the material, stress-relieves it, and softens it slightly from the T851 condition.

Copper Plating. The basic requirements for the copper facing on the mirrors are: a) High thermal conductivity; b) Freedom from inclusions that can act as foci for laser damage and impair final surface finishing; c) high reflectivity; d) machinable by SPDT; and e) complete adhesion to the aluminum. High-quality electroplating satisfies all these requirements. In addition, copper plating is a well-developed commercial process and is of relatively low cost. Considerable favorable experience has been gathered by LASL with the process and the product.

The Antares large-mirror substrates are being plated by Metal Surfaces, Incorporated, Bell Gardens, CA. They use a standard double-zincating process followed by a standard copper-cyanide strike. After striking, the copper is checked for adhesion by vigorously wire brushing the surface. The parts are then masked and shielded and electroplated with a process perfected by Union Carbide Corporation, Y-12 Plant, Oak Ridge, TN. Careful control of the chemistry, temperature, and cleanliness of the various baths is maintained. Circulation of the plating bath is critical. Filtering of the plating bath is critical so that there are few, if any, particles in the bath that can lodge on the surface and remain as inclusions or serve as foci of nodules. The result is a bright, fine-grained, dense plate with low-residual stress, few nodules, and minimal edge and corner buildup. The zincating and copper strike takes less than 30 minutes. The electroplate is built up to approximately 1.5 mm in about 40 hours.

Small-Mirror Design

Basic Design

The basic design for a representataive small mirror for Antares is shown in Fig. 3. It consists of a copper alloy substrate electroplated on one face with pure copper. After plating, the copper is trimmed then the substrate is figured by conventional optical techniques.

① ALUMINUM BRONZE SUBSTRATE
② FIGURED COPPER PLATE
③ TAPPED HOLES
④ PILOT HOLE
⑤ PART NO. AND SERIAL NO.
⑥ INDEX MARK
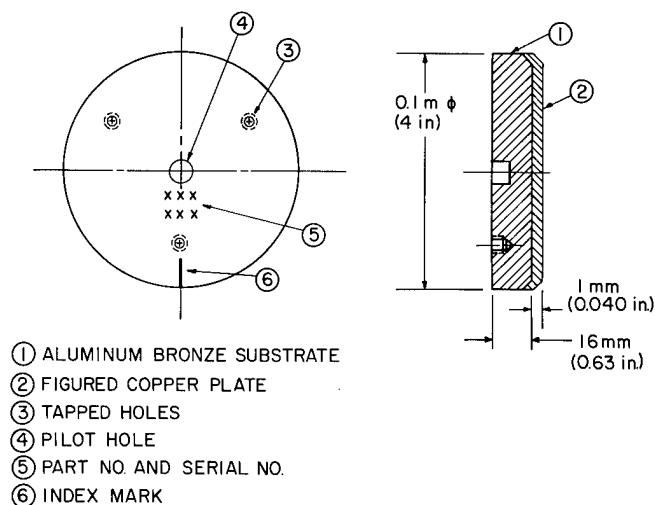
Fig. 3. Typical small Antares mirror.

*Heat treatment recommended by Alcoa.

Substrate. The bimetallic effect on small mirrors (Fig. 2) indicates that the possible figure error introduced with copper-plated aluminum substrates is unacceptable. This effect can be reduced or eliminated by selecting a substrate material that matches copper in thermal expansion. A wrought aluminum bronze was selected. The particular alloy depends on availability. Copper 613,* copper 614,* Ampco 8 alloy, or Ambroloy 614 are all essentially the same and are acceptable. All have 6 to 8% aluminum, 1.5 to 3.5% iron, some minor alloying elements, and the balance copper. All have relatively high yield strengths of around 35,000 psi. All machine readily. The most commonly available alloy is Ampco 8 alloy.

Substrate material is obtained as hot-rolled and annealed plate. After rough machining, the substrates are stabilized by heat treating at 725-775°F for 1 hour, then cooled in still air.

Aluminum bronze was selected because it is readily available, its thermal expansion closely matches that of copper, and it appears to be dimensionally stable. Other coppers were considered and rejected. Copper 102 (OFHC) was rejected because of dimensional instability and low yield strength. Copper 104 and copper 150 were satisfactory from a stability viewpoint, but were available only as cast billets. Subsequent forging made them too expensive in both time and dollars. Aluminum bronze is of reasonable cost, running $3 to $4 per pound.

Copper Plating

The substrates are plated on one side with pure copper. The process is basically to copper-cyanide strike all over, check for adhesion, mask, shield, and electroplate. Adhesion is checked by baking the substrate for 2 hours at 375°F, waiting 24 hours, then visually checking the copper strike for blisters. The electroplating is done with the same process as for the aluminum substrates. Plating thickness is approximately 1.0 mm to allow for several refinishings.

Mirror Production

Large-Mirror Production

Aluminum substrates are in production now. The process for production is as follows:

1. Procure material (By LASL).
2. Machine per Fig. 4 (By commercial machine shop).
   a. Saw blanks.
   b. Rough machine for thickness.
      Profile mill periphery.
      Trepan and rough bore pockets.
      Drill and tap holes.
   c. Stabilize heat treatment.
   d. Finish machine faces and bores.
   e. Inspect.
      Engrave PN and SN.
   f. Clean and ship to plater.
3. Plate per Fig. 5 (By Metal Surfaces, Inc. under contract to Union Carbide Corporation, Y-12 Plant, Oak Ridge, TN).
   a. Zincate and copper strike.
   b. Inspect for adhesion.
   c. Plate.
   d. Inspect and ship back to Machine Shop.
4. Trim per Fig. 6 (By machine shop of item 2).
   a. Machine.
   b. Inspect.
   c. Clean and ship to Union Carbide Corp.
5. Optically finish per Fig. 7 (By Union Carbide Corporation, Y-12 Plant, Oak Ridge, TN).
   a. Single-point diamond turn copper.
   b. Inspect.
   c. Clean, package, and ship to LASL.

Small-Mirror Production

Prototype mirrors are being produced at present. Production mirrors will be produced by the following process:

---

*Copper Development Assoc. designations.
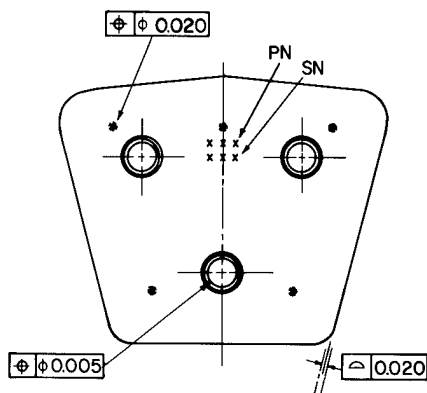
Fig. 4. Substrate machining.
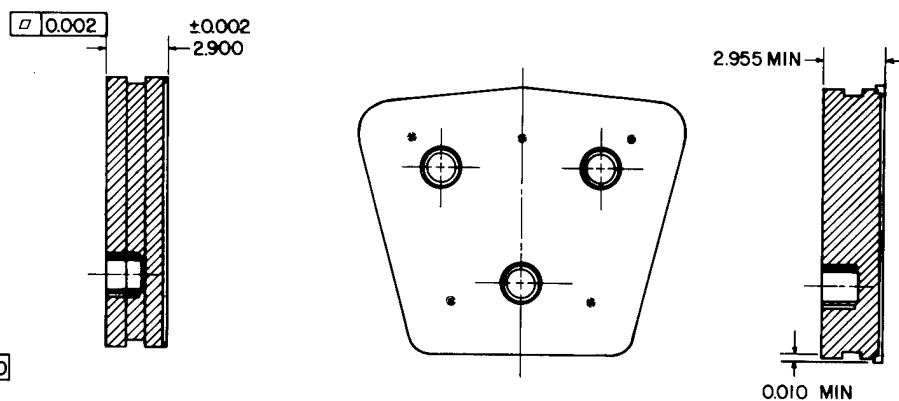
Fig. 5. Substrate plating.
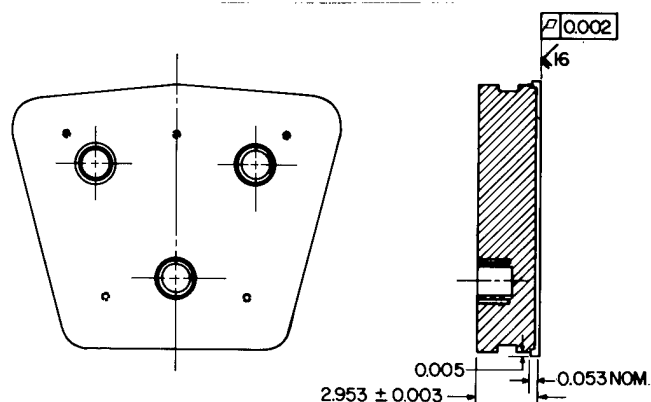
Fig. 6. Substrate trimming (after plating).
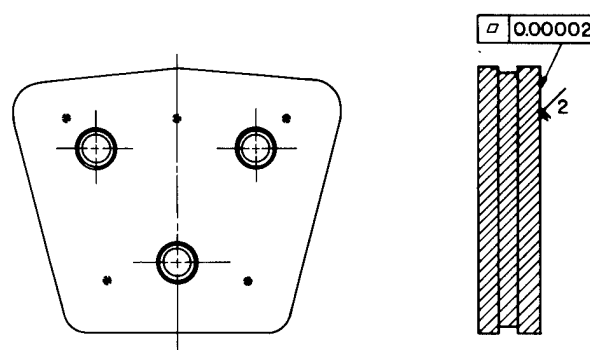
Fig. 7. Mirror Figuring.

1. Procure material (By Machine Shop).

2. Machine substrates per Fig. 8 (By Machine Shop).
    a. Rough machine.
    b. Heat treat.
    c. Finish machine.
    d. Inspect.
    e. Engrave PN and SN.
    f. Clean and ship to plater.
3. Plate per Fig. 9.*
    a. Copper strike.
    b. Check for adhesion.
    c. Plate.
    d. Inspect.
    e. Clean and ship.
4. Trim per Fig. 10 (By Machine Shop).
    a. Trim.
    b. Inspect.
    c. Clean and ship to optician.
5. Finish optical surface per Fig. 11 (By conventional optician).
    a. Grind, polish, and figure.
    b. Inspect.
    c. Clean, package, and ship.

Summary

Antares mirror design and fabrication is based on consideration of many factors. LASL has selected what appears to be the optimum materials for substrates, the best plating procedures, and the most practical optical finishing methods.

*Plating to date has been done by Electronics Metal Finishing Corporation, Oak Ridge, TN.

±0.005
4.000 in.

±0.002
0.625 in.

⊡ 0.001

DYE PENETRANT INSPECT

Fig. 8. Substrate machining.

PLATE PER LASL SPEC.

0.665 in. MIN.

Fig. 9. Substrate plating.

+0.002
3.995 in.

±0.001
0.662

⊡ 0.0005
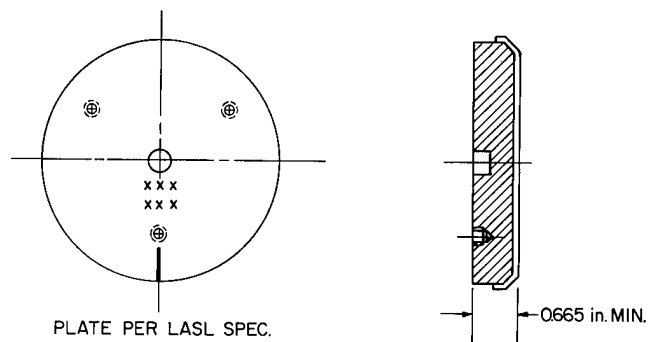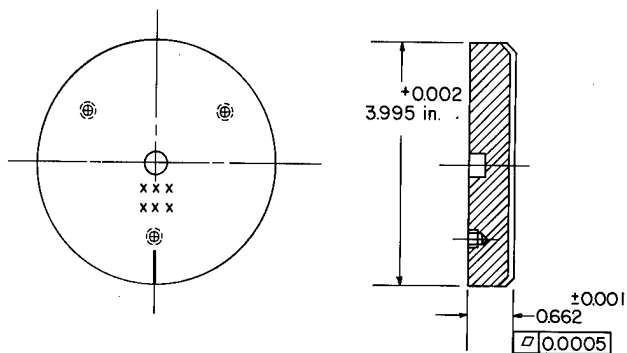
Fig. 10. Plated substrate trimming.

10 mm

CLEAR
APERTURE

FIGURED SURFACE
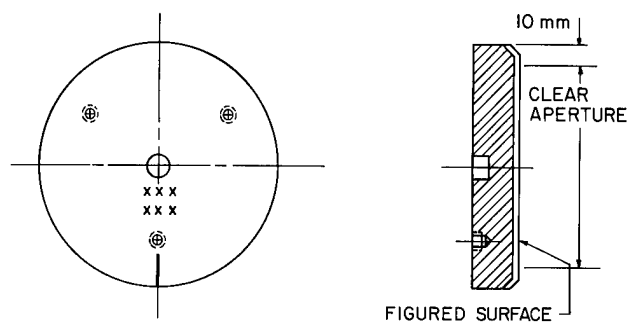
FLATNESS: λ/4 PEAK TO VALLEY
λ = 633 nm
SURFACE QUALITY: 60/40 per MIL-O-13830

Fig. 11. Mirror figuring.

APPLICATION OF SPUTTERING TO THE REPAIR OF METAL MIRRORS

Richard Esposito and Graham Flint
International Laser Systems, Inc.
Box 9316 International Airport
Albuquerque, New Mexico 87119

Abstract

Typical mirrors used in high power gas laser applications are of molybdenum construction and employ thin faceplates which overlay a multitude of narrow gauge cooling channels. Since such mirrors are extremely costly, it is desirable that they be refurbished rather than replaced when their surfaces are burned by laser radiation. However, the faceplates are quite thin (0.010 - 0.020 inch); allowing only a limited number of refurbishments by straightforward grinding and polishing techniques. To overcome this lifetime restriction, we have adopted a refurbishment procedure which employs the sputtering of pure molybdenum upon the damaged surface prior to grinding. In this manner it has become possible to resurface mirrors without reduction in structural integrity. Described are details of the techniques currently employed together with the precautions necessary for the production of defect free sputtered coatings.

Introduction

The principal aim of this work was to develop techniques and procedures for the realization of optically and structurally sound sputtered molybdenum films on molybdenum water cooled mirrors; thereby providing an expedient and cost effective method for the refurbishment of such mirrors.

At this time several operational mirrors have been successfully sputtered, polished and coated. We are approaching the stage where totally defect-free sputtered films can be produced. Of prime concern in producing such coatings are the cleanliness of the mirror and of the vacuum system prior to sputtering; a true clean room environment being highly desirable in this regard. Also, during sputtering, consistent results require that all sputtering parameters be controlled and monitored continuously.

Preliminary Studies

The initial phase of this program addressed four basic areas. In the order in which they are discussed subsequently these areas comprise optimization of deposition parameters, the influence of R.F. biasing on film growth and film stress, R.F. etching and pre-sputtering, and the identification of contaminants.

Optimization of Deposition Parameters

R.F. Biasing has a number of effects on sputtered films. One is its use as a film cleaning process.* In sputtering, because of the relatively high gas pressure involved, large amounts of gas can be incorporated into deposited films. To help eliminate this gas entrapment a bias or low negative charge can be put on the substrate. As the film is deposited, it is lightly scrubbed by ions which remove the loosely held gas atoms without disturbing the adherent sputtered film. A film of higher density and better adherence results.

The purity of sputtered films can, in some cases, be improved by the use of an R.F. bias. This improvement is based upon the preferential removal during resputtering of most impurities. This technique is particularly suited to metals such as molybdenum where the oxide bond is weaker than the metallic bond.

Biasing also influences the structure of the deposited film. From tests conducted in this laboratory it was found that a bias of about 4.7%, used in conjunction with an argon pressure of 8μ, will produce an amorphous molybdenum film. Electron microscope photographs of such a film are shown in Figure 1. Removal of the bias will produce the dendritic structure shown in Figure 2. The amorphous structure is more desirable in that it produces a mirror having a lower level of scattering.

The compressive stress in a molybdenum film increases with the amount of bias. This relationship is shown in Figure 3. Here the deposition rate was approximately 1.0 microns per hour.

R.F. Etching

R.F. sputter etching, sometimes called back-sputtering, is used to clean and prepare substrates prior to film sputtering. This is accomplished by electrically reversing the R.F. power flow. A shutter is placed between the target and substrate, thereby preventing contamination of the target by impurities which are sputtered off the substrate. Typical Nomarski photographs taken before and after etching of a 1.5 inch O.D. molydbenum substrate are shown in Figure 4. In this series of tests the etching parameters were held

*The Basics of Sputtering, Materials Research Corporation, Orangeburg, New York.

constant; etching times ranging from one to six minutes. As can be seen from an examination of these photographs, structural change becomes apparent after an etch time of five to six minutes.

Pre-sputtering is a means by which the target is cleaned and prepared prior to sputtering. This is accomplished in a similar manner to substrate etching, i.e., a shutter is actuated to prevent impurities from the target reaching the substrate, and has been used as a standard procedure throughout the program.

Identification of Contaminants

The primary problem encountered with sputtered Molybdenum films has been particulates that appear on the mirror surface after sputtering. To identify these contaminants, several samples were examined on the Scanning Electron Microscope. Predominant contaminants were found to be comprised of silicon, phosphorus, chlorine, potassium and calcium (Figure 5). Since these elements are common to dust particles, it is believed that this type of contaminant is air borne; entering the system prior to closing of the vacuum chamber. A second type of contaminant, which is easily seen under microscopic examination, but which cannot be detected as a foreign material by the Scanning Electron Microscope, is thought to be molybdenum carbide, molybdenum nitride, or molybdenum oxide. The form of this type of inclusion is shown in Figure 6. Unfortunately, the analytic equipment employed is not capable of detecting elements below atomic number 12. This makes it impossible to analyze organics and alkaline salts. Examination of the target surface reveals a fine dendrite structure. Analysis of this structure shows its content to be mainly molybdenum, with a small amount of silicon, and traces of nickel. Material Research Corporation, the manufacturer of the target, indicates that this is a growth inherent in the target material. The dendritic structure appears in refractory metal targets and is especially noticeable on targets used with high bias backsputtering.

Current Procedures

From the initial study has evolved the presently employed technique. For convenience we will divide our discussion of the technique into three topics; these being surface preparation, sputtering parameters, and electrostatic masking.

Surface Preparation

The mirrors submitted to this laboratory for refurbishment have usually undergone some degree of catastrophic failure. Typically, they will retain a high reflectivity coating which has been burned and/or damaged in localized regions. Thus, a first step in surface preparation usually requires the removal of the coating residue.

The most common coating (Cr/Au/ThF$_4$, ZnS) has been removed successfully by the following multistep process. First, the overlying dielectric layers are removed with concentrated hydrochloric acid applied at room temperature. Second, the surface is wetted with mercury, thereby removing the gold by amalgamation. Finally, the chromium binder layer is removed by the use of a mixture of chromium powder and hydrochloric acid (the chromium acts as a catalyst).

Having exposed the molybdenum substrate, the surface can be examined to determine the degree of penetration, if any, of the remaining damage. From this examination the necessary thickness of molybdenum sputtering can be established.

Prior to sputtering, the mirror surface should be polished to the extent that it contains no visible inclusions. The mirror is then cleaned in the following manner:

Step I   - Apply a protective film of strippable vinyl coating on mirror surface.

Step II   - Clean edges and back of mirror with scouring cleanser then flush with de-ionized water.

Step III - Remove the vinyl coating with Scotch tape.

Step IV   - Place mirror in vapor degreaser containing trichlorethylene for twenty minutes.

Step V   - Remove mirror from trichlorethylene and flush with methanol. Blow off with water pumped nitrogen.

Step VI   - Place mirror in a vacuum oven and pump chamber down. The oven should be set at a temperature consistent with the construction of the mirror, i.e., water cooled, electro-plated, etc.

Step VII - Remove mirror from vacuum oven and inspect under a blue light. If no staining appears, flush with methanol, blow off with nitrogen and place in vacuum chamber for coating. If staining does appear, Steps IV through VII are repeated.

Sputtering Parameters

The cleaned mirror is placed in the vacuum system, blown off with ionized nitrogen gas, and evacuated to a base pressure of 5×10^{-7} torr. Sputtering is then performed in the following manner:

Step I   - Close throttle valve and backfill with argon gas to a pressure of 8 microns. The argon
            is bled through a gettering furnace, at a temperature of 820°C. The gettering removes
            residual impurities, such as oxygen or water vapor.

Step II   - With shutter closed and system set in etch mode, the mirror is etched for three minutes.
            For the MRC system currently used, the R.F. power is set to 600 watts incident with less
            than 3 watts reflected. The R.F. peak voltage is set at 900 volts.

Step III - With the shutter closed and the system set in the R.F. bias mode, the target is presputtered
            for fifteen minutes. For this stage the R.F. power is set to 1200 watts incident with less
            than 5 watts reflected. The R.F. peak voltage on the target is in the neighbourhood of
            1500 volts. The R.F. peak voltage on the mirror is approximately 70 volts.

Step IV   - With the shutter open, and the system set in the R.F. bias mode, the target is then raised
            to within three inches of mirror. The R.F. power is set at 1200 watts incident with less
            than 5 watts reflected. The R.F. peak voltage on the target is set at 1500 volts. The R.F.
            peak voltage on the mirror is about 70 volts. This gives a bias of approximately 4.7%.
            Sputtering then proceeds. For the conditions described a deposition rate of about 1.0µ
            an hour can be expected.

Other general procedures followed are aimed at the minimization of defects caused by stray particulate
matter. To eliminate "film flaking" from chamber walls and fixturing, aluminum foil is used to cover as much
of the stainless steel as possible. There are two reasons for the use of foil. First, sputtered molybdenum
adheres far better to aluminum foil than it does to stainless. Second, the shrouds can be changed both easily
and quickly. To reduce the probability of particulates falling from the target and/or the shutter during
sputtering, the conventional anode-cathode geometry has been reversed; thereby sputtering upon a downward-
looking surface. An ideal approach, which has not yet been tried, may involve horizontal sputtering. Finally,
a laminar flow hood has been installed around the system. Collectively, these precautions have proven most
successful.

Electrostatic Masking

When sputtering layers of several microns, the sputtered thickness variations result in significant changes
in the surface figure. Specifically, those areas adjacent to edges (high field regions) receive less material.
For coatings in the 10 micron region this effect becomes unacceptable. It has, therefore, become the practice
of this laboratory to use electrostatic shielding whereby the surface is extended artificially. In this
manner the non uniformities in thickness are reduced to a negligible level.

In practice, reiterative sputtering has become a workable procedure. First the mirror is sputtered, then
polished. If the desired figure or surface quality is not obtained, the mirror is then resputtered. This
polishing/sputtering sequence is then repeated until the desired specifications are met.
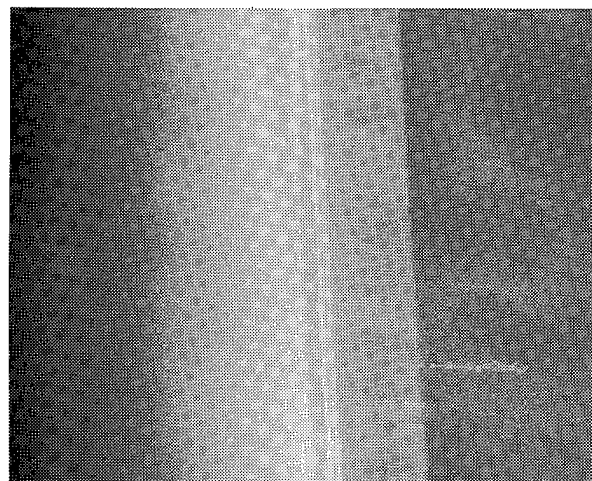
Fig. 1. Molybdenum deposited with 4.67% bias
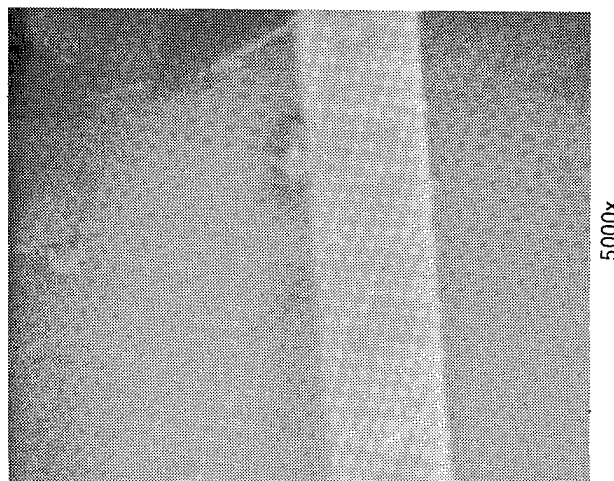
Fig. 2. Molybdenum deposited with no bias
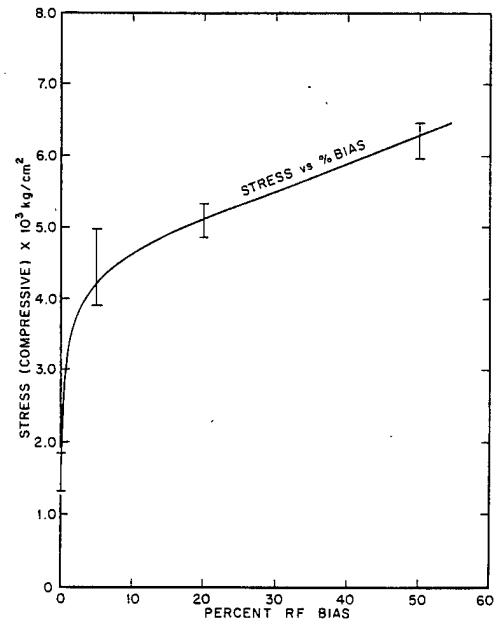
Figure 3. Stress vs % bias in a molybdenum film
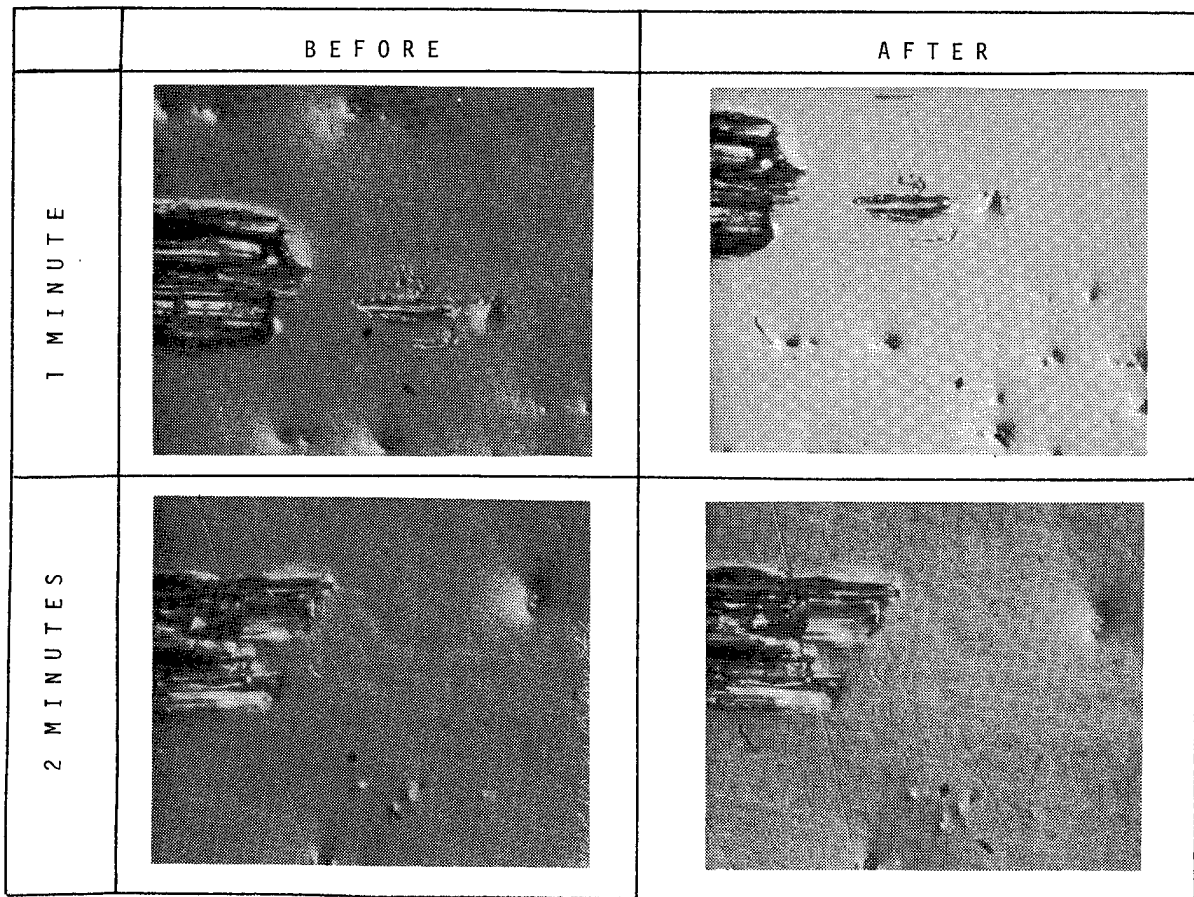
Figure 4. Influence of etch time on molybdenum samples. (500x)

(Cont'd)
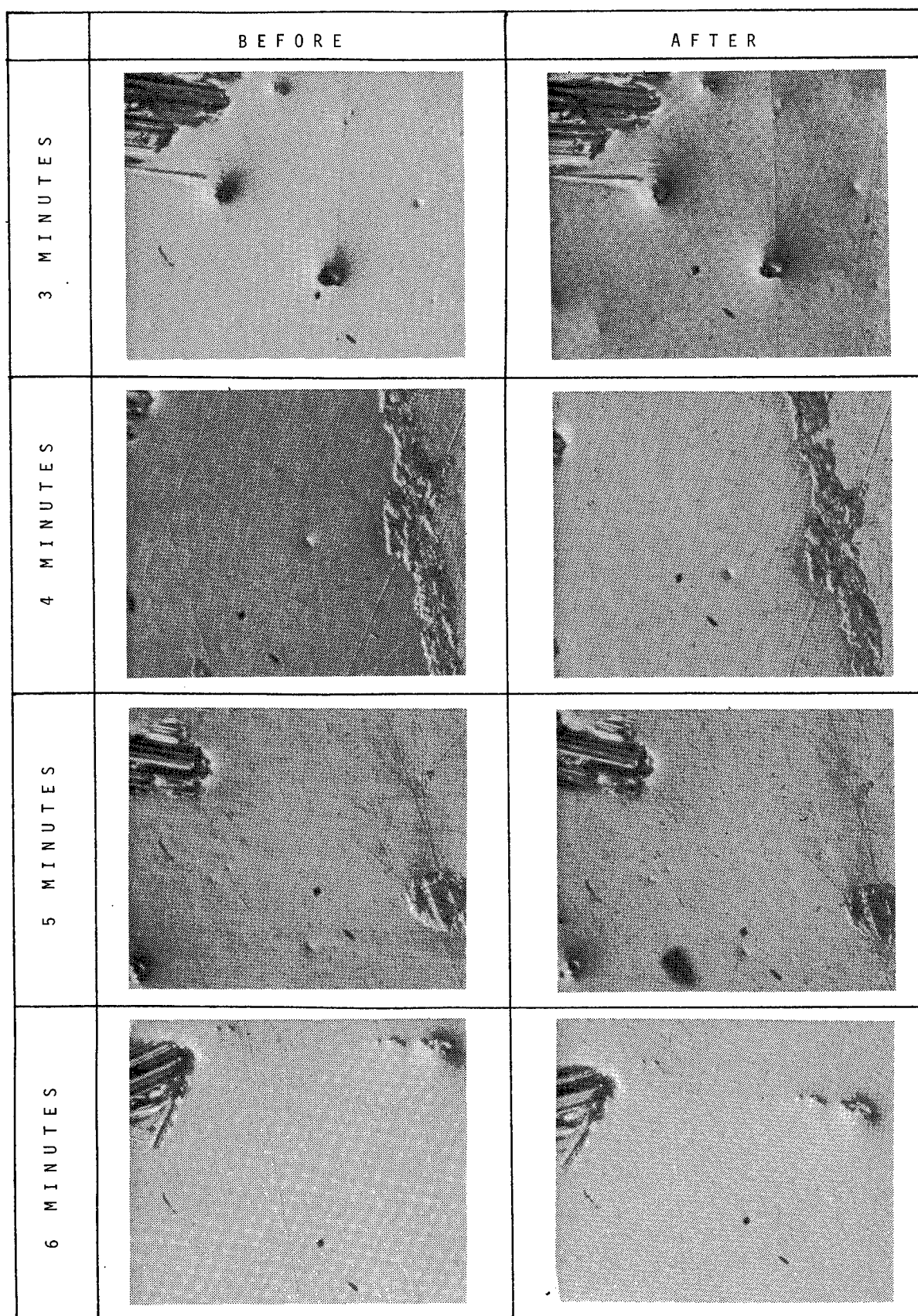
Figure 4 (Cont'd). Influence of etch time on molybdenum samples. (500x)
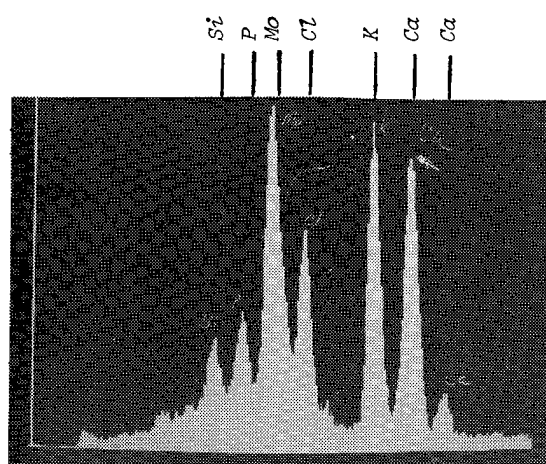
Figure 5. Element analysis by S.E.M.
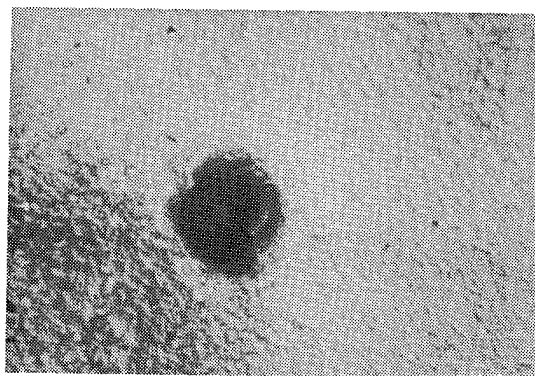
Figure 6. Unidentified surface defect. (500x)

NONLINEAR HOLOGRAPHIC GRATINGS FOR HIGH ENERGY LASER BEAM SAMPLING*

Dr. John M. Fitts
Hughes Aircraft Company
Culver City, California 90230

Abstract

Nonlinear holographic gratings developed for high energy laser systems have led to new possibilities in large, lightweight primary mirror designs. The beam sampling technique has made the concept of local loop adaptive optics correction much more attractive because all optical distortions including those in the primary mirror can be corrected.

Introduction

Nonlinear holographic gratings have been fabricated and investigated in detail at both the component and systems level at Hughes Aircraft Company under ARPA funded and RADC monitored contracts. The gratings are in general nonlinear in that the grating lines can be curved and have nonuniform spacing resulting in the diffracted orders having different optical power as well as other geometrically different characteristics from the 0th order. The gratings are generated holographically by first exposing a photo-resist coating on a reflecting mirror substrate to a desired interference pattern generated by a Krypton laser and associated construction optics as is illustrated in Figure 1. This forms a photo-resist mask for ion machine illumination which results in the nonlinear grating lines being etched into the reflective substrates. This last step is the key to making holographic gratings suitable for high energy laser applications. Hughes has demonstrated the practicality and feasibility of generating these gratings through novel construction optics, and laser beam stabilization techniques.

Beam Sampling

One of the most significant applications of the holographic gratings for high energy laser systems is in the area of beam sampling – particularly at the last optical element of an optical train. For example, a nonlinear holographic grating can be constructed on a primary mirror of a gimballed telescope pointing and laser transmitting system in a straightforward fashion as is illustrated in Figure 2. Due to the focusing property of the diffracted beam sample, a wavefront sensor can be conveniently located within the pointer. An extensive investigation has shown the effectiveness of using this approach in an auto-alignment system to measure the full aperture and consequently true tilt (i.e., line-of-sight direction) of a laser beam as it exits the system. A further investigation has shown that a local loop adaptive optics system can be used effectively to correct for higher order phase aberrations from the phase measurements associated with the primary mirror holographic grating sample and a deformable mirror located somewhere in the optical train. As an example of the effectiveness of the sampling technique, consider the spot diagrams in Figure 3 of the main beam and sampled beam for a particular design where the main beam has 3.5 waves of comma. Note that except for the magnification ratio, the spot diagrams are almost exactly the same and thus would allow for local loop correction.

Another property of holographic gratings is that their quality is much superior to conventional ruled gratings as is illustrated in Figure 4. As a result of this property, the optical sampling efficiencies of the grating have been found to be remarkably predictable. By tailoring the grove shape, a wide range of optical efficiencies can be obtained as indicated in Figure 5 for a trapezoidal profile. Figures 6 and 7 illustrate the generation of two different trapezoidal grating profiles for low efficiency and high efficiency sampling, respectively.

Primary Mirror Distortions

One unexpected property of holographic gratings may have a major impact on the development of large primary mirrors. A preliminary investigation has shown that for certain primary mirror grating designs, out of plane distortions in the primary mirror itself will be effectively reproduced in the beam sample and thus compensated for in a local loop adaptive optics system. This property is true whether the distortions occurred after the gratings were generated in the primary mirror or before the gratings were generated. Consider a primary mirror in which a major out-of-phane distortion due to vibrations, sag,

---

thermal heating, etc., occurred after holographic grating construction. As indicated in Figure 8, for a particular example, an outgoing wavefront with as much as ten times diffraction limited aberration can be almost totally corrected with proper use of the holographic sample in a local loop adaptive optics system. This property does not hold true for in-plane distortion such as that from thermal loading which results in line spreading. However, this phenomena is easily predicted and compensated for and has not been a problem in high energy laser system design. Inexpensive, lightweight, large mirror design may be now possible through the use of holographic gratings.

The results of Figure 8 and 9 were obtained from extensive ray trace computer codes. However one intuitive explanation of the phenomena centers on the treatment of the primary mirror holographic grating as a transmissive phase hologram and a primary mirror reflective surface combination as is illustrated in Figure 10. Note that the playback of a transmissive phase hologram is undistorted to first order, even though the hologram is bent. The playback wavefront, however, will have mapped into its reflection the distortions of the primary mirror, as is illustrated in Figure 10. Thus, except for a scale factor, the holographic sample beam will have essentially the same distortion as the 0th order outgoing beam - a property which allows for local loop correction of distortions in the primary mirror.

Conclusions

In conclusion, nonlinear holographic gratings opens up new design approaches to more reliable, maintainable, and durable high energy laser systems. This is because all optical elements including the primary mirror can be practically compensated for with a local loop adaptive optics subsystem and a holographic grating beam sampler.

- **ASPHERIC ELEMENT CORRECTS RESIDUAL SPHERICAL ABERRATION**
  - **CONSTRUCTION WAVELENGTH = 0.4416 μM**
  - **HOLOGRAPHIC FINGES ARE OF HIGH STABILITY AND QUALITY DUE TO EFFECTIVE POINT SOURCES**
  - **FRINGE PATTERN IS GENERATED ON PHOTORESIST LAYER**
  - **MIRROR IS ETCHED WITH ION BEAM TRANSMITTED THROUGH PHOTORESIST LAYER**
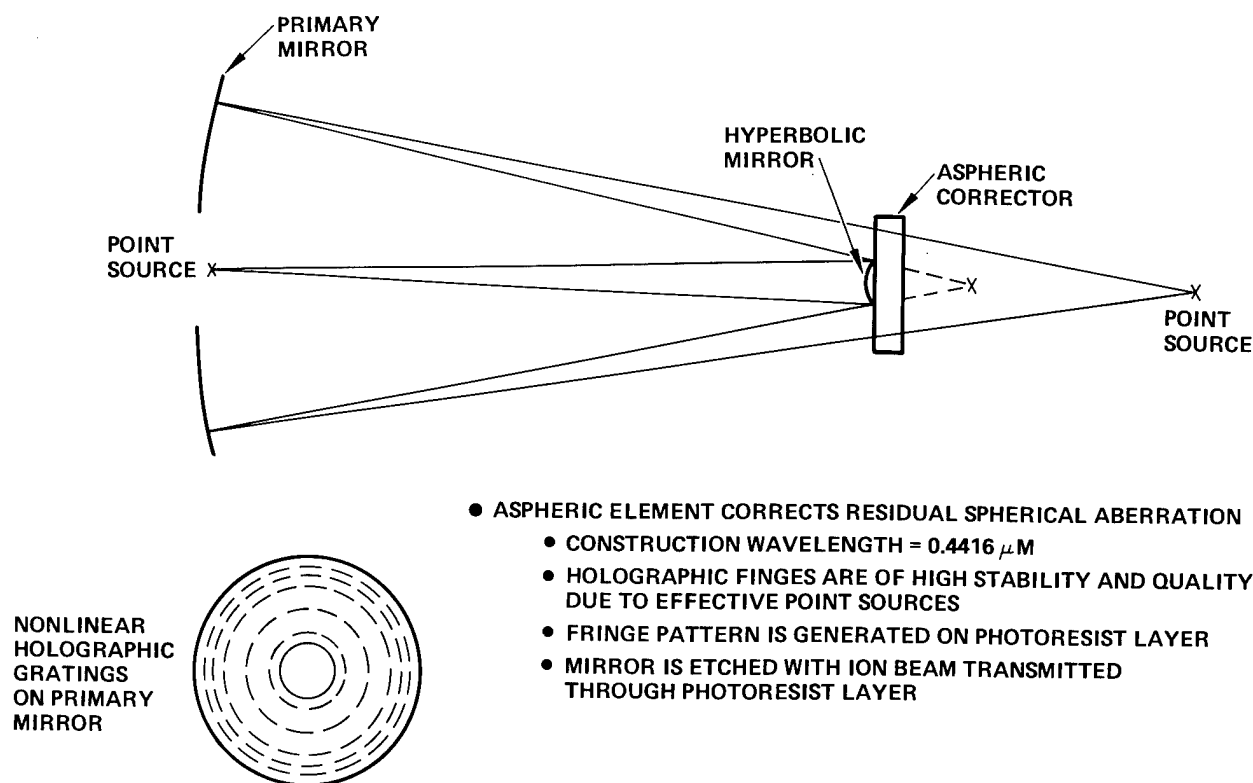
Fig. 1. Hologram construction optics.

- FULL APERTURE SAMPLING
- SMALL STABLE REFERENCE PACKAGE
- MINIMAL SIZE AND WEIGHT
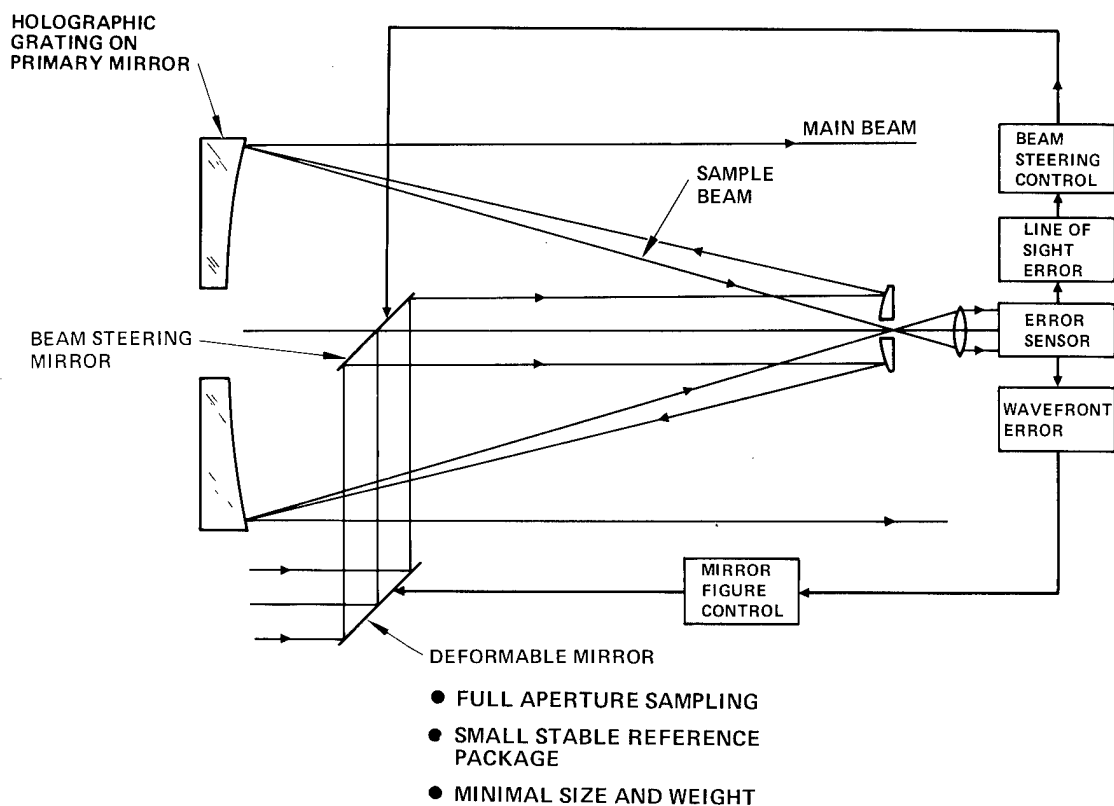
Fig. 2. Holographic grating beam sampling can avoid problems of conventional techniques.

- 3.5 WAVES COMMA ON MAIN BEAM

SPOT DIAGRAM OF MAIN BEAM

8.3 μR

SPOT DIAGRAM OF SAMPLED BEAM

293 μR
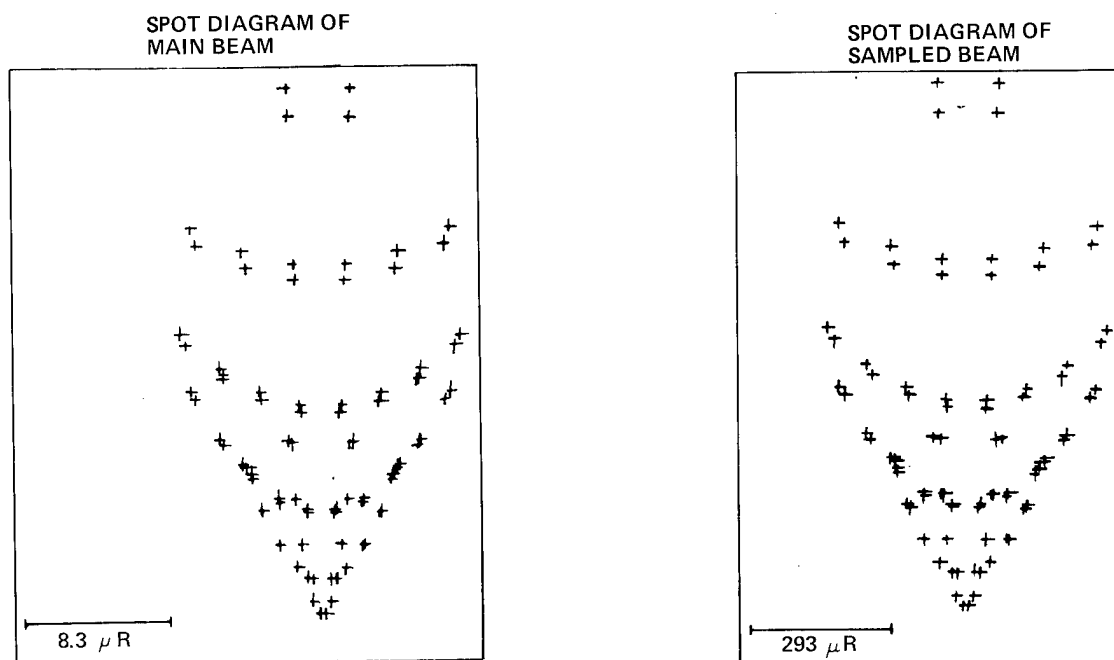
- MAIN BEAM AND SAMPLE BEAM MATCH AFTER SCALING FOR MAGINIFICATION RATION

Fig. 3. The holographic beam sample contains the same phase information as the outgoing beam.

RULED GRATING
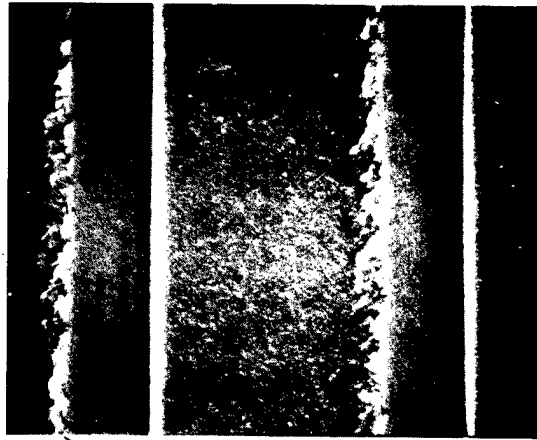
"BURR"   TOP VIEW
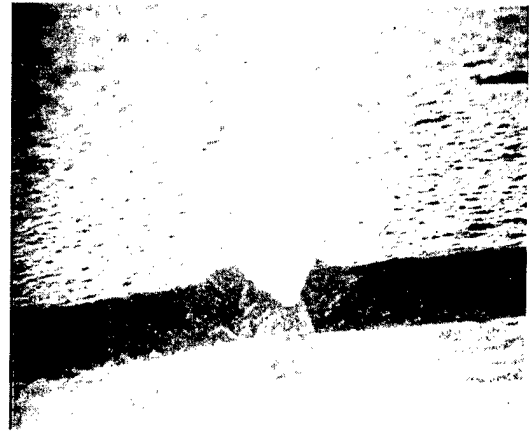
EDGE VIEW

HOLOGRAPHIC GRATING
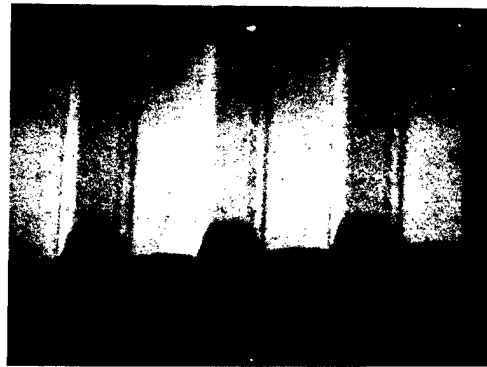
Fig. 4. Quality of holographic grating is much superior to conventional ruled grating.
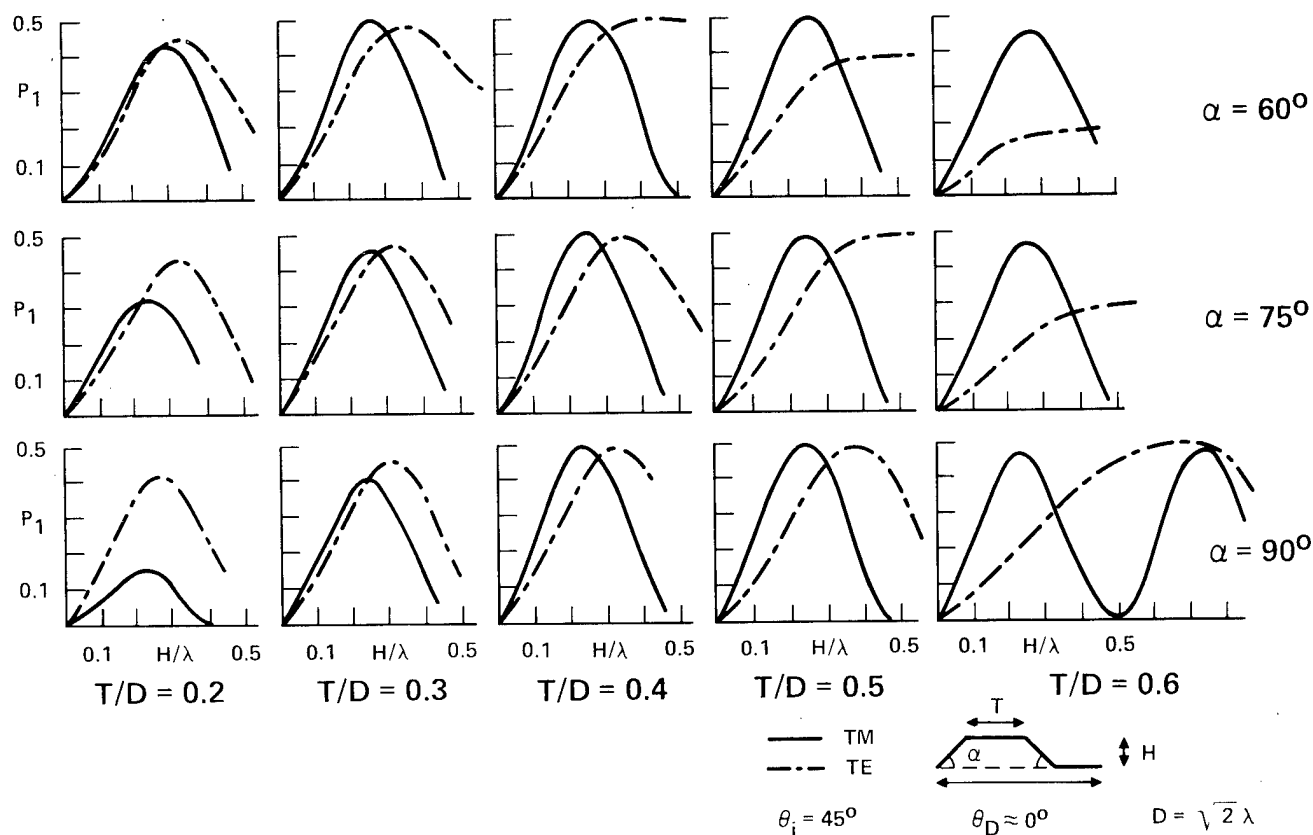
Fig. 5. Diffraction efficiency design curves: beam sampler or mixing axicon.

1.4 μM PEAK-TO-TROUGH HEIGHT
25 PERCENT DUTY CYCLE

PHOTORESIST GRATING

4.84 μM PERIOD
RESIST TOP
INTACT

ETCHED GRATINGS

0.2 μM PEAK-TO-TROUGH HEIGHT
34 PERCENT DUTY CYCLE
60 DEGREE ANGLE
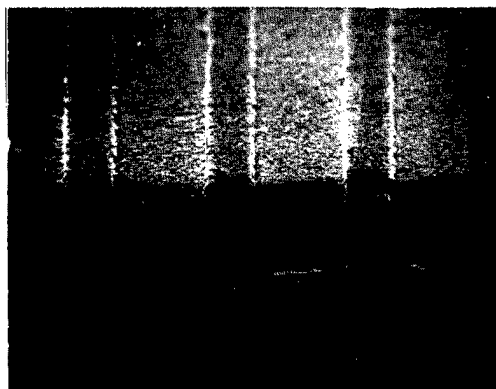
ETCHED PHOTORESIST REMOVED

Fig. 6. Ion-etched low efficiency gratings.
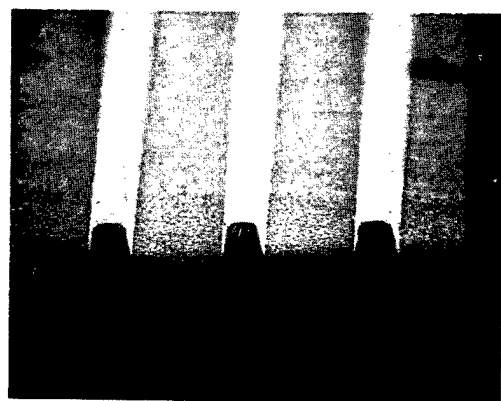
1.30 µM PEAK-TO-
TROUGH HEIGHT
20 PERCENT DUTY
CYCLE
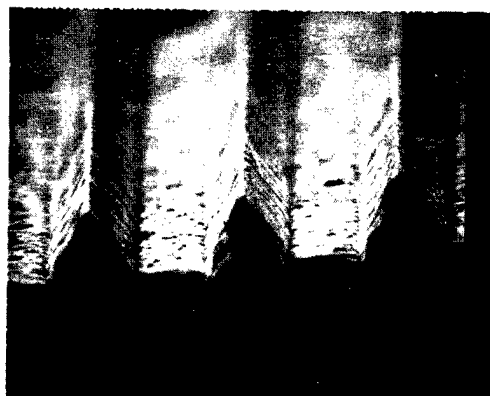
RESIST TOP
DEFORMS
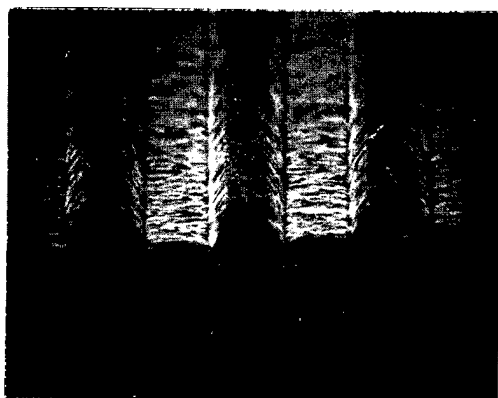
1.0 µM PEAK-TO-
TROUGH HEIGHT
28 PERCENT DUTY
CYCLE
60 DEGREE ANGLE

Fig. 7.   Ion-etched high efficiency gratings.

UNCORRECTED MAIN BEAM
ABERRATION

CORRECTED MAIN BEAM
ABERRATION BASED ON
HOLOGRAPHIC SAMPLE

DUE TO OUT-OF-
PLANE DISTORTION
COMPONENT

IF OUT-
OF-PLANE
DISTORTION
ONLY

PRIMARY MIRROR, f/NO.

PRIMARY MIRROR, f/NO
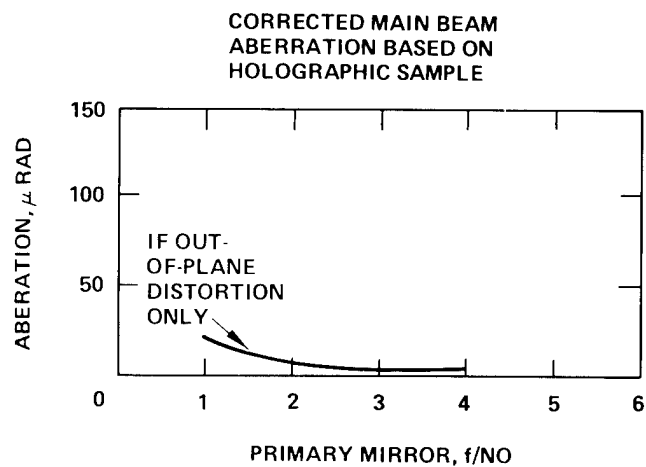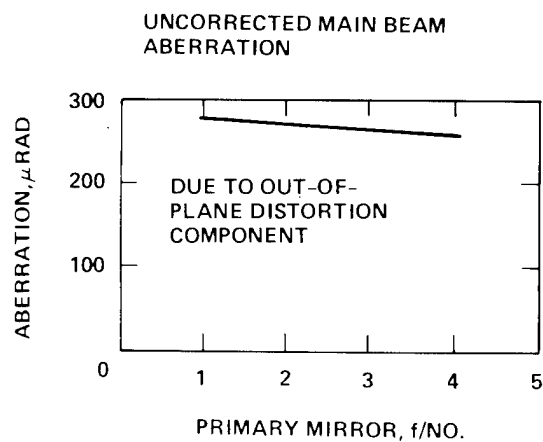
1 – METER MIRROR
λ = 3.8 µ

DISTORTIONS OCCURRED AFTER
GRATINGS WERE PUT ON PRIMARY

Fig. 8.   Primary mirror out-of-plane distortions are correctable.
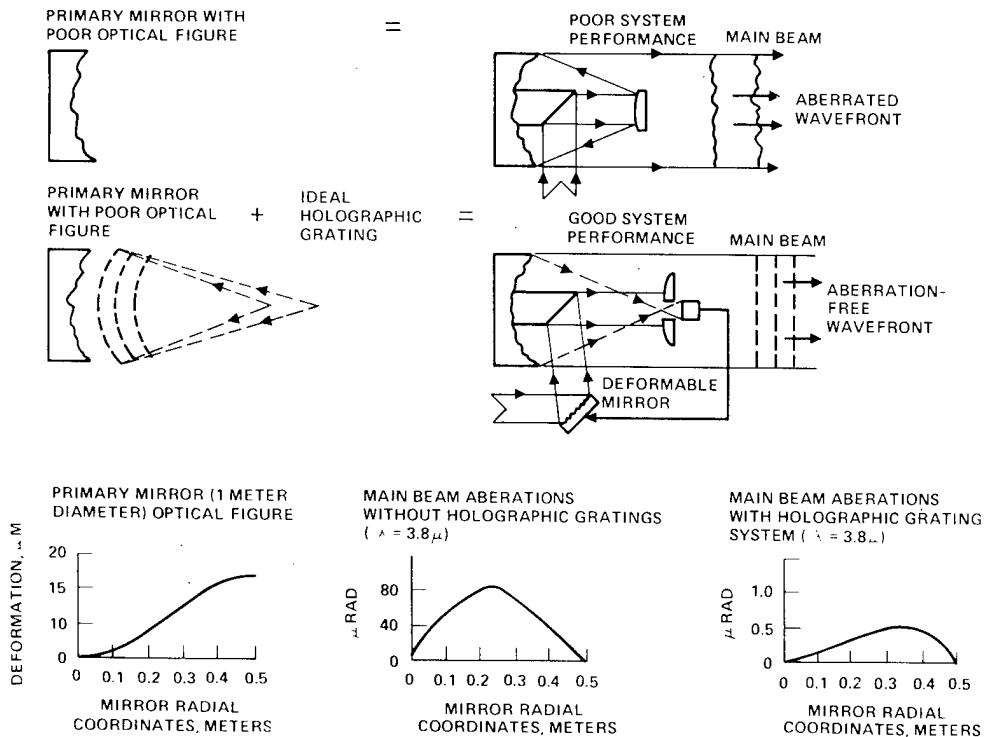
Fig. 9. Holographic gratings can be placed on a primary mirror having a poor optical figure to obtain good system performance.
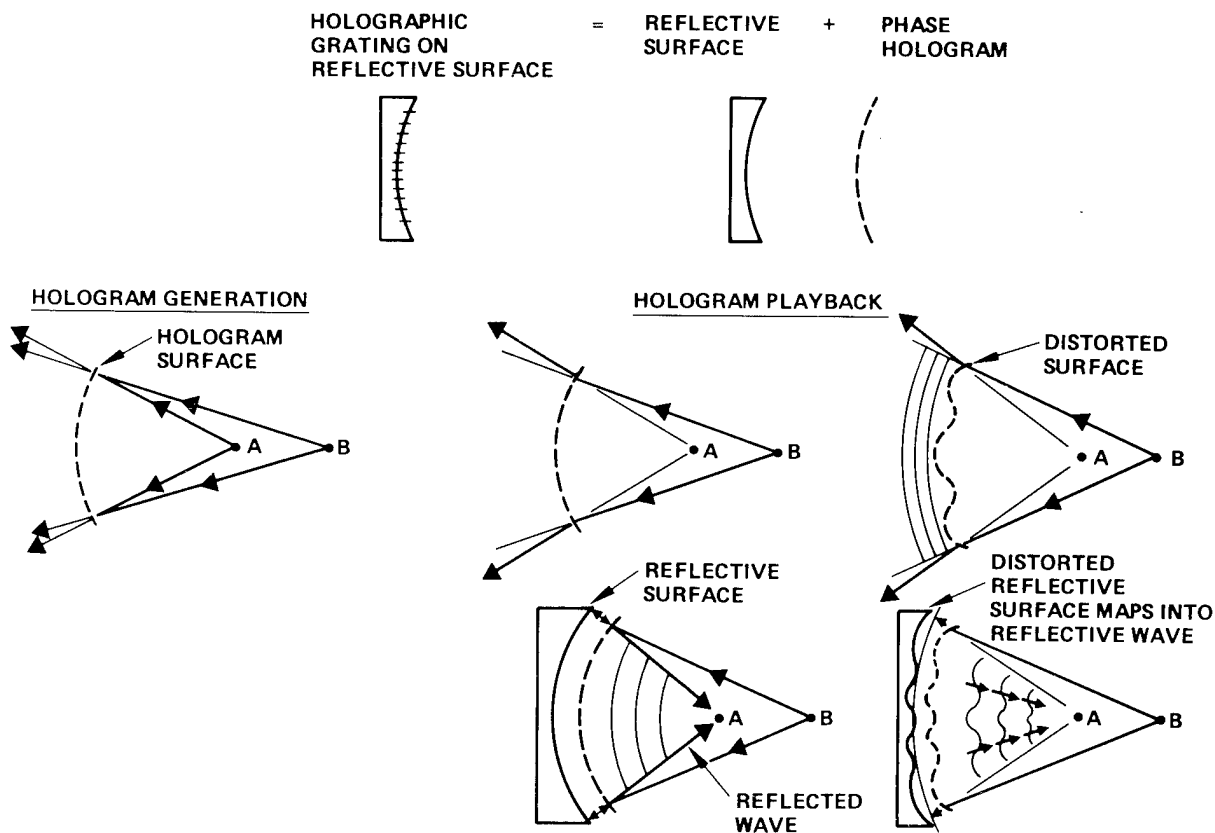
Fig. 10. Intuitive explanation of distorting holographic grating properties.

SPECTRAL SHARED APERTURE COMPONENT

Changhwi Chi
Hughes Aircraft Company
High Energy Laser Laboratory
Culver City, California

Norton B. James III, Peter L. Misuinas
Department of the Air Force
Air Force Weapons Laboratory Office
Kirtland Air Force Base, Albuquerque, New Mexico 87117

Abstract

A dichroic (or multichroic) beam splitter operating in the high energy laser HEL environment is called a shared aperture component and is becoming an increasingly desirable component in the design of HEL systems. At present, there are four basic types: Buried Short Period (BSP) grating, Buried Long Period (BLP) grating, Dichroic Beam Splitter (DBS) and Compound Interlaced (CI) grating. The BLP grating and CI grating are new types of grating which have recently been proposed and are currently under development. This paper describes the four basic types and their characteristics. Their design and fabrication issues and present technology status are also discussed.

Introduction

As high energy laser (HEL) systems begin to require high precision alignment and tracking and concentration of maximum energy density on the target objects, it becomes more desirable to use the shared aperture approach in which the HEL beam, the infrared (IR) beam returning from the target object, and the alignment and tracker beams all share the same optical path. A dichroic (or multichroic) beam splitter operating in a HEL environment, called a "shared aperture component", is used to inject the test beams into or split them from the HEL beam.

A spectral shared aperture concept offers several advantages. First, since all beams share the common optical path, the tracking, alignment, and beam control performance are immune from the jitter, misalignment, and aberrations occurring within the common optical path. Second, there is no need for a second set of alignment or pointing optics, reducing system size, weight, and complexity. Third, the IR radiation returning from the object can provide aberration information along the actual beam path, allowing detection of beam induced aberrations as well as those caused by the atmosphere.

The HEL beam is a single line or sometimes a multiline unpolarized beam with more than one micron spectral range. The IR radiation from the target object is incoherent and very low power, and ranges over 3 to 12 μm spectral band. The spectral band of 8 to 12 μm is called the long wave infrared (LWIR). The alignment and tracker beams originate from the lasers on board of moderate power level.

The performance requirements imposed on a shared aperture component are formidable. The HEL beam should be reflected with high efficiency and sampled with low efficiency and the IR and alignment beams should be sampled or combined with high efficiency. The component should handle very high, medium and very low power beams simultaneously, while maintaining precise alignment among the beams and a good optical figure.

A government contract was awarded to Hughes Aircraft Company to develop shared aperture components. The material presented in this paper includes some of the results of the effort accomplished under the Cooled Spectral Shared Aperture Concept, or COSSAC, program.

Buried Short Period (BSP) Grating

The construction of a buried short period (BSP) grating is shown in Figure 1. The term "short period grating" refers to the ordinary diffraction grating but is called this to distinguish it from the "long period grating" which is a new type of component discussed later in this paper. The grating is diamond ruled in gold and covered by a burying material, such as ZnSe, which transmits long wave infrared (LWIR) beams. Since this burying material follows the grating profile, its top surface is polished flat. A multilayer dichroic filter is then deposited on top of the burying layer. This filter is designed to reflect the laser beam but transmit the low power beam.

BSP grating samples have been fabricated and tested in the past. A BSP grating is, therefore, a practical and workable approach; it is used in a double rhomb configuration (Figure 2) to eliminate the spectral dispersion and shear, and obtain the desired LWIR wavefront form for interferometric sensors.
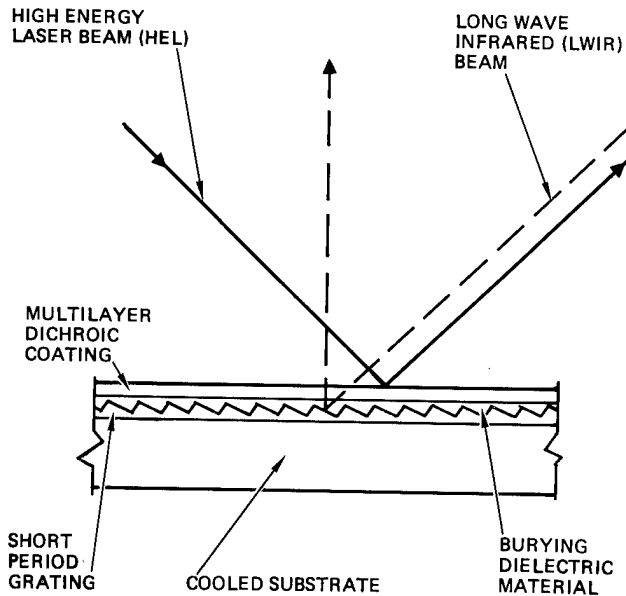
Fig. 1. Buried short period (BSP) grating.

The diffraction grating is designed to diffract the LWIR beam into first order with high efficiency. To aid in this design, a computer code developed by D. Maystre* has been used. This code predicts diffraction efficiencies in the presence of dielectric layers covering the grating. The grating parameters for a typical design are listed in Table 1. The grating period here was chosen to be large in order to keep grating dispersion low, which simplifies design of dispersion correcting optics.

Table 1. Grating Parameters

Diffraction Grating Parameters	
Incidence Angle	30 degrees
Grating Blaze Angle	3.5 degrees
Grating Apex Angle	90 degrees
Grating Period	.34 μm
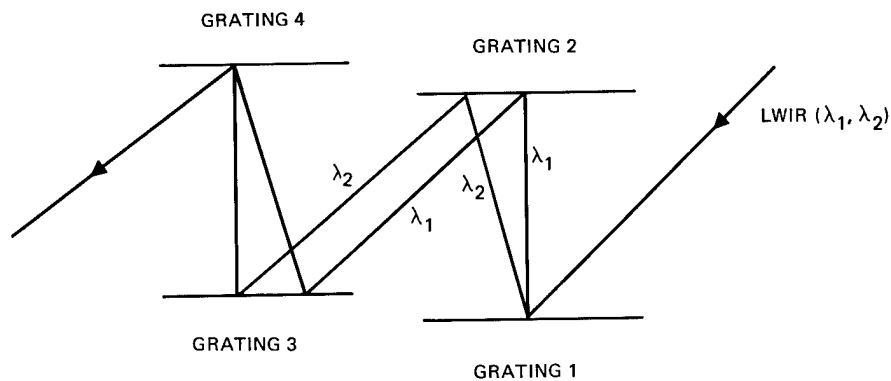
Fig. 2. Double grating rhomb configuration which corrects the spectral dispersion.

Typical results for the first order diffraction efficiency are shown in Figures 3, 4. The diffraction efficiency at a given wavelength varies considerably with burying layer thickness. Figure 3A shows the efficiency at 10 μm (for a grating which is blazed for 10 μm) as the burying layer thickness varies up to 3 μm (measured from the top of the grating groove). Both TE and TM polarization are shown. Figure 3B shows the variation of efficiency with burying layer thickness for various wavelengths. The results for TE and TM polarization have been averaged for each wavelength. The diffraction efficiency versus wavelength for much larger burying layer thicknesses (up to 50 μm) is shown in Figure 4.

For many applications, the quantity of interest is the average diffraction efficiency over the entire 8 to 12 μm band rather than the efficiency at any particular wavelength. When the efficiency is thus averaged for each polarization, the averaged quantity is found to vary only a few percent over the range of thicknesses examined above. Thus in constructing a buried grating component, the exact thickness of the burying layer is not critical to achieving high efficiency. The actual value of the average efficiency is typically 75 to 90 percent, depending on grating design and on the transmission of the dichroic filter in the 8 μm to 12 μm wavelength band. The average efficiency was also found to be insensitive to small variations in groove apex angle and blaze angle, so that manufacturing tolerance is relaxed somewhat. This result is important for ruled gratings, since such grating often depart significantly from the intended groove profile.

*D. Maystre, "A New General Integral Theory for Dielectric Coated Gratings," J. Opt. Soc. of Am. Vol. 68, p. 490, 1978.
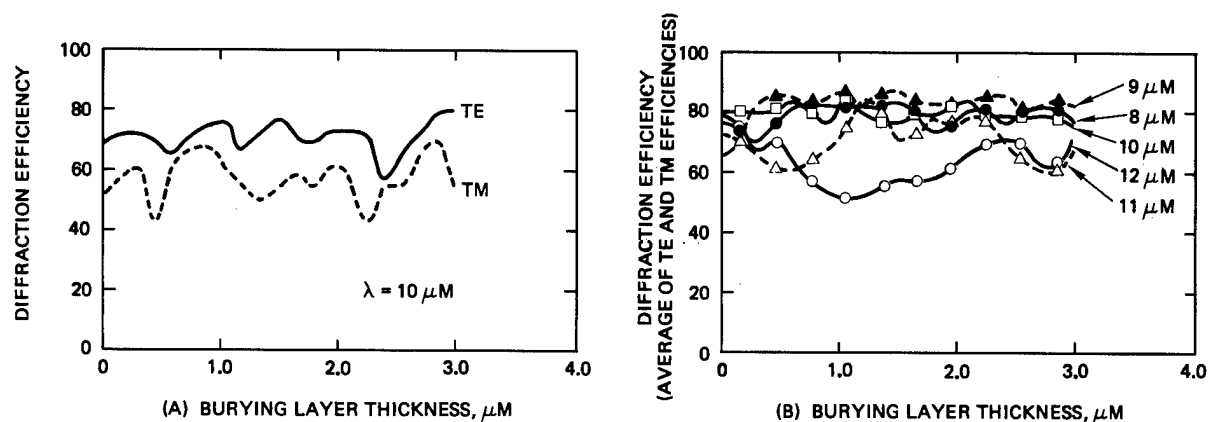
Fig. 3. Diffraction efficiency versus burying layer thickness.
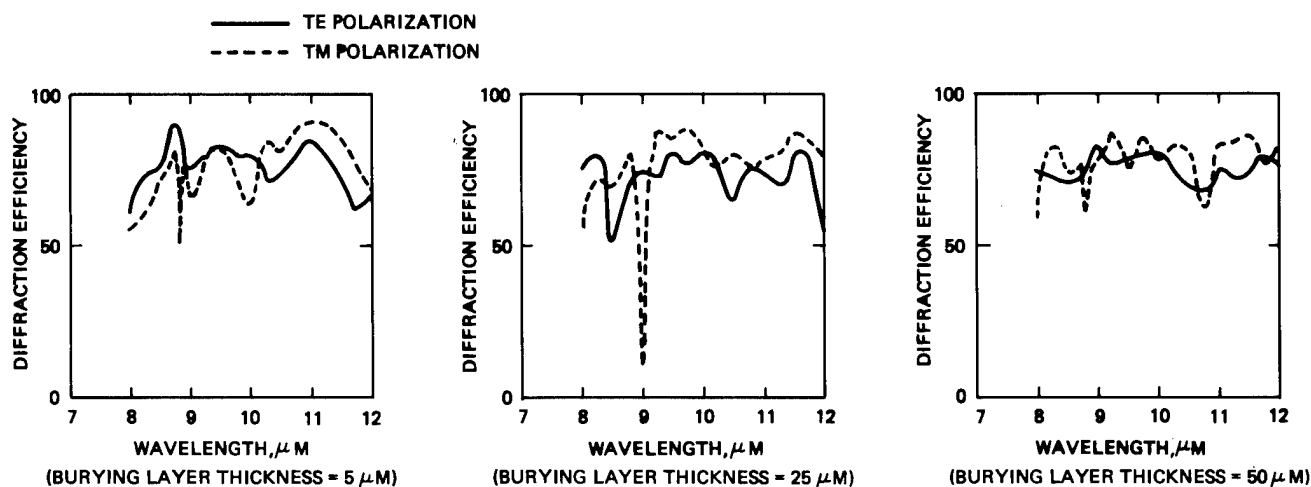
Fig. 4. Diffraction efficiency versus wavelength for various burying layer thicknesses.

A dichroic reflector filter is an essential part of several of the concepts for shared aperture components. Considerable care is required in the design of such filters if optimum performance is to be obtained from the component. This applies not only to the theoretical design of the filter, but also to the fabrication, since survivability of dielectric coatings under intense laser illumination remains a problem with present day components. Breakdown mechanisms in such films are not well understood and are a topic of ongoing research.

As an example of the optical performance of a filter designed for a shared aperture component, Figure 5 shows the transmission of three similar filters which were prepared by several laboratories. These filters are composed of alternating layers of ThF_4 and ZnSe and were designed to be highly reflective in the DF laser wavelength band ($\approx$3 to 4 μm) and to be transparent in the 8 to 12 μm wavelength band. Figure 5A shows the transmission curve for a simple filter composed of ten pairs of alternating quarter wave layers of high index and low index material. The filter in Figure 5B, (designed by Optical Coating Laboratories, Inc. (OCLI)) shows considerable improvement over Figure 5A in the 8 to 12 μm wavelength transmission, achieved by altering the thickness of some of the filter layers. The filter in Figure 5C, (designed by Perkin-Elmer) shows further improvement in the 8 to 12 μm transmission, giving greater than 98 percent transmission over most of this band. This filter is also a modified form of the simple quarter-wave stack filter.

High electric field strengths in the dichroic filter layers may adversely affect coating survivability. The field distribution which will occur in a particular filter design can be computed to determine whether excessive field strengths will exist. For reflector filter designs, the field strength decreases rapidly in successive layers of the filter, so that only the topmost layers are exposed to the high incident field strengths. Figure 6 shows the electric field distribution in the OCLI filter design, normalized to unity incident field strength. In this example the peak field strength occurring in any layer is approximately 1.2 times the incident field.
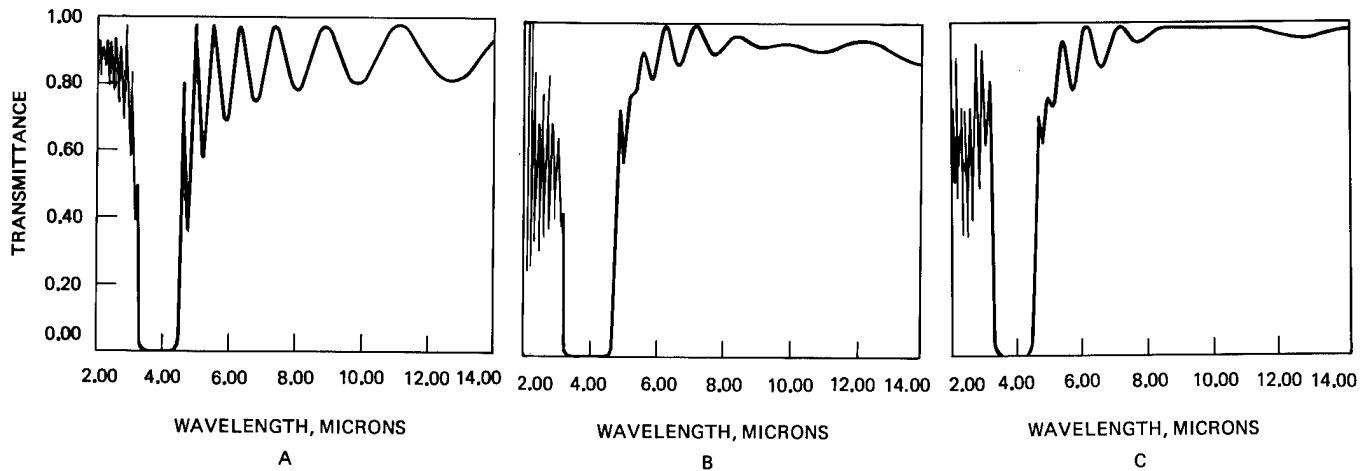
Fig. 5. Transmission of multilayer dichroic coating (incident angle = 0 degree).
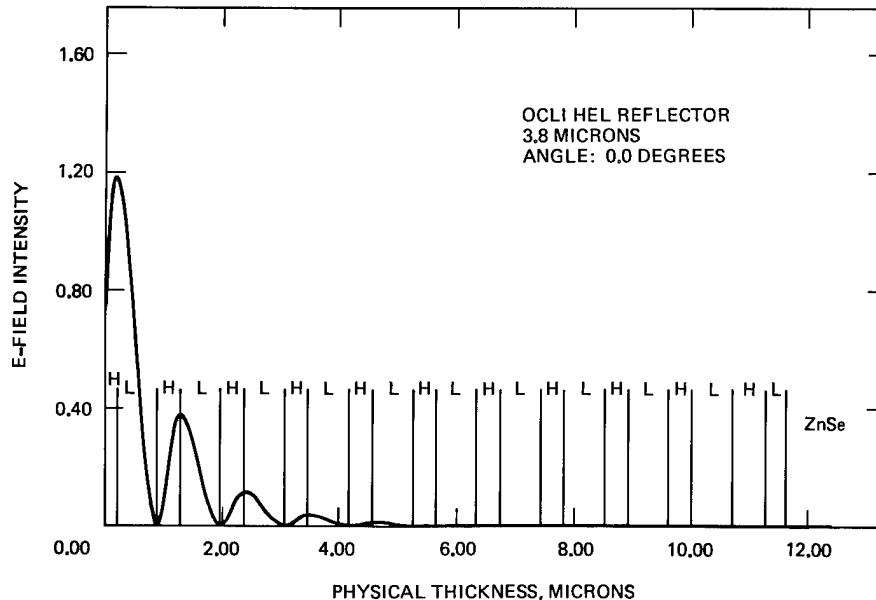
Fig. 6. Dichroic filter E-field distribution.

The packaging of BSP grating rhombs is a formidable task in terms of both the structural rigidity required (to hold four gratings aligned) and the available space to install the gratings (while remaining outside the HEL and LWIR beam path). The skew grating configuration, shown in Figure 7, provides some relief in this respect. In this configuration the grating is rotated so that the groove is not perpendicular (in the Figure 1, it is parallel) to the incident beam, and the diffracted beams are in the direction out of the plane of incidence. Consequently, the space outside the plane of incidence which is not available in the ordinary grating configuration becomes available for packaging. The grating analysis shows that the diffraction efficiency remains approximately the same when the skew configuration is implemented.

The BSP grating is a workable approach but it has shortcomings also. The BSP grating is sensitive to polarization and wavelength, has large spectral dispersion and a limited spectral range, requires four gratings, and the total efficiency is significantly reduced by the time the LWIR beam diffracts through the four gratings.

Present activities concerning BSP grating technology include design optimization of a short period grating and dichroic coating, alternative methods to double grating rhombs, and the investigation of improved coating materials and coating techniques.

Buried Long Period (BLP) Grating

The buried large period (BLP) grating is a new shared aperture component and is considered to be an important technique because it eliminates most of the shortcomings of BSP gratings.

In the BLP grating shown in Figure 8, the period is so large (on the order of a few millimeters) that the grating facet becomes a mirror for the wavelength of interest (10 µm in the present case) and consequently the diffraction effect is minimal. The large period grating is placed on a cooled molybdenum substrate, buried with a dielectric material, and overcoated with a multilayer dichroic coating which reflects the high energy laser (HEL) beam and transmits the LWIR beam.

Since the grating facet is a mirror, the BLP grating exhibits the following desirable characteristics:

1. High efficiency for LWIR (mirror has good reflectivity)
2. Insensitive to the polarization
3. Insensitive to the wavelength
4. Works for a wide spectral range
5. Minimal spectral dispersion
6. Easy to align, as is the mirror alignment
7. Requires no double rhomb but a BLP grating pair (one is a low power replica).

A small spectral dispersion of the BLP grating originates from the wedge shaped burying material which acts like a prism, but is compensated by the BLP grating replica.

It should be noted that when a LWIR plane wave is incident on one BLP grating, the reflected wavefront has the phase discontinuity, as shown in Figure 8, because the rays reflected by different facets have traveled different path length. The beams having a discontinuous wavefront are detrimental to the interferometric sensors especially when the discontinuity is larger than the coherence length of the LWIR. To recover the original wavefront and recover the phase information, a second BLP grating (which is a replica of the first) is used. The replica BLP grating is a low power unit and does not need a cooled substrate.

TOP VIEW SHOWING BEAM SEPARATION

Fig. 7. Skew oriented grating configuration (incident HEL and LWIR beams are parallel to the grating grooves).

Fig. 8. Buried long period (BLP) grating pair.

The BLP grating pair thus constructed recovers the original wavefront by introducing the extra beam path length to the ray that traveled less in the first BLP grating, thus compensating for the optical path difference (OPD) introduced by the first BLP grating. Introduction of the replica BLP provides other advantages. The fabrication tolerance of the first BLP grating parameters such as the blazed angle is significantly reduced because the error in the first BLP grating is also present in the replica BLP but in the opposite sense, thereby compensating the effect of fabrication errors. The spectral dispersion introduced by the first BLP grating is also compensated by the replica and converted to a lateral spectral shear of minimal amount.

An error in the BLP grating parameters and an imperfect replica will result in a wavefront OPD coming out of the BLP pair. To determine the fabrication tolerance, ray tracing through the BLP grating pair was performed. The parameter notation and tolerance analysis results are shown in Figures 9 and 10 respectively. It is to be noted that the intra-facet parameters (between facets within one BLP grating) have a large tolerance, which means that the fabrication tolerance for the first BLP grating is quite loose. The inter-element parameters (between the mating facets of two BLP gratings) have relatively tight tolerances, which

ANGLE β IS IN THE PLANE NORMAL TO THE PLANE OF PAPER

Fig. 9. BLP grating parameter notation.

INTRA-FACET PARAMETERS
(BETWEEN FACETS WITHIN ONE BLP GRATING)

PARAMETER RATIO	SENSITIVITY DERIVATIVES	PARAMETER ERROR THAT PRODUCES 1.0 μM OPD
OPD/$\Delta\alpha$	0.38606 CM/RAD	53.5 ARC SECONDS
OPD/$\Delta\beta$	0.42880 CM/RAD	48.2 ARC SECONDS
OPD/Δb	10^{-11} μM/μM	—
OPD/ΔL	10^{-15} μM/μM	— } NEGLIGIBLE
OPD/ΔBL	10^{-15} μM/μM	—
OPD/Δd	10^{-13} μM/μM	—

INTER-ELEMENT PARAMETERS
(BETWEEN THE MATING FACETS OF TWO BLP GRATINGS)

	PARAMETER RATIO	SENSITIVITY DERIVATIVES	PARAMETER ERROR THAT PRODUCES 1.0 μM OPD
*	OPD/Δ /LENGTH	5.127 μM/μM-RAD	4.0 ARC SECONDS
**	OPD/Δ /LENGTH	4.781 μM/μM-RAD	0.22 ARC SECONDS
	OPD/Δb	4.781 μM/μM	0.21 μM
	OPD/ΔL	10^{-15} μM/μM	— } NEGLIGIBLE
	OPD/ΔBL	10^{-15} μM/μM	—
	OPD/Δd	0.38746 μM/μM	2.6 μM

* ASSUME FACET WIDTH OF 1.0 CM
** ASSUME FACET LENGTH OF 20 CM

Fig. 10. Fabrication parameter tolerance errors for BLP grating pair.

means that a reasonably good replica is needed. The BLP grating pair fabrication is within the present precision machining capability.

The BLP grating operates in the regime where the diffraction effect is negligible. To determine the acceptable range of the BLP grating period, a diffraction calculation was performed. It is interesting to find the diffraction effect as the LWIR beam travels from the high power BLP grating to the replica BLP grating. The diffraction effect is determined by the Fresnel number N, $N = d^2/4\lambda L$ where d is the width of equivalent slit representing one facet as shown in Figure 11, L is the grating separation, λ is the wavelength. An equivalent slit is used in Figure 11 to represent the aperture size of the facets.
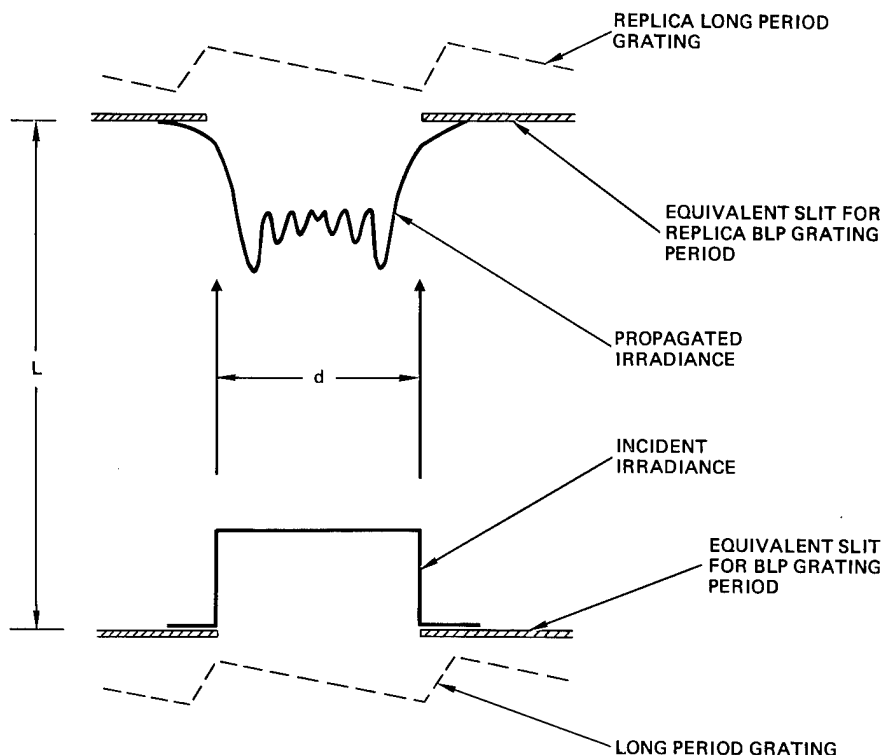
Fig. 11. Equivalent geometry for diffraction analysis of a single period of BLP grating.

The LWIR energy diffracted outside the geometrical shadow and thus lost is shown in Figure 12. It indicates that the diffraction loss is low when the Fresnel number is larger than 4.

When the LWIR wavefront coming from the BLP grating pair is focused, the resulting airy disks for different Fresnel numbers are shown in Figure 13. It should be noted that the airy disk degradation is minimal even for the extreme case of N = 1. Therefore, the image resolution and efficiency are not degraded by the diffraction effect.

When performing the diffraction calculation, the amplitude distribution of the wavefront emerging from the BLP grating pair contains a significant fluctuation due to edge effect. It should be remembered, however, that the phase distribution is the important parameter and it is hardly degraded. This is the reason why a good airy disk is obtainable even with a Fresnel number of 1.

As the BLP grating period is increased the average distance from the multilayer coating to the cooled substrate increases. Eventually the cooling effect disappears and a failure will result. The failure mechanism of a BLP grating is not well understood at this time. To gain an insight into the failure mechanism an investigation is in progress concerning the electromagnetic field behavior and the thermal/mechanical stress and deformation within the dielectric media.

Thermal/mechanical analysis within one period was performed on the model shown in Figure 14. It represents one period on which a uniform thermal irradiation is incident on the dichroic coating. The bottom of the substrate is held at a temperature T_o and the same boundary conditions are imposed at both the vertical boundaries since the BLP grating is periodic.
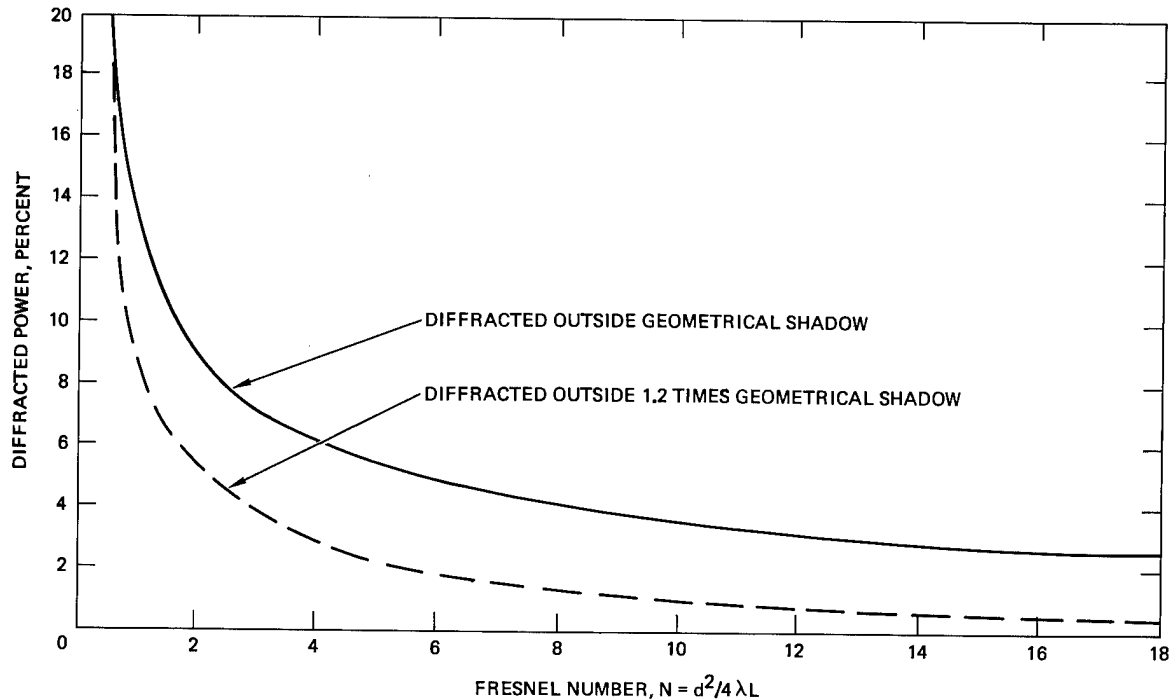
Fig. 12. Power diffracted outside geometrical shadow of a slit.
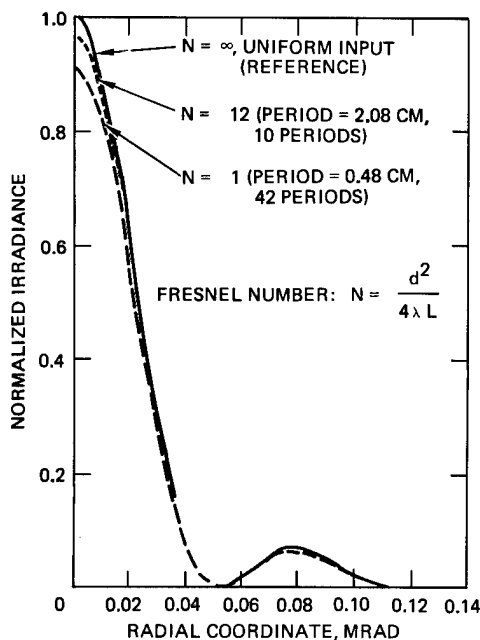
Fig. 13. Point spread function of the BLP grating pair.

The thermal and structural analysis also predicted the stresses in the CVD ZnSe burying layer. The maximum values of the stresses (compression, shear and tension) for the principal axes are plotted as a function of period, d, in Figure 15. The breaking stress for CVD ZnSe is on the order of 5500 psi. For a safety factor of 5 it is necessary to keep the stresses at or below 1000 psi. This criterion is satisfied for a period of 1 cm where the compression is just over 700 psi.

The locations of the maximum temperature gradient, distortion and stress are indicated in Figure 16. The thermal conductivity of CVD ZnSe is one-eighth that of molybdenum. The maximum temperature should occur in the vicinity of the thickest CVD ZnSe, i.e., vertically above the valley of the molybdenum facet (point A). The minimum dichroic surface temperature occurs in the vicinity of the region above the minimum vertical CVD ZnSe thickness, i.e., the peak of the molybdenum facet (point B). Points A and B are close together and the maximum temperature gradient is located between these two points. Hence the maximum stresses are also located in this region (C). By lowering the facet slope in the peak to valley transition region, as indicated by the dotted lines, the thermal gradient and material stresses should be decreased. The thermal expansion of ZnSe is 1.7 times that of molybdenum, and the thicker the ZnSe the larger the vertical distortions. Hence the maximum out-of-plane distortions occur near point A or equivalent point A'. These out-of-plane distortions tend to force the ZnSe wedge (shaded region) in a horizontal direction, which results in maximum in-plane distortions at point D, or equivalently near point B, or equivalently to the left of C.

The present effort on the BLP grating is centered on the investigation of various fabrication techniques which includes the diamond turning, sputtering, electro forming, replication process, room temperature coating and low absorption coating.
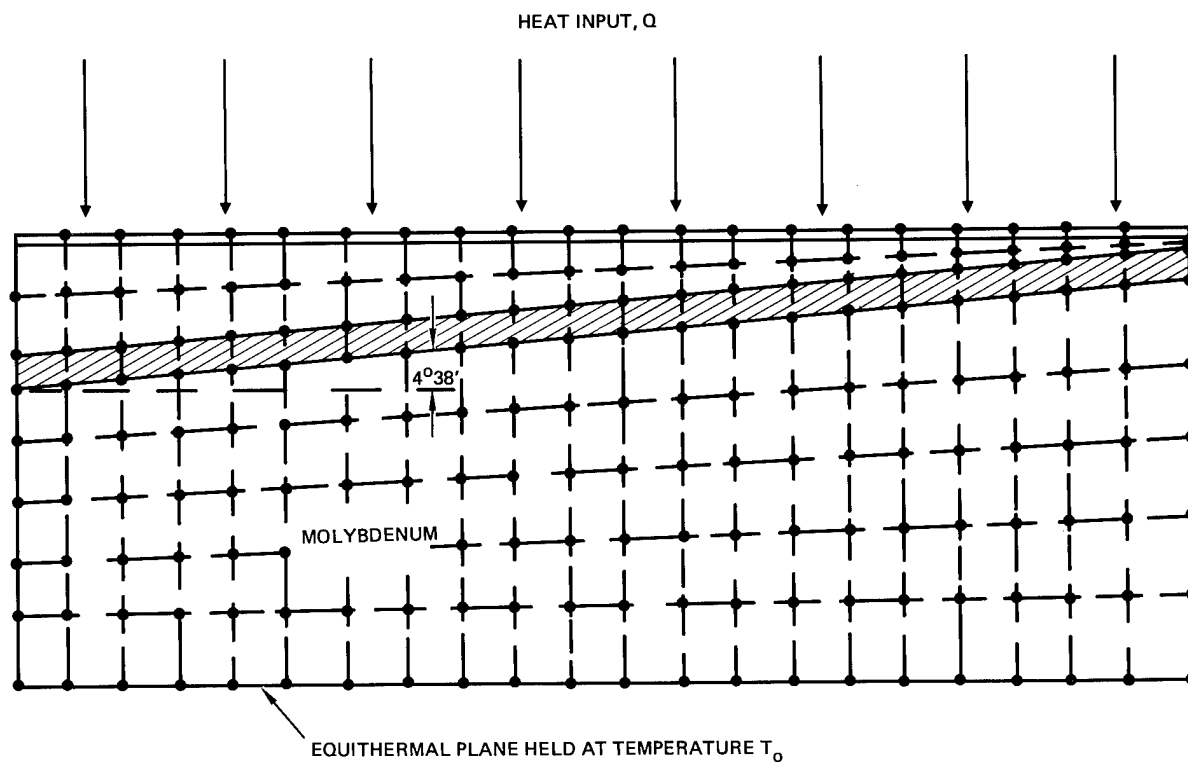
Fig. 14. Model used for thermal/mechanical analysis within one BLP grating period.
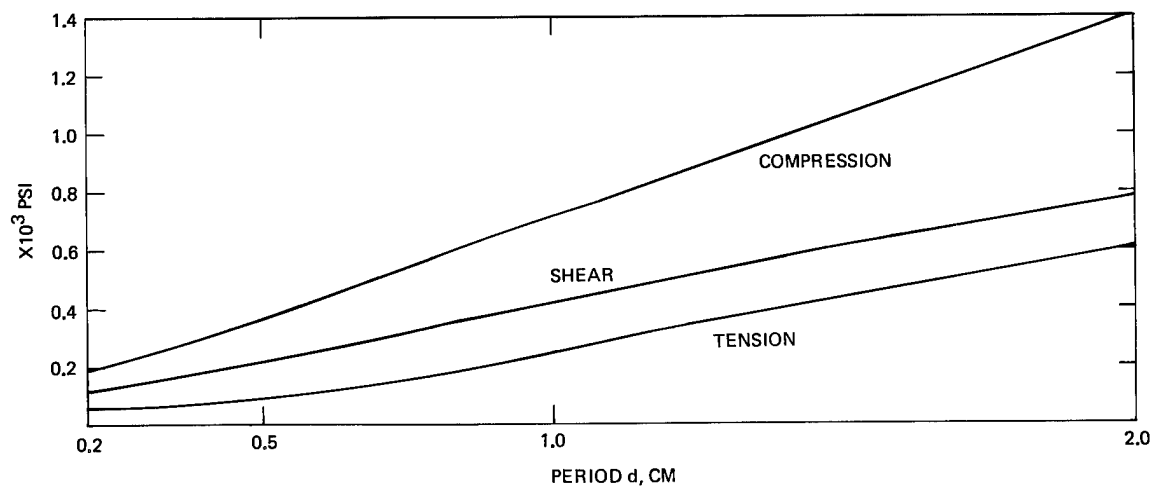
Fig. 15. Maximum stresses, about the principal axes, resulting from the temperature gradients.
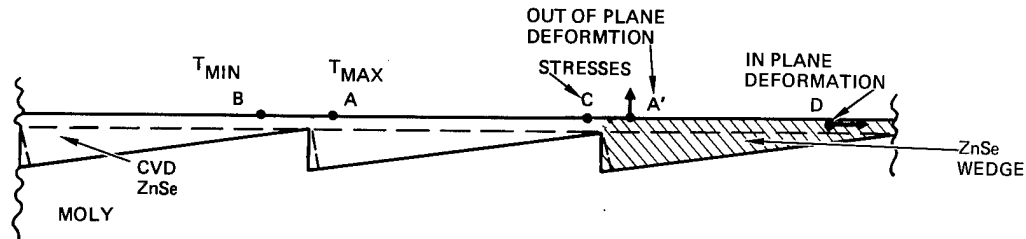
Fig. 16. Locations of surface temperature gradient, distortion
and stress extrema.

Dichroic Beam Splitter (DBS)

The DBS shown in Figure 17 is a more traditional approach to the shared aperture component. In both the rotating and stationary approach the multilayer dichroic coating is designed to reflect the HEL beam and transmit the LWIR.

In the rotating DBS, the substrate is larger than the HEL beam (typically six times); therefore, the HEL beam energy absorbed at the dichroic coating is spread over an annular region larger than the HEL beam foot print and the effective density of the absorbed energy is reduced (by a factor of six). The DBS is cooled by gas jets impinging on the DBS within the stationary cooling shroud. For most applications the DBS substrate rotational speed is not critical and can be as low as several hundred rpm.

a. ROTATING DBS
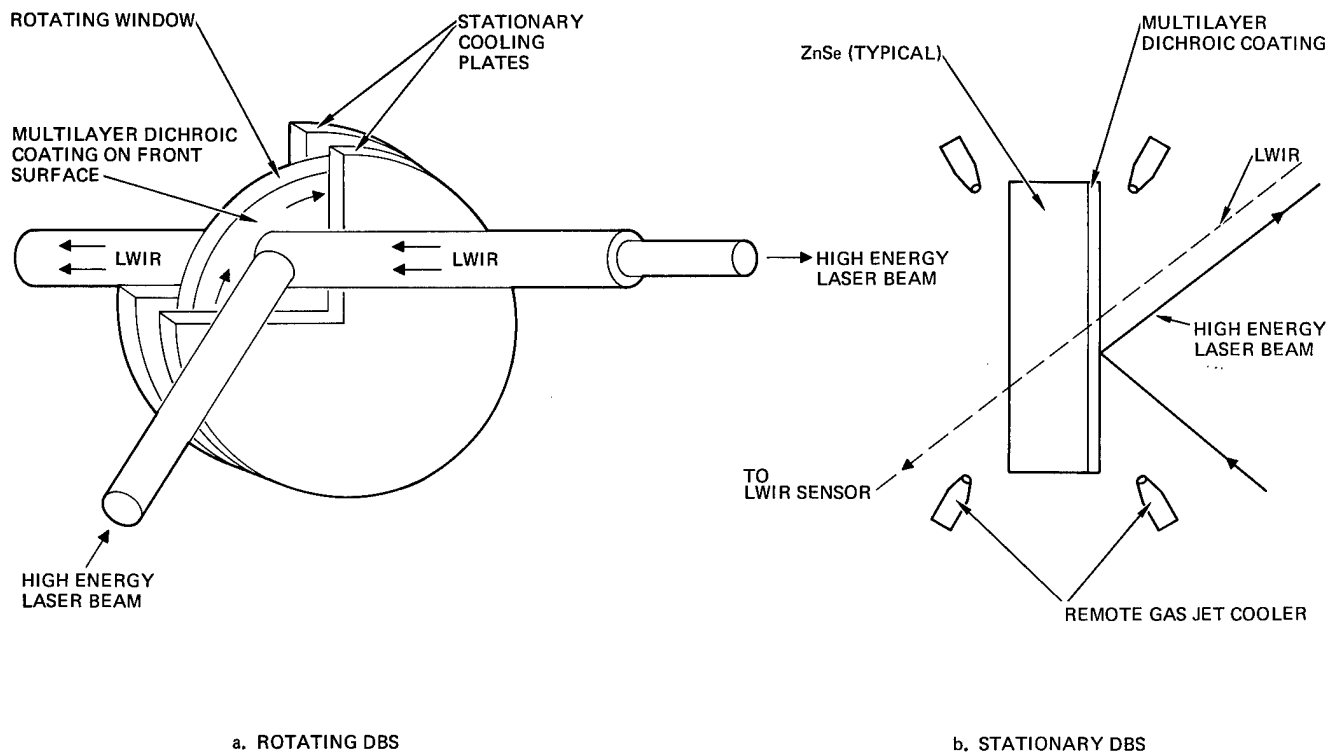
b. STATIONARY DBS

Fig. 17. Dichroic beamsplitter (DBS).

A much simpler configuration is the stationary DBS in which the substrate is the same size as the HEL beam foot print. The coolant gas is blown by the jet nozzles located outside the path of HEL and LWIR beams. In the stationary DBS (unlike the rotating DBS) the absorbed HEL beam is not spread over a wider area and the cooling capacity is much less.

The rotating DBS is the simplest aperture sharing concept if the cooling system is ignored. It is basically a large dichroic filter which provides good isolation between the HEL and LWIR, has high efficiency, is polarization insensitive and exhibits no spectral dispersion. This concept does not require unconventional optical finishing, spectral dispersion correction elements, nor replicated correction elements as do the other concepts. However, proper design of the cooling system is a significant task. Issues include the amount required and subsequent disposal of the coolant gas, fogging of substrate, and over-cooling which is as undesirable as the overheating. Also, the rotating mechanism adds complexity in that a finite start-up time will be required and dynamic steering errors due to window wobble and substrate wedge may require correction.

The stationary DBS offers the advantage of the configuration simplicity. It has no moving parts, thereby eliminating all the auxiliary subsystems attached to the rotating mechanism, and has a much smaller size which impacts optic size, fabrication techniques, mounting structures and overall weight. However, its usage is limited by its low cooling capacity.

It should be noted that the material window, which is used to separate two environments and allow transmission of the HEL beam, employs a similar configuration. Significant differences exist, however, between the material window and the DBS. The material window is a refractive element (transparent plate) with an antireflection coating on the substrate for the HEL beam; therefore, the substrate deformation results in a minimal degradation of the HEL beam quality. The DBS, on the other hand, is a reflective element (mirror) for the HEL beam and a refractive element for the LWIR beam; therefore, the HEL beam is highly sensitive to the DBS substrate deformation. DBS, consequently, requires more stringent optical figure control, a more careful cooling design and an optical compensation system to correct for the substrate deformation.

A simplified one-dimensional analysis and heat balance equations for DBS plate are useful for determining the performance bounds of various DBS configurations. The parameters of interest include the mechanical stress which determines the failure threshold, the DBS substrate deformation which degrades HEL beam quality, and OPD for LWIR beam.

The causes of mechanical stress are gravity, centrifugal force (in the case of rotating DBS), coolant gas impingement pressure, and the thermal gradient induced stress. The dominant source of the mechanical stress is the thermal gradient in a typical rotating DBS configuration, which consists of a ZnSe substrate, having 60 cm diameter, 3 cm thickness, rotation speed of 500 rpm, and the gas impingement cooling from the jet nozzle of a cooling shroud providing the heat transfer coefficient (H) of 0.1 watt/cm^2/°C.

The CVD processed ZnSe substrate has the flexural strength of 7500 psi when 4-point loaded. Allowing a design safety factor equal to 5, the allowable stress becomes 1500 psi. The thermal stress factor of ZnSe is 80 psi/°C. Therefore, the allowable temperature rise is 20°C. Since the absorption of HEL beam occurs on one face of the ZnSe plate, thereby causing expansion of that face, the plate exhibits a bowing deformation and assumes a curvature. The OPD caused by the substrate deformation for the LWIR beam results from the variation of the index of refraction with the temperature, and the increased path length caused by the material expansion.

The nominal values of the material constants of substrate materials are listed below.

Material	Thermal exp coeff (α)	Poisson coeff (ν)	dn/dT	Index of refraction (n)
ZnSe	8.0×10^{-6}/°C	0.3	6×10^{-5}/°C	2.4
CaF_2	2.0×10^{-5}/°C	0.3	-5×10^{-5}/°C	1.3
K Cl	3.4×10^{-5}/°C	0.3	-3×10^{-5}/°C	1.45

Substrate Material Constant

The effectiveness of the cooling technique is expressed by the thermal transfer coefficient (H) in watts of heat removed per area for each degree centigrade difference between the heated surface and the cooling gas temperature (watt/cm^2/°C). In a rotating DBS, the cooling shroud containing the gas cooling jet nozzles provides H = 0.1 watt/cm^2/°C. The cooling nozzle parameters are

orifice diameter = 0.08 cm
orifice density = 3/cm^2
separation between the nozzle and the substrate plate = 0.13 cm

In the stationary DBS, the separation between the substrate and the nozzle is greater. Assuming this separation to be 15 cm, the thermal transfer coefficient (H) is 0.006 watt/cm^2/$^\circ$C. The thermal transfer coefficient (H) of the free air convection cooling is 0.0006 watt/cm^2/$^\circ$C.

The required amount of coolant gas is also a parameter of interest. With N_2 as the coolant gas and assuming a complete thermal transfer, the required amount of gas is 4 lb/sec for removing 1 kw heat when the temperature difference between the heated surface and coolant gas is 1°C. In some HEL applications, the amount of coolant can be considerable.

It is useful to find the conditions necessary to reach the thermal equilibrium. In the rotating DBS, the following condition must hold: (Power Density Absorbed) (HEL Duty Cycle) = (Thermal Transfer Coefficient) (Cooling Duty Cycle) (Temperature Difference Between Coolant Gas and Substrate).

Case 1. In a rotating DBS, the size of HEL is one sixth of the total substrate area, and the cooling occurs over three-fourths of the substrate area. For a cryogenic temperature cooling gas (80°K) a room temperature DBS plate (300°K), and a heat transfer coefficient of 0.1 watt/cm^2/$^\circ$C (the upper limit for current gas impingement cooling technology), the thermal equilibrium equation becomes, Q(1/6) = (0.1) (3/4) (300-80), or the allowable thermal input (Q) = 100 watt/cm^2 maximum. It should be noted that complications arise in the implementation of this technique to carefully match cooling to the DBS substrate heating so that deleterious performance effects due to over-cooling do not occur.

Case 2. When a cooling gas temperature of 0°C and the DBS substrate temperature of 22°C are assumed in the system of Case 1, Q = 10 watts/cm^2. This configuration has the advantage of using a chilled coolant instead of the cryogenic coolant.

Case 3. In a stationary DBS, the HEL beam size, substrate cooled are approximately the same. For a chilled coolant gas (0°C), a room temperature DBS substrate (25°C), and a heat transfer coefficient of 0.006 watt/cm^2/$^\circ$C (for coolant jet nozzles located outside the beam path), Q = (0.006) (25) = 0.15 watt/cm^2. Although this is a significantly reduced cooling capacity, the simplicity of this technique provides an overwhelming advantage for those situations where small cooling is adequate.

Present state-of-the-art techniques for high-power dichroic coating fabrication and cooling make the rotating DBS a feasible approach for the shared aperture component. The stationary DBS has none of the complexity of the rotating DBS but has a reduced cooling capacity which makes this approach unsuitable for present HEL applications. The realization of stationary DBS approach awaits further technology development in the dichroic coating design and fabrication which provides better than 0.1 percent absorption currently possible, and simpler and more efficient substrate cooling techniques.

Compound Interlaced (CI) Grating

Various types of CI grating are shown in Figure 18. This type of grating is much simpler to fabricate than other types of shared aperture components. It has a superior overall performance and has no survivability problems. However a CI grating works only for cases where the HEL wavelength is much larger (2 to 3 times) than the test beam wavelength (alignment, tracking or target object radiation).

An example of the application is when the HEL beam is 10.6 μm, the alignment beam is 0.6238 μm and target object radiation is 3 to 4 μm. Another example is when HEL is 3 to 4 μm (chemical lasers), alignment beam is 0.6238 μm, and active tracker is 1.06 μm.

The CI grating has two gratings: One of period b, called a b-grating, for the diffracting long wavelength (i.e., 10.6 μm when the HEL is a CO_2 laser for instance), and one of period d, called a d-grating, for diffracting short wavelength (visible or near IR). When a 10.6 μm beam impinges on the CI grating it does not "see" the d-grating because its period is much smaller than the wavelength. The d-grating will, however, contribute to the scatter of the 10.6 μm beam and also tilt it slightly toward the blazed direction.

When the short wavelength (visible) beam impinges on the CI grating it will be diffracted both by the d-grating in the manner and direction desired and by the b-grating, which generates multiple ghost orders between the main d-grating orders. The amplitudes of the ghost orders can be minimized by properly designing the groove shape, period and duty cycle.

Different types of CI grating are shown in Figure 18. The d-grating diffraction efficiency for a full CI grating is larger than for a partial CI and degenerate CI grating. In a skew CI grating, the b-grating and d-grating are not parallel so that the diffractions of two gratings do not lie in the same plane (as shown in Figure 19).

A partial CI grating is obtained when the d-grating (fine) is ruled first and the b-grating (coarse) is ruled second. A full CI grating is obtained when the b-grating is ruled first and d-grating is ruled second. A skew grating is obtained when the d-grating is ruled unparallel to the b-grating.
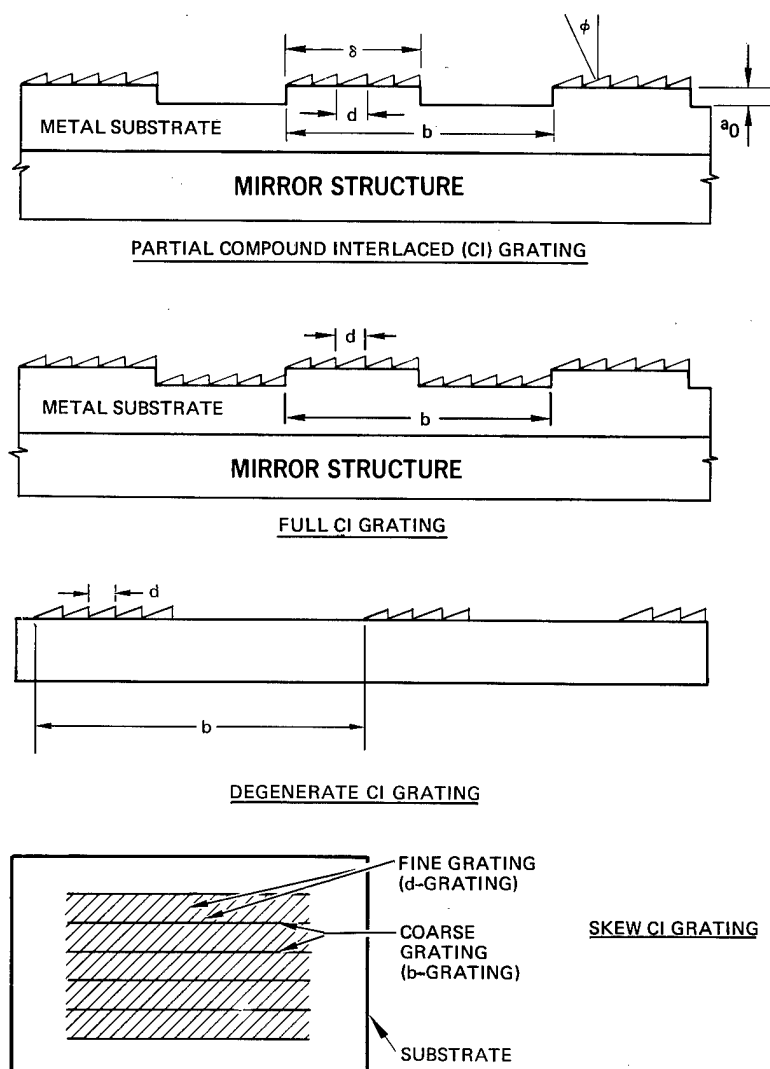
Fig. 18. Compound interlaced (CI) grating types.

There are two methods for ruling gratings presently in use: (1) "planing" and (2) "embossing". The planing method involves pushing the diamond tool across the substrate to "gouge" out the groove. This method actually removes material from the substrate. Embossing involves pulling the diamond across the surface substrate to plow a groove. In this pulling method, the material is pushed aside, but none is removed. A number of small (1 inch by 1 inch) samples and one large prototype CI grating (4 inches by 5 inches) on a 9-inch cooled mirror substrate have been fabricated to verify feasibility and evaluate the performance. The embossing method was used in the prototype fabrication. A typical design for the prototype unit is shown in Figure 20, in which HEL beam is high efficiency reflected and also low efficiency diffracted by the shallow b-grating, and the visible (0.6 μm) and mid IR (3-4 μm) are high efficiency diffracted.

The scalar wave diffraction theory for the CI grating was formulated, assuming the substrate having infinite conductivity and shallow grooves (i.e., the multiple reflections within a groove are ignored). Figure 21 is a typical diffraction energy distribution between the major and minor orders. Figure 22 indicates that the CI grating diffraction efficiency is approximately 10 percent below the ordinary grating efficiency for the prototype CI grating design and that the experimental data with HeNe laser beam show a good agreement with theory.

Present activities include optimization of design using a more comprehensive theoretical analysis, fabrication and groove measurement techniques, coating effect, and large scale unit fabrication.
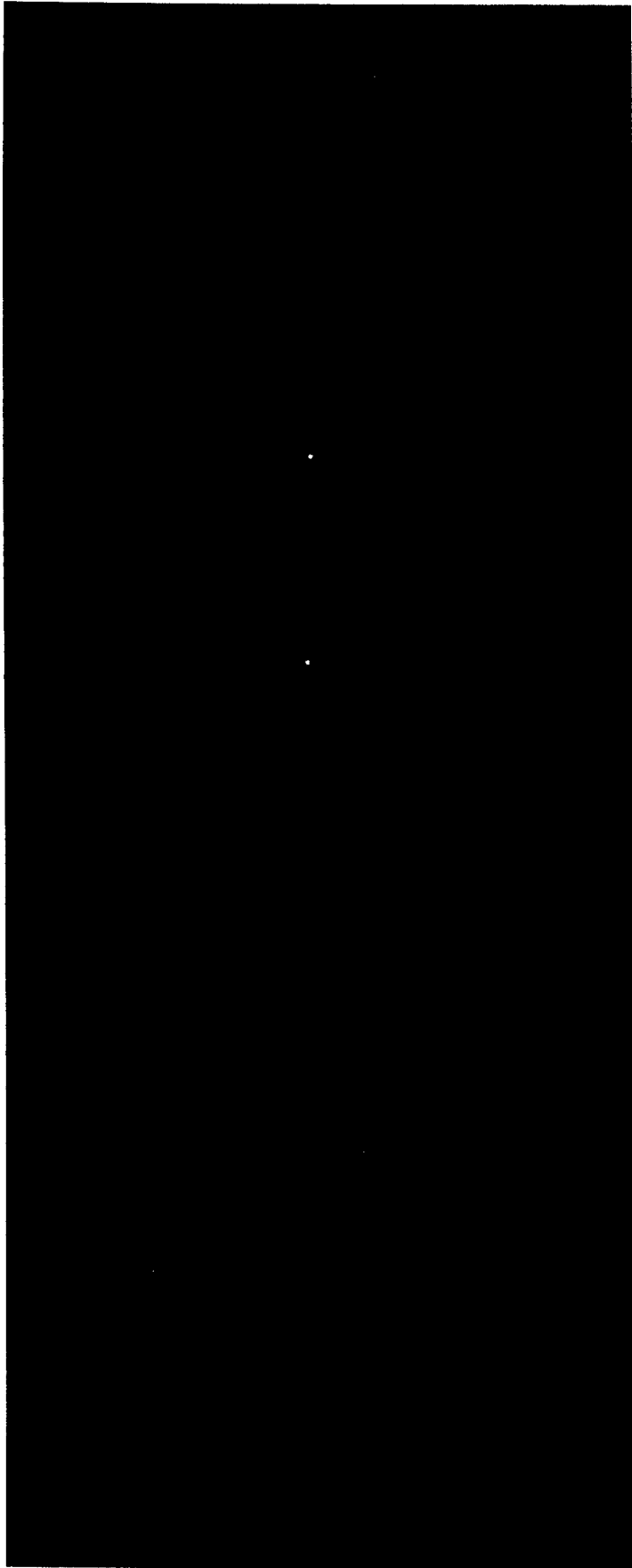
Fig. 19. Diffraction pattern of a skew CI grating.

d-GRATING

b-GRATING

CI GRATING

0.08 μm

0.2°

2.8 Å

22.9μ   14.551μ

37.451μ
(26.7 gr/mm)

b-GRATING (COARSE)

10.6μ

12.5°

36.75°   36.75°

3.0 μm
0.62 μm

3.0 μm
0.62 μm

10.6 μm
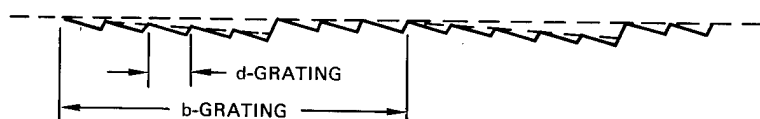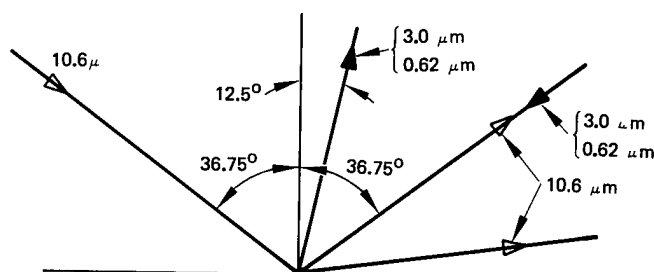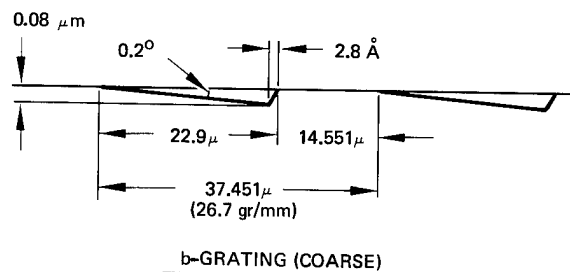
FULL PARALLEL CI GRATING

B = 24.625°

3.7451μ

0.642 μ

4.3871
(225 gr/mm)
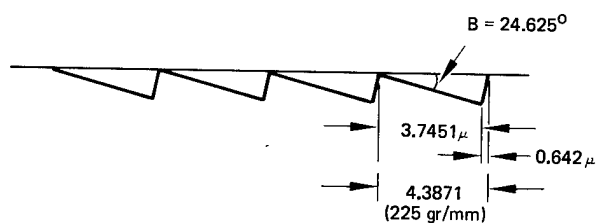
d-GRATING (FINE)

$\lambda_d(1) = 3.5$ μ   (n = 1)

$_d(2) = 0.61$ μ   (n = 6)

Fig. 20.   CI prototype grating design.

FULL COMPOUND INTERLACED GRATING (H-MODE)

b-GRATING:
   PERIOD (b) = 35.12 μM
   BLAZE ANGLE (ψ_1) = 0.2°
   DUTY CYCLE = 5/8

d-GRATING:
   PERIOD (d) = 4.39 μM
   BLAZE ANGLE (ψ) = 24.425°

λ = 0.54μM
INCIDENT ANGLE (β) = -36.750°

MAIN ORDERS

GHOST ORDERS

RELATIVE INTENSITY

1.00
0.63
0.67
0.50
0.33
0.17
0.00

-30.00   -24.00   -18.00   -12.00   -6.00   0.00   6.00   12.00   18.00   24.00   30.00

DIFFRACTION ANGLE, DEGREES
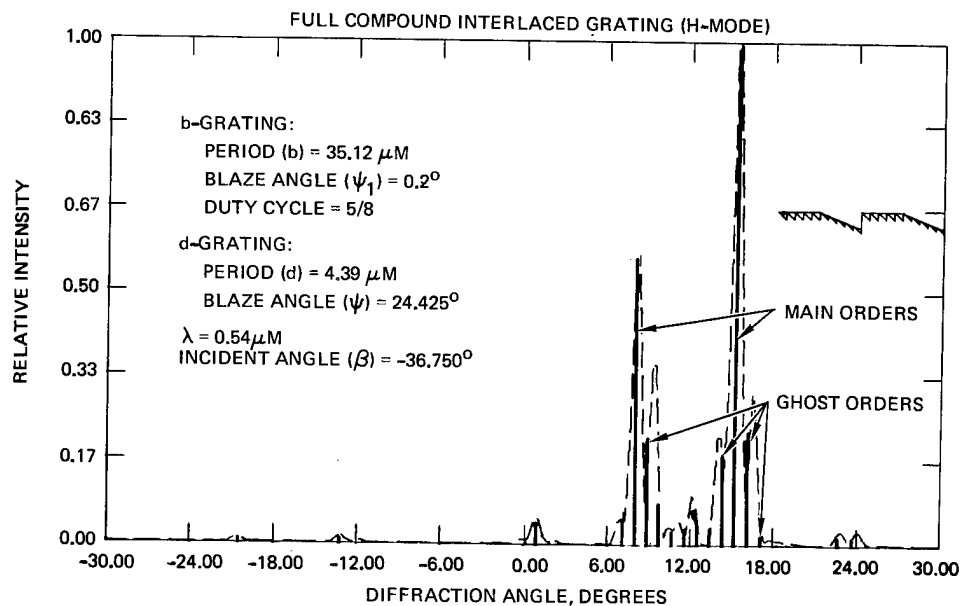
Fig. 21.   CI grating diffraction pattern (theoretical).
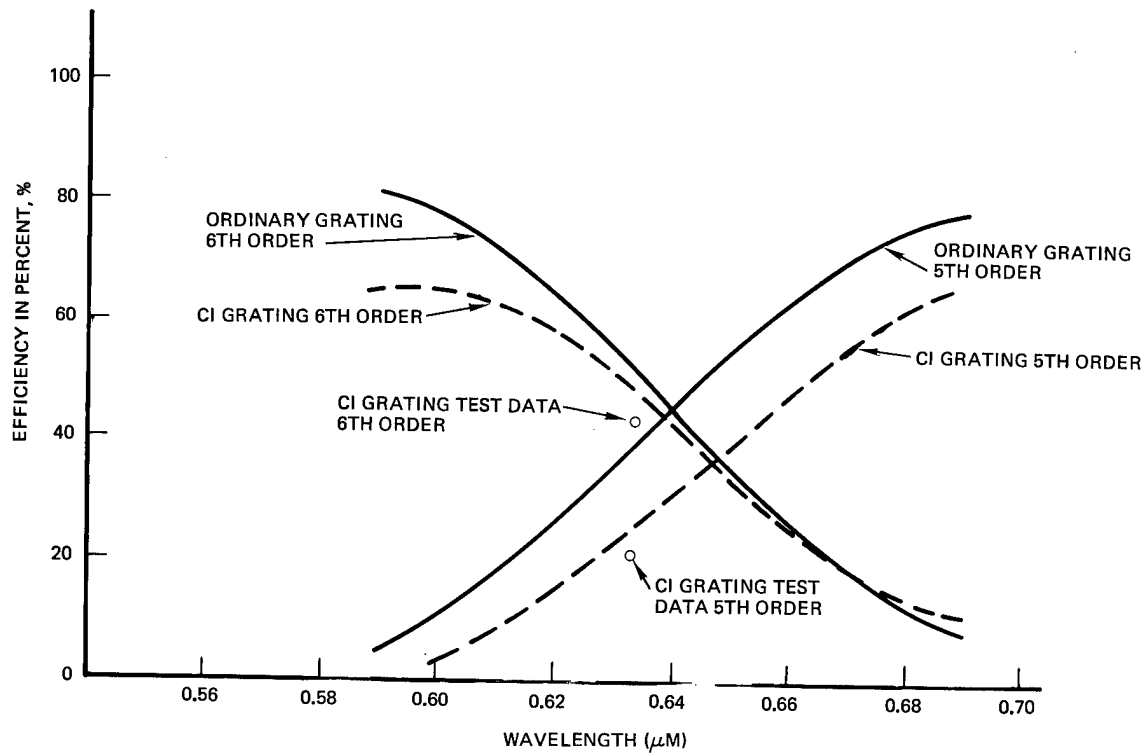
Fig. 22. CI grating theory and test data (prototype TE mode).

Acknowledgement

PRODUCTION OF HIGH HOMOGENEOUS FLUOROPHOSPHATE LASER GLASS

Roger K. Sandwick, R. J. Scheller, K. H. Mader

Schott Optical Glass, Inc.
400 York Avenue
Duryea, PA 18642

Abstract

The production technique used for high homogeneity, fluorophosphate laser glass is reviewed. Different types of inhomogeneities are discussed and methods of prevention are given. An experiment on the effect of annealing on homogeneity is investigated.

Introduction

The production of high homogeneity glass is essential for application in high power laser systems, such as the one currently in operation at Lawrence Livermore Labs. This requirement of high homogeneity applies to all glass (active or nonactive) employed in the system. This includes glass used for undoped lenses and turning mirrors, Faraday rotators, polarizing substrates, and neodymium-doped rods and disc amplifiers.

At present in the Shiva system, LLL uses silicate-based glass types (ED2, BK7, FR5, etc.) for all components. However, in order to achieve the objectives of the next steps of the project, (Nova) where attempts will be made to prove scientific feasibility, improvement in the figure of merit for all optics will be required. To achieve this, a factor termed the nonlinear refractive index must be taken into consideration. It has been realized that lowering this factor results in minimizing the loss of focusable energy to the fusion target. Since the n_2 is directly related to the refractive index (n_d) and Abbe value (v_d) by the formula

(1)

$$n_2 \ (10^{-13} \ esu) = \frac{68 \ (n_d-1) \ (n_d^2 + 2)^2}{V_d \ (1.517 + [\ (n_d^2 + 2) \ (n_d + 1) \ V_d] \ / \ 6 \ n_d)^{1/2}}$$

glasses of low index of refraction and low dispersion are desired. This generally means switching from oxide-host glasses to fluoride glass types. Improvement would thus be made in n_2 values from approximately 1.2×10^{-13} esu for silicates to a minimum 0.25×10^{-13} esu for fluorides (BeF_2). Fluorophosphates, which are being developed especially for this project, will have n_2 values of approximately 0.5×10^{-13} esu. This results in an improvement of the figure of merit for lenses of approximately a factor of two and for laser rods and discs of approximately a factor of three.

Due to the necessity of keeping the loss of focusable energy to a minimum; fluorophosphate glass of extremely high homogeneity is required. Any deviation in refractive index will cause the beam to be distorted in shape and length resulting in less total energy being directed to the deuterium-tritium target. The inhomogeneities of optical glass are divided into two major categories; inclusional and refractive index differentials.

The inclusional inhomogeneities include any of a number of different types of particles (bubbles, crystals, metallic particles) that can scatter or absorb the laser energy as it passes through the glass. An important aspect of this is that with the addition of a sufficient quantity of laser energy onto an inclusion, damage (in a small explosion) occurs which results in a much larger scattering center. Minimizing the amount of particles (especially metallic inclusions and crystals), therefore, raises this damage threshold to acceptable limits required by all high power lasers. This is a very critical factor in the production of fluorophosphate glass types. The high fluorine level in glass often causes instability which results in crystallization or phase separation. Fluorophosphate glasses typically have low damage threshold values of approximately 2-3 J/cm^2 (at a 1.0 n sec. pulse width). Optimization of the LG 812 composition combined with improvements in the melting process at Schott Optical have increased this value to 8-10 J/cm^2. Further developments in these two areas will hopefully result in damage threshold values of greater than 25 J/cm^2, as specified by LLL.

Refractive index inhomogeneities may exist as either a rapid index change (striae, cord) or a gradual deviation in the index of refraction across a piece. Typical glass specifications would not allow any striae and would limit the gradual refractive index deviation across the piece to be no greater than $\pm 1 \times 10^{-6}$.

Discussion

Much effort has to be taken to assure that the final result of the production of fluorophosphate laser glass ends in high homogeneity. This process begins in the batch house where all raw material is chemically analyzed for cation and fluoride levels prior to melting. Impurity levels are also checked. A thorough mixing of the correctly calculated batch is then undertaken using a standard P-K, twin shell mixer.

Due to the high corrosion of fluoride-based glasses on ceramic refractories and to the extremely large tendency for these glass types to crystallize, a completely platinum discontinuous melting system is used. This system centers around an insulated pot of a 35 liter capacity which has the capability of being heated to temperatures up to 1300°C. The thoroughly mixed batch is slowly added into this area by hand until the pot is completely filled. At this time a stirrer is inserted and then a cover installed to close the system so as to inhibit fluorine evaporation.

The glass is then taken through two refining cycles to assure complete melting of raw materials and elimination of bubbles, followed by a stirring down cycle which brings the glass to the correct viscosity for pouring. At all times the four blade stirrer is continuously revolving to distribute the heat and to blend the molten glass thoroughly. This accomplishes two things which can affect the final homogeneity of the laser glass - (1) it helps distribute heat to assure complete melting and prevent stones, bubbles, and other nucleating agents and (2) the blending of the molten glass helps in preventing any chemical segregation (either rapid or gradual).

When the correct temperature (viscosity) of the glass is reached, the glass is then allowed to pass through a short, heated downpipe into a graphite-lined mold. This requirement of obtaining the right viscosity is very critical for fluorophosphate glass types. If the viscosity is too low (temperature too high), turbulence occurs during casting causing surface glass to be pulled down into the center of the block which results in striae. If the viscosity is too high (temperature too low) the glass fails to fill out sufficiently and a large piece is not obtainable. Also, because of the fluorophosphate's relative instability, the crystallization range occurs very close to the lower limit of casting. Allowing the temperature of the glass to dip into this region would, therefore, result in major crystallization. These factors combine to significantly reduce the region of casting of fluorophosphates laser glass types to around 5°C. Strict temperature controls (± 1°C) are required.

After the glass has been given a quick anneal to relieve enough strain in the glass to allow for an inspection polish, the glass is analyzed for inclusions and striae. Inclusions are investigated by eye or microscope by passing a dense beam of white light or red Ne-He laser light through the piece. Striae is analyzed by a near-field shadowgram or schlieren knife-edge test.

Gradual refractive index deviations across the piece are analyzed by use of an interferometer. These index deviations can be of two sources: (1) chemical changes existing through the piece and (2) birefringence caused by stress in glass. The first type of deviation is function of the melting process. Complete mixing prior to and during melting followed by proper forming techniques should eliminate these chemical inhomogeneities. The second type of deviation is directly a function of annealing. At this time in the process, the glass is given a second annealing, much slower than the first, at a rate of between 0.1°C/hr. and 0.8°C/hr. This significantly reduces most of the stress in the glass and, consequently, eliminates the inhomogeneity (birefringence) caused by this stress.

Experimental Procedure

An experiment was run on Schott's LG 812 laser glass to investigate the amount of effect annealing has on improvement of the homogeneity. Two large ellipsical pieces (600 mm x 300 mm x 60 mm; 750 mm x 400 mm x 65 mm) were first given a fairly rapid annealing at 4°C/hr. and analyzed for refractive index deviation. These pieces were then reannealed at a rate of 0.8°C/hr. and analyzed a second time. The difference in homogeneity between these two annealings would, therefore, be directly related to the function of the amount of stress reduced when using a slower rate.

All measurements were done using a Fizeau interferometer made by Zygo. The wavelength of the beam is 632.8 nm.

Results

Pictures taken of the pieces #1 and #2 of LG 812 with the Zygo interferometer are shown as Figures #1 and #2 respectively. In both cases the 4°C/hr. values are given as "A" and the 0.8°C/hr. values are given as "B".
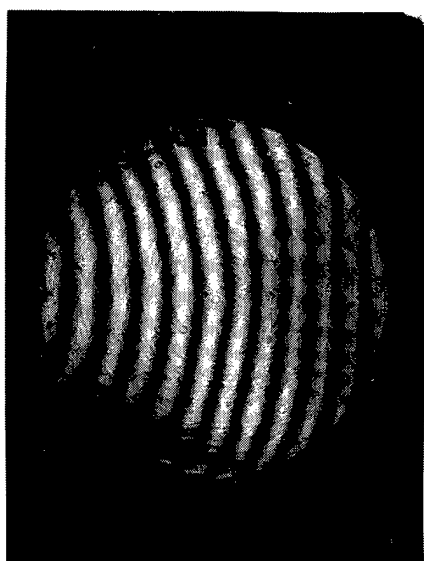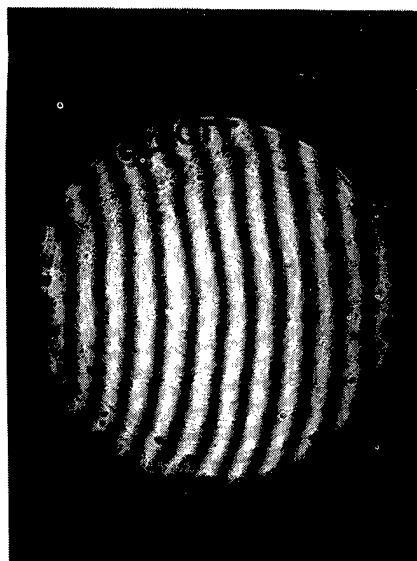
"A"   "B"

Figure #1

"A"   "B"
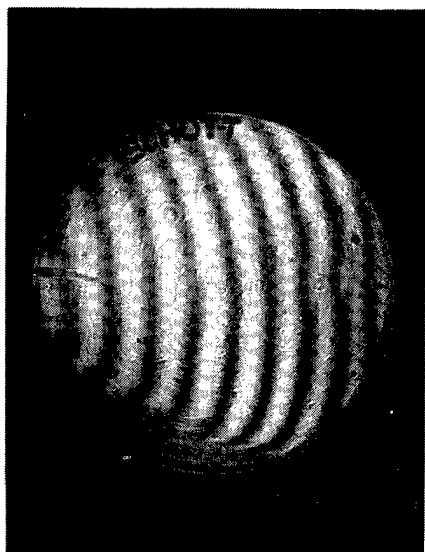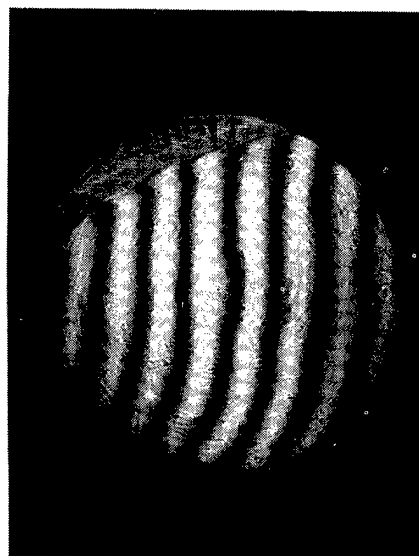
Figure #2

	4°C/hr.			0.8°C/hr.		
	Thickness	Fringe Deviation	Refractive Index Deviation	Thickness	Fringe Deviation	Refractive Index Deviation
Piece #1	59.7	2.2	$\pm$ 5.9 x 10^{-6}	36.6	0.9	$\pm$ 3.9 x 10^{-6}
Piece #2	49.4	1.2	$\pm$ 3.8 x 10^{-6}	45.4	0.6	$\pm$ 2.1 x 10^{-6}

TABLE #1

Table #1 gives the results of the annealing experiment. After calculations by measuring the fringe deviation and computing the refractive index deviation, Piece #1 showed a 66% improvement in homogeneity while Piece #2 improved by 55%.

Conclusion

The method of producing fluorophosphate laser glass of high homogeneity was reviewed. In order to produce the quality required by high power laser systems, much emphasis has to be placed on maintaining a completely uniform composition by melting, homogenizing (stirring), and forming; followed up by annealing. Using proper annealing techniques, the refractive index deviations across a piece of laser glass can be lowered significantly. An experiment with fluorophosphate laser glass shows an average of $\pm 1.85 \times 10^{-6}$ change in homogeneity between a 4°C/hr. and an 0.8°C/hr. annealing.

Acknowledgments

AUTHOR INDEX

SUBJECT INDEX